Investigations into the reduction of soft tissue artefacts using projection of markers and microwave imaging

Vignesh Radhakrishnan

PhD

University of York

School of Physics, Engineering and Technology

September 2024

Abstract

Movement analysis is a widely applied clinical tool for the diagnosis of neurological and musculoskeletal pathologies and in the evaluation of surgical interventions. The clinical gold standard for movement analysis is skin-mounted marker-based systems, whose clinical usability in computing the underlying movement of bones are impeded by soft tissue artefacts (STA). STA are discrepancies in bone movement calculated from skin-mounted markers, and are caused by the interposition of soft tissues.

Multibody kinematic optimisation (MKO) methods are the most widely applied solution to reduce STA. However, the efficacy of MKO methods varies between subjects and investigated motions, with most MKO methods not validated on participants with higher body mass index (BMI) scores.

This thesis proposes a practical solution to reduce the deleterious effects of STA. Two novel marker projection schemes, wherein the markers are projected onto the bone surface, are proposed. The projection schemes are validated on a dataset containing both skin-mounted marker trajectories and reference kinematics, of participants with varying BMI scores performing a wide variety of movements. Additionally, a novel imaging modality for biomechanics, microwave imaging, is investigated to project the markers onto the bone surface during both static and dynamic motion. The feasibility of this application of microwave imaging is investigated using both human models and tissue-mimicking phantoms.

Our results indicate that the projection schemes reduce errors in rotations most affected by STA, and also improves the quality of computed kinematics for all subjects and investigated motions. Additionally, the location of the bone can be detected using microwave imaging and a wearable system, in both static and dynamic situations. Our findings underscore the efficacy and generalisability of our multidisciplinary solution to reduce the effects of STA on computed kinematics, and represent a potential solution to improve the clinical usability of skin-mounted marker-based data.

Contents

List of Figures

List of Tables

Glossary

STA: Soft tissue artefacts

BMI: Body mass index

MKO: Multibody kinematic optimisation

IK: Inverse kinematics

CAST: Calibration Anatomical System Technique

GO: Global optimisation

EKF: Extended kalman filter

CGM: Conventional gait model

DOF: Degree of freedom

MRI: Magnetic resonance imaging

CT: Computed tomography

WBCT: Weight-bearing computed tomography

MI: Microwave imaging

BIM: Born iterative method

DBIM: Distorted born iterative method

GNI: Gauss-newton inversion

MIST: Microwave imaging via space-time beamforming

DAS: Delay-and-sum confocal imaging

DMAS: Delay, multiply and-sum confocal imaging

UWB: Ultra-wide band

TSAR: Tissue sensing adaptive radar

PiG: Plug-in gait model

T3D: Total 3D Gait

SAFLo: Servizio di Analisi della Funzione Locomotoria

LAMB: Laboratorio per l'Analisi del Movimento nel Bambino

UOMAM: University of Ottawa motion analysis model

MUSIC: Multiple signal classification

Acknowledgements

Pursuing a PhD is not an individual event, despite being an individual's research. There is an entire team behind the project encouraging the PhD candidate's personal and professional growth as they develop into an independent researcher. I had an amazing team driving me forward and I would like to take this opportunity to extend my gratitude to them.

I would firstly like to thank my supervisors Adar Pelah and Samadhan Patil for providing me with the freedom to pursue my research interests to the fullest. I would especially like to extend my gratitude to Adar for accepting a new PhD student at the end of the student's first year and ensuring their seamless transition to a completely new PhD topic. I would also like to thank Martin Robinson and my TAP advisors Youngwook Ko and Peter Ellison, who have been instrumental in making my PhD project a reality. A special thanks is owed to Martin who, despite not being an original member of my PhD project, was willing to spend countless hours discussing and enhancing my project.

I would like to thank two external collaborators who helped to shape my PhD. Niccolo Fiorentino, who not only shared his data but also took an active interest in my research and provided valuable guidance, and Peter Serano, whose guidance and advice in developing antennas in Ansys HFSS was instrumental in the PhD project's success.

Lastly, I would like to thank the people who have been in my corner throughout the PhD. My partner, Meghan Bradley, who proof-read my entire thesis and all my papers. She has been instrumental in me successfully navigating both the technical and political waters of the PhD. My colleagues and friends, James, Cameron, Vlad, Alex, Erion, Vishwadeep, Johnathan, Joseph, Anirudh and Shashank, who provided encouragement and timely distractions during the PhD. My family, both in India and the UK, who provided unwavering support throughout my PhD. And, most importantly, my dog Ruskin, who provided more pastoral support with his unspoken words than anyone else with their spoken ones.

Finally, I would like to thank the School of Physics, Engineering and Technology and the University of York for providing me with the opportunity to pursue this PhD.

Declaration and Related publications

I declare that this thesis is a presentation of original work and I am the sole author. This work has not previously been presented for a degree or other qualification at this University or elsewhere. All sources are acknowledged as references.

Parts of this thesis have been submitted to academic journals and conferences, where I am the first author. Co-authors in the submitted papers who are not the supervisors were responsible for guiding the papers and projects. I am solely responsible for the content.

Journal papers

1. Chapter 3:

   Vignesh Radhakrishnan, Samadhan Patil, Adar Pelah, Peter Ellison. Influence of multibody kinematic optimisation pipeline on marker residual errors. *Journal of Biomechanics*, Published, https://doi.org/10.1016/j.jbiomech.2024.112395

2. Chapters 4- 5:

   Vignesh Radhakrishnan, Martin Robinson, Niccolo M Fiorentino, Samadhan Patil, Adar Pelah. Reducing soft tissue artefacts through projection of markers and microwave imaging: An exploratory study. *Nature Scientific Reports*, Published, https://doi.org/10.1038/s41598-025-89586-w

Conference Papers

1. Vignesh Radhakrishnan, Samadhan Patil, Adar Pelah, Peter Ellison. Analysing the effect of body fat on musculoskeletal modelling

systems: A pilot study. *Annual Meeting of the Clinical Movement Analysis Society 2023 - London, United Kingdom*

2. Vignesh Radhakrishnan, Peter Ellison, Samadhan Patil, Adar Pelah, Martin Robinson. Determining bone position from wearable antennas using microwave imaging: A feasibility study. *URSI General Assembly and Scientific Symposium 2023 - Sapporo Convention Centre, Sapporo Business Innovation Centre, Sapporo, Japan*

3. Vignesh Radhakrishnan, Martin Robinson, Peter Ellison, Samadhan Patil, Adar Pelah. Determining bone position using microwave imaging: A feasibility study. *IPEM Science, Technology and Engineering Forum 2023 - University of Strathclyde, Technology & Innovation Centre, Glasgow, United Kingdom*

Chapter 1

Introduction

1.1 Background and motivation

Human walking, or human gait, is a complex pattern of limb movements involving the nervous, musculoskeletal and cardiorespiratory systems. A deviation from typical development of these systems, pain or fatigue can disrupt normal gait, resulting in pathological or abnormal gait [154]. For example, cerebral palsy (CP), a group of lifelong neurological disorders occurring in 2-3 per 1000 livebirths [246], can result in various forms of pathological gait, such as intoeing gait. This is one of the most common gait abnormalities, occurring in >60% of children with CP [261] and can lead to pain, discomfort, and severe functional issues such as difficulties with foot clearance and tripping [186, 260]. Another example of pathological gait is miserable malalignment syndrome (MMS), an abnormality caused by a combination of excessive proximal femoral anteversion and external tibial torsion, which can result in knee pain and functional issues [89].

Gait analysis — the most widely applied clinical branch of human movement analysis — is the study of the factors which disrupt typical gait, and is extensively used to assess and treat individuals with conditions affecting their ability to walk, such as CP and MMS[53, 226]. For example, treatment for intoeing gait is achieved through femoral derotation osteotomy, which is an orthopedic surgical procedure wherein a cut (osteotomy) is made to the upper part of the femur with the femur's alignment subsequently corrected. The success of femoral derotation osteotomies are dependent on pre-operative, intra-operative and post-operative factors. The criteria for performing surgery are dependent on variables computed during gait analysis, such as passive internal rotation greater than 50° , external hip rotation less than 30° and at least 15° of internal hip rotation during the stance phase of gait [83, 186].

One of the key outputs of a clinical gait analysis are the computed linear

and angular positions (and their time derivatives) of the skeletal system, which is referred to as kinematic analysis. The clinical gold standard systems for performing kinematic analysis are optoelectronic systems. These systems utilise reflective markers which are placed on specific anatomical landmarks on the human body, and their recorded trajectories are analysed to calculate the position and velocities of the underlying bones. Whilst commercial optoelectronic systems offer accuracies of a tenth of a millimeter in tracking of the reflective markers, the clinical usability of computed kinematics are undermined due to soft tissue artefacts (STA) and marker-misplacement errors [54].

STA are errors in bone movement computed from the reflective markers when compared with actual bone movement, and are caused by the interposition of soft tissues between the reflective markers and the underlying bone. For example, the recommendation of 15° for performing femoral derotation osteotomy for intoeing gait was to account for inaccuracies in computing hip rotation angles in clinical gait analysis due to STA [228], with McGinley [163] reporting that the hip internal/external rotation angle had the most error in clinical 3-D gait analysis, undermining pre-operative planning for femoral derotation osteotomies.

STA are considered the most critical source of error in gait analysis [58, 141, 194]. Due to their deleterious effect on computed kinematics, STA have been extensively studied, with several solutions proposed to compensate for, or mitigate, their effects. However, despite the plethora of solutions proposed to mitigate the effects of STA on kinematic analysis, no single solution has been proven to be effective for all analysed motions and for all individuals. In addition, the majority of the experimental research undertaken in the field of STA have used participants with a healthy body mass index (BMI) score [194], despite evidence of a direct correlation between higher BMI scores and increased magnitudes of STA [54].

With the prevalence of obesity increasing in both adults and children over the last few decades [34, 61] [75% of adults between the ages of 45 and 74 and 25% of children below the age of 11 are obese in England [34]], this thesis investigates the impact of STA on computed kinematics in clinical gait analysis and proposes solutions to mitigate these effects. The thesis aims to enhance the accuracy of clinical gait analysis by addressing the challenges posed by STA.

1.2 Problem Statement

STA has been termed the most critical source of error in clinical gait analysis, due to the difficulty in compensating for STA. The main reasons for this difficulty, are that STA are marker-location-, subject- and task-specific, and vary during a gait cycle. For example, one study [27] reported that STA affecting thigh markers is maximum at the stance phase of the gait cycle, with STA at the shank markers

reaching its maximum in the swing phase. Additionally, they also reported that the magnitude of STA at the thigh is greater than the magnitude of STA at the shank. Another study [74] reported that different locations of thigh marker underwent different magnitudes of STA during the same motion and affected the computed kinematics differently. For example, the authors reported that proximal thigh markers produced lesser knee varus-valus range and smaller hip rotation range than distal thigh markers, indicating lesser influence of STA. STA has also reportedly been affected by the motion and the subjects: [240] reported that a hopping motion produced more STA than walking and [54] reported that subjects with higher BMI had greater magnitudes of STA.

In addition to being dependent on the task, subject and marker-location, STA have a similar frequency content (around 6 Hz) to that of actual movement, thereby rendering traditional filtering techniques ineffective [141]. Due to the aforementioned reasons, developing a generalisable solution to compensate for STA has been difficult, as most of the existing solutions have been tailored towards a specific motion, marker-location or specific source of STA.

Amongst the various solutions proposed, multibody kinematic optimisation (MKO) methods are the most widely applied, and are incorporated in commonly used musculoskeletal modelling software. The efficacy of MKO methods are dependent on the: joint models of the underlying musculoskeletal model, marker placements and marker weights. Furthermore, studies have shown that MKO methods are optimal only when subject-specific joint models and subject- and task-specific marker weights are incorporated necessitating the development of subject-specific models, which do not allow for the development of a generalisable solution [57, 242]. In addition to optimal MKO methods not being generalisable, the majority of MKO methods are predominantly analysed using participants with healthy BMI scores [42], therefore not indicating their potential to be applied to the general population and therefore improve the accuracy of clinical gait analysis.

In this thesis we propose and validate a generalisable (applicable to individuals with varying BMI scores) and practical solution to reduce the impact of STA on clinical gait analysis and improve the accuracy of computed kinematics. Specifically, this thesis proposes two marker-projected MKO methods to reduce joint angle error caused by STA. Marker-projection is enabled by the application of microwave imaging: a safe, cost-effective, and operator-independent imaging modality.

The decision to analyse the projection of markers was informed by studies reporting that complementing optoelectronic systems with actual bone movement — obtained using intracortical pins, percutaneous trackers or imaging modalities such as fluoroscopy, magnetic resonance imaging or computed tomography — reduces the effect of STA[72, 173]. The decision to investigate microwave imaging

was undertaken to overcome the limitations of ultrasound imaging, which has been previously been investigated to reduce STA [129, 160].

We present evidence that our proposed, multi-disciplinary solution — which is designed to complement optoelectronic systems — not only reduces the deleterious effects of STA on computed kinematics, but also improves the quality of computed kinematics for clinical gait analysis.

1.3 Thesis outline and contributions

The thesis follows a chapter-based structure, where each chapter explores a key aspect of the problem statement with sequential chapters building and exploring on the results of the previous chapters. The thesis structure and the contributions are listed below:

- **Chapter 2** provides a comprehensive review of the existing methods to reduce STA, emphasizing the difficulty of developing a generalisable solution to reduce STA. In addition, it reviews imaging modalities currently applied in biomechanics. Ultimately, it introduces the principle underpinning microwave imaging and reviews studies leveraging microwave imaging to image the object of interest. The key objectives of this chapter are to: emphasise the difficulty of reducing the effects of STA and the ineffectiveness of existing MKO methods, introduce different imaging modalities applied in biomechanics, and introduce microwave imaging and the advantages of applying microwave imaging in biomechanics

- **Chapter 3** proposes and investigates a new metric — residual error — to evaluate the efficacy of MKO methods in the absence of ground-truth bone movement data. It investigates the factors which affect residual error and the relationship between residual error and joint angle errors in the presence of increasing body fat. The main objectives of this chapter are: to propose residual error as a metric to evaluate MKO methods in the absence of ground truth data, to evaluate the efficacy of MKO methods in the presence of increasing body fat, and to evaluate their generalisability

- **Chapter 4** proposes two novel marker projection techniques to reduce the effect of STA on clinical gait analysis. Joint angles obtained from our novel marker projection techniques are compared with ground truth joint angles (obtained using fluoroscopy) and joint angles obtained using conventional (un-projected) markers. The main objectives of this chapter are: to propose and experimentally validate our marker-projection schemes, and highlight

the improvement in joint angle accuracy obtained from our marker-projection schemes for clinical gait analysis

- **Chapter 5** introduces and investigates the feasibility of applying microwave imaging in the field of clinical gait analysis, through simulations. Specifically, the efficacy of microwave imaging in determining the location of the bone from the skin surface — to enable marker projection which was described in the previous chapter — under specific conditions is investigated. The main contributions of this chapter are to show the efficacy of microwave imaging in detecting the location of the bone in models of varying BMI scores, in both static and posed states, with data collected under specific conditions. The results support the potential application of microwave imaging as an alternative imaging modality to ultrasound imaging in the field of biomechanics

- **Chapter 6** expands on the investigations discussed in the previous chapter, by moving to experimental validation of microwave imaging. Tissue-mimicking phantoms of bone and muscle are developed to represent the thigh. Microwave imaging, using novel antennas and with data collected under the same conditions of the previous chapter, is applied to detect the location of the bone in the phantom. The main contributions of this chapter are: to discuss the development of a novel multi-layered solid phantom representing the bone; to validate the efficacy of incorporating microwave imaging in biomechanics experimentally.

- **Chapter 7** summarises the results and conclusions of the thesis. It discusses clinical implications and the improvement in accuracy in clinical gait analysis obtained from our proposed solutions. It further discusses limitations of the research undertaken and the potential future directions of this research.

Chapter 2

Background

2.1 Introduction

As discussed in Chapter 1 soft tissue artefacts (STA) are considered the most critical source of error in stereophotogrammetry systems [58, 141] due to the difficulty in compensating or ameliorating their effects on kinematic analyses. Errors in joint angle calculation due to STA can invalidate the clinical interpretability of clinical gait data. For example, errors due to STA can affect the pre-operative planning of surgical interventions such as femoral derotation osteotomies.

Whilst multiple solutions have been proposed to reduce the deleterious effect of STA on kinematic analyses, no single solution has been proven to be effective for all investigated motions, participants and marker locations.

In this review chapter we aim to highlight the magnitude of joint angle errors caused due to STA and the joint angles most affected by STA. We additionally review existing methods to reduce STA, including multibody kinematic optimization (MKO) methods. This chapter reviews these methods, highlighting their strengths and limitations, and identifies gaps that the proposed solutions aim to address. Through this review section, we aim to provide a comprehensive background on the research undertaken to quantify the effects of STA and research done in reducing their effects.

Furthermore, in this chapter we review studies which have leveraged different imaging modalities to study the movement of bones, highlighting the benefits and drawbacks of different imaging modalities. The chapter finally introduces and reviews research done in the field of microwave imaging, a novel, non-ionising and cost-effective imaging modality, which we have investigated as a potential imaging modality to image the bone and as a potential alternative to the previously reviews imaging modalities.

The structure of this chapter is as follows:

- Section 2.2 provides a brief introduction to movement analysis and describes the basic principles of kinematic analysis
- Section 2.3 reviews the research undertaken in the field of STA: Subsection 2.3.1 covers the studies quantifying STA, Subsection 2.3.2 reviews studies proposing novel approaches to reduce the effect of STA, and papers validating existing and novel methods proposed to reduce the effect of STA, with the conclusions and key-takeaways provided in Subsection 2.3.3
- Section 2.4 discusses the different imaging modalities which have been applied in movement analyses, specifically fluoroscopy, computed tomography, magnetic resonance imaging and ultrasound. Subsection 2.4.1 discusses our conclusion and key-takeaways from this section
- Section 2.5 introduces microwave imaging and reviews studies which leverage the basic principles of microwave imaging to detect the object of interest. Subsection 2.5.1 reviews work done in quantitative microwave imaging with qualitative microwave imaging reviewed in Subsection 2.5.2. Subsection 2.5.3 reviews papers proposing novel antennas and papers analysing the sensitivity of microwave imaging algorithms. Our conclusion and key-takeaways are provided in Subsection 2.5.4
- Section 2.6 discusses our conclusion and key-takeaways from this chapter

2.2 Kinematic Analyses

Variations in gait and/or movement associated with activities of daily living are often manifestations of neuromuscular pathologies, pain or fatigue. Therefore, clinical gait analysis is widely applied to aid in the diagnosis of musculoskeletal and neurological pathologies, to quantify dysfunction and to assess the outcomes of a rehabilitation or surgical procedure [53].

Clinical gait analysis is predominantly described in three planes (Figure 2.1): the sagittal plane, which divides the body into left and right symmetrical parts, the frontal plane, which divides the body into anterior and posterior parts, and the transverse plane, which divides the body into superior and inferior parts.

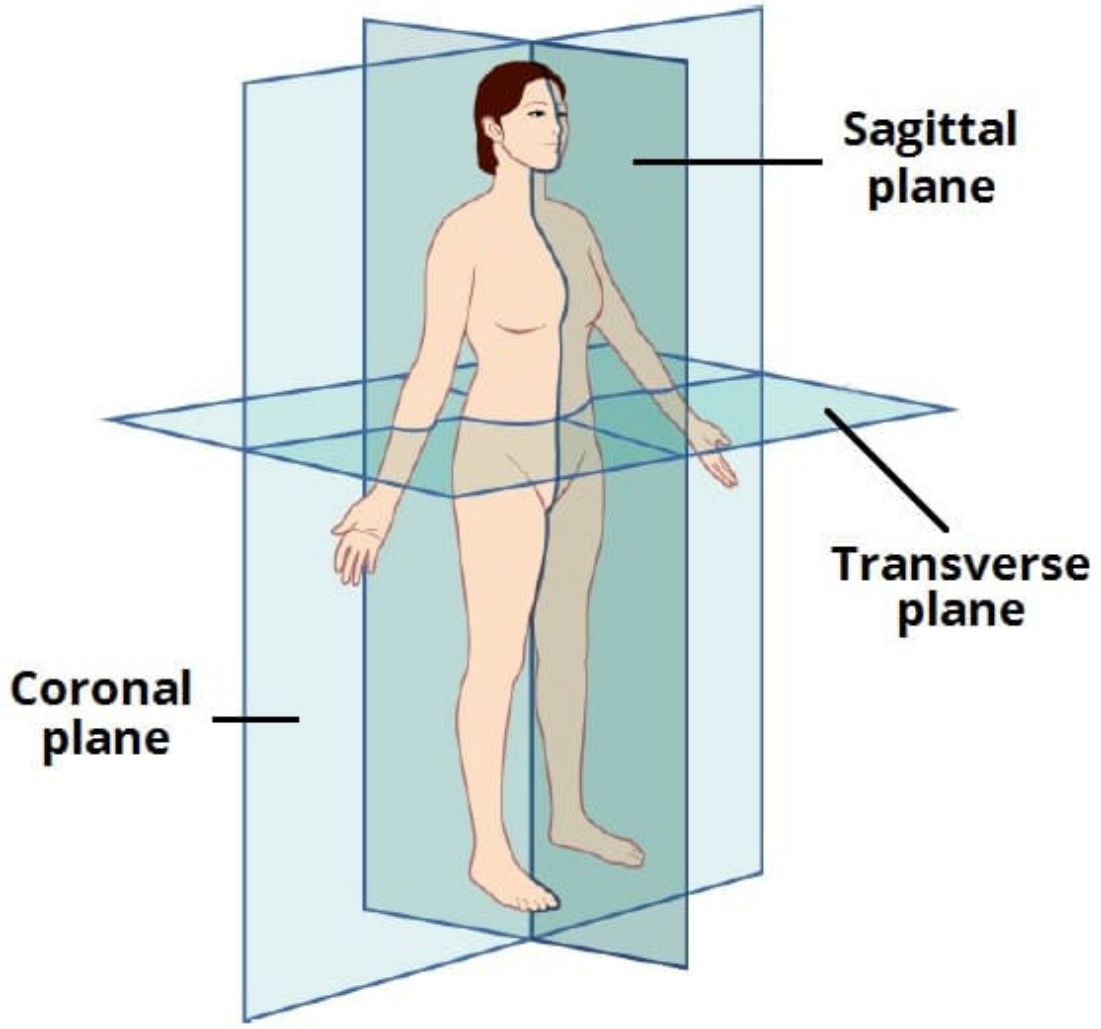

Figure 2.1: Pictorial representation of the three anatomical reference frames of movement: Sagittal plane, Frontal/Coronal plane and Transverse plane [13]

Clinical gait analysis can be performed either qualitatively using video vector technology — which comprises of interpreting variations in gait by visually analysing movement acquired using video cameras in the sagittal and/or frontal plane — or quantitatively using 3 dimensional (3-D) gait analysis. Whilst, visual analysis of gait in the sagittal plane can be accurate, visual analysis of gait in the frontal and transverse plane using a frontal camera is prone to errors due to the small magnitude of movement in these planes. Therefore, 3-D gait analysis is required for a quantitative analysis of movement in all three planes.

Stereophotogrammetry systems are the clinical gold standard for 3-D gait analysis (and biomechanics) and work by placing reflective (or active) markers on spe-

cific landmarks on the human body; the marker's recorded trajectories are then analysed to evaluate the motion of the body (Figure 2.2). Stereophotogrammetry systems typically require a designated area which is spanned by multiple infrared cameras to record the markers, and are often used in conjunction with force plates.

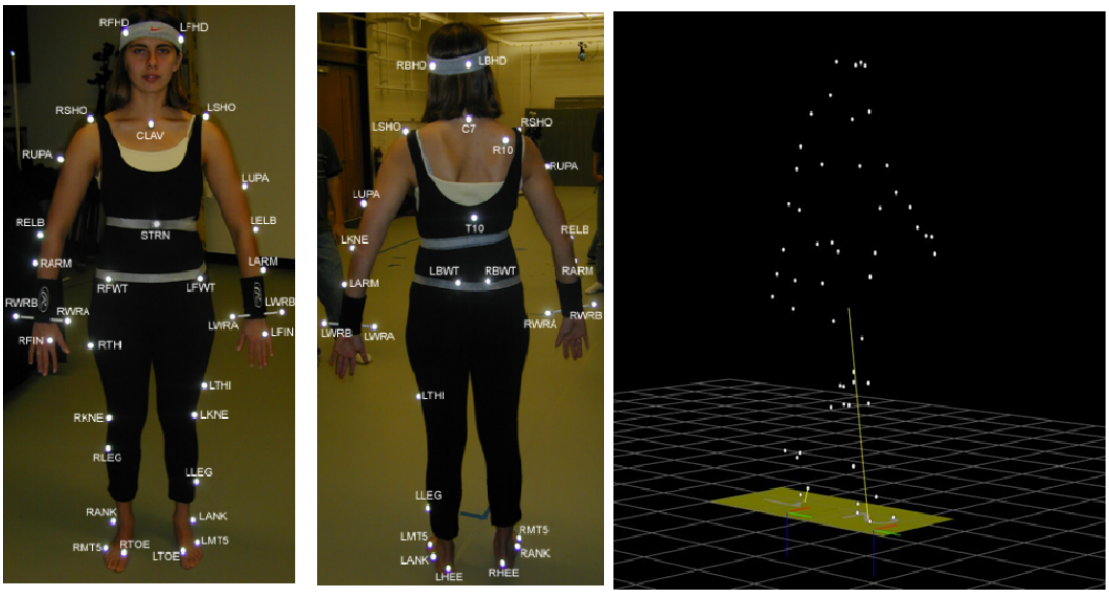

Figure 2.2: Skin-mounted markers placed at specific anatomical locations on the human body. For example in the above picture the markers are placed at anatomical landmarks stated in Vicon's full body markerset [2, 3]. Marker labels can vary from system to system with the location and number of markers generally consistent between markersets. For example, in the above picture: RFHD and LFHD are the right and left head markers, C7 is the cervical marker, RSHO and LSHO are the right and left shoulder markers, CLAV is vertebrae cervical marker, STRN is the sternum marker, T10 is the vertebra thoracic marker, RUPA and LUPA are the right and left upper arm markers, RELB and LELB are the right and left elbow markers, RARM and LARM are the right and left arm markers, RWRB, RWRA and LWRB, LWRA are the right and left wrist wand markers, RFIN and LFIN are the right and left finger markers, RFWT and LFWT are the right and left anterior iliac spine markers, RBWT and LBWT are the posterior iliac spines, RTHI and LTHI are the right and left thigh markers, RKNE and LKNE the right and left lateral epicondlye markers, RLEG and LLEG are the right and left shank markers, RANK and LANK are the right and left lateral malleoli markers, RHEE and LHEE are the right and left heel markers, RMT5 and LMT5 are the right and left fifth metatarsal marker, RTOE and LTOE are the right and left first metatarsal markers. Marker locations are determined based on markersets where are designed for specific purposes. A snapshot of a gait cycle observed using the marker trajectories is shown on the right.

Clinical gait analysis includes three main components [212]:

- Kinematic analysis, which quantifies the linear and angular positions of the

body, and is the study of motion without regard for the causes of motion

- Kinetics, which is the study of why the observed motion occurs and examines the underlying linear forces and rotational torques that dictate the kinematic motion

- Electromyography, which is the study of muscle activation and recruitment of muscles

The work described in this thesis and therefore the studies reviewed in this chapter are focused exclusively on kinematic analyses. However, since the outputs of kinematic analyses are used in the study of forces and muscle recruitment, the impact of the research is not purely limited to kinematic analyses. For example, uncertainties in kinematics have been reported to affect calculation of moments, forces and muscle activation [172, 174, 179, 252] with uncertainties in kinematics found to contribute more to dynamic residuals than uncertainties in force plate data [172].

Kinematic analysis is the study and calculation of linear and angular positions of every body segment with respect to one another. Joint angles are calculated as the orientation of one segment with respect to another segment, with the latter segment considered the reference segment. For example, hip angles are computed as the variation of the thigh segment with respect to the pelvis, with the pelvis considered as the reference segment (Figure 2.3). One exception are the pelvic angles, which are computed against the laboratory coordinate system (described below). The segment and reference segment for the lower-body joint angles are provided in Table 2.1.

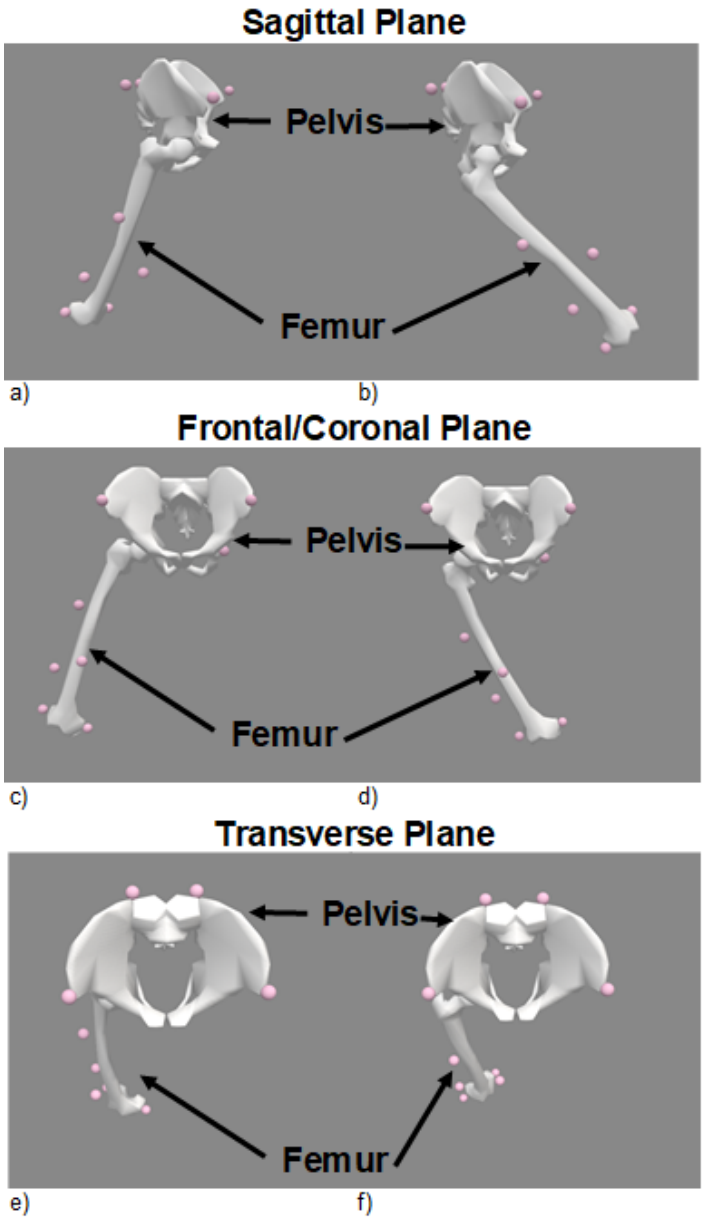

Figure 2.3: Pictorial representation of hip joint rotations in the three planes at the hip and knee. a) Hip extension measured in the sagittal plane. b) Hip flexion measured in the sagittal plane. c) Hip abduction measured in the coronal/frontal plane. d) Hip adduction measured in the coronal/frontal plane. e) Hip external rotation measured in the transverse plane. f) Hip internal rotation measured in the transverse plane. All hip joint rotations are measured between the femur and pelvis.

Joint angle	Plane	Segment	Reference segment
Pelvic tilt	Sagittal	Pelvis	Global/Lab coordinate system
Pelvic Obliquity	Frontal/Coronal	Pelvis	Global/Lab coordinate system
Pelvic rotation	Transverse	Pelvis	Global/Lab coordinate system
Hip Flexion/Extension	Sagittal	Thigh	Pelvis
Hip Abduction/Adduction	Frontal/Coronal	Thigh	Pelvis
Hip Internal/External Rotation	Transverse	Thigh	Pelvis
Knee Flexion/Extension	Sagittal	Shank	Thigh
Knee Varus/Valgus	Frontal/Coronal	Shank	Thigh
Knee Internal/External Rotation	Transverse	Shank	Thigh
Ankle Dorsiflexion/Plantarflexion	Sagittal	Foot	Shank
Ankle Inversion/Eversion	Frontal/Coronal	Foot	Shank
Ankle Internal/External Rotation	Transverse	Foot	Shank

Table 2.1: Definition of segment, observing plane and reference segment for lower body joint angles.

Body segments, in biomechanics, are represented as rigid segments, with interaction between two segments described by joint models which permit between zero to six degrees of freedom (DoF) motion between the two segments. A collection of rigid segments constitutes a biomechanical model [212], with each rigid segment associated with a local coordinate system (LCS). The global coordinate system (laboratory coordinate system, GCS) is described by the stereophotogrammetry system. The orientation and position of rigid segments are described as transformations from the GCS to the LCS, with the orientation between two segments (LCSs) is defined by rotations about their axes. LCSs for each segment on the lower body are defined using anatomical landmarks and vector definitions [59, 262, 263] which are listed in Table 2.2. Typically, three non-collinear markers (pink marker in Figure 2.3) are required to describe and track a segment (LCS), with the definition and determination of LCSs performed during a standing static trial. For example, for computation of hip joint angles, the markers on the thigh are used to track the thigh LCS, with the markers on the pelvis used to track the pelvic LCS. Hip joint angles are defined as the rotation and translation of the thigh LCS with respect to the pelvis LCS.

Algorithms implemented to determine the pose (the position and rotation) of a LCS can be broadly classified into three main categories and have been labelled for the sake of this review as follows: [153, 212]:

- Category 1: Direct pose estimation
- Category 2: Segment optimisation methods
- Category 3: MKO methods

Whilst the three categories differ in their approaches for calculating segmental poses, they share a principle assumption: that the markers are rigidly attached to the body segments i.e. the location of the marker in the LCS remains constant.

Direct pose estimation (Category 1 algorithms) computes the orientation and position of each segment using the LCS at every frame of a motion trial, with the LCSs redefined at every frame using the same markers and unit vector definitions employed during the static trial (Table 2.2). This enforces the requirement that the same markers used for creating the LCS are tracked during a motion trial. This removes the possibility of either redundancy in the number of markers used or of leniency in marker placement. This approach also enforces that the required markers are visible in all frames. As a result of the above requirements, direct pose estimation is extremely prone to marker misplacement errors (errors in the placement of markers) and STA, with any error in marker location directly reflected in the computed kinematics. Other limitations of direct pose estimation are the propagation of errors from distal to proximal segments (due to segments below the pelvis sharing a virtual joint centre created by the proximal segment), and the inability of direct pose estimation to measure joint translations as each distal segment shares a common point with the proximal segment [212]. Direct pose estimation is used by the Conventional Gait Model (CGM) [79, 142].

Segment name	**Origin**	$\hat{i}'$	$\hat{k}'$	$\hat{j}'$
Pelvis	$\vec{O}_{\text{PELVIS}} = 0.5 * \left(\vec{P}_{\text{RASIS}} + \vec{P}_{\text{LASIS}}\right)$	$\hat{i}' = \frac{\vec{P}_{\text{RASIS}} - \vec{O}_{PELVIS}}{\lvert\vec{P}_{RASIS} - \vec{O}_{PELVIS}\rvert}$	$\hat{v} = \frac{\vec{O}_{PELVIS} - 0.5*\left(\vec{P}_{RPSIS} + \vec{P}_{LPSIS}\right)}{\lvert\vec{O}_{PELVIS} - 0.5*\left(\vec{P}_{RPSIS} + \vec{P}_{LPSIS}\right)\rvert}$ $\hat{k}' = \hat{i}' \times \hat{v}$	$\hat{j}' = \hat{k}' \times \hat{i}'$
Thigh	$\overrightarrow{\text{P}}'_{\text{RHIP}} = \begin{bmatrix} 0.36 * \lvert\overrightarrow{\text{P}}_{\text{RASIS}} - \overrightarrow{\text{P}}_{\text{LASIS}}\rvert \\ -0.19 * \lvert\overrightarrow{\text{P}}_{\text{RASIS}} - \overrightarrow{\text{P}}_{\text{LASIS}}\rvert \\ -0.30 * \lvert\overrightarrow{\text{P}}_{\text{RASIS}} - \overrightarrow{\text{P}}_{\text{LASIS}}\rvert \end{bmatrix}$ $\vec{O}_{RTHGH} = \vec{P}_{RHIP}$	$\hat{i}' = \hat{j}' \times \hat{k}'$	$\hat{k}' = \frac{\vec{O}_{RTHGH} - 0.5*\left(\vec{P}_{RLK} + \vec{P}_{RMK}\right)}{\lvert\vec{O}_{RTHGH} - 0.5*\left(\vec{P}_{RLK} + \vec{P}_{RMK}\right)\rvert}$	$\hat{v} = \frac{\left(\vec{P}_{RLK} - \vec{P}_{RMK}\right)}{\lvert\vec{P}_{RLK} - \vec{P}_{RMK}\rvert}$ $\hat{j}' = \hat{k}' \times \hat{v}$
Shank	$\vec{O}_{RSHANK} = 0.5 * \left(\vec{P}_{RLK} + \vec{P}_{RMK}\right)$	$\hat{i}' = \hat{j}' \times \hat{k}'$	$\hat{k}' = \frac{\vec{O}_{RSHANK} - 0.5*\left(\vec{P}_{RLA} + \vec{P}_{RMA}\right)}{\lvert\vec{O}_{RSHANK} - 0.5*\left(\vec{P}_{RLA} + \vec{P}_{RMA}\right)\rvert}$	$\hat{v} = \frac{\left(\vec{P}_{RLK} - \vec{P}_{RMK}\right)}{\lvert\vec{P}_{RLK} - \vec{P}_{RMK}\rvert}$ $\hat{j}' = \hat{k}' \times \hat{v}$
Foot	$\vec{O}_{\text{RFOOT}} = 0.5 * \left(\vec{P}_{RLA} + \vec{P}_{RMA}\right)$	$\hat{i}' = \hat{j}' \times \hat{k}'$	$\hat{k}' = \frac{\vec{O}_{RFOOT} - 0.5*\left(\vec{P}_{RMH5} + \vec{P}_{RMH1}\right)}{\lvert\vec{O}_{RFOOT} - 0.5*\left(\vec{P}_{RMH5} + \vec{P}_{RMH1}\right)\rvert}$	$\hat{v} = \frac{\left(\vec{P}_{RLA} - \vec{P}_{RMA}\right)}{\lvert\vec{P}_{RLA} - \vec{P}_{RMA}\rvert}$ $\hat{j}' = \hat{k}' \times \hat{v}$

Table 2.2: RASIS and LASIS are the right and left anterior iliac spine markers. RPSIS and LPSIS are the right and left posterior iliac spine markers. RLK and RMK are the lateral epicondyle marker and medial epicondyle marker for the right thigh. RLA and RMA are the lateral malleoli and medial malleoli for the right shank. RMH5 and RMH1 are the markers at the fifth metatarsal and first metatarsal respectively. The same conventions are used for the left leg markers. $\vec{P}$ is the position of the marker and $\vec{O}$ is the origin of the segment.

Category 2 algorithms, in contrast to category 1 algorithms, computes both joint rotations and joint translations, and are referred to as segment optimisation methods (six degrees of freedom [6-DoF] methods, SOM). They estimate all six variables — three position and three rotation — to determine the pose of a segment. The methods do not assume any explicit linkage between segments, with the movement of endpoints between the proximal and distal segments directly computed from the motion capture data [212]. SOM use the same LCSs definitions as direct pose estimation (Table 2.2), and therefore require markers at the same anatomical landmarks during the static trial. However, segment poses during the motion trial are determined using three or more additional markers (tracking markers) attached rigidly to each segment. This enables less rigidity in the placement of anatomical markers required for the static trial and provides more flexibility in the placement of tracking markers for the motion trial. Notably, areas with less soft tissues are predominantly chosen to reduce the impact of STA on calculated kinematics [212]. SOM determines the orientation and position of each segment at every frame by minimising the sum of squared errors (Equation 2.1) subject to orthonormal constraints (Equation 2.2).

$$E = \sum_{i=1}^{m}((\vec{P}_{\mathrm{i}} - R'_{SEG}\vec{P}'_i) - \vec{O}_{SEG})^2 \tag{2.1}$$

subject to orthonormal constraint:

$$R'_{SEG}R_{SEG} = 1 \tag{2.2}$$

Where:

- E: The total error to be minimized
- m: Number of markers
- $\vec{P}_i \in \mathbb{R}^n$: Position of the marker as computed from the optoelectronic system in the global coordinate system
- $\vec{P}'_i \in \mathbb{R}^n$: Position of the marker in the local coordinate system acquired during the static trial
- $R'_{\mathrm{SEG}} \in \mathbb{R}^{n\times n}$: Estimated rotation matrix of the segment
- $\vec{O}_{\mathrm{SEG}} \in \mathbb{R}^n$: Origin of the segment

Various implementations of SOM have been proposed to determine the rigid body transformations, with the most widely applied SOM implementations proposed by Spoor and Veldpaus [239] and Soderkvist [247]. Spoor and Veldpaus [239] promoted the use of Lagrangian multipliers and eigen value decomposition to determine the optimal rotation and translation matrices, a method which was subsequently improved by Veldpaus and Woltring [257], who avoided the computation of eigenvectors thereby reducing the computational load. This improved method is incorporated in Visual3d [1]. Soderkvist [247] proposed the use of singular value decomposition (SVD) instead of eigen value decomposition, with the proposed method observed to improve stability and performance in ill-conditioned problems. This implementation has been applied in pycgm2 [143]. Whilst SOM overcomes the drawbacks of direct pose estimation, by assuming that the segments are linked implicitly (and not explicitly using a shared joint centre) and by providing flexibility in terms of marker placement, the excessive movement of markers (due to STA) may still result in non-physiological joint translations, dislocations and unreliable joint kinematics [141, 153].

Multibody kinematic optimisation (MKO) methods (MKO, Category 3 algorithms) [153] were proposed to overcome the limitations of SOM (computing non-physiological kinematics) by simultaneously computing the optimal pose of all segments of a multi-link model to best match the motion capture data at each frame.

The first MKO method proposed was the global optimisation method (GOM) [153], whose underlying principle was that by incorporating physically realistic joint constraints and simultaneously minimising the difference between measured and model-derived marker positions across the entire body, the impact of STA and measurement error on pose estimation will reduce [141, 153, 212]. GOM was initially proposed by Lu and Connor [153], who demonstrated the superior performance of their proposed algorithm (GOM) over SOM by using simulated gait trials with artificial noise added to the marker trajectories. GOM was reported to produce higher fidelity kinematics and reduce the effect of artificial noise when compared to SOM.

GOM was further extended to generalised coordinates by Van-den Bogert [256], where generalised coordinates are a minimum set of independent variables which can be used to describe the pose of the model. The formulation proposed by Van-den Bogert [256] is applied in OpenSim, a widely used musculosekeletal modelling software [81, 231] for performing kinematic analyses.

Whilst the initial GOM method proposed by Lu and Connor [153] was based on least-squares formulation and incorporated spherical joint models, several algorithms leveraging the underlying principle of GOM — simultaneously minimising the difference between measured and model-derived marker positions across the entire body to compute the optimal joint angle — have since been proposed. These algorithms employ different joint models, initial conditions and cost functions to improve kinematic accuracy. They can also be based on either the least-squares formulation or kalman filters. All algorithms, including GOM, which calculate joint angles by simultaneously minimising the difference between measured and model-derived marker positions across the entire body, have been termed as multi-body kinematic optimisation (MKO) methods to ensure consistency across literature [42]. In this thesis, we will leveraging the MKO method proposed by Lu and Connor: GOM.

Another advantage MKO methods have over SOM methods are that fewer than three markers may be incorporated per segment — as the incorporated joint models reduces the number of DoFs — providing greater flexibility in marker placement.

2.3 STA

Whilst stereophotogrammetry systems are extremely accurate — capable of obtaining sub-millimeter accuracy — the fidelity of their data is affected by four main errors [54]:

1. Kinematic measures and processing errors

2. Errors in measurement and processing of ground reaction forces (GRF)

3. Errors in determination of joint model parameters

4. Errors in estimation of inertial parameters

.

Pertinent to our work, kinematic measures and processing errors (kinematic errors) — which encompass apparent marker movements (errors caused by the resolution of the camera system), STA and marker-misplacement errors (systematic and mutually-dependent errors primarily caused by the interposition of soft tissues between the skin-mounted markers and the underlying bones [54]) — result in the invalidation of skin-mounted marker-based data [54]. Whilst apparent marker movements can be compensated through the use of digital filters or splines, and marker-misplacement errors can be reduced through both improved clinician training and the use of digital pointers, compensating for STA is difficult due to its task-, subject-, and location- dependent nature. Additionally, STA has a similar frequency content to that of actual bone movement, making traditional filtering methods ineffective. These challenges with compensating for STA have resulted in it being recognised as a critical source of error in clinical gait analysis using stereophotogrammetry systems [58, 141, 194].

Consequently, a significant amount of research has been undertaken to quantify STA and its effects on joint kinematics; to develop novel approaches to ameliorate STA; and to validate the proposed approaches. The following subsections aim to provide a comprehensive review of the scientific literature concerning STA, to highlight the magnitude of errors caused by STA and to highlight the strengths and limitations of the existing solutions to reduce the effect of STA.

2.3.1 Quantification of STA

The following subsection will review literature concerning the quantification of STA. Through this subsection we aim to highlight the magnitude of errors caused by STA, the variation in errors due to differing motions, participants and marker-location, and the joint angles most effected by STA.

The three classes of algorithms leveraged to determine the pose of the body (direct pose estimation, SOM and MKO methods, see previous section for further details) assume that each body segment is rigid. I.e the location of the marker in the LCS remains constant throughout the motion trial. Therefore, any deviation from this reference position during the motion trial is attributed to STA and is used to quantify STA [108, 141].

Studies quantifying STA have primarily reported their results using two metrics:

1. Errors in joint kinematics (calculated by comparing kinematics computed using skin-mounted markers with ground-truth kinematics or joint angles of the actual bones)

2. Magnitude of marker (cluster) deformation and displacement in the segment LCS. I.e magnitude of marker movement from the reference location in the LCS.

For the latter metric (displacement and deformation in the segment LCS), the impact of STA on individual markers and a cluster of markers is determined using the rigid movement of the marker (or cluster of markers) in the LCS, and the non-rigid deformation of a clusters of markers. To standardise the latter metric, the following metric were proposed by Grimpampi[108]:

1. Metrics for a single marker were described as peak-to-peak displacement of the marker position in the LCS

2. Metrics for a cluster of markers were described as the variation in position, orientation, size and shape of the cluster during the motion trial

Another important requirement to quantify STA is ground-truth kinematics or the true joint angles of the underlying bones, henceforth referred to as artefact-free bone movement. To acquire artefact-free bone movement studies have incorporated both invasive (intracortical pins and percutaneous trackers) and noninvasive (imaging modalities) methods. This review covers research leveraging both methods to acquire artefact-free bone movement.

Benoit [45, 46] quantified STA during walking and cutting motions leveraging intracortical pins to determine artefact-free bone movement, with STA quantified as errors in joint kinematics. They authors observed that joint errors were larger during the cutting motion compared with walking, and that STA patterns were repeatable within-subject but not between-subjects [46]. Additionally, they also reported that internal/external and abduction/adduction rotations were significantly impacted by STA. In their subsequent study, the authors leveraged both bi-planar radiographs and intracortical pins to define the LCS, and calculated the displacement of the marker in the LCS to quantify STA. They reported that the rigid component of STA was more significant than the non-rigid component of STA [45].

Similarly, intracortical pins were also used to quantify STA in the shoulder and arm complex during functional motions of daily life and sport by Blache [48]. STA was quantified as marker displacements in the LCS, with authors reporting that STA varied between participants and motions and that the rigid component contributed the most to STA.

Another invasive method used to determine artefact-free bone movement are percutaneous trackers. They are metal devices which are rigidly attached to bony segments using a number of halo pins [141] and are instrumented with four reflective markers. Percutaneous trackers were designed to provide artefact-free bone movement through minimally invasive methods compared to intracortical pins. These devices were used by Holden [118] to quantify STA in the shank during walking. The authors observed longitudinal rotation errors of 8° due to STA, which were comparable to the true internal/external knee rotations. They also observed different STA patterns and magnitudes between subjects, a finding echoed by the above studies.

The application of invasive methods to calculate artefact-free bone movement had the following limitations: bending of intracortical pins thereby adding additional errors to artefact-free bone movement, restricted motion of the participant and the need for surgical procedures to affix the pins to the underlying bone. To overcome the above operational limitations in additional to technical ones, a non-invasive method of quantifying STA at the knee was undertaken by Sati [224]. The authors quantified STA using fluoroscopy and stainless steel balls attached to the skin. They observed that STA (quantified as marker movement in the LCS) varied significantly with marker position, with magnitudes twice as large as actual marker movement; markers on the joint lines also exhibited larger magnitudes of STA. Following on their research [224], fluoroscopy has been extensively applied to quantify STA.

Stagni [242] quantified STA at the thigh and shank using data acquired simultaneously from both fluoroscopy and stereophotogrammetry systems. Data was obtained from two subjects with total knee replacements, across a variety of tasks, with the LCS defined using the fluoroscopy-tracked prosthesis components. The authors reported that STA nullified the clinical usefulness of computed abduction/adduction and internal/external rotation angles, with the largest magnitudes of STA reported at the proximal thigh markers. Additionally, they observed that markers on the thigh were affected more by STA than markers on the shank. Similarly, fluoroscopy was also leveraged to quantify STA and analyse variations between rigid and non-rigid components of STA across a large number of participants with total knee prosthesis [39]. Simultaneous data from fluoroscopy and skin-mounted marker-based system were acquired for 19 participants while walking on a treadmill. The authors reported that the rigid component of STA was significantly greater than the non-rigid component. Similar to the results of the previous study, the authors observed that both the internal/external and abduction/adduction rotations were greatly affected by STA. A subsequent study (by the same authors Barre [40] and using the same dataset) analysing the spatial distribution of STA on the thigh and shank found that the proximal and lateral

aspects of the thigh had the greatest and lowest magnitudes of STA respectively, a similar result to that reported by Stagni [242].

Artefact-free bone movement acquired using fluoroscopy have also been used to quantify STA using metrics such as deviations in clinically relevant factors such as: estimated joint centre positions, calculated instantaneous helical axes, and computed kinematics and moments [19, 27, 95, 96, 136]. Fiorentino [95] observed that hip joint centres (HJCs) computed using skin-mounted markers — a practice widely applied in clinical gait analysis — were found to deviate significantly when compared with HJCs computed using dual-fluoroscopy. Additionally, they also observed that hip kinematics computed using skin-mounted markers were significantly underestimated when compared with dual-fluoroscopy based kinematics [96]. Underestimation of kinematics computed using skin-mounted markers were also observed by Kuo [136], who compared kinematics computed using fluoroscopy and skin-mounted markers during sit-to-stand motion. They also reported that the effect of STA was largest at peak joint angles and moments. Contrary to the trend of underestimation observed in kinematics, Ancillao [27] observed that the computed instantaneous helical axes rotation and distances were overestimated when computed using skin-mounted markers when compared to those obtained using dual-fluoroscopy. However, inline with studies reviewed in the previous paragraphs, all three studies observed greater magnitudes of STA at the thigh, with STA being dependent on the anatomical direction, dynamic activity and subject being considered.

In summary, the studies reviewed in this subsection indicate that STA:

1. Is dependent on motion-, participant- and location of the marker
2. Pertinently to clinical gait analysis, STA has a significant negative impact on internal/external and abduction/adduction angles
3. The rigid component of STA has a greater effect/contribution than the non-rigid component

The magnitude of errors reported by the above reviewed studies are listed in Tables 2.3- 2.7. The findings summarised by our review is also echoed in two two review papers, who have comprehensively covered research undertaken in quantifying STA [141, 193]. These authors summarised that STA is task- and subject-specific, with STA accounting for more errors than other kinematic errors. They also reported that the majority of the participants included in the studies quantifying STA had BMI scores < 25 (indicating a healthy weight for their height) [194]. Notably, our review includes studies which have quantified STA in participants with BMI > 25 (see Tables 2.3- 2.7).

Paper	**Participants**	**Task**	**Metrics**	**Reference Kinematics**	**STA Magnitudes**
[46]	8 male subjects, Age: 22-32, Avg. BMI: 24.5	Walking, cutting-motion	Errors in joint kinematics	Intracortical pins	Flexion/Extension: 2.63° (Walk), 4.15° (Cutting-motion) Adduction/Abduction: 3.33° (Walk), 8.57° (Cutting-motion) Internal/External: 2.46° (Walk), 5.33° (Cutting-motion) Medial/Lateral: 6.17mm (Walk), 9.03mm (Cutting-motion)
[45]	8 male subjects, Age: 21-31, Avg. BMI: 24.5	Walking, cutting-motion	Marker displacement, orientation	Intracortical pins	Position: 22mm (Walk), 15mm (Hop), 20mm (Cutting-motion) Orientation: 8° (Walk), 12° (Cutting-motion)
[48]	4 male participants, Age: 27-41, Avg. BMI: NA	Functional arm movements	Marker displacement, orientation	Intracortical pins	Clavicle: Position: [20%-80%], Orientation: [10%-20%]
[118]	3 healthy male, Age: 28-36, Avg. BMI: NA	Level walking	Errors in shank kinematics	Percutaneous skeletal tracker	Displacement: 3.4mm (anterior/posterior), 4.76mm (medial/lateral)

Table 2.3: Summary of STA magnitudes - Part A

Paper	Participants	Task	Metrics	Reference Kinematics	STA Magnitudes
[224]	3 healthy males, Age: NA, Avg. BMI: NA	Dynamic knee flexion	Marker displacement	Fluoroscopy	Marker movement (RMS): [2.5mm - 17mm]
[39]	19 subjects (8 men, 11 women) with total knee prosthesis, Age: 64-76, Avg. BMI: 28	Treadmill gait	Marker displacement	Fluoroscopy	Thigh: [0-60% gait cycle]: 5.4mm (rigid), 2.7mm (non-rigid)
[40]	19 subjects (8 men, 11 women) with total knee prosthesis, Age: 64-76, Avg. BMI: 28	Treadmill gait	Cluster position	Fluoroscopy	Thigh: [4.4-24.9mm], Shank: [2.5-15.3mm]
[242]	2 female with knee arthroplasty, Age: 58-60, Avg. BMI: 23	Stair climbing, step up/down	Marker displacement	Fluoroscopy	Subject 1: Thigh: 9.7mm (Stair climbing)

Table 2.4: Summary of STA magnitudes - Part B

Paper	Participants	Task	Metrics	Reference Kinematics	STA Magnitudes
[136]	10 subjects with total knee replacement, Age: 71-84, Avg. BMI: 28.9	Sit-to-stand	Marker displacement	Fluoroscopy	Thigh markers: -8mm (anterior/posterior)
[27]	6 subjects (5 male, 1 female) with instrumented total knee arthroplasty, Age: 63-73, Avg. BMI: 29.4	Level walking	Marker displacement	Fluoroscopy	Thigh: 9° (Stance), 18mm (Stance)
[95]	11 healthy subjects (6 male, 5 female), Age: 21-25, Avg. BMI: 21.1	Standing, hip abduction/adduction	Marker displacement	Fluoroscopy	Static STA: 15.7mm (ASIS markers), 26.6mm (PSIS markers)
[96]	11 healthy subjects (6 male, 5 female), Age: 21-25, Avg. BMI: 21.1	Standing, level walk	Marker displacement	Fluoroscopy	Dynamic STA: Greater trochanter marker: 5.2cm (anterior/posterior)

Table 2.5: Summary of STA magnitudes - Part C

Paper	Participants	Task	Metrics	Reference Kinematics	STA Magnitudes
[19]	4 healthy males, Age: 27-33, Avg. BMI: 22.6	Open-chain knee flexion, hip axial rotation	Marker position error	MRI + Fluoroscopy	Thigh markers: Open-chain knee flexion: 6.8mm (anterior/posterior)
[143]	13 subjects with total knee prosthesis, Age: 62-74, Avg. BMI: 27.3	Treadmill gait	Mean absolute errors	Fluoroscopy	Marker misplacement MAE: 0.1° (hip sagittal angle)

Table 2.6: Summary of STA magnitudes - Part D

Paper	Participants	Task	Metrics	Reference Kinematics	STA Magnitudes
[240]	5 healthy subjects (2 male, 3 female), Age: [25-29], Avg. BMI: NA	Level walking	Errors in hip and knee joint angles and moments	Nominal hip joint centre position	Hip Angles: 1° (Flexion/extension), 0.5° (Abduction/adduction), 0.5° (Internal/external)
[54]	5 healthy subjects (3 male, 2 female), Age: [37-48], Avg. BMI: 26.92	8 static postures: orthostatic, star-arc movement, mid-stance	Marker position differences, pelvic orientation errors	MRI	STA amplitude: LASIS: [3.3-33.8] mm, RASIS: [2.4-52.1] mm, LPSIS: [1.9-29.4] mm, RPSIS: [2.6-25.9] mm, SACR: [0.1-20.2] mm

Table 2.7: Summary of STA magnitudes - Part E

2.3.2 Existing solutions to reduce STA

As illustrated in the previous subsection, STA is task-, subject-, and marker location-dependent, which results in kinematic errors of 15° and 40mm, invalidating the clinical applicability of skin-mounted marker data. Due to the significant effect of STA on computed kinematics, various methods have been proposed to minimise the effect of STA.

Studies have proposed different methods to reduce the effect of STA: STA models [49, 56, 84], novel SOM pose estimators [71, 248], novel MKO methods [43], various markersets [35, 36] and protocols and subject-specific modeling and marker weights [44]. In this subsection we shall review these methods, highlighting their strengths and limitations and identifying gaps.

2.3.2.1 STA models

Modelling the dynamic behavior of STA has been proposed as a potential method to understand how they impact computed kinematics and therefore compensate for STA. Different STA models have been proposed in literature, with modelling STA based on joint angles being the most widely applied approach.

Both, Camomilla [56] and Bonci [49] proposed STA models, as a function of joint angles, to minimise a specific source of STA: skin-stretching and skin-sliding respectively. Camomilla leveraged the quasi-linear relationship between STA and hip angular displacements to develop a model which produced realistic estimates of STA at the thigh due to skin-stretching. Similarly, Bonci proposed a STA model which was a linear function of joint angles to model skin-sliding at the thigh, and reported that observed errors in predicted and measured STA was lower than 25%. However, both the models had drawbacks which limit their usability in clinical gait analysis: determination of a large number of subject-specific parameters (the STA model is not generalisable), requiring knowledge of the time histories of the hip and knee angles in addition to the STA measured during a selected calibration movement, and that the model only compensated for a specific source of STA.

To overcome the above limitations, Dumas [84] proposed a generic STA model which could replicate both rigid and non-rigid components of STA. The model leveraged a modal approach which ranked modes based on their deformation energy and only selected modes which cumulatively contributed to a preset threshold. This proposed modal approach was leveraged by Camomilla [55] who modelled the rigid component of the STA at the thigh and reported significant improves in joint angles calculated after removing errors caused due to STA. Pertinently, the STA models reduced errors in joint angles most affected by STA: internal/external and abduction/adduction. Despite promising results, incorporation of the above model in clinical gait analysis is hampered by: the determination of large subject-specific parameters (24), increase in computational demand of the pose-estimation due to increases in variables requiring convergence.

2.3.2.2 Pose estimators

STA models — proposed by the above reviewed papers — have indicated their potential suitability in modelling the dynamic behavior of STA, from a specific source, and in reducing the errors in computed joint angles. However, their application in clinical gait analysis is limited due to:

1. Lack of generalisability: Each model requires determination of parameetrs which are subject- and task- specific, with above proposed STA models reducing in efficacy when applied to a different subject or motion

2. Requires specific calibration routines: The STA models require a specific motion for calibration which may not be viable by majority of the clinical population

3. Increase in computational demand: Majority of the above reviewed STA models incorporate optimisation parameters into the pose estimators thereby increasing computational demand for convergence of the pose estimators

The above factors invalidate the generalisability of STA models as a potential solution to reduce joint angle errors due to STA in clinical gait analysis. Therefore, they have not been further investigated in this thesis.

Pose estimators are already an integral aspect of clinical gait analysis and biomechanics in general. Therefore, extensive research has been undertaken to improve the above described pose estimators to improve their STA reduction capability. In this subsection we shall review novel pose estimators, both SOM and MKO methods, which have been proposed to reduce the effects of STA. However, as MKO methods were proposed to overcome the limitation of SOM, this subsection shall mainly focus on the strengths and limitations of existing MKO methods.

Addendum to the SOM proposed by Soderkvist [247] was proposed to address issues regarding cluster deformation effects (the non-rigid component of STA) and to identify erroneous frames [71]. The proposed method determined three optimal marker positions which best fit a solid triangle that was least perturbed during the entire motion trial, with the three optimal marker positions subsequently used for kinematic analysis. Numerical simulations with artificial noise added to marker trajectories were used to assess the efficacy of the proposed method, with the authors reporting that their proposed method was able to recover nominal knee kinematics which were comparable to those obtained from SOM leveraging SVD [247].

Similarly, another method proposed to reduce the effects of the non-rigid component of STA in a cluster of markers was the point cluster technique (PCT) [20, 31]. PCT is based on a cluster of markers uniformly distributed on the limb segment, with each marker assigned a variable mass. The mass of each marker is adjusted at every step to reduce the difference between eigenvalues (of the inertial tensor of the cluster of markers) at the first time step with that of the current time step, with variation in eigenvalue attributed to the non-rigid component of STA. The authors reported that the method improved computed kinematics and marker position estimates on both simulated and in-vivo data [31]. An enhancement to PCT, wherein a functional form was imposed on marker trajectories (based on *a priori* knowledge of the motion to be studied), was proposed to compensate for segment deformation [20]. The enhanced method was observed to reduce error of the overall pose by 25%.

The above reviewed studies proposed novel SOMs for further reducing the effect of STA on computed kinematics. However, despite the increase in the accuracy of computed kinematics, their application in clinical gait analysis is limited due to the additional operational steps required compared to traditional SOMs proposed by either Soderkvist [247] and Spoor and Veldpaus [257]. For example, Cheze's method requires selection of three optimal markers while PCT requires prior knowledge of the functional form of marker trajectories. Additionally, both the above methods reduce the non-rigid components of STA, which has been shown to have a significantly lesser impact than the rigid component of STA (refer to the quantification of STA subsection). MKO methods (encompassing both constrained least-squares formulations and kalman filter formulations) were developed to compensate for both the rigid and non-rigid components of STA in addition to overcoming the shortcomings of SOM (which are described in the previous section).

Various studies have proposed novel MKO methods which differ in: their formulation, initial conditions, joint models and cost function. Additionally, a general implementation of an MKO method follows the below pipeline (Figure 3.1): scaling of a generic musculoskeletal model (segment scaling), registering model-derived

markers to their experimental counterparts (marker-registration) and calculating joint angles using an MKO method, with the option of altering marker weights. Consequently, studies have also investigated and proposed addenda to each aspect of the pipeline, to reduce the effects of STA.

Extended kalman filters based MKO methods were proposed and applied for real-time pose estimation and to reduce the effect of STA on kinematics [63, 64, 65]. The pose-estimator (named local motion estimation) leveraged an underlying biomechanical model with hinge joints, extended kalman filters, and an objective function minimising the distance between points measured on a TV camera with the corresponding back-projected points, with the underlying principle being that the extended kalman filter decoupled local motion of markers from their global motion through filtering, thereby removing STA. The authors reported that this proposed method provided a more accurate kinematic estimation compared with SOMs. However, the limitation of LME was the determination of filter parameters such as the order of the Taylor series expansion and the covariance factor of the process noise. Additionally, the method was only tested on simulated movement and not real-human movement data.

Similarly, Bonnet [51] reported significant improvements in the accuracy of computed kinematics, model parameters and intersegmental moments when applying extended kalman filters compared to a classical estimation method. The authors additionally reported that adding constraints to the state variables of the kalman filter resulted in more accurate kinematics and intersegmental moments when compared to classical estimation methods. However, the improvements in accuracies of computed kinematics, and intersegmental moments were calculated on a 2D model and only using movement in the sagittal plane, which has been shown to be least affected by STA. Extending the proposed algorithm to 3D movements would require more parameters to compute and calibrate. Another novel MKO method ,which enhanced the local marker enhancement estimation method proposed by Cerveri [63] through the integration of a kalman smoother, was proposed by Groote [80]. The proposed method was reported to improve the smoothness and accuracy of computed kinematics when compared to both local marker estimation method and the global optimisation [153] method. when applied to data with both instrumental errors and STA errors added to the markers. Additionally, their method produced lower residual errors compared with global optimisation.

As stated studies have also proposed novel addenda to each aspect of the generic MKO pipeline — scaling of a generic musculoskeletal model, registration of model markers to experimental markers, joint models and marker weights — to reduce the effects of STA on computed kinematics.

Novel joint models were proposed to improve kinematics computed using MKO methods. Artefact-free movement data of the knee joint for walking, hopping and

cutting tasks were combined to develop adaptive knee joint models with maximum physiological boundaries, which were then integrated into musculoskeletal models in OpenSim [198]. Significant differences in computed knee joint kinematics were found between models with and without adaptive boundary conditions [198]. A subsequent study analysing how well adaptive knee boundary conditions aid the analysis of ACL injuries observed reasonable reductions in STA and improved knee kinematics in models with adaptive knee boundary conditions when compared with knee models without adaptive boundary conditions, particularly in the transverse plane [236]. Another novel joint model was proposed by Fohanno [98], wherein an upper extremity model with personalised axes of rotation was investigated. The authors reported that the model improved estimation of the pronation-supination angles, as indicated by lower residual errors. Similarly, a new upper limb model, which incorporated closed-loop kinematic chains and subject-specific modelling was proposed by Laitenberger [137]. The model was reported to produce improved kinematic estimates when compared with four conventional models, as indicated by lower residual errors. Clement [73] proposed subject-specific modelling of knee joints in combination with parallel mechanism to reduce the effect of STA on computed kinematics. Subject-specific models of the knee were constructed using information obtained for both motion-capture system and a fluoroscopy system. The authors reported that subject-specific models were effective in reducing the effect of STA, especially in reducing errors for abduction/adduction and internal/external rotations.

However, despite the above studies reporting that kinematics computed using subject-specific models or through novel joint models, studies have reported the contrary. For example, Andersen [29] reported that the addition of spherical and revolute joint constraints at the knee increased joint angle error when compared with models with no joint constraints (6 DoF) and therefore exerted no overall improvement. Similarly, a comparison of the kinematics obtained using models with different joint models at the hip, knee and ankle indicated variable model performance depending on the movement analysed. Notably, joint angle error was relatively large despite STA compensation by multi-joint models [72]. Additionally, studies by Gasparutto [101], Richard [211] and Pomarat [195] indicated that no significant improvement in kinematics were obtained with anatomically accurate joint models or joint models with hinge, parallel, coupling and elastic constraints when compared to spherical joint models.

Studies have also researched optimising other aspects of the MKO pipelines to reduce the effect of STA: marker-registration, segement scaling, marker placement and marker weights. For example, Dunne [86] proposed a novel marker-registration method, orientation-registration, wherein the model is initially posed using angles computed using anatomical markers, with the virtual markers subsequently

registered to their experimental counterparts. The proposed method was found to produce lower marker residual errors than user-registration methods and also indicated no inter-user variability when compared to user-registration methods. However, their proposed method was only tested on a humanoid robot, with the authors not accounting for marker-registration errors due to STA.

Two novel scaling and marker-registration methods were proposed [155], to reduce the need for manual adjustment during scaling and marker-registration. The authors proposed two methods, anatomical landmark scaling (scaling performed using a static trial and radial basis functions) and kinematic scaling (which leverages an optimisation routine and a functional trial), and compared their methods against linear scaling (which used a gait trial to scale the model and register the markers). They reported that no method could be chosen over another due to similar residual errors computed for linear and kinematic scaling with similar kinematics computed in the saggital plane for all three methods [155]. Similarly, Puchaud investigated [199] different scaling and marker-registration pipelines proposed to improve the fitting of a generic musculoskeletal model to subject-specific dimensions [155] to evaluate their efficacy in reducing STA. Specifically, the authors compared five scaling methods — three marker-based scaling methods with and without optimisation and two image-based scaling methods with and without optimisation — and indicated that the scaling pipeline leveraging marker-based segment scaling with optimisation-based marker-registration produced both, lowest residual errors and kinematics similar to that of reference kinematics [199]. Additionally, they reported that adding segment lengths to the optimisation routine led to over-fitting of the model [199]. Despite the improvements in marker-registration and scaling indicated in the above studies, translating them to clinical practice is difficult, as most of the clinical population would not be able to perform the optimisation-routines required to apply the above methods. Additionally, none of the above methods leveraged datasets from subjects with large BMI scores, underscoring the need for a generalisable protocol for clinical validation.

Other aspects of the MKO pipeline investigated were the placement of markers (markersets) and marker weights. The optimal placement of thigh markers — which are more susceptible to STA than other markers — were investigated by comparing kinematics obtained using lateral thigh markers placed at two different heights [74]. The authors found that different thigh marker locations resulted in significant differences in hip rotation, knee flexion and knee varus-valgus angles, with thigh markers placed at the proximal-third height exhibiting significantly less STA compared with markers at the distal-third height. Studies have also indicated that the removal of thigh markers does not significantly affect kinematics [36, 235]. In particular, when using a shape-scaled model, Bakke [35] found that kinematics obtained by the removal of thigh segment markers were similar to those obtained

using a contemporary markerset. Similarly, removal of thigh and shank segment markers were reported to produce saggital plane kinematics which were in strong agreement with those obtained using a complete markerset: which was used as reference. However, the removal of thigh and shank markers were reported to adversely impact estimation of knee joint centre kinematics and consequently knee load [235].

However, neither Slater[235] or Bakke[35], reported the effect of removing thigh markers on coronal and transverse plane kinematics, which are the most affected by STA and which are leveraged for surgical planning for children with CP. Additionally, studies analysing the effects of various markersets [T3Df (Total 3D Gait), PiG (Plug-in Gait), SAFLo (Servizio di Analisi della Funzione Locomotoria), CAST (Calibration Anatomical System Technique) and LAMB (Laboratorio per l'Analisi del Movimento nel Bambino)] on their ability to reduce STA and improve kinematics, and in their within- and between-sessions repeatability [75, 93, 157], reported that the consistency of the underlying model plays a greater role than the location of markers. They also reported that whilst the markerset widely applied in clinical gait analysis, PiG, exhibited greater within-session repeatability for the pelvis in all three planes, it produced a greater range of motion in the frontal and transverse planes compared to other markersets. Again, the above studies only used data obtained from subjects with healthy BMI scores.

Studies have also investigated marker-weighting, a key aspect of MKO pipelines and SOMs. Three novel weighting schemes — progressive weighting, conditional weighting and posture preservation weighting — were proposed to overcome errors due to missing/occluded markers and STA [32]. Progressive weighting and conditional weighting schemes reduced the weight of a marker or activated additional driving conditions respectively, when a marker was missing/occluded. The posture preservation weighting scheme constrained the relative position between bodies when the pose of the bone could not be determined due to STA. The authors reported that the three weighting schemes were observed to successfully reconstruct the pose in the presence of missing markers or implausible poses.

Studies have also investigated the feasibility of determining optimal weights for reducing the effect of STA. For example, Begon [44] analysed the effects of optimal weights whilst applying SOM for upper-extremity movement, and reported that optimal marker weightings reduced kinematic errors significantly. However, they also observed that optimal weights could not be generalised between subjects or between movements, with marker redundancy also effective at reducing STA in the application of SOMs. Similarly, Lefebvre [145] also found that optimal marker weighting were task- and subject-specific with optimal marker weighing improving computed scapular kinematics.

Despite the above studies regarding marker-weights underscoring the benefits

obtained from subject-specific weighting or task-specific weighting, they are difficult to implement in clinical settings.

As stated previously, majority of the above reviewed studies use data obtained from participants with healthy BMI scores, despite evidence of a direct correlation between higher BMI scores and increased magnitudes of STA [54]. For example, a study comparing the different classes of pose estimators found that the frontal plane kinematics of obese children were significantly different when computed using direct estimation method or MKO methods, with no significant differences found for children with healthy BMI scores [119, 120]. These discrepanices can affect the outcome of surgical interventions.

To overcome this gap, studies have proposed solutions to reduce STA in participants with varying BMI scores. For example, an obesity-specific markerset was proposed to overcome the difficulty in palpating anatomical landmarks for marker placement, and to reduce the effects of subcutaneous fat on STA [147]. Specifically, a digital pointer — an instrumented pointer with reflective markers — was depressed until the underlying bone was reached to locate the anterior-superior iliac spine (ASIS), with the underlying ASIS locations registered in the software. The ASIS locations are subsequently tracked using the relative information between the digitally-registered point and other skin-mounted markers. The authors reported that kinematics obtained using this proposed obesity-specific markerset and a conventional markerset were similar for non-obese participants; however, higher fidelity pelvic tilt angles and significantly smaller muscle forces were computed using the obesity-specific markerset when compared to the conventional markerset, when applied to obese participants.

Similarly, studies have also proposed incorporating wobbling masses (additional mass to emulate movement of subcutaneous fat and soft tissues) into MKO methods to compensate for STA. However, kinematics computed using models with and without wobbling masses indicated no significant differences, despite reductions in residual error obtained for models with wobbling masses [250]. In contrast, Masters [158] observed higher fidelity hip joint power (calculated using inverse dynamics) in models with wobbling masses incorporated when compared with models with no wobbling masses. Additionally, the authors stated that the differences between the models (with and without wobbling masses added) become more extreme when the virtual leanness of the model decreases, underscoring the need for either incorporating wobbling mass into the MKO pipeline or in developing generalisable methods applicable to subjects with varying BMI scores.

Whilst the above reviewed studies have reported novel pose estimators and novel steps in the MKO pipeline to reduce the effect of STA, the clinical impact and the efficacy of pose estimators is still questioned. For example, Stagni [241] compared the performance of the three classes of pose estimators in reducing the

effects of STA. Double calibration, single calibration (CAST, Calibration Anatomical System Technique) and global optimisation were compared to evaluate their suitability for clinical gait analysis [241]. Using fluoroscopy and skin-mounted marker data from various tasks, the authors found that joint kinematic curves varied between the three methods; in particular, abduction/adduction and internal/external curves varied between global optimisation and double calibration, with larger kinematic errors observed with global optimisation.

However, an innovative constrained least-squares MKO method, which projected all or selected markers onto an axis of the LCS, stated that MKO methods reduce kinematic errors compared to non-MKO methods [43]. The proposed marker-projection method was validated using intracortical pins and was investigated on models with different joint constraints. The results indicated that the use of MKO improved accuracy by 40-50% compared with SOM, and that the projection of markers increased the accuracy by a further 20%. However, the projection of a subset of markers was found to be more accurate than the projection of all markers; the loss of information (from the coordinates made 0 on the projected axis) was attributed to the decrease in accuracy.

Therefore, despite a significant amount of research undertaken to reduce joint angle errors due to STA, a generalisable solution which can be applied to different participants, motions has not been proposed. Additionally, a consensus of which method is most suitable for clinical gait analysis has not been established, with current clinical gait analysis leveraging the PiG model, despite multiple studies showing its limitations. Furthermore, the existing solutions in general are not validated against subjects of varying BMI scores, which is representative of the clinical population.

Therefore, there is a need for a generalisable solution which can improve the joint angles computed in clinical gait analysis, which forms the basis for the solutions proposed in this thesis.

In addition to the papers reviewed in this section, two literature reviews of note [42, 140] have extensively reviewed MKO methods and the underlying models, and have indicated similar observations to our review. Their reviews suggest that MKO is a key step in musculoskeletal modelling, specifically in kinematic and dynamic analysis where it is incorporated to compensate for STA (especially the rigid component). Their study reviews MKO methods with different implementations based on the design variables, objective function, constraints and initial proposed guesses. They report that the results of MKO methods are highly correlated with the quality of joint models chosen, with anatomical models providing better results once the model parameters can be identified; this is particularly important in pathological joints. Their review also indicates that MKO methods have the potential for considerable STA compensation.

2.3.3 Summary and key takeaways from STA

The previous subsections have shown the breadth and depth of studies undertaken in quantifying STA, in proposing novel methods to reduce STA and in validating existing and novel methods proposed to reduce the effects of STA. Despite the substantial number of solutions provided, there is no generalised method which has been found effective for all subjects and all investigated motions. Based on our review, these are our key takeaways:

- STA has a deleterious effect on computed kinematics with the potential to clinically invalidate skin-mounted marker-based data
- STA is task-, subject- and marker location-dependent. STA is generally intra-subject repeatable but not inter-subject (although few studies have shown results in contrary to this)
- Among the proposed solutions to reduce STA, MKO methods, SOM methods and markersets seem to be the most widely accepted, with STA models not commonly incorporated
- MKO methods have produced more realistic kinematics while reducing STA. Their improved performance over SOM or DK depends on the task and subject being analysed
- Joint models, a key aspect of MKO methods (part of the underlying model), play a significant role in the fidelity of the produced kinematics. Joint models which are subject-specific, more anatomically accurate and with adaptive boundary constraints, seem to produce better results. However, as of now, spherical joints seem to be more widely used as their performance does not differ greatly compared with more complicated joints.
- Marker weights and marker placements also play an important role in reducing STA, with marker placement being the most important
- Reducing the effect of STA, by incorporating artefact-free bone movement by either digitising anatomical landmarks or projecting markers onto an axis, has shown to improve kinematics

The limitations and gaps in current existing solutions form the basis for the solutions proposed in the following chapters.

2.4 Techniques to image the bone

The previous section illustrated the deleterious effect STA has on kinematics computed using skin-mounted markers and underscored the fact that, although many solutions have been proposed to ameliorate the effect of STA on computed kinematics, there is no single solution which can be applied globally for all observed motions and participants. Amongst the studies reviewed above, some incorporate artefact-free bone movement (actual bone movement) to improve kinematics and have been reported to be effective in reducing the deleterious effect of STA on both obese and non-obese participants [43, 147]. In this section we will briefly review imaging modalities, both ionising and non-ionising, which have been applied to determine artefact-free bone movement.

Artefact-free bone movement obtained using intra-cortical pins, percutaneous trackers or through imaging are considered as error-free (reference, gold-standard) bone movement, as skin-mounted marker-based systems are affected by kinematics errors (please refer to the previous section). As discussed in the previous section, artefact-free bone movements are used for quantifying the effect of STA on computed kinematics and for determining the efficacy of a proposed solution to reduce the impact of STA. In addition, studies have suggested that replicating or incorporating artefact-free bone movement in kinematic analysis can reduce the effect of STA [43, 198]; therefore, underscoring the advantages of incorporating artefact-free bone movement into kinematic pipelines. Whilst the widespread use of intra-cortical pins or percutaneous trackers are limited by the need for surgical interventions and the discomfort to the participants, imaging modalities have been widely applied to obtain artefact-free bone movement, which are reviewed below.

Fluoroscopy is a medical ionising imaging modality that uses X-rays to visualise internal organs and tissues moving in real-time, and has been widely applied in movement analysis. In particular — as described in the previous section — fluoroscopy has been used to obtain artefact-free bone movement which has then been leveraged to quantify STA ,and to obtain reference kinematics for musculoskeletal model validation and/or validation of methods proposed for STA reduction [38, 39, 72, 95, 101, 242, 249]. Artefact-free kinematics obtained using fluoroscopy have also been applied to study the mechanical behavior of knee joints [225], investigate the correlation between physical measures of femoral skeletal alignment with those obtained using imaging [259], and to compare total knee anthroplasty (TKA) designs during walking [173]. In addition to obtaining artefact-free bone movement, incorporating fluoroscopy into study designs enables the analysis of individual bone movement, which may be difficult to obtain using skin-mounted markers or multi-segment bone models [128].

Computed-tomography (CT) is another ionising imaging modality which has

been applied to study motion of bones, which are difficult to analyse using skin-mounted markers. CT imaging uses a combination of x-rays and computer technology to produce cross-sectional slices of the interior of the body and is extensively applied in clinical settings to image bones, muscles, fat, organs and blood vessels. In biomechanics, Rowe [216] leveraged weight-bearing CT (WBCT) to determine the position of tallonavicular and calcaneocuboid joints during eversion and inversion of the subtalar joint. Results from their study indicated that motion through the two joints was more complex than previously described using skin-mounted marker systems. Similarly, Lin [150] used axial CT scans to determine the clinical significance of both patella tilt angle of sasaki and of patella misalignment, in limb alignment procedures used to reduce patellofemoral pain. They leveraged axial CT images of the knees in extension, with quadriceps in both relaxed and extended states, to observe the influence of femoral rotation relative to the tibia on patella tilting, with their results indicating that the readings were dependent on the method used to measure the patella tilt angle, and that patella tilt angles of sasaki remained stationary with changes in femoral rotation, tibial rotation and femoral rotation relative to tibia.

Incorporating fluoroscopy or CT images in biomechanics can elucidate greater details on how the internal bone structure moves: information which is either too small to be captured by skin-mounted marker-based systems, or is masked by errors such as STA. However, despite the advantages these systems offer in movement analysis, incorporating fluoroscopy or CT in regular clinical movement analysis is restricted by their cost and ionising nature. For example, in one study investigating the effect of STA on hip joint kinematics through the use of fluoroscopy and skin-mounted markers, the authors noted that the amount of radiation participants were exposed to during a single session of data collection was equivalent to what they would be exposed to in four years from natural radiation [94, 96].

To reduce the exposure of participants to harmful radiation, studies have investigated the feasibility of incorporating non-ionising imaging modalities—such as magnetic resonance imaging (MRI) and ultrasound — for acquiring artefact-free bone movement. MRI is a non-ionising medical imaging modality which uses a combination of radio waves and strong magnetic fields to create images of organs, bones, muscles and blood vessels. Whilst closed-MRI systems (MRI systems which feature a capsule-like space where the patient lies down) are commonly used for regular MRI scans, open-MRI systems (MRI systems which are open on four sides with magnetic bottom and top sides) have been applied in movement analysis. For example, Higuchi [117] investigated the biomechanics of the medial patellofemoral ligament (MPFL) during knee extension and flexion using an open-MRI system. Their results indicated that the length change of the MPFL observed using MRI was contrary to that observed in cadavers, with inferences

obtained using cadavers commonly applied in biomechanics [49, 56]. These results highlighted the benefit of using MRI for in-vivo biomechanical studies [117]. Similarly, Nomura [177] reported that different MPFL injury patterns could be observed using MRI with analysis using MRI able to correctly diagnose 81% of MPFL injuries. They state that their findings indicate that MR imaging is a acceptable method of diagnosing MPFL injuries when direct observation is not possible or recommended. Open-MRI was also leveraged to investigate cam and spincer morphologies, with subject-specific kinematics computed using MRI, resulting in accuracies of 1.1° and 0.5° (acceptable error in biomechanics is 5°) for squatting and sitting motions, respectively [166].

Whilst MRI may be beneficial for in-vivo biomechanics, MRI systems are extremely expensive, scans are time-consuming and have a limited field of view, restricting which motions can be studied. Another non-ionising imaging modality — whose application in biomechanics has been extensively investigated and which offers a flexible field of view when compared with MRI— is ultrasound imaging. Ultrasound imaging uses high-frequency sound waves to generate images of the interior of the body with images able to capture movement of the body's internal organs including blood flow. Advantages of ultrasound imaging over MRI, in addition to providing a flexible field of view, are: providing finer details, real-time dynamic imaging, the flexibility to image different locations and to image patients with surgical hardware. Due to these advantages, ultrasound imaging has been used as an alternative to MRI [175]. One study comparing ultrasound imaging and MRI of the patella position in patients with patellofemoral pain syndrome, found no statistical differences in the performances of the two imaging modalities [116].

Systems incorporating ultrasound imaging have also been proposed to reduce the effects of STA. A computer-aided tracking and motion analysis system with ultrasound (CAT & MAUS) was proposed to reduce the effect of STA and improve the fidelity of hip joint kinematics [129]. Specifically, the authors developed an automatic bone segmentation protocol to reconstruct the 3d bone surface from ultrasound images. In-vivo and in-vitro validation of the CAT & MAUS sytem indicated it was capable of achieving errors in femur position of less than 1.2° . An augmentation to the system, to dynamically locate the greater trochanter during gait was proposed by Jia [130]. Results from the augmented system indicated that the error produced by the CAT & MAUS system in reconstructing the femur shape was 1/10th of those obtained using skin-mounted markers alone. The drawbacks of the current system, as identified by the authors, are that the system is only capable of imaging the greater trochanter and that an ultrasound probe needs to be held to the surface of the greater trochanter during motion. One additional limitation is that manual segmentation is required for images where the bone surface is not

clearly identifiable, thereby requiring radiologist expertise.

Similarly, an intelligent skin-mounted marker system incorporating ultrasound was proposed to reduce the effect of STA [159, 160, 161]. The underlying principle of their proposed system was that the incorporated ultrasound transducers would determine the distance of the bone from the skin, thereby enabling calculation of movement errors due to soft tissue movement. The authors validated their proposed system on a femur, whose internal structure was kept visible, and obscured by an opaque balloon, embedded in a water-filled container which simulated the behaviour of muscle tissue, and reported high accuracies within 0.1mm and 0.1° . In their subsequent investigations they proposed an improvement to the calibration procedure, involving a novel calibration setup that reduced the number of slices required during calibration, thereby reducing the computational complexity of their system. However, they have not validated their system ex-vivo nor have they proposed how to make the system wearable thereby limiting its application in its current form [159].

The above studies have shown that acquiring and analysing artefact-free bone movement data — acquired using non-invasive imaging modalities such as fluoroscopy, CT, MRI and ultrasound — can help to reduce the effects of STA, and can enable the undertaking of biomechanical studies which may not be viable or accurate using traditional skin-mounted marker-based systems. Whilst the regular use of fluoroscopy and CT are impeded by their cost and ionising nature, MRI and ultrasound are non-ionising alternatives. However, the use of MRI is restricted due to its high operational cost, limited field of view and time-consuming nature.

Ultrasound imaging, on the other hand, provides the versatility and cost-effectiveness to be applied in regular movement analysis, and studies have investigated its potential to reduce STA. However, despite promising results, the use of ultrasound imaging has not been explored beyond the greater-trochanter, requires radiologist training (or additional resources for automatic detection) and the need for an ultrasound probe to be held at the location of the bone to be observed. These factors may somewhat limit the broader application of ultrasound imaging in clinical movement analysis. For example, studies analysing the effect of attaching an ultrasound probe to the body has found significant differences in kinematics in both typically developing children and in children with CP [171]. This further limits their application in clinical gait analysis.

The following section will introduce a new imaging modality which is also non-ionising, cost-effective and additionally does not require any specialised training for analysing the images generated. Whilst this imaging modality has not been applied in biomechanics, its potential for image acquisition using wearable sensors makes it a promising alternative to ultrasound in the challenge of reducing the effects of STA. Despite, it having a lower spatial image resolution than ultrasound

imaging, it offers benefits which overcome the above limitations of ultrasound imaging and thereby could potentially be applied in clinical gait analysis.

2.4.1 Summary and key takeaways from bone imaging techniques

The previous section has reviewed research which has incorporated various imaging modalities to determine artefact-free bone movement. Based on our review and analysis, these are our key takeaways:

- Fluoroscopy is the most widely applied imaging modality to determine artefact-free bone movement. Studies using fluoroscopy have been used to quantify STA and to analyse movements which would not be possible using skin-mounted markers.
- WBCT is another ionising imaging modality which has been applied to determine artefact-free bone movement. However, its applications is also limited due to its ionising nature
- MRI, a non-ionising imaging modality, has been proposed as an alternative safe imaging modality to determine artefact-free bone movement. Open-MRI systems have been widely applied in patellofemoral studies
- Despite the benefits of incorporating artefact-free bone movement in biomechanical studies, neither fluoroscopy, WBCT, or MRI are cost-effective, thereby limiting their application in clinical gait analysis
- Ultrasound imaging has been proposed as a safe, cost-effective alternative modality, with systems incorporating ultrasound imaging proposed to reduce the effects of STA and to determine artefact-free bone movement. However, these systems have not yet been tested on human movement and/or have only been optimised to identify one part of the skeleton

These studies illustrate the advantages of incorporating artefact-free bone movement into kinematic pipelines, with research to develop a safe and cost-effective system still ongoing.

2.5 Microwave imaging

The previous section highlighted the advantages of incorporating artefact-free bone movement into biomechanics, specifically in reducing the effects of STA, and in investigating motions which may not be viable using skin-mounted marker-based

systems. The previous section also briefly touched upon different non-invasive imaging modalities, which can be used to acquire artefact-free bone movement. Amongst the imaging modalities reviewed, ultrasound imaging is advantageous as it does not expose the participant to harmful radiation, it provides a flexible and wide field of view, and it can be applied in real-time dynamic motions. Studies have leveraged these advantages to propose systems which can be used to reduce the effects of STA [129]. However, despite promising results, the application of ultrasound imaging in conjunction with skin-mounted marker-based systems are limited due to the need for coupling liquid, the need for the probe to be held at the location to be imaged and for specialist knowledge to read ultrasound images [130].

In this section we review a new imaging modality, namely microwave imaging, which offers the same advantages of ultrasound imaging (non-ionising nature and flexible field of view) but is also cost-effective and does not require the need for a trained radiologist. This section will cover the basic principles of microwave imaging and review studies which have leveraged microwave imaging to visualise internal organs and tissues. This section will also review the imaging algorithms and the hardware that have been proposed to improve the resolution of the images generated by microwave imaging.

Biomedical microwave imaging (MI) uses non-ionising electromagnetic waves at microwave frequencies (300 MHz - 300 GHz) to create images of internal organs and tissues. Microwave imaging leverages the differences in electrical properties (permittivity and conductivity) between various tissues, and between diseased and healthy tissues to generate images. The differences in electrical properties cause the incident electromagnetic field to scatter and this scattering is then used to generate images. Subsequently, many studies have quantified the electrical properties of different tissues at microwave frequencies (Figure 2.4) [100].

Biomedical MI has primarily been applied to detect and localise breast tumours, and to image the brain for strokes and cerebral edema. However, it has also been used to image joint tissues and fractures. Commercial companies, such as EMTensor [14] and Micrima [8], have developed systems based on biomedical MI to image the brain and breast respectively, with the principles of microwave imaging also leveraged in applications such as through-the-wall imaging, ground penetrating radars and in-airport scanners.

In general, MI systems are usually low cost and constitute of the following: an array of antennas which act as transmitters and receivers of microwave signals, a vector network analyser, and a radio-frequency switch to alternate between different antennas (Figure 2.5), with the antennas and the object to be imaged immersed in a coupling liquid.

The typical operation of the MI setup is for each transmitter antenna to trans-

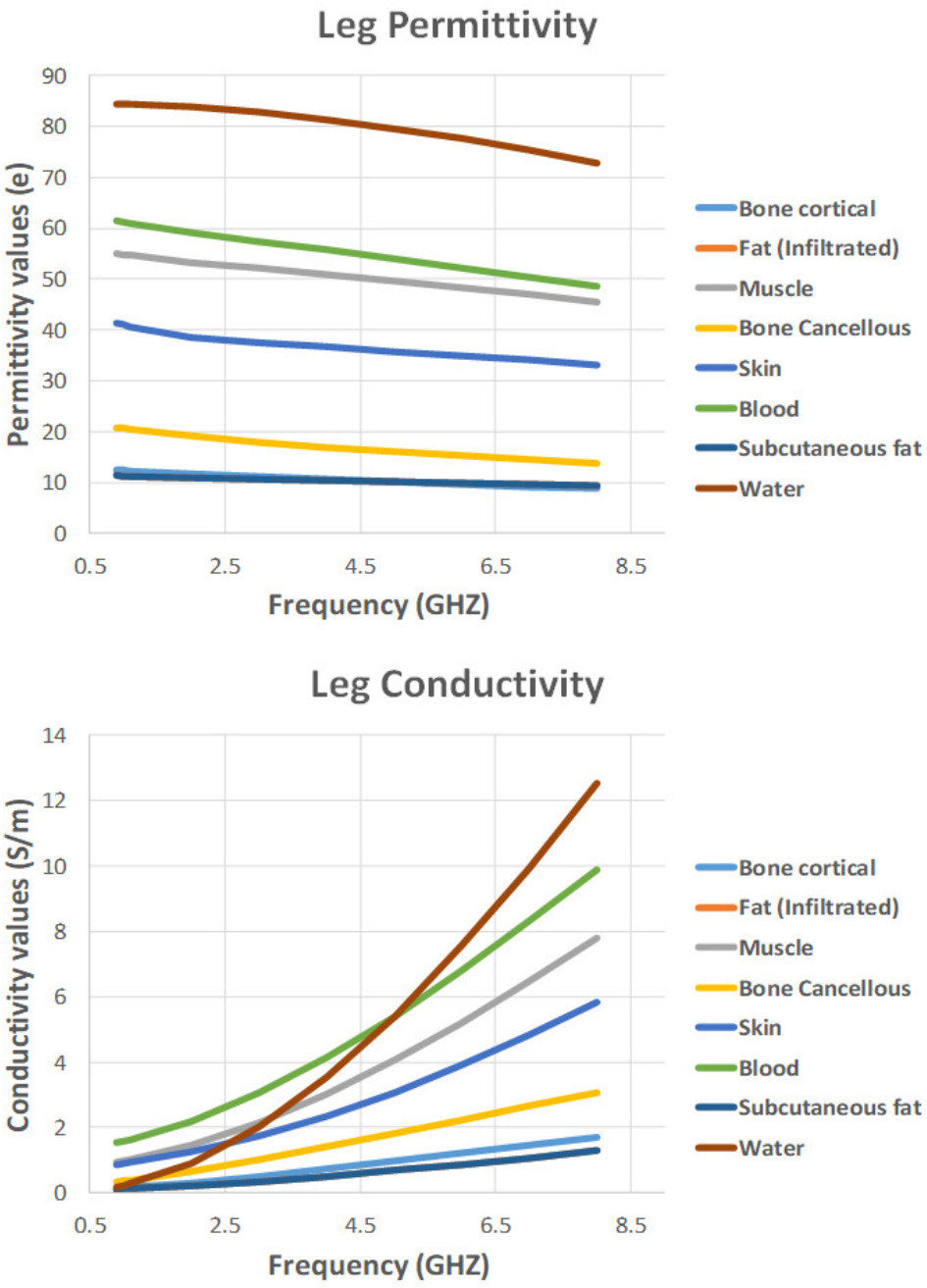

Figure 2.4: Variation of permittivity (top graph) and conductivity (bottom graph) of tissues in the leg between 0.5GHz to 8GHz

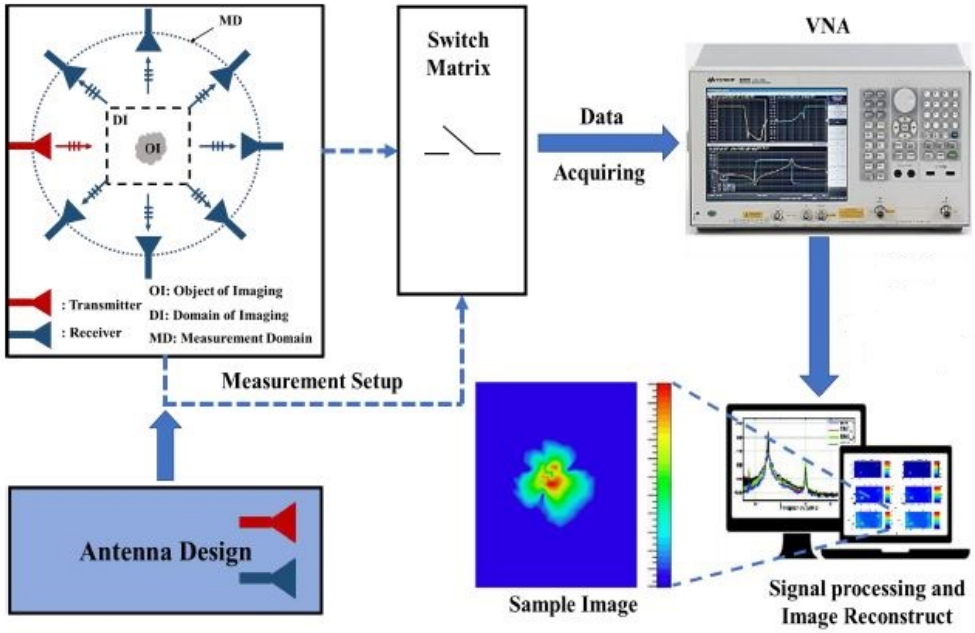

Figure 2.5: Pictorial representation of a general setup of microwave imaging systems which consist of an array of antennas, vector network analyser and a radio-frequency switch [126].

mit a pulse consecutively, with the scattered signals recorded by all receiving antennas. The data recorded by the antennas are scattering parameters (S-parameters) which may be defined as the operator which maps the incident power waves to that of the reflected power waves. S-parameters observed by the same antenna as the transmitting antenna (when receivers and transmitters are collocated) are referred to as reflection parameters, and S-parameters observed by antennas different to that of the transmitting antennas are referred to as transmission parameters. The general naming convention for reflection and transmission parameters are Sii and Sji respectively, where i is the transmitting antenna and j the receiving antenna. For example, S11 are the reflection parameters observed by antenna 1 when antenna 1 is transmitting and S21 are the transmission parameters observed by antenna 2 when antenna 1 is transmitting.

S-parameters are influenced by the frequency of operation, the design of antennas, and the permittivity and shape of the surrounding environment. Any variation in this environment results in changes to the S-parameters, which has been leveraged in microwave imaging. For example, variation in transmission parameters (S21) from two on-body dual-patch antennas placed on either side of the wrist were analysed to detect the presence of osteoporosis [156]. This analysis found that the magnitudes of S21 parameters recorded for osteoporotic and osteopenic patients were greater than those of healthy controls, and were correlated with dual-energy x-ray absorptiometry (DXA) or bone densitometry measurements. The increase in S21 magnitude was ascribed to the increase in bone porosity due to osteoporosis and osteopenia.

Variation in transmission parameters (S21) have also been utilised to assess the feasibility of a MI system (the Muscle Analyzer System) to detect muscle deterioration [162]. The proposed system was verified using both laboratory and clinical data, with the S21 parameters of deteriorated muscle exhibiting shifts of 30Hz when compared with healthy muscle. Similarly, studies have also indicated that variation in S-parameters can be leveraged to detect fractures [47] and to detect changes in blood flow during pathological conditions [229].

Whilst the aforementioned studies have indicated that MI can be applied to detect the object of interest (a fracture, tumour or deterioration of muscle) they do not provide the location of the object of interest i.e they do not generate a 2-D or 3-D image to localise the object of interest. Such applications, where no image is generated but variations in S-parameters are leveraged to detect the object of interest, are sometimes referred to as microwave-sensing applications [67]. MI applications which generate a map (an image) to determine the location of the object of interest, not only require the recorded scattered signals but also the location of the antennas.

Algorithms applied to generate an image can be broadly classified into two cat-

egories: Qualitative (or radar-based imaging) and Quantitative (or tomographic-based imaging). Radar-based imaging algorithms are used to detect the presence of a strong scatterer (e.g., a tumour, stroke, or fracture) in the imaging domain, without determining the electrical properties of the scatterer. Tomographic imaging provides both the location of a scatterer as well as a map of the distribution of electrical properties in the image. Tomographic imaging algorithms are based on inverse scattering problems, while radar-based imaging leverage radar-like techniques to locate the scatterer. The following subsections will review the two classes of imaging algorithms.

2.5.1 Quantitative or microwave tomographic imaging

Microwave tomographic (MWT) imaging algorithms generate an image mapping the electrical properties (permittivity and conductivity) of the imaged body in addition to the location of the scatterer [68, 170]. A general configuration for microwave tomography imaging is shown in Figure 2.6, wherein the body to be imaged lies in a bounded domain D, with antennas located in the measurement domain S. The setup is generally immersed in a homogeneous medium with known permittivity (eb), with the object of interest (OI) successively illuminated by some antennas and the scattered field recorded by other antennas [68, 170]. MWT can either reconstruct images at a single frequency or at multiple frequencies wherein reconstructed images at lower-frequencies are used as starting points for image reconstruction at higher frequencies [104].

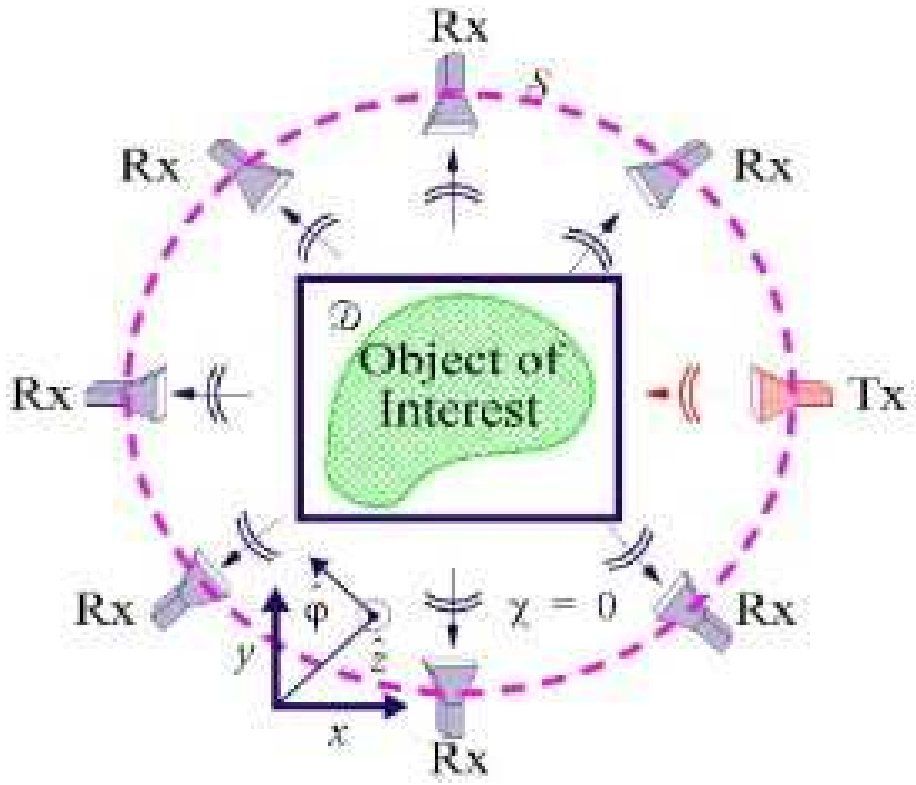

Figure 2.6: General configuration for microwave tomographic imaging studies. The body to be imaged lies in a bounded domain D with antennas located in the measurement domain S [169].

The formulation of the MWT problem can be broken down into two equations, Equations 2.3, 2.4. The objective of the MWT problem is to determine $\chi(\boldsymbol{r})$ in D by solving the two equations. The equations are ill-posed and non-linear due to the dependence of $\mathbf{E}^{\text{scatt}}$ on $\chi(\boldsymbol{r})$, with commonly applied approximations such as Born or Rytov (linearising the equations with a constant value for $\mathbf{E}^{\text{total}}$) approximations not feasible due to the large contrast in dielectric properties of tissues. Therefore, a large number of algorithms have been proposed, to solve the non-linear problems, with these algorithms broadly classified into iterative algorithms (wherein the forward equation[2.3] is solved at every iteration using an updated value of the contrast) or non-iterative algorithms [68].

$$\mathbf{E}^{\text{scatt}}(\boldsymbol{p}) = k_b^2 \int_{\mathcal{D}} \mathcal{G}(\boldsymbol{p}, \boldsymbol{r}')\, \chi(\boldsymbol{r}')\, \mathbf{E}^{\text{total}}(\boldsymbol{r}')\, dv(\boldsymbol{r}') \tag{2.3}$$

Where:

- $\mathbf{E}^{\text{scatt}}(\boldsymbol{p})$: Scattered electric field at the observation point p
- k_b: Background wavenumber
- $\mathcal{D}$: Bounded domain where the object of interest lies
- $\mathcal{G}(\boldsymbol{p}, \boldsymbol{r}')$: Green's function of the background medium
- $\chi(\boldsymbol{r}')$: Contrast function
- $\mathbf{E}^{\text{total}}(\boldsymbol{r}')$: Total electric field at location $\boldsymbol{r}'$

$$\mathbf{E}^{\text{total}}(\boldsymbol{r}) = \mathbf{E}^{\text{inc}}(\boldsymbol{r}) + k_b^2 \int_{\mathcal{D}} \mathcal{G}(\boldsymbol{r}, \boldsymbol{r}')\, \chi(\boldsymbol{r}')\, \mathbf{E}^{\text{total}}(\boldsymbol{r}')\, dv(\boldsymbol{r}') \tag{2.4}$$

Where:

- $\mathbf{E}^{\text{total}}(\boldsymbol{r})$: Total electric field at location $\boldsymbol{r}$
- $\mathbf{E}^{\text{inc}}(\boldsymbol{r})$: Incident electric field at location $\boldsymbol{r}$
- k_b: Background wavenumber
- $\mathcal{D}$: Bounded domain where the object of interest lies
- $\mathcal{G}(\boldsymbol{r}, \boldsymbol{r}')$: Green's function for the background medium
- $\chi(\boldsymbol{r}')$: Contrast function
- $\mathbf{E}^{\text{total}}(\boldsymbol{r}')$: Total field at integration point $\boldsymbol{r}'$

As mentioned above, linearisation of the non-linear relationship between $\mathbf{E}^{\text{scatt}}$ and $\chi(\boldsymbol{r})$ through Born or Rytov approximations are not feasible in biomedical microwave imaging. Therefore, two methods were proposed to calculate the total electrical field ($\mathbf{E}^{\text{total}}$) in the data equation (Equation 2.3) at every iteration using the updated value of contrast: Born Iterative method (BIM) and Distorted-Born Iterative method (DBIM). BIM was proposed by Wang [258], who developed an iterative algorithm which provided better approximations of the total field inside the imaging domain based on the contrast from the previous iteration. The initial guess was taken as the contrast obtained using Born approximation. In their proposed method, the Green's function in the integrand remains unchanged at every iteration. A modification of BIM, known as DBIM, was proposed by Chew [69],

who in addition to updating the total electric field also updated the Green's function at every iteration. Compared to BIM, the proposed DBIM method converged faster, but was less tolerant to noise.

Various enhancements and novel implementations of BIM and DBIM have subsequently been proposed. For example, an enhanced version of BIM was proposed by Costa-Batista [76], who leveraged quadratic programming optimisation to solve the inverse scattering problem. The novelty of their proposed method was based on four novel features: suitable mechanism to enforce *a priori* information, efficient implementation, integration of different regularisation strategies and a multi-frequency approach. The authors reported that their proposed method outperformed the original BIM in 14 out of 19 cases; specifically, it was more robust and able to image objects of large contrast with respect to the background.

Similarly, a modified version of DBIM (the DBIM-IMATCS algorithm) was proposed to visualise the dielectric contrast between cortical bone and trabecular bone, in order to differentiate diseased trabecular bones from healthy bones [23, 24]. The proposed DBIM-IMATCS algorithm was tested both numerically (using a simulated two-layer bone immersed in a coupling liquid) and experimentally (using a bone phantom built using tissue-mimicking liquids), with results indicating that the DBIM-IMATCS method was able to differentiate between osteoporotic and osteoarthritic bones based on differences in reconstructed complex permittivity. Similarly, another version of DBIM, the DBIM-TWist (a two-step iterative shrinkage/thresholding algorithm), was proposed and leveraged for stroke imaging in numerical brain models and in stroke imaging phantoms [134]. The DBIM-TWist algorithm was reported to be able to identify both the location and permittivity of strokes, even when the background permittivity had uncertainties in its values. Another variation of the DBIM algorithm have also been applied for functional microwave imaging, where permittivity changes due to flow reduction and compartment syndrome were studied [230].

Another widely applied MI algorithm, sharing similar principles to the DBIM, is the Gauss-Newton inversion (GNI) algorithm. The GNI algorithm is based on Newton optimisation, where the cost function is approximated using a quadratic form [169]. Variations of GNI has been widely applied in microwave imaging applications. For example, the multiplicative regularised Gauss-Newton inversion method (MR-GNI) was leveraged to successfully reconstruct the electrical properties of human forearms immersed in a background medium of high permittivity (77.3 +j8.66) [167], with improvements to the MR-GNI algorithm proposed by Ostadrahimi [185]. The improvements were mainly focused on the incorporation of prior-information in the optimisation function, with prior information regarding the ratio of imaginary and real parts and that of the contrast value reported to reduce artefacts in the reconstructed image.

Another version of the GNI algorithm, which incorporated soft-priors and variance-stabilising logarithmic transformation [164], was applied to study the efficacy of microwave imaging to detect permittivity changes in the bones of two patients required to reduce weight-bearing exercise on an injured leg for several weeks [165]. CT-images of the heel were used to provide structural information as soft-priors to the reconstruction algorithm. The heel was immersed in a background medium of high permittivity (23.2), with results indicating that the bones were clearly identifiable. In addition, the permittivity changes in the bone (due to the lack of weight-bearing exercise) were observed when using soft-prior regularisation [165].

The BIM, DBIM and GNI algorithms reviewed above converge in less number of iterations. However, they require the forward equation (Equation 2.3) to be solved at each iteration making them computationally demanding, which limits their applicability, especially in full 3-D vectorial inversion. An alternative microwave tomography imaging approach, which does not require the forward problem to be solved at every iteration, are the contrast source inversion (CSI) methods [255]. In CSI methods the tomography problem is formulated in terms of contrast and contrast sources (the product of contrast and field) with the cost function for the CSI method given in Equation 2.5. At every step of the CSI method, the contrast source is updated assuming the contrast is constant, and then the contrast is updated assuming the contrast source is constant.

$$F = \frac{\Sigma_j \left\| f_j - G_j^S w_j \right\|_S^2}{\Sigma_j \left\| f_j \right\|_S^2} + \frac{\Sigma_j \left\| \chi_j u_j^{\text{inc}} - w_j + \chi_j G_j^D w_j \right\|_D^2}{\Sigma_j \left\| \chi_j u_j^{\text{imC}} \right\|_D^2} \tag{2.5}$$

Where:

- F: The total cost function to be minimized
- $\sum_j$: A summation over j field points
- f_j: measured scattered field at point j
- G_j^S: Green's function in the measurement domain (S)
- w_j: contrast source
- χ_j: contrast function
- u_j^{inc}: the incident field at point j
- G_j^D: Green's function in the image domain D

Whilst many variations of CSI have been applied in electromagnetics and acoustics, one proposed version of the CSI algorithm, the MR-CSI method, has been investigated for biomedical imaging applications [16]. MR-CSI incorporates multiplicative regularisation to improve both the stability and outcome of CSI methods with the proposed algorithm validated using both experimental data — comprising of image reconstructions of a cylindrical phantom, human arm phantom and a human forearm — and simulated data, comprising of models of a human forearm and neck. The MR-CSI method was found to effectively determine both, the locations and complex permittivity of the object of interest. However it failed to reconstruct tissues with dimensions less than half the wavelength of the incident frequency. Another limitation of the MR-CSI method was the requirement for the background medium to be homogeneous, which was essential for the computation of the Green's function. In order to overcome these limitations and apply MR-CSI to applications incorporating heterogeneous background medium, Abubakar [16] proposed the finite-difference formulation of MR-CSI (FD-MR-CSI), wherein the finite difference operator was used in-lieu of the Green's function. Through numerical simulations, the proposed FD-MR-CSI method was reported to successfully reconstruct unknown objects in applications such as through-the-wall imaging and biomedical imaging, with an improved performance observed when compared with the MR-CSI method. The FD-MR-CSI method was also reported to perform better in applications requiring reconstruction of object with a high-contrasts when compared with background medium.

A finite-element formulation of CSI (FEM-CSI) was proposed [266] in order to overcome the following limitations of FD-MR-CSI: difficulty in modelling arbitrary shaped boundaries and including *a priori* information about the target when working with structured rectangular grids. The proposed FEM-CSI method was subsequently applied to reconstruct images of the human forearms and human legs [22, 105], with the thickness of the adipose tissue reported to affect the accuracy of the reconstructed image.

Whilst, the above reviewed CSI algorithms do not require a forward solver at each iteration, the number of unknowns are larger than the Newton-based approaches, therefore requiring a larger number of iterations to converge [68].

The tomographic methods reviewed above — both Newton-based methods and CSI methods — primarily work on electric field (E-field) values of the scattered field and incident field (Equations 2.3-2.5). However, data collected experimentally, or collected in simulations using full-antenna models, are S-parameters, thereby necessitating the conversion of S-parameters to E-field values [184]. These methods are commonly referred to as calibration methods, as they also aim to resolve the disparity between experimental and simulation setups used in the forward model.

Two main classes of calibration methods have been proposed: the conversion of S-parameters to E-field values [184], and the modification of Equations 2.3-2.4 to directly leverage S-parameters [113, 114]. Two different calibration methods were proposed for converting S-parameters to E-field values [184]: incident calibration and scattered field calibration. Coefficients for conversion were either calculated based on the ratio between measured incident S-parameters and modelled incident field measurements, or the ratio between measured scattering S-parameters and modelled scattering field values using a canonical reference object. The results indicated that, for an air-based microwave tomography system, the scattered field calibration method produced better results even when an inaccurate incident field was used. These calibration methods have subsequently been applied in numerous studies [24, 170].

Modifying Equations 2.3-2.4 to directly leverage S-parameters has been proposed as an alternative calibration method [41, 91, 112, 114]. The dyadic Green's function in Equation 2.3 was modified to directly provide S-parameters, by incorporating an antenna model based on the source-scattering matrix formulation [113, 114]. This formulation was successively applied to reconstruct the permittivity of different objects from experimental data by using BIM, with the antenna characterisation performed using Ansys HFSS [112].

Another calibration method which modifies the Green's function to directly leverage S-parameters has been proposed by Haynes [112]. Specifically, this method replaces the Green's functions with field values computed using a high fidelity simulation (simulations incorporating exact antenna models, coupling liquid etc) [91, 115]. This method has been applied to detect the permittivity and location of strokes in a head phantom using experimentally collected S-parameters [91], and also been applied to successfully reconstruct the changes in permittivity due to temperature alterations [115].

2.5.2 Qualitative microwave imaging

The quantitative tomographic methods discussed in the previous subsection aim to recover both the location and the permittivity of the object of interest. However, the equations solved in tomographic methods are ill-posed, nonlinear and require computationally expensive algorithms [16, 112, 170, 266]. Conversely, qualitative (or radar-based) imaging algorithms which aim to purely detect the presence (location) of a scatterer, are computationally inexpensive and can be applied in real-time. These algorithms do not compute the permittivity of the object of interest; and have been widely applied in breast and brain tumour imaging studies. The following section will review the two main classes of qualitative algorithms: radar-based imaging algorithms applied to scattered signals obtained from ultra-wide band (UWB) antenna systems, and imaging algorithms built on the principle

of time-reversal. All qualitative algorithms can be directly applied to recorded S-parameters without requiring any conversion to E-field values.

As stated radar-based imaging algorithms have been primarily applied to detect and locate tumours in the breast and brain [90, 233]. One type of radar-based imaging algorithms are the confocal imaging algorithms, wherein the collected scattered signals (at every antenna) are artificially time-delayed and focused to detect the location of a scatterer. Scattered signals collected from regions without a scatterer cancel out each other while scattered signals from region with a scatterer constructively add up. The feasibility of applying confocal imaging algorithms to detect tumours was initially investigated by Fear [90] through numerical simulations. Specifically, they probed planar and cylindrical models of the breasts (emulating patients lying supine and prone) using bowtie antennas, and focused the collected S-parameters using the Delay and Sum (DAS) confocal imaging algorithm (Equation 2.6). Their results indicated that DAS was able to successfully detect tumours in both the models.

$$I(\vec{r}) = \left[\sum_{i=1}^{M} b_i\left(\tau_i(\vec{r})\right)\right]^2 \tag{2.6}$$

where:

1. b_i is the scattered signal
2. τ_i is the time delay computed from i antenna to location $\vec{r}$
3. M is the number of observation points (antennas)

To further validate the aforementioned confocal imaging method on experimental data, Fear [90] incorporated the DAS algorithm and UWB antennas into the Tissue Sensing Adaptive Radar (TSAR) system to detect tumours in the breast, and performed initial feasibility studies on phantoms consisting of polyvinyl chloride (PVC) pipes with wooden hemispheres of 2.5 cm [90]. The PVC pipe represented the skin in the phantom, the spheres represented the tumors, and the breast tissue was represented by air. The phantom was probed using a monopole antenna, with the phantom and antennas immersed in a coupling liquid. The collected signals were pre-processed using the Woody averaging method to reduce the reflection caused by the skin. The authors reported that the DAS confocal imaging algorithm was able to detect tumours in both simulations and physical experiments.

An enhancement of this TSAR system (namely the second generation TSAR system) was subsequently proposed. The second generation TSAR system incorporated a Wu-king monopole antenna and a novel pre-processing step, and has

been experimentally tested on a breast phantom immersed in a coupling liquid [233, 234]. The novel pre-processing step incorporated both the Woody skin averaging algorithm and an adaptive filtering method based on recursive least squares. The phantom was made using silicone sheets and a mixture of canola oil and flour, with the tumours made using alginate powder. This second generation TSAR system was reported to be able to locate tumours with spatial errors of 0.1cm. The second generation TSAR system was also employed to detect tears in the meniscus [222]. Salvador [222] initially validated whether microwave imaging can detect tears through simulations, by probing a healthy meniscus and a meniscus with a tear using an antipodal vivaldi, with results indicating that the reconstructed images could detect tears. The authors further validated it experimentally on a bovine menisci (with and without a tear) and the second generation TSAR system, with results indicating that the tear could be identified in the differential image generated.

Whilst the TSAR system uses the DAS confocal imaging algorithm, other variations of DAS have been proposed to reduce artefacts in reconstructed images, to improve resolution and enhance accuracy. One widely-applied variation of DAS is the Delay-Multiply and Sum (DMAS) algorithm [149], where the backscattered signals at all antennas are first time shifted (similar to the DAS algorithm) and then pair multiplied before being summed to create a synthetic focal point (Figure 2.7). The efficacy of the proposed DMAS algorithm was validated using a variety of numerical breast phantoms, with images produced using DMAS found to have lesser image artefacts and improved localisation errors when compared with images generated using DAS.

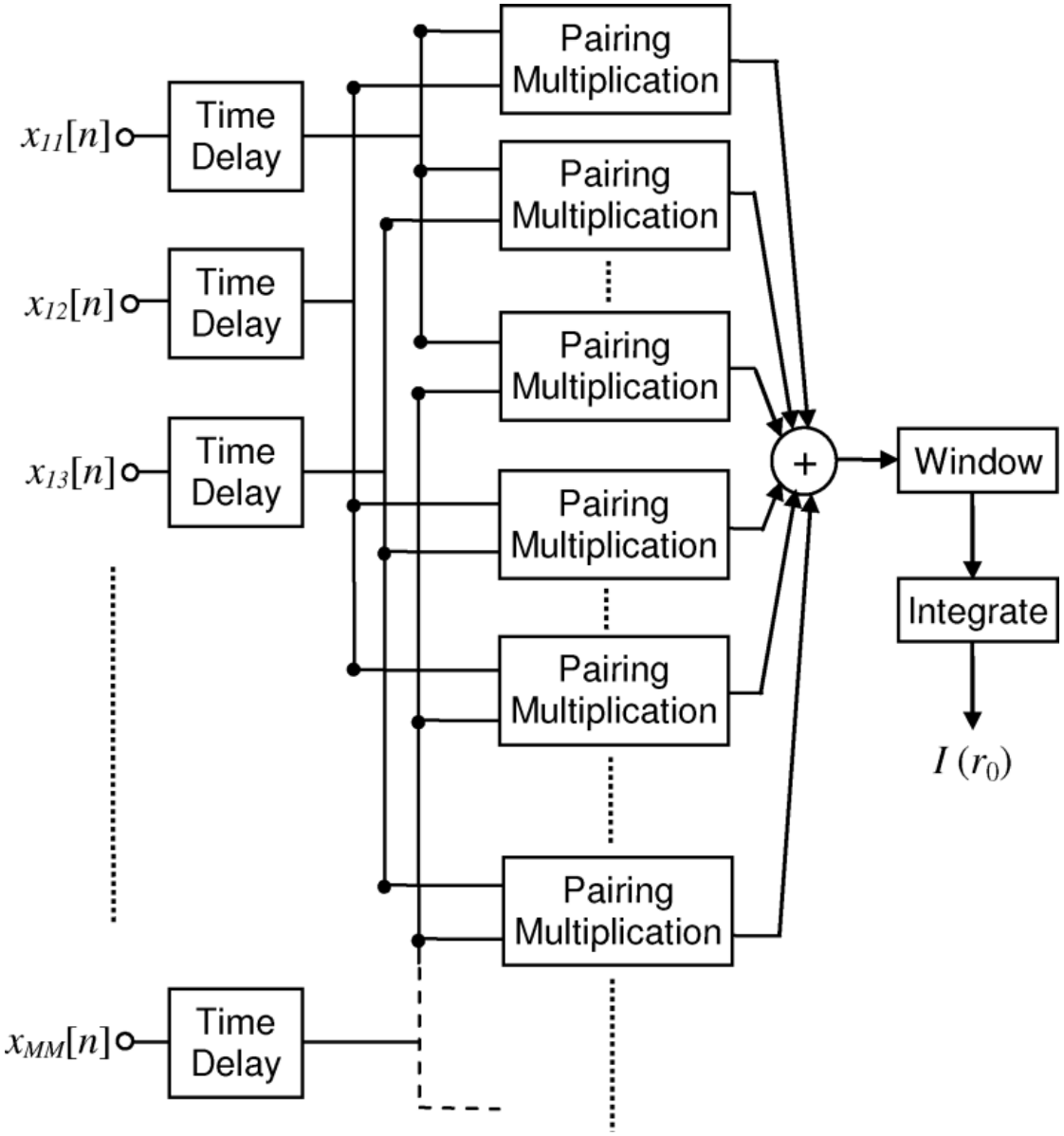

Figure 2.7: Pictorial representation of delay multiply and sum algorithm [149].

A novel iterative DAS/DMAS method was proposed by Reimer [207], who compared its performance with conventional DAS/DMAS using the following metrics: signal-to-clutter ratio (SCR; the ratio of the maximum response in the region known to belong to the tumour to that of the maximum response outside the tumour region) and signal-to-mean ratio (SMR; the ratio of the maximum response in the region known to belong to the tumour to that of the mean response in the region outside the tumour). SCR and SMR values above 0 denote the presence

of a scatterer; with negative values being reported for tumour detection in denser breasts. The proposed and conventional confocal imaging algorithms were applied to scattering data obtained from breast phantoms of different sizes and with different percentages of fibroglandular volume, with higher SMR and SCR observed for all images reconstructed using the proposed algorithms. However, no significant differences were observed in the localisation error between the four imaging algorithms.

The same authors also conceptualised the radar-based reconstruction method into an optimisation problem, and proposed an optimisation-based radar-reconstruction (ORR) algorithm [208]. The ability of the proposed ORR algorithm to detect tumours in breast phantoms was compared with DAS and DMAS algorithms. They found that DMAS and ORR algorithms had higher SCR than DAS. Notably, ORR was the only algorithm capable of detecting tumours of 15mm diameter and was also the only algorithm which did not produce a hot-spot artefact (a localized high-intensity region within a reconstructed image that does not correspond to any physical phantom feature).

Similarly, Elahi [88] compared the performance of different data-independent and data-adaptive confocal imaging algorithms on patient data. Specifically, six different imaging algorithms [DAS; DMAS; improved DAS; coherence factor DAS; channel ranked DAS; and robust Capon beamformer (RCB)] were tested on patient breast tumour data. The results indicated that, whilst conventional DAS was able to detect most malignancies, it also generated multiple artefacts in the reconstructed image. Conversely, improved DAS and coherence factor DAS improved image quality but failed to correctly localise the malignancy, especially in the presence of multiple lesions and heterogeneous breast tissue. Pertinently, DMAS performed the best amongst the six algorithms and RCB performed the worst, suffering severe degradation.

An alternative to the confocal imaging used in the TSAR system, is the microwave imaging via space time (MIST) beamforming algorithm proposed by Bond [50]. In the MIST system, the patient lies in a supine position with imaging performed over the naturally flattened breast, in contrast to TSAR, where the patient lies in the prone position with the breast imaged using a hole in the examination table [233]. Whilst the MIST beamforming also works with UWB antennas (similar to the TSAR system), the spatial focusing is achieved by first time shifting the received signals to align the scattered signals from every candidate location. The time-aligned signals are then passed through a bank of finite-impulse response (FIR) filters, one for each antenna channel, and summed to produce the beamformer output. The summed signals are then time-gated, after which the energy at each location is calculated [50]. Weights for the FIR filters are determined using a least squares approach. The MIST system has been reported to successfully locate

tumours in heterogeneous medium, and has been shown to be robust to noise. Li [148] extended MIST to reconstruct 3D images and to demonstrate its efficacy using experimental data. The experimental phantom consisted of a thin layer of skin stimulant separating the breast phantom from the antenna immersion medium. Breast and tumours were made of normal and malignant tissue stimulants, with image artefacts removed using a data adaptive algorithm which subtracted the signal received at each location from a filtered combination of signal received at other locations. Results indicated that the tumours were detected within 2mm of the actual edge of the tumour. MIST was further successfully applied to detect strokes and tumours in a phantom and simulated brain phantom using a wearable antenna system [221].

The qualitative imaging algorithms reviewed above are commonly applied to signals acquired from UWB systems. Data collected from UWB antennas encompass scattering data collected across a wide range of frequencies, which are then shifted and focused to generate an image. However, developing UWB antennas for each application is not feasible, therefore qualitative imaging algorithms which primarily work on a single frequency have been proposed to detect the location of scatterers. These algorithms leverage the Green's function — an integral part of quantitative algorithms — to time-reverse the acquired signals and determine the location of the scatterer.

Mathematically, in time-reversal imaging, the location of one or more scatterers is found to correspond, in a one-to-one manner, with the eigenvectors of the hermitian time-reversal matrix (Equation 2.7) [82]. The hermitian time-reversal matrix is computed using Equation 2.7.

$$\begin{aligned} K_{j,k} &= \psi\left(\boldsymbol{\alpha}_j, \boldsymbol{\alpha}_k\right) \\ &= \sum_{m=1}^{M} \tau_m G\left(\mathbf{x}_m, \boldsymbol{\alpha}_j\right) G\left(\mathbf{x}_m, \boldsymbol{\alpha}_k\right) \end{aligned} \tag{2.7}$$

where:

1. $K_{j,k}$ is the multistatic time reversal matrix
2. $\psi\left(\boldsymbol{\alpha}_j, \boldsymbol{\alpha}_k\right)$ is the scattered field when antenna $\boldsymbol{\alpha}_k$ acts as a transmitter and antenna $\boldsymbol{\alpha}_j$ acts as the receiver
3. τ_m is the scattering coefficient
4. $G\left(\mathbf{x}_m, \boldsymbol{\alpha}_j\right)$ is the Greens's function computed at point $\mathbf{x}_m$ when antenna $\boldsymbol{\alpha}_j$ is the receiver
5. $G\left(\mathbf{x}_m, \boldsymbol{\alpha}_k\right)$ is the Greens's function computed at point $\mathbf{x}_m$ when antenna $\boldsymbol{\alpha}_k$ is the transmitter

However, time-reversal imaging has been reported to fail when the targets are not well-separated, or when the antenna array is sparse, a situation typical in biomedical imaging [82]. These factors have resulted in the proposal of multiple variations of time-reversal imaging algorithms which can overcome the shortcomings of the traditional time-reversal imaging algorithm. One such variation is the Multiple Signal Classification (MUSIC) algorithm, which was initially proposed to determine the direction of arrival (DOA) of signals [227]. Devaney [82] compared the performance of the MUSIC algorithm and time-reversal imaging to detect scatterers which were both well separated and which were located close to each other in an inhomogeneous medium. The authors reported that MUSIC was successfully able to determine the position of scatterers in both scenarios whilst time-reversal imaging could only determine their location when the scatterers were well separated. They also indicated that the performance of both MUSIC and time-reversal degraded when the wrong Green's function was used.

Variations of time-reversal and MUSIC algorithms have been hence proposed such as beamspace-decomposition of time reversal operator (beamspace-DORT) and beamspace-time reversal-MUSIC (beamspace-TR-MUSIC). These two methods were proposed to overcome the low imaging resolution of DORT and the degradation of MUSIC when signal correlation between antennas increases [122]. The proposed methods were reported to locate tumours in simulations of highly dense breasts, obtaining higher SCR than DORT or MUSIC.

Compared to time-reversal imaging algorithms, MUSIC has been more widely applied in microwave imaging applications [187, 190, 218]. For example, in one study, the shape and location of anomalies in the imaging domain were detected by applying MUSIC at a single frequency [187, 190]. The authors reported that whilst the existence (location) of all anomalies and the shape of small anomalies were accurately detected using MUSIC, the full shape of an extended (large) anomaly was not reconstructed. Anomaly size in the above study was determined based on their size with respect to the wavelength of the incident waveform.

Similarly, an algorithm inspired by MUSIC, interferometric-MUSIC (I-MUSIC), was investigated for the detection of breast tumours [218, 219, 220]. I-MUSIC uses a multifrequency approach — where images reconstructed at each frequency is multiplied with each other to reduce the artefacts in the final image — with reflection S-parameters (S11), collected in a multi-monostatic configuration, provided as input. The proposed I-MUSIC algorithm was tested on data collected using a simulated antipodal vivaldi antenna and a simulated cylindrical breast phantom immersed in a coupling liquid. The reconstructed images using I-MUSIC were also compared with reconstructed images using non-coherent migration and wideband MUSIC. Reportedly, the I-MUSIC algorithm was able to detect single and multiple tumours in breast tissues with and without fibroglandular structures. Authors

additionally reported a maximum localisation error of 2.8mm for tumours located close to the skin with localisation errors less than 1.5mm for tumours located in the centre of the imaging domain. Additionally, I-MUSIC also reportedly produced images with greater SCR and SMR when compared with other algorithms and located tumours with smaller errors. When applied to experimental data, spatial errors of 26mm were obtained using I-MUSIC. The proposed I-MUSIC algorithm was also successfully leveraged to image the bones of a pig shank immersed in a coupling liquid. Localisation errors of 2.78, 2.85 and 4.23cm were obtained at different heights of the bone [217].

Qualitative imaging algorithms, which are neither based on the principle of time-reversal nor leverage radar-based techniques (like the algorithms reviewed above), have also been proposed for biomedical microwave imaging, such as algorithms based on huygens principle and the wave-migration algorithm. In one study reconstructed images, obtained by applying huygens principle to multi-bistatic (S21) measurements, were able to detect and localise hemorrhagic strokes in both simulations and a brain phantom [237]. Similarly, huygens principle has also been successfully applied to detect and localise skin cancer in a phantom mimicking the human forearm using novel artefact-removal algorithms [135].

Another qualitative algorithm applied to biomedical imaging is the wave-migration algorithm, which was proposed in conjunction with a non-contact, coupling liquid-free system, to detect fractures in a bone phantom [223]. Data fed to the wave-migration algorithm are S11 parameters collected at multiple locations on the bone using a vivaldi antenna, with the antenna moving on a cylindrical surface over the bone. The collected signals are then filtered using a novel regional filter. The algorithm and system were leveraged to detect fractures in the bone [223]. However, the proposed algorithm has not been shown to detect fractures which do not break the skin surface.

The above reviewed qualitative algorithms — radar-based, time-reversal based, huygens principle and wave-migration — are computationally inexpensive when compared with quantitative algorithms, and can therefore be applied in real-time. However, the majority of the qualitative imaging algorithms have been applied to detect the location of small scatterers, and their performance typically degrades in the presence of extended scatterers. In addition, qualitative imaging algorithms based on time-reversal requires the Green's function to be computed, which requires both *a priori* knowledge of the background medium and (ideally) a homogeneous background medium, as computation of Green's function for an inhomogenous medium is computationally demanding. However, as reviewed in the previous subsection, studies have proposed novel methods to overcome the limitations of the Green's functions [115]. However, these methods have not been integrated with qualitative imaging algorithms.

2.5.3 Antennas and sensitivity of algorithms

The accuracy and efficacy of both quantitative and qualitative imaging algorithms depend on several factors: the hardware used, the magnitude of coupling of the electric field with the object to be studied, and the sensitivity of the imaging algorithm to factors such as the presence of fibroglandular tissues, Green's function (or propagation speed of wave) and artefact removal methods; Therefore, research has been undertaken to develop novel antenna models and artefact removal methods, and to understand the sensitivity and specificity of the imaging algorithms to various factors.

Novel antenna designs have been proposed to either remove the need for coupling liquid or to improve coupling with the object of interest. For example, fern antipodal vivaldi antennas [180], metamaterials based antennas [121, 125, 127, 267] and cavity-backed antennas [60] have been proposed to improve the coupling of the electric field with the human body. The proposed designs have been able to improve the efficiency and gain of the antennas markedly, generating reconstructed images with reduced artefacts. Another novel antenna — which uses a dielectric medium matching the permittivity of dense breast tissues — was proposed to improve coupling into the human body and to eliminate the need for coupling liquid [25, 26]. The authors demonstrated the improved ability of their proposed antenna to detect tumours in the breast when applied in raster scanning applications. Similarly, a dual-patch antiphase antenna [156] was also proposed to improve coupling with the human body and remove the need for a coupling liquid. This antenna design resulted in greater penetration when compared with contemporary antennas, and has been applied to detect changes in bone permittivity due to osteoporosis and osteopenia. Guerrero-Orozco [109] proposed a novel monopole antenna (surrounded by a lossy-gel) to remove the need for a coupling liquid and to reduce multipath reflections and improve image quality. Simulated and measured data indicated that the gels reduced multipath signals, and the reconstructed images indicated that a muscle rupture was successfully imaged (with lesser image artefacts) using the proposed antenna.

Other studies have investigated the sensitivity and specificity of the imaging algorithms. For example, with the increasing uptake of microwave imaging for breast cancer detection, and the diversity in breast composition and tumour shape (and size) found in the general public, O-Loughlin [181] investigated the sensitivity and specificity of confocal imaging algorithms to the permittivity of breast models. Specifically, the authors evaluated the efficacy of patient-specific estimation of propagation speed within the breast by assessing three idealised permittivity estimation methods: 1). fixed-value permittivity estimation, where the fixed-value represents the population mean; 2). glandular-dependent permittivity estimation, where the reconstruction permittivity varies based on the glandular content of the

breast phantom; and 3). patient-specific permittivity estimation, where the reconstruction permittivity varies based on each subject. Their results indicated that, in phantoms mimicking purely healthy tissues, an increase in breast density was positively correlated with the number of false-positives for fixed-value estimation; specificity was neither improved nor impaired for glandular-dependent and patient-specific estimation for the most dense breast phantoms. Increased breast density was also associated with reductions in the sensitivity of all three estimation methods; however, the overall sensitivity was higher using both glandular-dependent and patient-specific estimation than it was for the current standard, fixed-value estimation.

Similarly, Yavuz [265] investigated the sensitivity of time-reversal imaging algorithms to model perturbations. Three perturbations were analysed: performance under clutter and additive noise, variation in performance due to losses in intervening medium, and effects of translation perturbations on the time-reversal array. Two time-reversal imaging algorithms, DORT and MUSIC, were investigated in both narrow-band and ultrawide-band operation. The results indicated that in homogeneous medium, narrowband-MUSIC and UWB-MUSIC outperform the DORT method, both in terms of range and cross-range resolution. However, under increased clutter and noise levels, DORT methods were more robust than MUSIC methods. Additionally, both UWB-MUSIC and time domain-DORT produce stable images due to their incorporation of multiple frequencies.

Another study investigating factors which may affect microwave imaging results, studied the impact of the shape and size of human models used in simulations on the performance of a dual-band antenna [66]. Specifically, four virtual population models and three homogeneous models in Sim4Life [11] were compared based on S11 parameters and the variation in antenna gain and efficiency. The results indicated that variation in the shape and size of human models had a greater influence on antenna characteristics than the influence tissue permittivity and thickness had.

2.5.4 Summary and key takeaways from microwave imaging

The previous section has shown the breadth of research undertaken in the field of microwave imaging. Based on our review and analyses, these are our key takeaways:

- Microwave imaging, which leverages the difference in electrical properties of various tissues and between healthy and diseased tissues, has been widely applied in breast and brain tumour detection

- Microwave sensing, an application of microwave imaging which does not generate a map but studies the difference in S-parameters, has been used to detect the location of fractures and to investigate variation in bone properties due to osteoporosis and osteopenia
- Generation of an image using microwave imaging can be classed into quantitative and qualitative imaging algorithms
- Quantitative imaging algorithms provide both the location and dielectric properties of the object of interest. However, they are computationally heavy, require iterative algorithms to determine the solution and might require a forward solver at every iteration. In addition, they require conversion from the collected S-parameters into electric field values
- Qualitative imaging algorithms only provide the location of a scatterer, but are computationally inexpensive and work directly on S-parameters
- Microwave imaging has been applied to study the bone in human forearms and legs, and to image the breast and brain
- In general, microwave imaging requires the object of interest to be immersed in a coupling liquid to improve penetration of the electric field. However, studies proposing novel antennas and algorithms have been undertaken to remove the need for coupling liquid

The studies reviewed above indicate that microwave imaging is a viable biomedical imaging modality, as it is safe (non-ionising) and potentially more cost-effective than contemporary imaging modalities such as fluoroscopy, MRI and CT. Additionally, microwave imaging has been applied to image bones and muscles with better clarity than ultrasound. Although it has not yet been applied within the biomechanical field, microwave imaging has been successfully applied to locate and image the bone, and has the potential to be applied in a wearable fashion.

2.6 Conclusion and key-takeaways

The research reviewed in this literature review highlighted the following:

1. Soft tissue artefacts (STA) are one of the critical sources of error in movement analysis, and have a deletrious impact on kinematics computed from skin-mounted marker-based systems

2. Numerous methods have been proposed to reduce the impact of STA on computed kinematics; however none of the proposed solutions are effective for all motions or for all participants

3. Amongst the proposed solutions, multibody kinematic optimisation (MKO) methods are the most widely applied solution to reduce the effects of STA. However, majority of MKO methods (and other solutions in general) have only been validated on subjects with healthy BMI scores

4. Artefact-free bone movement acquired through imaging methods, intracortical pins, or percutaneous pins are considered as true bone movement.They have been leveraged in multiple studies to improve computed kinematic accuracy or to quantify STA

5. Fluoroscopy, computed-tomography (CT), magnetic resonance imaging (MRI) and ultrasound have been widely applied in biomechanical research to determine artefact-free bone movement. However, the ionising nature of fluoroscopy and CT, in addition to the high cost of MRI, fluoroscopy and CT prevent their regular use in biomechanics. As an alternative, biomechanical systems incorporating ultrasound imaging have been proposed as a safe and cost-effective solution

6. Microwave imaging, an imaging modality leveraging non-ionising radiation and the differences in electrical properties between various tissues and healthy and diseased tissues, has been proposed as a viable imaging modality in breast and brain tumour imaging. Studies have also used microwave imaging to detect bones in human forearms and legs

7. Microwave imaging has been shown to be more robust and to provide more information than ultrasound imaging. In addition, microwave imaging does not require specialised knowledge and can be applied using off-the shelf antennas

8. Algorithms for microwave imaging can be classed into quantitative imaging (which is computationally expensive but provides both the location and electrical properties of the object of interest) and qualitative imaging (which is computationally inexpensive but only provides the location of a small scatterer)

Chapter 3

Influence of body fat on the accuracy of MKO methods and the investigation of residual error as a goodness-of-fit metric

3.1 Introduction

This chapter evaluates the efficacy of multibody kinematic optimisation (MKO) methods when applied to participants of varying body fat or to data with varying magnitudes of soft tissue artefacts (STA). As highlighted in the previous chapter (Chapter 2), of the numerous solutions proposed for reducing the effect of STA, MKO methods are the most widely applied. However, they have only been validated on data obtained from participants of healthy body weight, or from data with small magnitudes of STA — neither of which are representative of the clinical population. Therefore, the results from this chapter will underscore the need for a generalisable method to reduce STA and improve the accuracy of clinical gait analysis: the challenge this thesis aims to address.

This chapter will also explore the feasibility of using residual error as a metric to evaluate the accuracy of computed kinematics, and therefore the viability of the pose estimation algorithm, in the absence of ground-truth data (artefact-free data) or a normality dataset.

Section 3.2 provides background on residual errors and MKO methods, and introduces the problem we investigate in this chapter. Section 3.3 describes the methods used to investigate the problem with the results reported in Section 3.4. The results are discussed in Section 3.5 with the conclusion and key takeaways from this chapter presented in section 3.6 .

3.2 Background

STA are discrepancies in bone movement computed using skin-mounted markers when compared with actual bone movement (artefact-free bone movement), and are subject-, task-, and marker-location specific [55]. As illustrated in the previous chapters (Chapters 2 and 2), STA has a large deleterious effect on the accuracy of kinematics computed using optoelectronic systems, often invalidating the usability of clinical gait analysis in pre-operative planning and post-operative assessment. For example, joint angle errors due to STA can affect the accuracy of femoral derotation osteotomy, a surgical intervention for in-toeing gait for children with CP.

Due to the significant impact of STA on computed kinematics, numerous solutions (STA models, novel segment optimisation methods, subject-specific joint constrains, etc) have been proposed to reduce the impact of STA on computed kinematics. However, none of the proposed solutions effectively reduce STA for all participants and for all investigated motions.

Multibody kinematic optimisation (MKO) is widely applied to reduce the effects of STA on computed kinematics [80, 131, 141, 153], with MKO approaches implemented in commonly used musculoskeletal modelling software such as OpenSim [81] and Anybody [78]. By incorporating rigid body and kinematic constraints, joint angles which minimise the difference between measured and model-derived (calculated) skin-marker trajectories are calculated (Equation 3.1). The following pipeline is commonly applied when leveraging MKO methods (Figure 3.1): scaling of a generic musculoskeletal model (incorporating joint models) to subject-specific dimensions (segment scaling), registering model-derived markers to experimental markers (marker-registration) and calculating joint angles using an MKO method, with the option of altering marker weights. Global optimisation [153], the MKO method incorporated in OpenSim, will be the MKO method investigated in this study.

$$\min_{\mathbf{q}(t)} \sum_{i=1}^{N} w_i \left\| \mathbf{p}_i^{\text{model}}(\mathbf{q}(t)) - \mathbf{p}_i^{\text{exp}}(t) \right\|^2 \tag{3.1}$$

Where:

- $\mathbf{q}(t)$ = vector of generalized coordinates (joint angles, translations, etc.) at time t
- N = total number of markers
- w_i = weight assigned to marker i

- $\mathbf{p}_i^{\text{model}}(\mathbf{q}(t))$ = position of marker i predicted by the model at time t, based on joint angles $\mathbf{q}(t)$
- $\mathbf{p}_i^{\text{exp}}(t)$ = experimentally measured position of marker i at time t

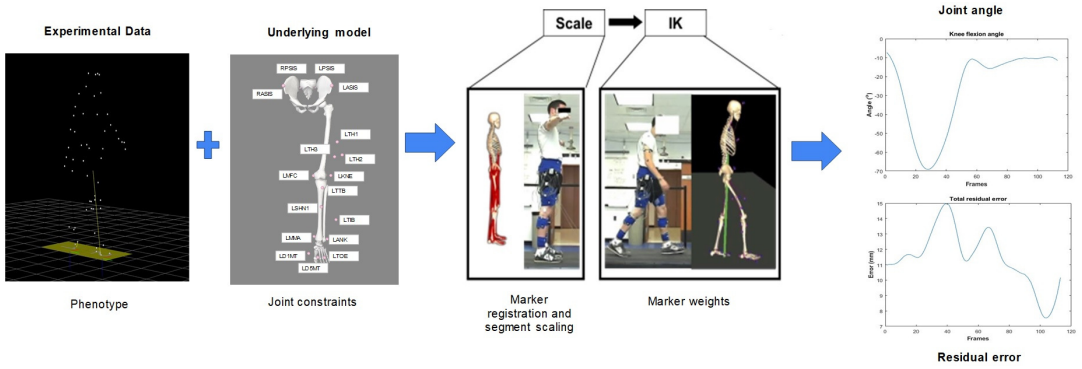

Figure 3.1: Experimental data from subjects of varying body fat or data with varying magnitudes of soft tissue artefacts are used as input to the pipeline. The impact of joint constraints is investigated by incorporating underlying models with differing joint constraints. Impact of errors during scaling (marker registration errors and segment scaling errors) are investigated. Markers (LASI: Left anterior superior iliac spine, RASI: Right anterior superior iliac spine, LPSIS: Left posterior superior iliac spine, RPSIS: Right posterior superior iliac spine, LTH1, LTH2, LTH3: Left lateral thigh cluster, LKNE: Left lateral femoral epicondyle, LTTB: Left tibial tuberosity, LSHN1, LTIB : Left shank cluster, LANK: Left lateral malleolus, LHEE : Left posterior distal aspect of the heel, LTOE: Left forefoot, LD1MT: Left heads of first metatarsals, LD5MT: Left heads of fifth metatarsals) with different weights are analysed to understand their influence on residual error and joint angles [9].

As detailed in Chapter 2, extensive research has been undertaken to investigate MKO methods, with multiple different MKO formulations [85], novel joint boundary conditions [198], design variables [33] and optimisation methods [80], proposed to improve kinematic estimation. However, the majority of these studies either use simulated data or experimental data from participants with a healthy body mass index (BMI) score. Despite the wide application of MKO methods to reduce the effects of STA, and evidence that a higher BMI score is associated with a greater magnitude of STA [54], a review indicated that only 6 out of 24 studies investigating MKO methods used experimental data which included participants with BMI scores > 24.9 (the threshold for overweight) [42]. The lack of representation of participants with high BMI scores in studies employing MKO methods is

a significant knowledge gap, and one which has not been adequately investigated or addressed. This problem is further exacerbated as many studies employ the exact same MKO method to investigate kinematic, kinetic and muscle activation differences in obese and non-obese participants [146].

In this study we evaluated the efficacy of global optimisation: 1). On data collected from participants with varying BMI scores and 2). and on simulated data with varying magnitudes of STA added to it. Specifically, we compared residual errors obtained from participants with higher BMI scores (and on simulated data with large magnitudes of added STA) with residual errors obtained from participants with lower BMI scores (and on simulated data with smaller magnitudes of added STA).

Residual errors (the optimised difference between measured and model-derived skin-marker trajectories)(Equation 3.2) derive from the MKO method and are often used to evaluate the MKO pipeline. For example, different scaling methods (segment scaling and marker-registration) were evaluated using residual errors as a metric [155, 199], with optimisation-based scaling reported to be more effective than linear scaling due to smaller residual errors observed. Similarly, residual errors were leveraged to evaluate different MKO formulations [52] with extended kalman filters (EKF) incorporating an STA model reported to reduce residual errors and joint angle errors. Studies have also reported that residual errors are sensitive to the MKO method [178] employed.

$$\mathbf{r}_i(t) = \mathbf{p}_i^{\text{model}}(\mathbf{q}(t)) - \mathbf{p}_i^{\text{exp}}(t) \tag{3.2}$$

Where:

- $\mathbf{r}_i(t)$ = residual error vector for marker i at time t
- $\mathbf{p}_i^{\text{model}}(\mathbf{q}(t))$ = position of marker i predicted by the model at time t (based on joint angles $\mathbf{q}(t)$)
- $\mathbf{p}_i^{\text{exp}}(t)$ = experimentally measured position of marker i at time t

Residual errors have also been used as a goodness-of-fit metric between the underlying model and the experimental data [42, 178, 235]. Lower residual errors have been reported as an indicator of: superior pose reconstruction capability of the proposed model [137], improved STA compensation [30] and higher accuracy in joint centre estimation [195]. In general, lower residual errors are indicative of lower kinematic errors, supporting the existence of a causal relationship between residual errors and kinematic errors.

However, the validity of residual errors as a goodness-of-fit metric has been questioned, with some studies reporting lower kinematic errors for higher residual errors [236], significant changes in computed kinematics with no change in residual

errors [86, 99] and, conversely, no significant change in kinematics with significant variation in residual errors [250].

Whilst the availability of true bone movement — acquired using intracortical pins, fluoroscopy or MRI — has allowed some studies to reduce kinematic uncertainty [29], acquiring true bone movement is impractical in general settings, thereby necessitating the need for a viable metric to evaluate the fidelity of computed kinematics. This need is further underscored by evidence that uncertainty in computed kinematics can significantly affect the reliability of subsequent biomechanical analysis [172, 174, 179].

Therefore, in this chapter, we also aim to further ascertain the viability of using residual errors as a goodness-of-fit metric. Specifically, we investigate: 1) The impact of the MKO pipeline (marker-registration, segment scaling, marker weights and joint models) on residual errors (Figure 3.1) ;2) The existence of a consistent causal relationship between residual errors and kinematic errors.

Through our dual investigations: residual error as a goodness-of-fit metric (and the impact of the MKO pipeline on residual errors) and efficacy of MKO methods on data with increased magnitudes of STA; we aim to further existing knowledge on the use of MKO methods to ameliorate the effects of STA, and to ensure their validation incorporates data from a wide variety of participants.

3.3 Methods

As stated above, two investigations were carried out in this chapter. The first investigation (Investigation 1) determined the validity of residual errors as a goodness-of-fit metric, and the second investigation (Investigation 2) analysed the efficacy of global optimisation (an MKO method) when applied to simulated data with varying magnitudes of STA, and to experimental data acquired from participants with varying ranges of BMI scores. Since the data and models for the two investigations are different, the methods for Investigation 1 are described first, followed by the methods used for Investigation 2.

3.3.1 Analysis of residual error: Investigation 1

3.3.1.1 Simulation Data

Data used in Investigation 1 were taken from the study conducted by Lamberto [138] and include 500 STA-affected marker trajectories of a single gait cycle. Reference marker trajectories were created by applying the point kinematics tool in OpenSim to joint angles of a single healthy gait cycle. STA were added (herein referenced as *Added*-STA) to the reference marker trajectories based on the models

listed in Table 3.1. Briefly, STA models for markers on the pelvis (RASIS, LASIS, RPSIS, LPSIS), shank (LSHN1, LTIB, LTTB, LANK), foot (LTOE, LHEE, LD1MT, LD5MT) and lateral epicondyle (LKNE) are sinusoidal functions of time with amplitudes varied non-uniformly using ranges reported in existing literature. STA models for the thigh markers (LTH1, LTH2, LTH3) are linear functions of hip and knee angles with mean values derived from the study undertaken by Bonci [49]. Further details regarding the marker trajectories can be found in the study by Lamberto [138].

STA Model	Marker Acronym	Segment	Equations	Range of parameters
Sinusoidal	RASIS, LASIS, RPSIS, LPSIS	Pelvis	$STA_X = A_X \bullet \sin(\omega \bullet t + \varphi)$ $STA_Y = A_Y \bullet \sin(\omega \bullet t + \varphi)$ $STA_Z = A_Z \bullet \sin(\omega \bullet t + \varphi)$	$A_x^{\mathrm{m}} = 17, A_y^{\mathrm{m}} = 20, A_z^{\mathrm{m}} = 26,$ $A_x^{95\%\mathrm{CI}} = 3, A_y^{95\%\mathrm{CI}} = 8, A_z^{95\%\mathrm{CI}} = 6$ $\omega \leq 25\frac{\mathrm{rad}}{\mathrm{s}}, \varphi \leq 2\pi$ $A_x^{\mathrm{m}} = 14, A_y^{\mathrm{m}} = 8, A_z^{\mathrm{m}} = 12$ $A_x^{95\%\mathrm{CI}} = 2, A_y^{95\%\mathrm{CI}} = 2, A_z^{95\%\mathrm{CI}} = 1$ $\mathrm{Amplitude} \leq 525\frac{\mathrm{mm}}{\mathrm{s}}, q \leq 2\pi$
Kinematics-dependent	LTH1, LTH2, LTH3	Left thigh	$\mathrm{STA}_{\mathrm{vector(i)}} = \boldsymbol{h}^{\boldsymbol{\alpha}} * h_i^{\mathrm{FE}}$ $+\boldsymbol{h}^{\boldsymbol{\beta}} * \boldsymbol{h}_p^{\mathrm{AA}} + \boldsymbol{h}^{\gamma} * \boldsymbol{h}_i^{\mathrm{IE}}$ $+\boldsymbol{h}^{\delta} * \mathrm{knee}^{\mathrm{FE}} + \boldsymbol{h}^{0},$ for $i = x, y, z$	$h^{\alpha}_{LTH1}, h^{\beta}_{LTH1}, h^{\gamma}_{LTH1}, h^{\delta}_{LTH1}, h^{0}_{LTH1}$ $h^{\alpha}_{LTH2}, h^{\beta}_{LTH2}, h^{\gamma}_{LTH2}, h^{\delta}_{LTH2}, h^{0}_{LTH2}$ $h^{\alpha}_{LTH3}, h^{\beta}_{LTH3}, h^{\gamma}_{LTH3}, h^{\delta}_{LTH3}, h^{0}_{LTH3}$
Sinusoidal	LKNE, LSHN1, LTIB, LTTB, LANK, LHEE, LTOE, LD1MT, LD5MT	Left thigh, left shank and left foot	$STA_X = A_X \bullet \sin(\omega \bullet t + \varphi)$ $STA_Y = A_Y \bullet \sin(\omega \bullet t + \varphi)$ $STA_Z = A_Z \bullet \sin(\omega \bullet t + \varphi)$	$A \leq 30, \omega \leq 25\frac{\mathrm{rad}}{\mathrm{s}}, \varphi \leq 2\pi$ $A \leq 15, \omega \leq 25\frac{\mathrm{rad}}{\mathrm{s}}, \varphi \leq 2\pi$ $A \leq 4.3, \omega \leq 25\frac{\mathrm{rad}}{\mathrm{s}}, \varphi \leq 2\pi$ $A \leq 2.56, \omega \leq 25\frac{\mathrm{rad}}{\mathrm{s}}, \varphi \leq 2\pi$ $A \leq 1.81, \omega \leq 25\frac{\mathrm{rad}}{\mathrm{s}}, \varphi \leq 2\pi$

Table 3.1: STA model added to reference marker trajectory. Equations for the STA models are acquired from literature [138]

3.3.1.2 Baseline model and MKO framework

The baseline model used was a 4-segment model (pelvis, thigh, shank and foot) with three joints (hip, knee and ankle). The baseline model was based on the musculoskeletal model, gait2354, in OpenSim [264] and contains an articulated joint with three degrees of freedom (DoF) for the hip (spherical joint model), a coupling joint for the knee, and a joint with one DoF for the ankle (hinge joint).

The baseline model was scaled based on the static trial provided, with scaling errors below the guidelines recommended by OpenSim (Root mean square error (RMSE) < 1cm and maximum marker error < 2cm).

To analyse the impact of each step of the MKO pipeline on residual errors, models differing from the baseline model were created to emulate possible errors/-variations at each step of the pipeline. Joint angles and total residual errors for the 501 trajectories (500 STA-affected trajectories and 1 reference marker trajectories) were calculated for every model using the inverse kinematic (IK) analysis in OpenSim. Total residual error was defined as the RMSE of all the markers and was calculated at every frame. All markers for the IK analyses were given an equal weight of 1 unless specified.

3.3.1.3 Model generation

Models emulating possible errors/variations at each step of the MKO pipeline were created as follows:

1. *Models with marker registration errors and segment scaling errors:* Models emulating errors during the marker registration and segment scaling steps were created following the pipeline outlined by Uchida [252]. Briefly, models emulating marker registration errors were created by altering the marker location (in the segment coordinate system, LCS) of the baseline model by adding a random perturbation. The models were verified to check if the new location of each marker was within a maximum allowable deviation from its original position. To simulate segment scaling errors, models differing from the baseline model only in their scale factors were generated. For each model, the scale factors for every segment were selected at random from the range [90%-110%] of the baseline scale factors. The model was posed using IK to verify that each marker on the new model was within the maximum allowable deviation (stated below) from its original position.

   Three models of increasing maximum allowable deviation (d) were generated for each (marker-registration and segment scaling) error. Maximum allowable deviation of d < 0.5cm, 0.5cm < d < 1.25cm and 1.25cm < d < 2cm were chosen as thresholds to reflect human-error during the processes [252].

2. *Models with different marker weightings:* Three marker weighting strategies were chosen. Weighting Strategy 1 (WS1), where all markers are given an equal weight (of 1 in this study). This weighting scheme is commonly applied in studies investigating marker weights [94, 235]. Weighting strategy 2 (WS2), where markers on anatomical landmarks such as on the pelvis (LASIS, RASIS, LPSIS, RPSIS), lateral epicondyle and lateral malleoli (LKNE,

LANK), and foot and heel markers (LTOE, LHEE, LD1MT, LD5MT) are given a weight of 5 with thigh and shank markers given a weight of 1. This strategy is recommended to ameliorate the effect of STA by under-weighting markers most affected by STA [28, 153]. Weighting strategy 3 (WS3), where thigh markers are excluded and remaining markers are given a weight of 1. The exclusion of thigh markers has been proposed to reduce the effect of STA [36, 235]. Marker names are listed in Figure 3.1.

3. *Models with different joint models:* Two models, incorporating joints with differing DoF to that of the baseline model, were created. The first model (Ball) had articulated joints at the hip, knee and ankle, and the second model considered every segment to be a free body (each segment having 6 DoF).

3.3.1.4 Data comparison and statistical analysis

Total residual errors of each of the models were compared with that of the baseline model. One-way repeated measures analysis of variance (ANOVA) tests (significance level 0.05) were conducted to investigate the effect of the MKO pipeline on residual errors. Post-hoc analyses using paired t-tests were performed with a corrected significance level based on Bonferroni corrections. Additionally, joint angles computed using each model were compared with that of the baseline model. Comparisons between joint angles were performed using paired t-tests (significance level 0.05). Additionally, a regression analysis between joint angle errors at every frame and mean total residual errors was performed.

For every significant result, Cohen's d effect sizes were calculated to determine the significance of the result. For all tests, Cohen's d < 0.2 was considered small, < 0.5 medium and > 0.8 large; Cohen's d was only calculated for frames with significant differences.

ANOVA, paired t-tests and regression analysis were performed using statistical parametric mapping (SPM, [191, 192]). SPM utilises the entire one-dimensional time series data to make probabilistic inferences. Non-parametric tests were conducted if normality could not be assumed with normality tests in SPM done using the D'Agostino-Pearson K2 test..

3.3.2 Efficacy of global optimisation when applied to data with varying magnitudes of STA (simulated and experimental): Investigation 2

3.3.2.1 Simulated data

The same simulated data used in Investigation 1 were also leveraged to investigate the relationship between magnitude of *Added*-STA and residual errors. *Added*-STA at each segment was calculated as the sum of RMSE errors between the artefact-affected trajectory and the reference trajectory for each marker in the relevant segment. Individual marker residual errors were computed as the RMSE difference between model-derived marker position and experimental-marker (trajectory) position at every frame. Total residual errors were defined as the RMSE of all the markers, and was calculated at every frame, and overall *Added*-STA was computed as the sum of individual segmental *Added*-STAs.

3.3.2.2 Experimental data

Skin-mounted marker gait data were collected from 50 healthy participants with varying BMI scores (Table 3.2). All participants provided written consent based on their understanding of the study with ethics for the study provided by the ethics committee at the School of Physics, Engineering and Technology, University of York, UK. Height, weight and body fat at the thigh and pelvis were recorded for each participant; body fat was acquired using skin-callipers (Table 3.2).

Characteristics	Low body fat (N=10)	High body fat (N=12)	Overall (N=50)
Age (years)	24.3±3.84	30±10.40	26.67±7.07
Height (cm)	180.8±4.97	178.08±8.23	175.46±8.78
Weight (kg)	67.44±7.53	91.75±11.46	75.73±15.04
BMI (kg/m^2)	20.60135±1.85	28.85±2.13	24.47±3.76
Body fat (%)	13.63±3.47	30.855±5.13	24.05±7.724

Table 3.2: Characteristics of the participants who took part in the gait study. Age, height, weight, body mass index (BMI) and body fat were collected or computed. Values presented are mean ± standard deviation

Treadmill gait data were captured using Motive 2.4 and 10 Flex 3 cameras from OptiTrack. Reflective markers were placed on each participant at specific anatomical landmarks on the lower body, as specified by lower body Helen Hayes biomechanical marker-set (Figure 3.2). As part of the data collection protocol, participants were asked to stand stationary in a 'T' pose followed by walking on

the treadmill at a speed of 0.3m/s. This speed value reflected the average self-selected walking speed of the participants.

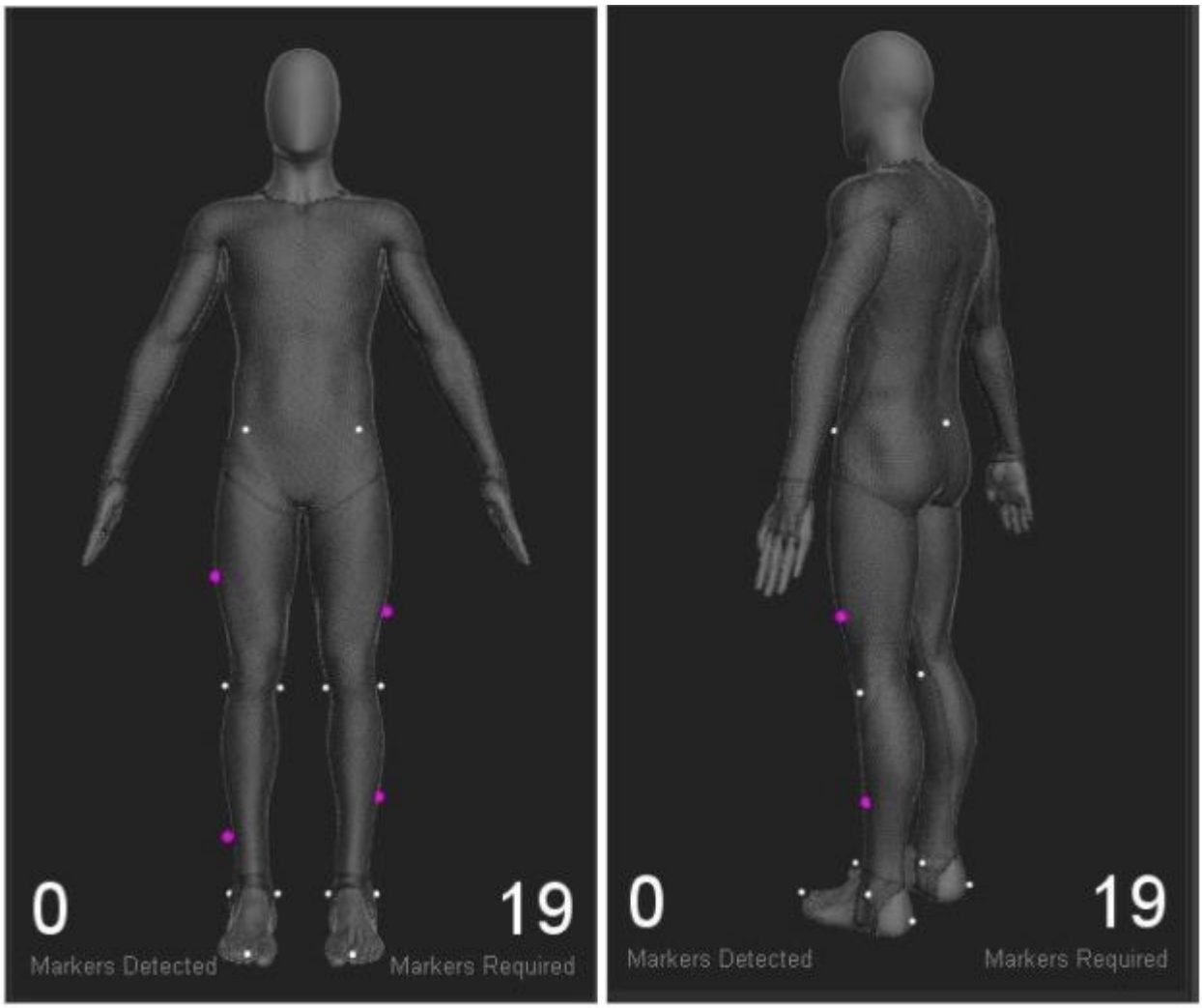

Figure 3.2: Marker placement based on lower body Helen Hayes biomechanical markerset as described in OptiTrak's Motive 2.4 [6].

Missing data frames in the raw data were filled by using either the cubic interpolation function, or the pattern fill function (based on the number of missing frames) in Motive 2.4 [10]. Data from 28 participants were discarded due to the following errors in data collection which affected subsequent processing: differences in marker position between static and motion trials due to marker falling between the two trials, or substantial amount of missing frames in a marker due to occlusion or clothing.

BMI scores were calculated for all participants using Equation 3.3. Participants were split into 2 groups based on their BMI: Group 1 (n=10, BMI < 24.9 [threshold for healthy BMI score]) and Group 2 (n=12, BMI > 24.9) [Table 3.2].

$$BMI = weight(kg)/height(m^2) \tag{3.3}$$

3.3.2.3 Residual Error Calculation

The static trials were used to scale a generic musculoskeletal model, Rajagopal2015 [205], to subject-specific dimensions, with scaling errors below the guidelines recommended by OpenSim (RMSE $<$ 1cm and maximum marker error $<$ 2cm). Total residual errors were calculated using the inverse kinematics (IK) analysis in OpenSim, with marker-specific residual errors computed as the RMSE difference between model-derived marker positions and experimental-marker positions at every frame. All markers for the IK analysis were given an equal weight of 1.

3.3.2.4 Data comparison and statistical analysis

As described earlier, efficacy of the global optimisation was analysed using residual errors. Accordingly, the following analyses were performed:

1. *Simulated data:* Regression analysis between residual errors and *Added*-STA at each segment and for the overall body was performed. R^2 values and correlation values were calculated for each regression analysis using the fitting tool in MALTAB. In addition, total residual errors and joint angle errors (as computed in the previous investigation [Investigation 1]) acquired using the top 50 and bottom 50 artefact-affected trajectories were compared with the trajectories grouped based on the magnitude of *Added*-STA. A multi-linear mixed model analysis was also performed to evaluate the effect of residual error and *Added*-STA on joint angle errors.

2. *Experimental data:* Median and spread of total residual errors and marker-specific residual errors were compared between the two groups using scalar statistical tests. Additionally, the trajectories of total residual errors and marker-specific residual errors were compared using t-tests in SPM (significance level 0.05). Non-parametric tests were conducted if normality could not be assumed with normality tests in SPM done using the D'Agostino-Pearson K2 test.

3.4 Results

3.4.1 Analysis of residual error: Investigation 1

3.4.1.1 Impact of MKO pipeline on residual errors

Our results indicate that every step of the MKO pipeline (marker registration, segment scaling, marker weights and joint models) had a significant effect on computed residual errors. For the sake of brevity, only cases for which at least one variation had a large effect size (Cohen's d > 0.8) are shown in this chapter; figures with smaller effect sizes are available in Appendix A.

Errors in the marker registration step of the MKO pipeline had a significant effect on total residual errors ($F = 4.744$, $p=0.001$, ANOVA; Figure 3.3 I) as indicated by the one-way repeated measures ANOVA test. Total residual errors computed using the 3 models (models with with increasing magnitudes of marker registration error) emulating errors in the marker registration step were greater than that of the baseline model for the entire duration of the gait cycle ($p=0.001$, paired *t*-tests; Figure 3.3 IIa–c). Cohen's d indicated a large effect for the model with marker registration errors > 0.5cm and < 1.25cm at frames 1–20 and 40–113, and for the model with marker registration error > 1.25cm and < 2cm for the entire duration of the gait cycle (Figure 3.3 IId). Median total residual errors were greater for the three models compared to the baseline model (Figure 3.3 III).

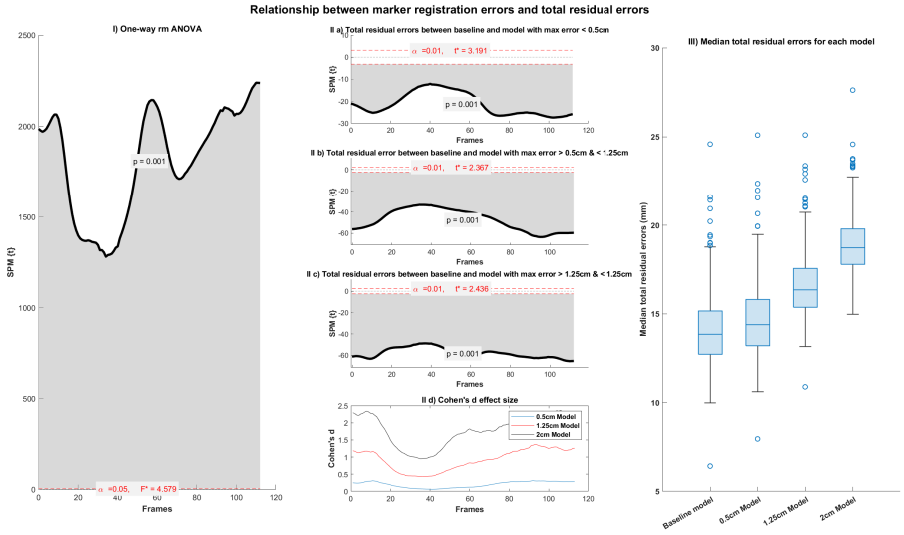

Figure 3.3: How to read SPM figures: The red lines (upper and lower for t-tests) indicate the critical threshold set at the respective alpha values (0.05 for ANOVA and 0.01 for post-hoc analyses). For ANOVA tests, if the critical f-statistic field vector (the thick black line) is above the critical threshold, the independent variables have a significant effect on the dependent variables. For paired t-tests if the t-statistic field vector (the thick black line) is either below or above the critical thresholds , the null hypothesis of equal means is rejected for those frames. The t-values are differences between the mean of the two sample sets and the variation that exists within the sample sets. For post-hoc analyses, if the t-statistic field vector is above the upper critical threshold, then (meanA>meanB) and vice versa if it is below the lower critical threshold. For all the post-hoc analyses, meanA was the mean of the baseline model and meanB the mean of the error incorporated model.
I) Results of a nonparametric one-way repeated measures ANOVA analysis between total residual errors acquired using the baseline model and three models with marker registration errors. The shaded area indicates marker registration has a significant effect on total residual errors (p=0.001). II) (a–c) Results of the post-hoc analyses using paired t-tests in SPM between total residual errors acquired using the baseline model and each of the models with marker registration errors. The shaded area shows a significant difference (p=0.001) in total residual errors with models with marker registration errors having statistically greater total residual errors. d) Cohen's d effect sizes between baseline model and three models with marker registration errors. III) The box plot shows the median total residual error between the four models. SPM: Statsitical parameteric mapping

Segment scaling errors also has a significant effect on computed residual errors ($F = 4.768$, $p = 0.001$, ANOVA), with greater total residual errors obtained for the models with segment scaling errors 0.5cm $<$ d and $<$ 1.25cm, and 1.25cm $<$ d $<$ 2cm compared with the baseline model for the entire duration of the gait cycle. Model with maximum segment scaling errors $<$ 0.5cm had greater total residual errors compared with the baseline model between frames 0–30 and 45–113. However, none of the differences indicated a large effect size (Cohen's d < 0.8; Figure A.1).

Similarly, despite marker weighting strategies having a significant impact on residual errors ($F = 5.960$, $p = 0.001$, ANOVA), with total residual errors of WS2 (16mm) greater than those of WS1 (13.5mm) and WS3 (14mm), none of the differences had a large effect size (Cohen's d < 0.8; Figure A.2).

Joint models incorporated in the underlying musculoskeletal model had a significant impact on total residual errors ($F = 5.654$, $p = 0.001$, ANOVA; Figure 3.4 I). The Ball model (spherical constraints) had the greatest residual errors ($p = 0.001$, paired t-tests; Figure 3.4 IIa,c), with the baseline model having greater residual errors than the 6 DoF model ($p = 0.001$, paired t-tests; Figure 3.4 IIb). Cohen's d indicated large effects between the baseline and 6 DoF model and between the Ball and 6 DoF model for the entire duration of the gait cycle, with large effects observed at frames 1–22 and 42–113 between the baseline and Ball model (Figure 3.4 IId).

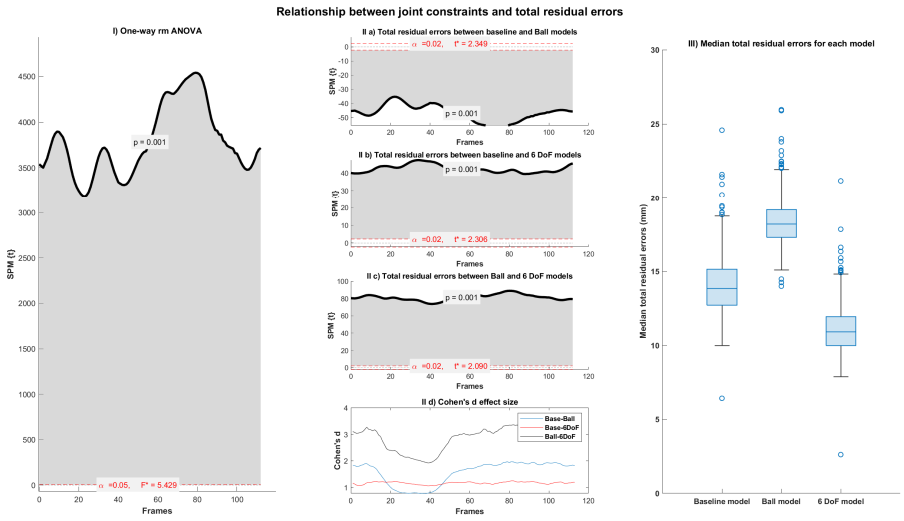

Figure 3.4: How to read SPM figures: The red lines (upper and lower for t-tests) indicate the critical threshold set at the respective alpha values (0.05 for ANOVA and 0.02 for post-hoc analyses). For ANOVA tests, if the critical f-statistic field vector (the thick black line) is above the critical threshold, the independent variables have a significant effect on the dependent variables. For paired t-tests if the t-statistic field vector (the thick black line) is either below or above the critical thresholds , the null hypothesis of equal means is rejected for those frames. The t-values are differences between the mean of the two sample sets and the variation that exists within the sample sets. For post-hoc analyses, if the t-statistic field vector is above the upper critical threshold, then (meanA>meanB) and vice versa if it is below the lower critical threshold.
I) Results of a nonparametric one-way ANOVA analysis between total residual errors acquired using the three models. The shaded area indicates the choice of joint models have a significant effect on total residual errors (p=0.001). II) Post-hoc analyses using paired t-test in SPM between total residual errors acquired using each of the models. a) Results indicate that the Ball model had significantly greater total residual (p=0.001) errors compared to the baseline model. MeanA is the baseline model and meanB is the Ball model. b) The shaded area shows that the baseline model had statistically higher (p=0.001) total residual errors compared to the 6 DoF model. MeanA is the baseline model and meanB is 6 DoF model. c) The plot indicates that total residual errors for the Ball model were significantly higher (p=0.001) than those for the 6 DoF model. MeanA is the Ball model and meanB is the 6 DoF model. d) Cohen's d effect sizes between baseline, Ball and 6DoF models. III) The box plot shows the median total residual errors acquired using the three models. SPM: Statsitical parameteric mapping

3.4.1.2 Relationship between residual errors and joint angles

For brevity, we have only reported joint angle variation for marker registration errors and joint models as their residual error variations had large effect sizes (Cohen's d > 0.8). The remaining results are available in Appendix A.

Joint angles computed using each of the models with marker registration errors differed significantly from those of the baseline model (p=0.001, paired *t*-tests; Figure 3.5 a–o). Large effect sizes were indicated by Cohen's d for the model with maximum marker registration error 0.5cm < d < 1.25cm for hip rotation angle (frames 45–90; Figure 3.5 q), and for ankle flexion angle (entire gait cycle; Figure 3.5 t); for the model with maximum marker registration error 1.25cm < d < 2cm for hip rotation angle (frames 1–8 and 50–113; Figure 3.5 q), for hip adduction angle (frames 18–23; Figure 3.5 r), for knee flexion angle (frames 20–25; Figure 3.5 s) and for ankle flexion angle (entire gait cycle; Figure 3.5 t).

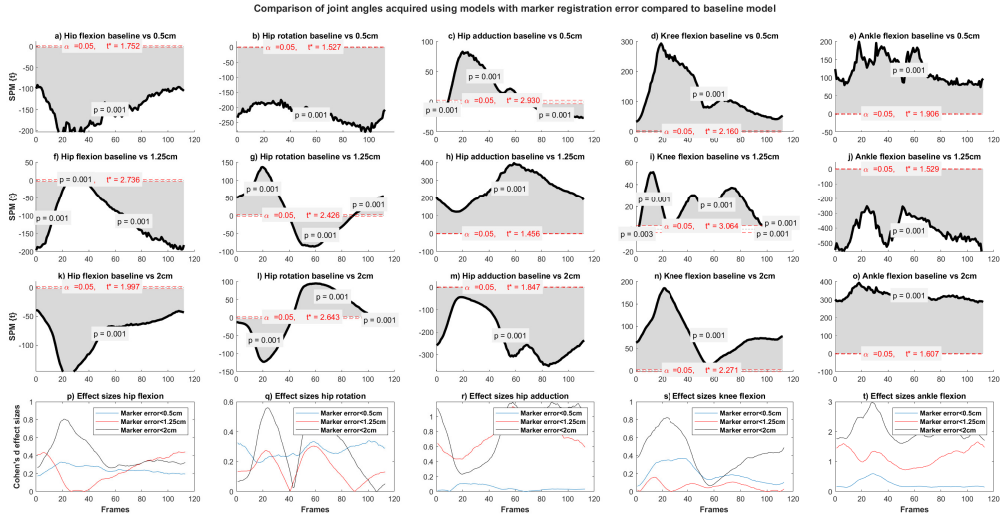

Figure 3.5: How to read SPM figures: The red lines (upper and lower) indicate the critical threshold set at the alpha values of 0.05. For paired t-tests if the t-statistic field vector (the thick black line) is either below or above the critical thresholds , the null hypothesis of equal means is rejected for those frames. The t-values are differences between the mean of the two sample sets and the variation that exists within the sample sets. For paired t-tests, if the t-statistic field vector is above the upper critical threshold, then (meanA>meanB) and vice versa if it is below the lower critical threshold. For all the paired t-tests, meanA was the mean of the baseline model and meanB the mean of the error incorporated model.
a–e) Paired t-tests between joint angles acquired using baseline model and model with maximum marker error of < 0.5cm. Shaded region indicates significant variation in joint angles (p=0.001). f–j) Paired t-tests between joint angles acquired using baseline model and model with maximum marker error of < 1.25cm with shaded region indicating significant variation between joint angles (p=0.001). k–o) Paired t-tests between joint angles acquired using baseline model and model with maximum marker error of < 2cm. Shaded region indicates significant variation in joint angles (p=0.001). p–t) Cohen's d effect sizes between the three models for hip flexion, hip rotation, hip adduction, knee flexion and ankle flexion. The columns are for hip flexion, hip rotation, hip adduction, knee flexion and ankle flexion joint angles respectively. SPM: Statsitical parameteric mapping

Similarly, kinematics obtained using models with differing joint models differed significantly from one another (p=0.001, paired t-tests; Figure 3.6 a–o). Large effect sizes (Cohen's d > 0.8) were observed between Base-Ball models for hip flexion angles (frames 38–58; Figure 3.6 p), hip rotation angles (entire gait cycle;

Figure 3.6 q), knee flexion angles (frames 10–82; Figure 3.6 s) and ankle flexion angles (entire gait cycle; Figure 3.6 t). Large effect sizes were also observed between Ball-6 DoF models for ankle flexion angle (frames 20–46; Figure 3.6 t).

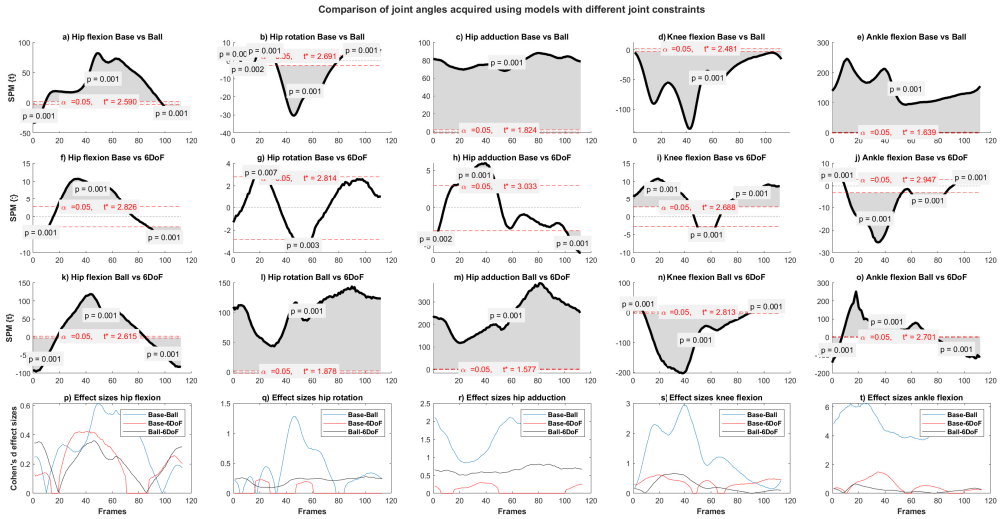

Figure 3.6: How to read SPM figures: The red lines (upper and lower) indicate the critical threshold set at the alpha values of 0.05. For paired t-tests if the t-statistic field vector (the thick black line) is either below or above the critical thresholds , the null hypothesis of equal means is rejected for those frames. The t-values are differences between the mean of the two sample sets and the variation that exists within the sample sets. For paired t-tests, if the t-statistic field vector is above the upper critical threshold, then (meanA>meanB) and vice versa if it is below the lower critical threshold.
a–e) Paired t-tests between joint angles acquired using the baseline model and Ball model. Shaded region indicates significant variation in joint angles (p=0.001). MeanA was the baseline model and meanB the Ball model. f–j) Paired t-tests between joint angles acquired using the baseline model and 6 DoF model with results indicating significant variation between joint angles (p=0.001). MeanA was the baseline model and meanB the 6 DoF model. k–o) Paired t-tests between joint angles acquired using the Ball model and 6 DoF model. Shaded region indicates significant variation in joint angles (p=0.001). MeanA was the Ball model and meanB the 6 DoF model. p–t) Cohen's d effect sizes between the three models for hip flexion, hip rotation, hip adduction, knee flexion and ankle flexion. The columns are for hip flexion, hip rotation, hip adduction, knee flexion and ankle flexion joint angles respectively. SPM: Statsitical parameteric mapping

Whilst segment scaling errors and marker weighting strategies did not have

large effect sizes in their variations of residual errors, joint angles computed using these models differed significantly (p=0.001, paired t-tests) when compared with those of the baseline model with large effect sizes observed for the ankle flexion angle and knee flexion angle (Appendix A, Figures A.3-A.4).

The results of a regression analysis between total residual errors and joint angle errors indicated significant positive correlations between: hip flexion angle errors and total residual errors (frames 48–53, 68–72; p=0.014; Figure 3.7 a), hip adduction angle errors and total residual errors (frames 51–54; p=0.022, p=0.014; Figure 3.7 c), knee flexion angle errors and total residual errors (frames 5–9, 48–60 and 80–86; p=0.006, p=0.004, p=0.006; Figure 3.7 d) and between ankle angle errors and total residual errors (frames 32–87; p=0.002; Figure 3.7 e).

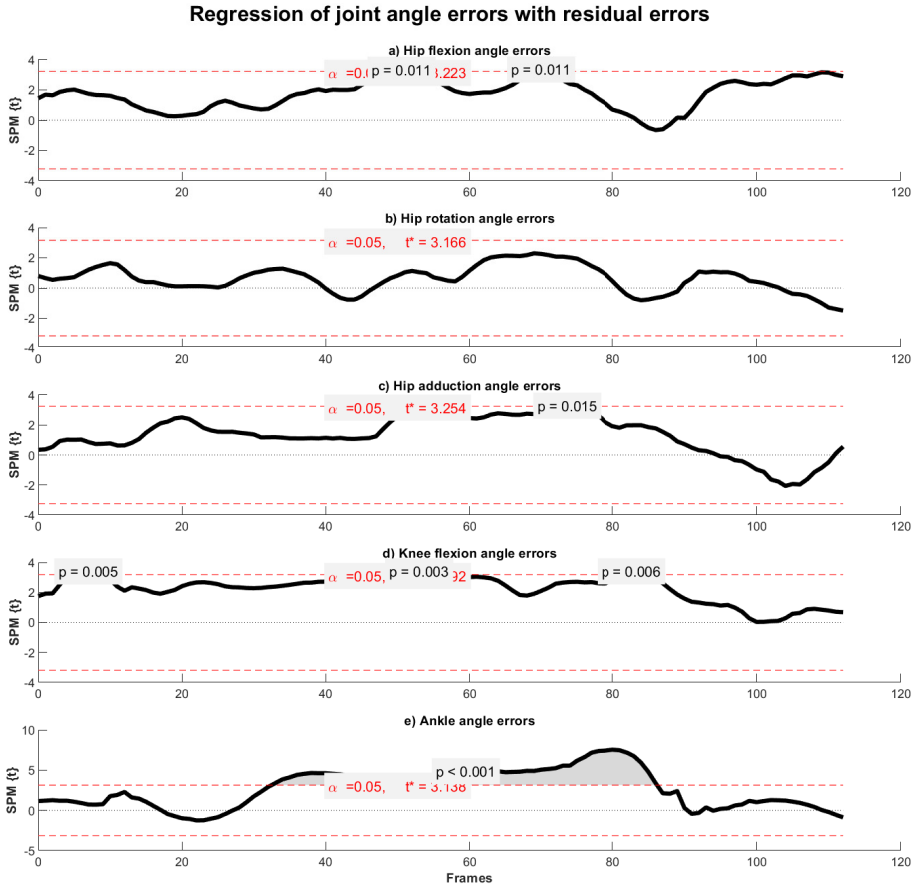

Figure 3.7: How to read SPM figures: The red lines indicate the critical threshold set at the respective alpha values (0.05 for regression tests). For regression tests if the t-statistic field vector transverse the critical threshold (shaded region), the null hypothesis of no relationship is rejected. For regression analyses, if the t-statistic field vector transverses the upper critical threshold, then there is a positive relationship between continuous variable (joint angle errors) and discrete variable (median total residual errors) and vice versa if it transverses the lower critical threshold.
Regression analysis between joint angle errors and total residual errors for: a) hip flexion angle errors. b) hip adduction angle errors. c) hip rotation angle errors. d) knee flexion angle errors. e) ankle angle errors. The shaded regions show statistically significant positive correlations. SPM: Statsitical parameteric mapping

3.4.2 Efficacy of global optimisation when applied to data with varying magnitudes of STA (simulated and experimental): Investigation 2

Our results indicate a strong positive relationship between *Added*-STA and residual errors, with higher residual errors obtained for data with greater magnitudes of *Added*-STA (Figure 3.8). Spearman-Pearson correlation and R^2 are provided in Table 3.3. Highest correlation and R^2 values of 0.8291 and 0.698 were observed between overall *Added*-STA and the total residual errors. Minimum R^2 value of 0.003 was obtained between *Added*-STA to the foot markers and foot residual errors, with a weak correlation of -0.07. Marker residuals at the thigh, pelvis and shank indicated statistically significant ($p < 0.05$) positive correlations with *Added*-STA at the respective segments (Table 3.3).

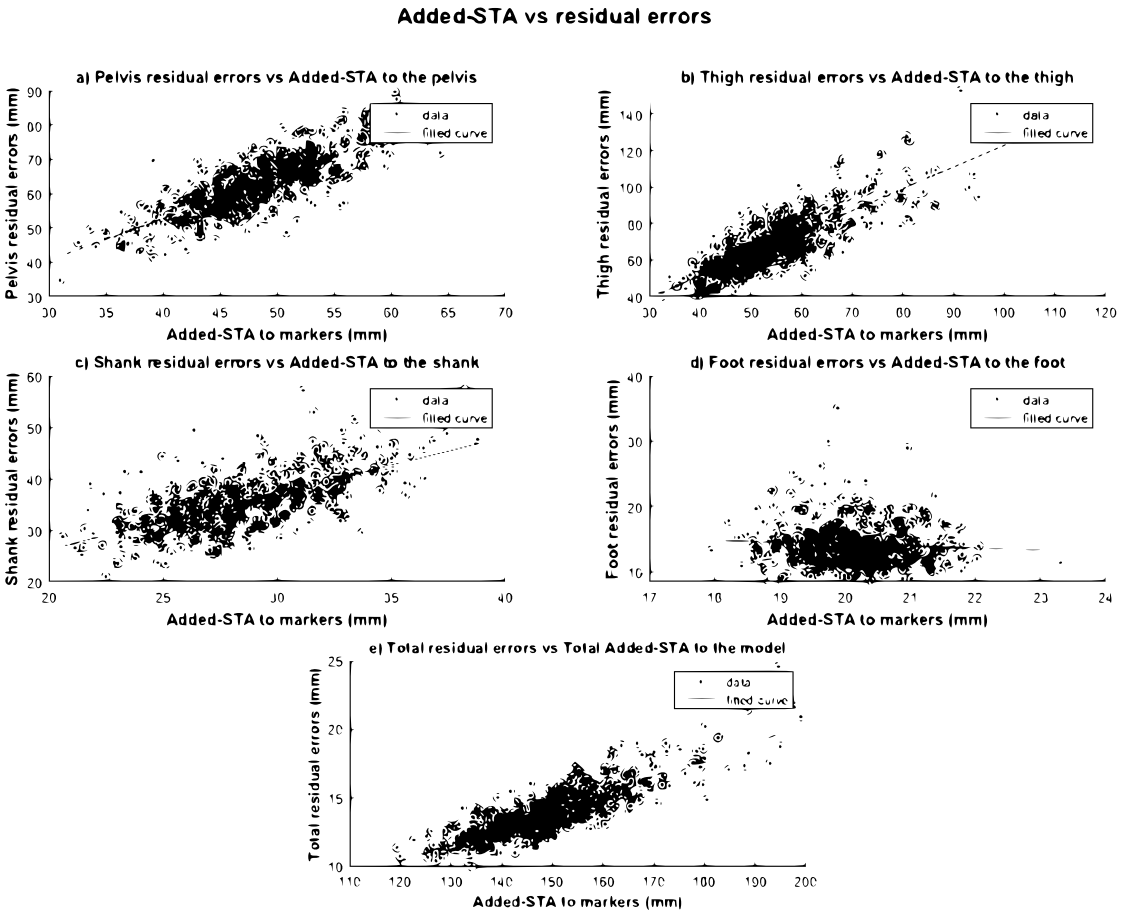

Figure 3.8: Regression analysis between *Added*-STA and computed residual errors for: a). The pelvis, b). The thigh, C). The shank, and d). The foot. e). Total residual errors vs the total *Added*-STA for all markers. STA: Soft tissue artefacts.

Segment	R^2	**Correlation**
Pelvis STA vs pelvis residual errors	0.6255	0.7915*
Thigh STA vs thigh residual errors	0.67	0.8173*
Shank STA vs shank residual errors	0.4273	0.6492*
Foot STA vs foot residual errors	0.003	-0.07
Total STA vs total residual errors	0.698	0.8291*
*:p < 0.05		

Table 3.3: R^2 and correlation values between *Added*-STA and segment residual errors

Comparison of total residual errors and joint angle errors calculated for simulated data — grouped based on the magnitude of *Added*-STA — indicated significantly greater errors for the data with larger magnitudes of *Added*-STA ($p < 0.05$; Figure 3.9 a,b). Statistics based on SPM indicated that residual errors were significantly greater for the entire duration of the gait cycle ($p < 0.05$, paired t-tests; Figure 3.9 c) with joint angle errors obtained using the top-50 affected trajectories significantly greater than those obtained using the bottom-50 affected trajectories at frames 8-12 and 42-82 ($p < 0.05$, paired t-tests; Figure 3.9 d).

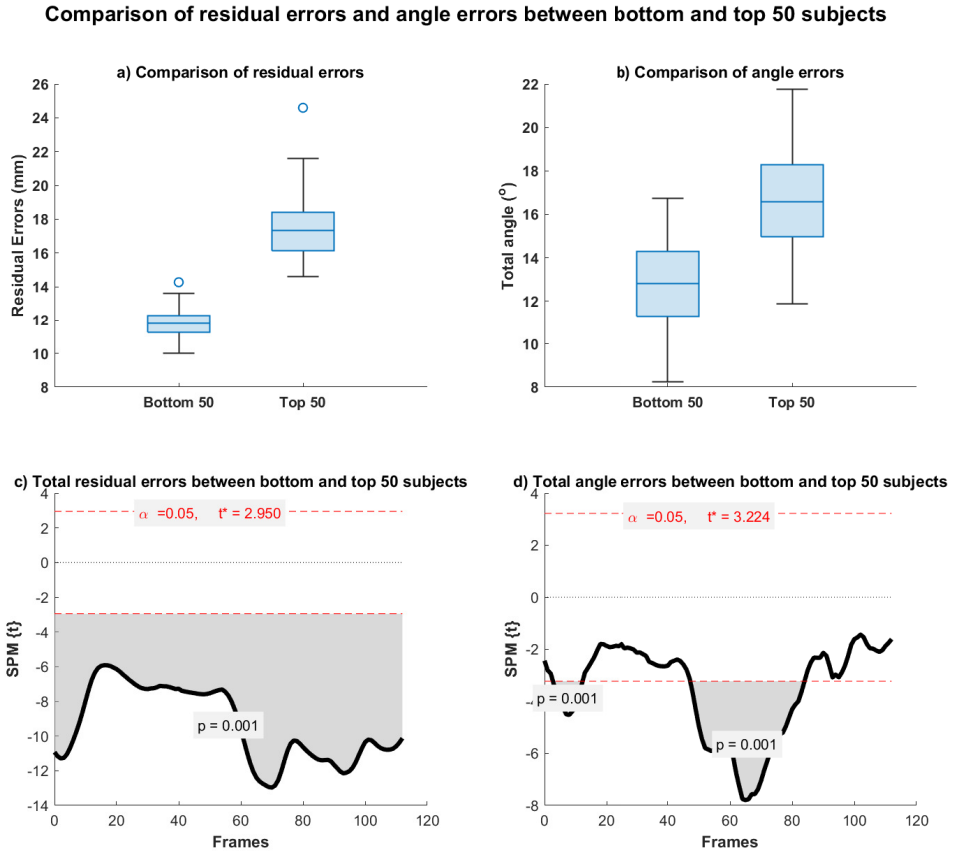

Figure 3.9: How to read SPM figures: The red lines indicate the critical threshold set at the respective alpha values (0.05 for t-tests). For t-tests if the t-statistic field vector (the thick black line) is either below or above the critical thresholds , the null hypothesis of equal means is rejected for those frames. The t-values are differences between the mean of the two sample sets and the variation that exists within the sample sets. For post-hoc analyses, if the t-statistic field vector is above the upper critical threshold, then (meanA>meanB) and vice versa if it is below the lower critical threshold.
Comparison of total residual errors and joint angle errors between bottom-50 and top-50 artefact-affected trajectories. a) Median and spread of total residual errors between bottom-50 and top-50 artefact-affected trajectories; b) Median and spread of joint angle errors between bottom-50 and top-50 artefact-affected trajectories. c) Comparison of total residual error trajectories between bottom-50 and top-50 artefact-affected trajectories using SPM. d) Comparison of joint angle error trajectories between bottom-50 and top-50 artefact-affected trajectories using SPM. SPM: Statsitical parameteric mapping

Comparisons of marker-specific residual errors between subjects with low and high BMI scores (threshold of 24.9) revealed higher residuals for all markers for participants with higher BMI scores (Figure 3.10); significantly greater residual errors were found for the left-thigh markers ($p < 0.05$; Figure 3.10 d). However, comparison of individual marker residual error trajectories between participants with low- and high-BMI scores, using paired t-tests in SPM, did not indicate any significant differences (Figure 3.11).

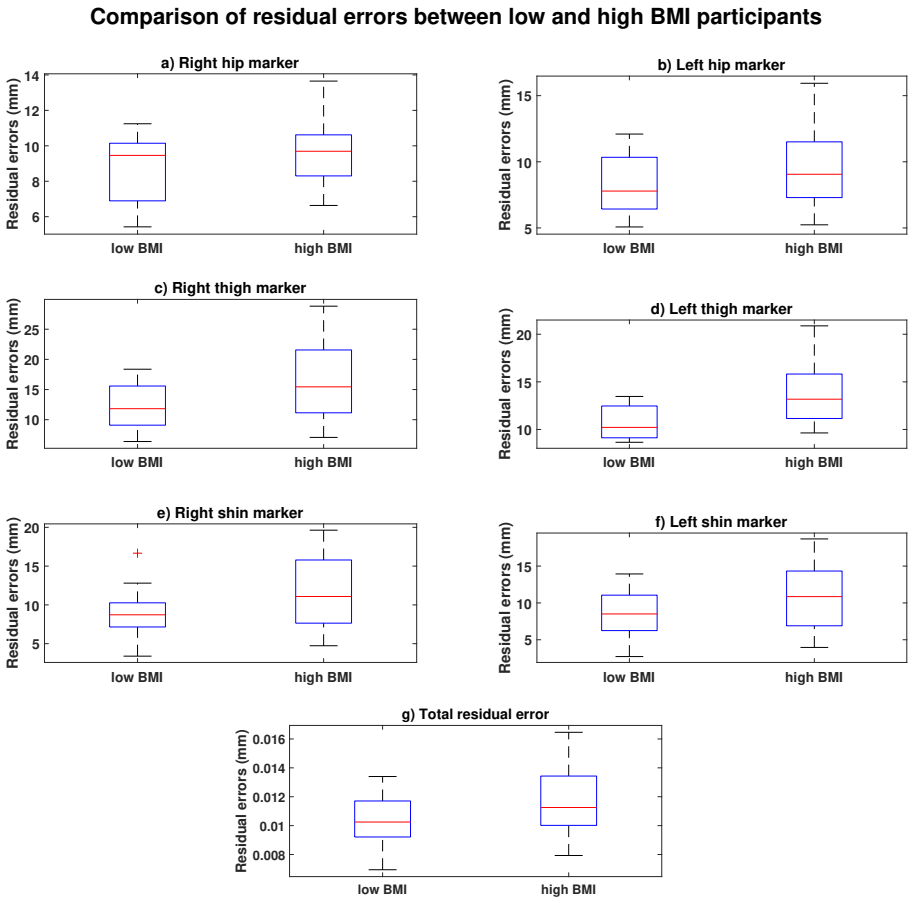

Figure 3.10: Comparison of median and spread of marker-specific and total residual error between participants with low- and high-BMI. a) Right hip marker specific residual error. b) Left hip marker specific residual error. c) Right thigh marker specific residual error. d) Left thigh marker specific residual error. e) Right shin marker specific residual error. f) Left shin marker specific residual error. g) Total residual error. BMI: Body mass index score

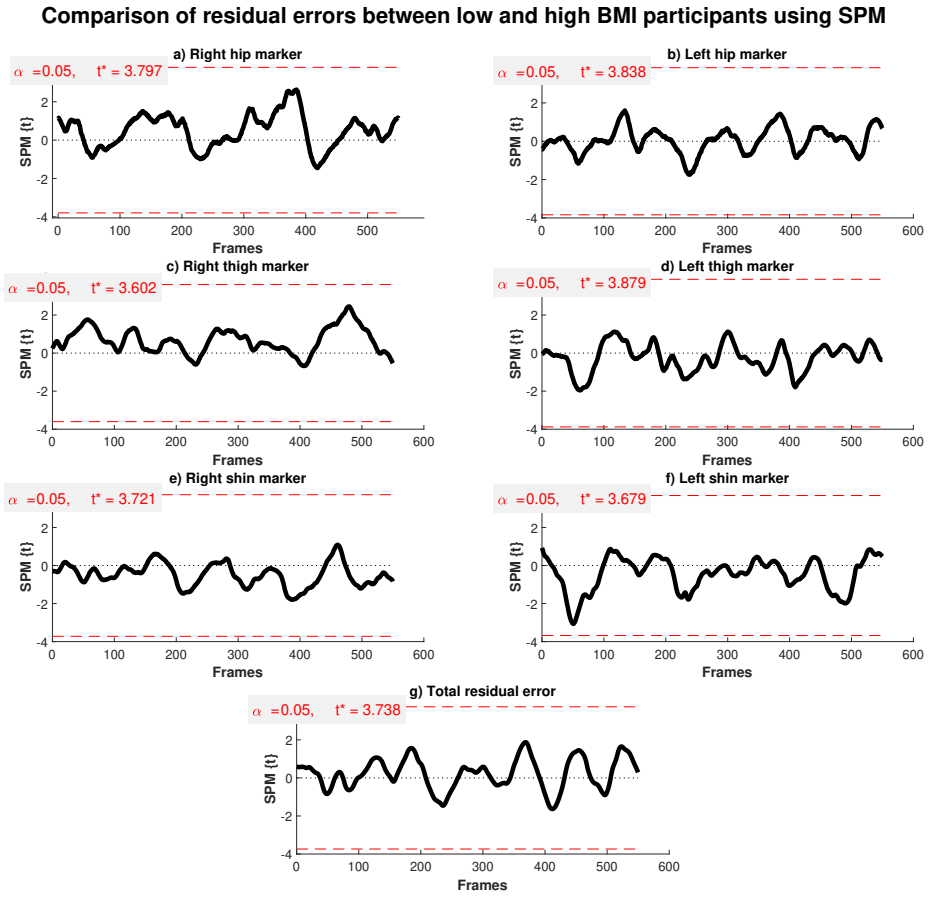

Figure 3.11: How to read SPM figures: The red lines indicate the critical threshold set at the respective alpha values (0.05 for t-tests). For t-tests if the t-statistic field vector (the thick black line) is either below or above the critical thresholds , the null hypothesis of equal means is rejected for those frames. The t-values are differences between the mean of the two sample sets and the variation that exists within the sample sets. For post-hoc analyses, if the t-statistic field vector is above the upper critical threshold, then (meanA>meanB) and vice versa if it is below the lower critical threshold.
Comparison of marker-specific and total residual error trajectories between participants with low- and high-BMI. a) Right hip marker specific residual error. b) Left hip marker specific residual error. c) Right thigh marker specific residual error. d) Left thigh marker specific residual error. e) Right shin marker specific residual error. f) Left shin marker specific residual error. g) Total residual error. BMI: Body mass index score, SPM: Statsitical parameteric mapping

3.5 Discussion

Results from our dual investigation indicated that: Residual errors can be used as a goodness-of-fit metric, supporting the existence of a causal relationship between residual errors and joint angles, and that every step of the MKO pipeline has a significant effect on residual errors. Additionally, the efficacy of global optimisation reduces when applied to data with large magnitudes of STA, or on data acquired from participants with high BMI scores. The reduction in efficacy was observed by increases in residual errors with increasing magnitudes of STA.

Marker registration and segment scaling are key steps in a MKO pipeline. Uchida [252] reported that errors in these steps lead to variation in computed peak joint angles; however, they observed no effect on marker residual errors. Contrasting this, our results indicate that errors in these steps lead to a 35% increase in residual errors ($p < 0.05$; paired t-tests) with large effect sizes observed for errors in marker registration. Discrepancies between our results and Uchida's [252] is likely attributable to differences in marker residual calculations. Specifically, they computed marker residuals as the RMSE difference between model-derived marker locations in their uncertainty-generated model and their baseline model, whilst ours were computed as the RMSE difference between model-derived marker position and input data.

Our findings, specifically the effect of marker registration errors, are similar to other studies investigating scaling methods [199]. We leveraged a marker-based segment scaling and optimisation based marker-registration method with a static trial employed in both. A study comparing five scaling methods indicated that the scaling pipeline used in our investigation, albeit with dynamic trials, produced both, lowest residual errors and kinematics similar to that of reference kinematics [199]. Additionally, they indicated optimising segment lengths resulted in overfitting of the model, with marker-registration having a greater effect on residual errors and joint angles [199].

Conversely, another study comparing three scaling methods reported that no method was superior over another with similar saggital kinematics obtained for all three methods and similar residual errors computed for the linear and kinematic scaling methods [155]. Key differences in our study compared to the above are: the use of SPM, the analysis of the effect of errors in the scaling pipeline and the use of static trials. We hypothesise that leveraging SPM and exploring the effects of errors might elucidate which scaling pipeline is superior. However, we believe using standing trials are the clinical standard, with functional trials infeasible for most clinical populations.

Marker weightings are used to reduce the impact of markers more prone to STA on computed kinematics, with marker weighting leveraged to reduce dynamic

residuals [172]. Despite up-weighting anatomical markers or determining subject- and task-specific optimal marker weights being the recommended practice [44, 145], the variation in residual errors due to different weighting strategies has not been investigated. Our results indicate that up-weighting anatomical markers (WS2) resulted in the greatest residual errors whilst assigning markers with equal weights (WS1) resulted in the least residual errors (13.5mm). However, the effect sizes were only small to moderate.

Constraints and joint models are an integral part of the MKO pipeline with residual errors being leveraged as a metric to investigate the effect of various constraints on the MKO pipeline [51, 97, 152]. For example, soft, hard and loop closure constraints were found to increase residual errors in both KF- and GO-based MKO methods [97] with loop closures found to affect residual errors when the constraint formulation was modified to a penalty-based formulation [152]. Similarly, a study reported reduction in residual errors when an STA model was added in the constraint equation [51] for both KF- and GO-formulations.

However, despite studies investigating the effect of differing joint models on computed kinematics [87, 101, 211], none investigated the variation in residual errors. Our results indicate that joint model types have a significant ($p < 0.05$; one-way repeated measures ANOVA) effect on computed residual errors with the least residual errors obtained for the 6 DoF model (11mm) and the Ball model resulting in the greatest residual errors (17mm). These results are in-line with results reported by Pomarat [195], who observed that the lowest residual errors were obtained for a model incorporating 6 DoF joints.

Whilst our investigation does not incorporate additional constraints and our joint models are defined using mobilisers [231], we hypothesise (based on our results and the above studies) that different formulations of joint types would affect residual errors with addition of any constraints having a significant impact on residual errors.

The above results indicate that every step of the MKO pipeline has a significant effect on computed residual errors. Mathematically, residual errors and joint angles are linked: with optimal joint angles obtained for lower residual errors, supporting a causal relationship. Therefore, variations in residual errors due to the MKO pipeline may indicate uncertainties in computed kinematics which could result in misclassification of pathologies [243, 252] or affect subsequent analyses. Uncertainties in kinematics have been reported to affect calculation of moments, forces and muscle activation [172, 174, 179, 252] with uncertainties in kinematics found to contribute more to dynamic residuals than uncertainties in force plate data [172].

However, despite the mathematical relationship, studies have questioned the existence of a causal relationship. Our results indicated that significant ($p < 0.05$;

paired t-tests) variations in residual errors from the baseline were generally reflected in significantly ($p < 0.05$; paired t-tests) different computed joint angles. Furthermore, large effect sizes in residual error variation resulted in large effect sizes in joint angle variation. Additionally, the regression analysis indicated that when employing the same MKO pipeline, increases in residual errors were positively correlated with increases in ankle flexion, hip flexion, hip adduction and knee flexion joint angle errors. These two results (variation and regression analysis) support the existence of a causal relationship between residual errors and joint angle errors.

Although our results support the existence of a causal relationship, a consistent causal relationship could not be established. Whilst in general, variations of large effect sizes in residual errors resulted in variations of large effect sizes in joint angles, their relationship was not always one-to-one at every frame. Additionally, effect sizes also varied between joint angles; and large effect sizes in joint angle variation were observed for small to moderate variations in residual errors (Appendix A).

The above findings are echoed in other studies. For example, whilst incorporating an STA model in the MKO pipeline resulted in smaller residual errors, only the formulation leveraging KF had a subsequent decrease in joint angle errors [51]. Similarly, differing markersets reported similar residual errors for different joint angles [99]. The inconsistent causal relationship reported in these and our results could be attributed to the MKO formulation, where the least-squares minimisation problem can result in a local minima, resulting in different kinematics depending on the initial state. This can be visualised in Figure 3.4 p, wherein the effect of differing marker registration errors results in differing effect sizes and joint angles across the gait cycle. This can be attributed to the algorithm spreading the marker error to find optimal joint angles, which could result in a local minima at every frame.

The general finding of a causal relationship and the nonlinear behavior shown in our results, and contrary to previous results, can be attributed to us leveraging the entire time-series data, rather than data condensed to a singular value. Information may be lost when analysing time-series data using a single value, leading to obscuring of variations and patterns. For example, greater residual errors with moderate effect sizes would not be observed by condensing residual errors to a singe value [box plots, (Figure 3.2 III)]. Additionally, despite significant variations reported in both joint angles and residual error variations using SPM, regression analysis using mean residual error values (scalar) could not capture the variation

Leveraging the results discussed above (results from Investigation 1), we evaluated the efficacy of global optimisation (the MKO method incorporated in OpenSim) on data of varying magnitudes of STA (Investigation 2). Our results indicate

that the efficacy of global optimisation reduces when applied to data with higher magnitudes of STA or on data obtained from participants with high BMI scores. Despite the fact that MKO methods are widely applied to reduce the effect of STA on computed kinematics, and evidence that a higher BMI score are associated with a greater magnitude of STA [54], very few studies have validated their proposed MKO methods on subjects with high BMI scores or on data with large magnitudes of STA.

The reduction in efficacy was indicated by the higher magnitudes of residual errors observed in data with higher magnitudes of STA when compared with data with lower magnitudes of STA. Segmental residual errors were positively correlated with segmental *Added*-STA, with marker-specific residual errors obtained for subjects with higher BMI scores greater than those obtained for subjects with lower BMI scores. Additionally, computed residual errors and joint angle errors were significantly greater when global optimisation was applied to data with larger magnitudes of *Added*-STA. The results of the mixed-effect linear model also showed that the joint angle error for data with higher *Added*-STA were significantly higher, with an average increase of 5.89 times compared with errors obtained from data with lower magnitudes of *Added*-STA. Combining this with the results from Investigation 1 — which indicated that increases in residual errors are linked to increases in joint angle errors (for the same MKO pipeline) — our results indicate that global optimisation fails to determine the optimal pose when applied to data with large magnitudes of STA. In other words, the optimal pose computed for data with higher magnitudes of STA differs from the ground truth by a large extent. This could be in part due to the MKO method searching for the local optimum at every frame, resulting in spreading of errors and sub-optimal joint poses being computed.

Whilst results obtained from SPM indicated the significant increase in residual errors and joint angle errors for simulated data with higher magnitudes of *Added*-STA, results obtained from SPM for experimental data did not indicate a significant increase in residual error, despite higher residual errors visualised in box plots for subjects with higher BMI scores. This could be attributed to the small sample size or the small number of participants available for both small and higher BMI scores.

In summary, in this chapter we investigated and reported that the efficacy of MKO methods — the solution most widely applied to reduce the effect of STA on computed kinematics — reduces when applied to data obtained from subjects with higher BMI scores or to data with large magnitudes of STA. We additionally reported that residual errors is a suitable metric to evaluate the quality of the MKO pipeline and subsequently the quality of computed kinematics, in the absence of ground-truth bone movement data. Results from this chapter highlight the need

for a more generalisable solution which can improve the quality of clinical gait analysis for all clinical populations. The subsequent chapters aim to develop the generalisable solution.

3.6 Conclusions, technical novelty and take-away messages

The investigations described in this chapter were driven by the fact that the efficacy of MKO methods — a widely applied method to reduce STA — have not been extensively validated on data with large magnitudes of STA. With studies showing that participants with higher BMI scores have greater magnitudes of STA, coupled with global increases in adult and child obesity rates (a complex disease defined as body mass index BMI > 30) over the last few decades [[34, 61]], the importance of analysing the efficacy of MKO methods on data with large magnitudes of STA cannot be understated. In addition, we also investigated the validity of residual errors as a goodness-of-fit metric or as a metric to evaluate the quality of computed kinematics in the absence of artefact-free bone movement (actual bone movement). The above investigations were driven by: the lack of studies incorporating participants of higher BMI scores in MKO studies; and that a validated global metric, which can be leveraged to analyse the efficacy of MKO studies, does not exist when artefact-free bone data or a database of age-, BMI- and gender-matched normative database is absent.

Our results indicate that:

1. Residual errors can be used as a goodness-of-fit metric, as increases in residual errors are linked to increases in joint angle errors for the same MKO pipeline. Additionally, every step of the MKO pipeline has a significant effect on residual errors, with variation in residual errors leading to variations in computed joint angles, supporting the existence of a causal relationship.

2. Higher residual errors are obtained when global optimisation is applied to data with larger magnitudes of STA, or on data acquired from participants with higher BMI scores. This indicates a reduction in the efficacy of global optimisation to ameliorate the effects of STA when applied to data from participants with varying BMI scores or to data with large magnitudes of STA.

The novelty of our results are:

1. Investigation 1: We were first to investigate the effect of each step of the MKO pipeline on residual errors and we reported that each step has a significant effect on computed residual errors, specifically marker registration

and joint models (Cohen's d ¿ 0.8). Additionally, when the same MKO pipeline was leveraged, higher residual error resulted in higher joint angle errors. This analysis was done using a novel statistical approach: Statistical parametric mapping. This investigation has been published in the Journal of biomechanics [201].

2. Investigation 2: We investigated the effect of higher magnitudes of STA and higher magnitudes of BMI on residual error. Our results indicated that higher magnitudes of STA are highly correlated with higher residual errors. Additionally, higher BMI is correlated with higher residual error. Our study was the first to investigate the variation of residual error due to STA and BMI. The results were published in Clinical Movement Analysis Society Conference,2023 [202].

3. By combining the results of the two investigations, we show that MKO produces higher residual errors for subjects with higher BMI or larger magnitudes of STA. Additionally, higher residual errors indicate higher magnitude of joint angle errors. Therefore, the efficacy of MKO methods reduce when applied to subjects of higher BMI or for data with larger magnitudes of STA.

The limitations of our investigations have been critical in shaping the lessons learnt. In particular, we made errors in our experimental data collection which resulted in the majority of the participant data being unusable. However, this helped us to develop protocols for accurate skin-mounted marker data collection. Unfortunately, the updated protocols could not be applied to this investigation as the trial period for the software (Motive 2.4) used to collect data had ended.

In addition, the absence or lack of artefact-free bone movement implies that joint angle errors are relative (and not absolute) and are dependent on the accuracy of the baseline data. The baseline data also produces residual errors albeit with a magnitude smaller than other residual errors. Whilst acquiring artefact-free bone data requires specialised equipment, an age-, BMI- and gender-matched normative database would have helped alleviate these limitations.

Lastly, whilst we have reported the results of a mixed effect linear model analysis for Investigation 2, we also explored the application of mixed effects linear models for Investigation 1. However, in Investigation 1, we studied the variation of residual error due to each step of the MKO pipeline independently, with the other steps kept constant. For example, the effect of marker registration error on residual error was investigated keeping segment scaling errors, marker weighting strategy and joint models constant. This was done to effectively decouple and highlight the effect of just marker registration variations on residual errors. Furthermore, whilst a dependent analysis of each step using mixed effects linear models can be done, we believe this would take away from the results we obtained

using SPM, which is critical to Investigation 1. We believe SPM takes into account the variation in the previous time step to compute significant difference, which would be lost when the values are averaged for mixed effects linear model analysis.

In conclusion, this chapter has explored a gap in existing literature in movement analysis: the efficacy of MKO methods when applied to data with large magnitudes of STA. We have shown that the most widely applied method to ameliorate STA reduces in efficacy when applied to data with large magnitudes of STA or on data from participants with high BMI scores, thereby necessitating the development of methods which can be applied to a wide variety of data and participants. We have also shown that residual errors can be applied to evaluate the quality of computed kinematics in the absence of artefact-free bone data, i.e as a goodness-of-fit metric; however, care must be taken as residual errors are affected by the MKO pipeline.

Chapter 4

Evaluating the fidelity of projection of markers to improve computed kinematics

4.1 Introduction

In this chapter we propose two novel marker-projection schemes and investigate whether our marker-projection schemes and other projection schemes reduces the effects of STA and improves the accuracy of computed kinematics when compared with conventional (un-projected) skin-mounted markers. Background for this chapter is provided in Section 4.2 with the methods described in Section 4.3. The results obtained are discussed in Section 4.4 with conclusions and take-away messages described in Section 4.5.

4.2 Background

Clinical gait analysis is a necessary step in the pre-operative planning for surgical interventions for children with CP [83, 186]. Joint angles computed from clinical gait analysis, specifically internal/external rotation, are used for computing the magnitude of femoral derotation osteotomy required to assist children with in-toeing gait, a common gait pathology occurring in children with CP. However, as highlighted in Chapter 2 STA negatively impacts the clinical usability of the computed joint angles, specifically the internal/external rotation and abduction/adduction angles.

In the previous Chapter 3 we have shown that the most widely applied method to reduce STA, multibody kinematic optimisation (MKO) methods, reduces in efficacy when applied to data with large magnitudes of STA or on data from par-

ticipants with high body mass index (BMI) scores (higher residual errors obtained with increased magnitudes of STA), who represent a significant portion of the clinical population.

Despite the plethora of solutions proposed to mitigate the effects of STA on computed kinematics, no single solution has been proven to be effective for all analysed motions and for all individuals. In addition, the majority of the experimental research undertaken to determine solutions to compensate for STA has used participants with a healthy BMI [194] score, despite evidence of a direct correlation between higher BMI scores and increased magnitudes of STA [54].

Amongst the numerous solutions proposed, some studies have indicated that incorporating artefact-free bone movement (true bone movement) into kinematic pipelines helps to reduce the effect of STA [43, 129, 147, 198]. For example, incorporating adaptive joint boundary conditions — obtained using intracortical pins — in musculoskeletal models resulted in significantly different kinematics when compared with kinematics obtained using conventional joint boundary conditions [198]. These differences in computed kinematics acquired using adaptive joint boundary conditions were found to reduce errors in joint rotations used to identify risk factors for musculoskeletal injuries [236]. Similarly, an obesity-specific markerset, which used a digital pointer to identify and track the underlying bony anatomical landmarks, produced similar results to a conventional markerset on non-obese participants, but produced higher fidelity pelvic tilt angles and significantly smaller muscle forces, compared to a conventional markerset, when applied to obese participants [147].

Whilst not directly leveraging artefact-free bone movement, a marker projection scheme was proposed to reduce the effects of STA [43]. Skin-mounted markers were projected onto a requested axis of the local coordinate system (LCS) to cancel out the deleterious effect of STA on computed kinematics. For example, the local coordinates of the upper-arm skin-mounted markers (x,z), except those along the longitudinal axis of the segment (axis parallel to the humerus, y), were set to 0. The results from the study indicated that projection of a subset of markers, or projection of all the markers on the cuff, reduced kinematic errors by 20% when compared with conventional (un-projected) skin-mounted markers. However, the authors also observed that the projection of all skin-mounted markers increases kinematic errors for some investigated motions. This was attributed to the loss of information when setting coordinates equal to 0 [43].

An alternative method of obtaining artefact-free bone movement, often applied to investigate small bone movements which are masked by STA, are imaging modalities such as fluoroscopy, MRI, computed tomography (CT) and ultrasound [128, 173, 177] (additional review available in Chapter 2). Two notable studies [129, 161] incorporated ultrasound imaging — a safe and cost-effective imaging

modality — to compensate for STA. One study proposed an intelligent ultrasound sensor which would be capable of determining the distance between bone and skin during motion and thereby reduce the effects of STA on computed kinematics [161]. The proposed sensor was reported to reduce kinematic errors in in-vivo tests comprising of a femur model immersed in a collagen solution and rotated using a motor. However, the proposed sensor has not been validated on tissue-mimicking phantoms nor on humans, with the STA compensation scheme yet to be validated [159]. The other study developed a system which combined ultrasound imaging with a skin-mounted marker-based system (CAT & MAUS) to determine the location and track the underlying greater trochanter landmark during motion: to reduce the effects of STA [129, 130]. Specifically, an automatic bone segmentation protocol was developed to reconstruct the 3d bone surface from ultrasound images during motion. The proposed system was validated using in-vivo and in-vitro tests with results indicating that the system was capable of achieving errors of less than 1.2° in estimating femur position, with errors of reconstructing the femur shape 1/10th of those obtained using just skin-mounted markers. However, the system is only capable of imaging the greater trochanter with an ultrasound probe required to be held at the surface of the greater trochanter during motion. Additionally, the system requires coupling liquid to improve image resolution and radiologist input to ensure that images can clearly discriminate between bones and soft tissues.
In this chapter we investigate a novel approach of reducing the effects of STA on kinematics, and which can be incorporated into the above reviewed studies. In this chapter we investigate whether projecting the markers onto the bone surface (rather than the longitudinal axis) improves kinematic accuracy and reduces the effect of STA when compared to conventional (un-projected) skin-mounted markers. We additionally compare kinematics computed using markers projected onto the bone surface with those obtained by projecting markers onto the longitudinal axis. We propose and evaluate two projection schemes: offset-projection and closestPoint-projection.

4.3 Methods

4.3.1 Data

Data used in this study were obtained from the dataset leveraged in studies [94, 96], with permission provided by the authors. The dataset contains skin-mounted marker trajectories and artefact-free trajectories of bony landmarks recorded using dual-fluoroscopy (and presented as virtual dual-fluoroscopy markers) for 11 subjects, of varying BMI scores, performing five activities: standing, level walk, incline walk, internal hip rotation to end range of motion and external hip ro-

tation to end range of motion. Reflective markers were placed on the following landmarks: anterior-superior iliac spines (ASIS), posterior-superior iliac spines (PSIS), iliac crests (ILC), lateral epicondlye, greater trochanter and a cluster of four markers on the lateral thigh. Bony landmarks recorded using dual-fluoroscopy (DF) were: ASIS , PSIS, ILC, lateral and medial epicondlyes, greater and lesser trochanter. Only the pelvis and thigh of the ipsilateral side were imaged, therefore the dataset only contains trajectories of skin-mounted markers and DF-markers of the pelvis and thigh of the imaged side [94, 96]. The dataset also contained setup files for segment scaling and marker registration on OpenSim [81] for all subjects.

4.3.2 Musculoskeletal modelling and projection of markers

A publicly available generic rigid-body musculoskeletal model [205] was used in OpenSim [81]. As only the pelvis and femur data are available, other body segments were removed from the generic model. The generic model was scaled to subject-specific dimensions using the DF-markers of the pelvis and femur of the standing trial. Skin-mounted virtual markers and DF-virtual markers were registered to their experimental counterparts using the standing trial. Errors for the scaling process (segment scaling and marker registration) were below the guidelines recommended by OpenSim (Root mean square error [RMSE] $<$ 1cm and maximum marker error $<$ 2cm).

Three projection schemes were implemented for the cluster of markers at the thigh:

1. Setting the anterior-posterior (x), lateral-medial (z) coordinates of each thigh marker in the LCS to 0. This scheme was proposed in paper [43]. This projection is henceforth called Begon-projection

2. Shifting the entire cluster of thigh markers radially to the bone surface. The location of the bone in the LCS was determined using the DF-markers. The lateral-medial (z) coordinate of the cluster of markers in the LCS was assigned the value of that of the bone. This projection is henceforth called Offset-projection

3. Projecting each marker of the thigh cluster to the closest point on the bone surface. The bone surface was determined in the LCS and each marker of the cluster was projected to the closest point on the bone surface in the LCS. This projection is henceforth called closestPoint-projection

The coordinates of the markers in the LCS were determined using the scaled model in OpenSim. The trajectories of the projected markers in the global (lab) coordinate system were computed using the PointKinematics tool in OpenSim

wherein the kinematics computed using just the DF-markers were leveraged to calculate the location of each projected marker in the global coordinate system at each time step. These trajectories were then combined with the un-projected skin-mounted marker trajectories of the pelvis to calculate joint angles.
Offset-projected markers have similar movement to conventional (un-projected) skin mounted markers in the anterior-posterior (x) and superior-inferior (y) directions with the lateral-medial movement restricted due to projection. ClosestPoint-projection restricts the movement in all three planes compared to conventional (un-projected) skin-mounted markers. The five different markersets: DF-markers, skin-mounted markers, Begon-projected markers, Offset-projected markers and closestPoint-projected markers, are shown in Figure 4.1.

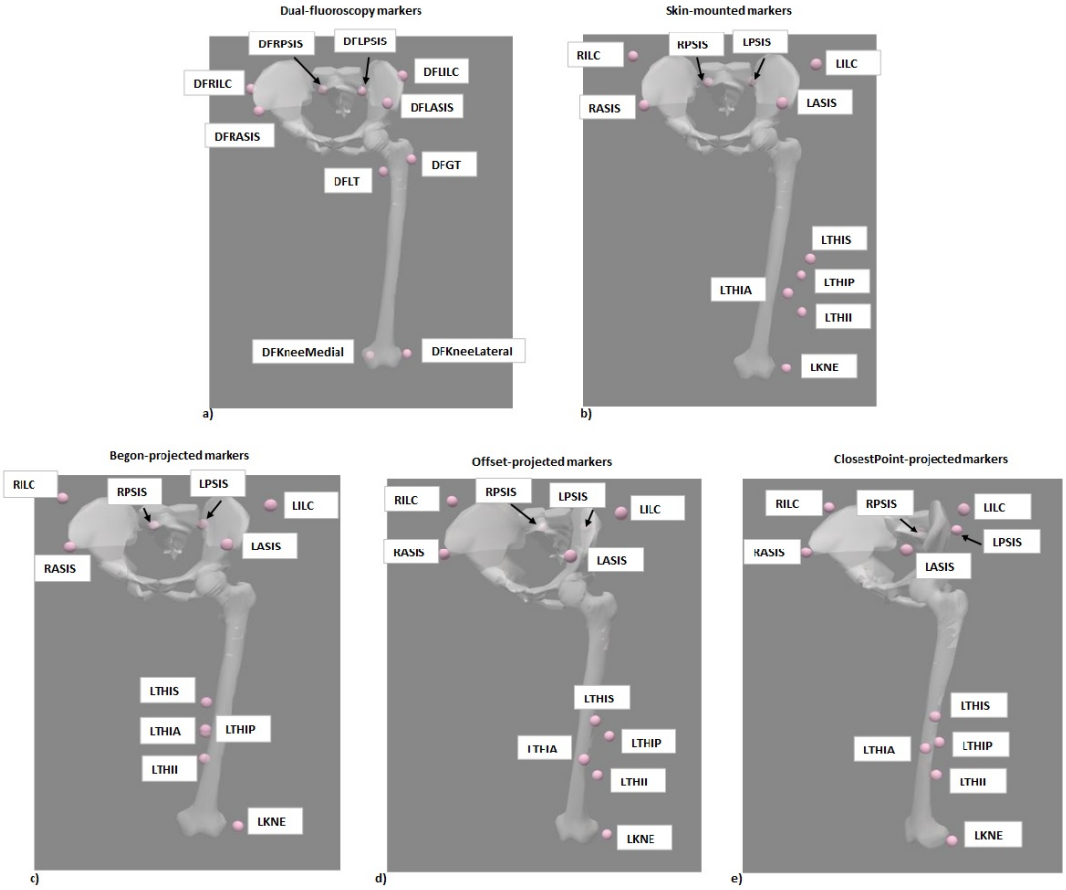

Figure 4.1: a) Dual-fluoroscopy markers of the pelvis and thigh. The marker names are DFRASIS: Dual-fluoroscopy based right anterior-superior iliac spine, DFLASIS: Dual-fluoroscopy based left anterior-superior iliac spine, DFRPSIS: Dual-fluoroscopy based right posterior-superior iliac spine, DFLPSIS: Dual-fluoroscopy based left posterior-superior iliac spine, DFRILC: Dual-fluoroscopy based right iliac crest, DFLILC: Dual-fluoroscopy based left iliac crest, DFGT: Dual-fluoroscopy based greater trochanter, DFLT: Dual-fluoroscopy based lower trochanter, DFKneeLateral: Dual-fluoroscopy based lateral epicondyle and DFKneeMedial: Dual-fluoroscopy based medial epicondyle. b) Skin-mounted markers on the pelvis and thigh. c) Begon-projected thigh markers and skin-mounted markers on the pelvis. d) Offset-projected thigh markers and skin-mounted markers on the pelvis. e) closestPoint-projected thigh markers and skin-mounted markers on the pelvis. The skin-mounted markers are RASIS: Right anterior-superior iliac spine, LASIS: Left anterior-superior iliac spine, RPSIS: Right posterior-superior iliac spin, LPSIS: Left posterior-superior iliac spine, RILC: Right iliac crest, LILC: Left iliac crest, LTHIS, LTHI,LTHIA, LTHIP: Left thigh cluster of markers, LKNE: Lateral epicondlyle.

Hip joint angles and total residual errors (the difference between model-derived marker location and experimental marker location) for level walking, incline walking, internal and external hip rotation were calculated using the inverse kinematic (IK) analysis in OpenSim. Hip joint angles and total residual errors were computed for the following cases:

1. DF-markers were given a weight of 1. All projected and conventional (un-projected) skin-mounted markers were given a weight of 0.

2. Conventional (un-projected) skin-mounted markers were given a weight of 1. All DF-markers and projected markers were given a weight of 0.

3. Begon-projected markers, the conventional (un-projected) lateral epicondlyle skin-mounted marker and pelvis conventional (un-projected) skin-mounted markers were given a weight of 1. Conventional (un-projected) skin-mounted markers on the femur, DF-markers and other projected markers were given a weight of 0.

4. Offset-projected markers, the conventional (un-projected) lateral epicondlyle skin-mounted marker and pelvis conventional (un-projected) skin-mounted markers were given a weight of 1. Conventional (un-projected) skin-mounted markers on the femur, DF-markers and other projected markers were given a weight of 0.

5. closestPoint-projected markers, the conventional (un-projected) lateral epicondlyle skin-mounted marker and pelvis conventional (un-projected) skin-mounted markers were given a weight of 1. Conventional (un-projected) skin-mounted markers on the femur, DF-markers and other projected markers were given a weight of 0.

The hip joint in the generic musculoskeletal model is modelled as a ball joint (only contains 3 degrees of freedom [DoF]). To investigate the effect of projection of markers on different joint models, the above steps were repeated for the hip joint modelled as a 6 DoF joint i.e no joint constraints between the pelvis and femur.

4.3.3 Data comparison and statistical analysis

Joint angles computed using just the DF-markers were taken as reference joint kinematics. Cross-correlation coefficients and RMS errors (joint angle errors) were calculated between joint kinematics computed using just the DF-markers and those computed using conventional (un-projected) skin-mounted markers and conventional (un-projected) skin-mounted markers with projected markers. Paired

t-tests between joint angle errors acquired using conventional (un-projected) skin-mounted markers and projected markers were performed for all joint angles.

In addition to comparing joint angle errors, residual errors computed using the different approaches (using just DF-markers, conventional [un-projected] skin-mounted markers and different projected markers) were compared. Residual errors are used as a goodness-of-fit metric between the model and the underlying data [42, 178, 179] in the absence of artefact-free bone movement.

All statistics tests were performed in MATLAB. Non-parametric tests were conducted if normality could not be assumed. Normality was tested using the Andersen-darling test in MATLAB..

4.4 Results

Substantial reductions in joint angle errors were obtained for both the models (Ball and 6DoF) using offset-projected and closestPoint-projected markers during all investigated motions (Figure 4.2-Figure 4.5) with the performance of each projection scheme (determined by the degree of joint angle error) compared with the performance of conventional (un-projected) skin-mounted markers for each studied motion.

Hip rotation errors computed using offset-projected markers significantly ($p < 0.05$, Figure 4.2 a) reduced during level walking for both the Ball model (reduction in error by 67.3%) and the 6DoF model (reduction in error by 78.8%). Considerable but non-significant reductions in hip rotation joint angle errors were obtained for level walking using closestPoint-projected markers and the Ball model (reduction in error by 11%) with significant ($p < 0.05$) hip rotation joint angle errors obtained when the 6DoF model was leveraged (reduction in error by 33.7%, Figure 4.2 a). Hip rotation errors obtained using Begon-projected markers increased by 1.9% for the Ball model and reduced by 2% for the 6DoF model with neither of the changes significant (Figure 4.2 a).

In addition to reduction in hip rotation joint angle errors, the correlation (the degree of similarity) between hip rotation angles computed using offset-projected skin-mounted markers and those obtained using artefact-free bone movement increased from 0.59 (conventional [un-projected] skin-mounted markers) to 0.91 (offset-projected markers, Table 4.1) during level walking for the Ball model and from 0.60 (conventional [un-projected] skin-mounted markers) to 0.89 (offset-projected markers, Table 4.1) for the 6DoF model. However, the correlation values reduced for hip rotation angles computed using closestPoint-projected markers and Begon-projected markers (Table 4.1).

Whilst the projection of markers resulted in lower hip flexion and hip adduction joint angle errors when compared with conventional (un-projected) skin-mounted

markers, none of the reductions were statistically significant (Figure 4.2 b,c). The RMS joint angle errors and R2 values for level walking is given in Tables 4.1.

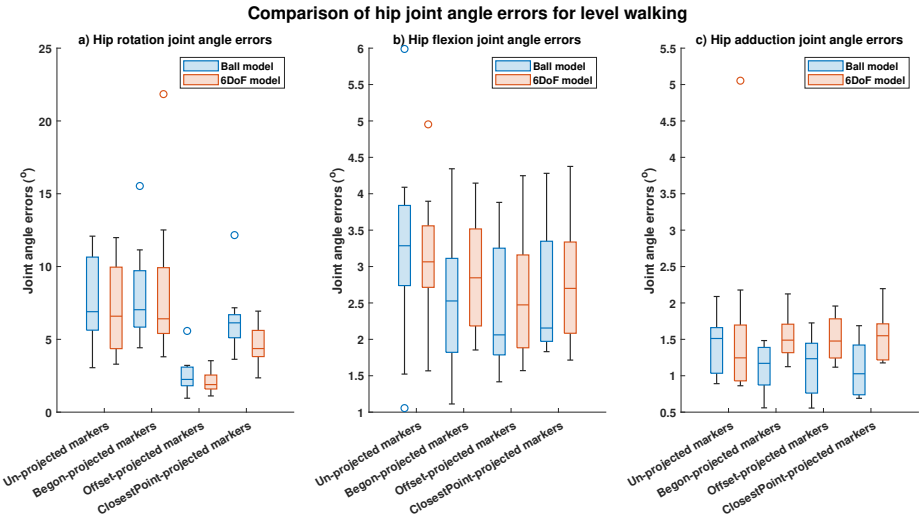

Figure 4.2: Comparison of median and spread of joint angle errors computed using four different projection methods (conventional (un-projected) skin-mounted marker, Begon-projection, offset-projection and closestPoint-projection) during level walking: a) Hip rotation joint angle errors. b) Hip flexion joint angle errors. c) Hip adduction joint angle errors.

Model	Joint Angles	Hip Flexion		Hip Rotation		Hip Adduction	
	Projections	RMSE (°)	R^2	RMSE (°)	R^2	RMSE (°)	R^2
Ball joint	Skin-mounted markers (No projections)	3.2	0.994	7	0.592	1.4	0.967
	Begon Projection	2.5	0.995	8	0.391	1.1	0.975
	Offset Projection	2.4	0.995	**2.5 (p=5.854e-5)***	0.912	1.1	0.977
	Closest Point Projection	2.7	0.993	6.2	0.46	1.1	0.976
6 degree of freedom joint	Skin-mounted markers (No projections)	3.1	0.991	7	0.605	1.6	0.973
	Begon Projection	2.8	0.989	8.5	0.217	1.5	0.957
	Offset Projection	2.6	0.993	**2.0 (p=5.979e-5)***	0.889	1.5	0.966
	Closest Point Projection	2.8	0.992	**4.6 (p=0.0309)***	0.247	1.5	0.954
bold and * : p <0.05							

Table 4.1: Joint angle root mean square errors (RMSE) and correlation coefficients (R^2) for hip flexion, rotation and adduction angles computed using the different projection methods for level walking. Significance was computed as a comparison between joint angle errors obtained conventional (un-projected) markers and joint angle errors obtained using various marker projection schemes. RMSE, Root-mean-square-error;R^2, Correlation index

Similar results to those obtained during level walking were also obtained during incline walking with significant ($p < 0.05$) reductions in hip joint angle errors obtained using offset-projected markers and closest-point projected markers for both the models (Ball model: reductions of 71.0% using offset-projected markers and of 42.2% using closestPoint-projected markers; 6DoF model: reductions of 75.1% for offset-projected markers and reductions of 44.2% for closestPoint-projected markers) (Figure 4.3 a). Hip rotation errors obtained using Begon-projected markers reduced by 11.9% for the Ball model and significantly ($p < 0.05$) by 24.9% for the 6DoF model (Figure 4.3 a). Reductions in hip flexion joint angle errors and hip adduction joint angle errors were not significant (Figure 4.3 b,c).
Correlation of kinematics computed using offset-projected markers increased from 0.7094 (conventional [un-projected] skin-mounted markers) to 0.82 (offset-projected markers) during incline walking for the Ball model and from 0.71 (conventional [un-projected] skin-mounted markers) to 0.83 (offset-projected markers) for the 6DoF model. Correlation values computed using closestPoint-projected markers and Begon-projected markers were similar to or lesser than those obtained using conventional (un-projected) skin-mounted markers (Table 4.2).

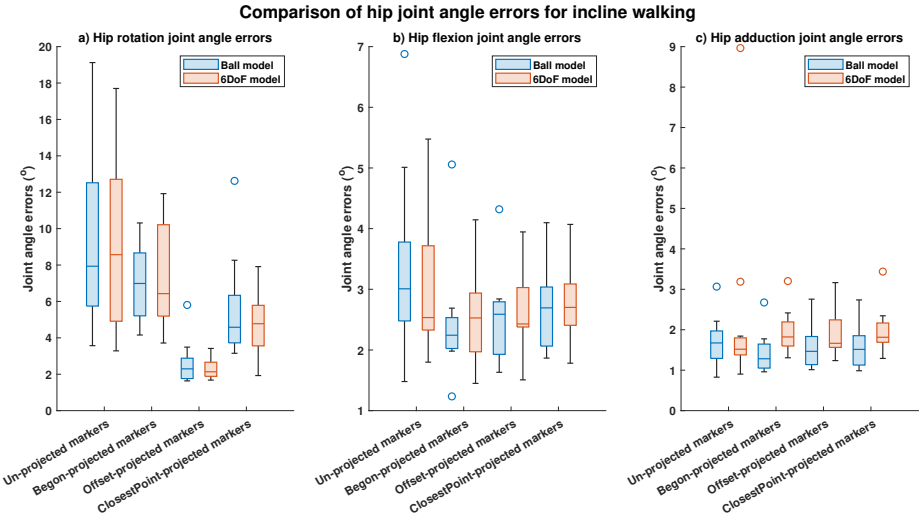

Figure 4.3: Comparison of median and spread of joint angle errors computed using four different projection methods (conventional (un-projected) skin-mounted marker, Begon-projection, offset-projection and closestPoint-projection) during incline walking: a) Hip rotation joint angle errors. b) Hip flexion joint angle errors. c) Hip adduction joint angle errors.

Model	Joint Angles	Hip Flexion		Hip Rotation		Hip Adduction	
	Projections	RMSE (°)	R^2	RMSE (°)	R^2	RMSE (°)	R^2
Ball joint	Skin-mounted markers (No projections)	3.4	0.996	9.2	0.709	1.7	0.96
	Begon Projection	2.4	0.997	**7.0 (p=1.32e-6)***	0.521	**1.4 (p=0.04)***	0.97
	Offset Projection	2.5	0.996	**2.7 (p=1.48e-6)***	0.823	1.6	0.967
	Closest Point Projection	2.7	0.996	**5.6 (p=2.58e-5)***	0.528	1.6	0.966
6 degree of freedom joint	Skin-mounted markers (No projections)	2.9	0.995	8.9	0.706	2.3	0.969
	Begon Projection	2.5	0.995	**7.4 (p=5.2e-5)***	0.406	1.9	0.963
	Offset Projection	**2.7 (p=0.01)***	0.996	**2.3 (p=4.54e-7)***	0.832	1.9	0.962
	Closest Point Projection	**2.8 (p=0.01)***	0.995	**4.8 (p=5.56e-7)***	0.35	1.9	0.959
bold and * : p <0.05							

Table 4.2: Joint angle root mean square errors (RMSE) and correlation coefficients (R^2) for hip flexion, rotation and adduction angles computed using the different projection methods for incline walking. Significance was computed as a comparison between joint angle errors obtained conventional (un-projected) markers and joint angle errors obtained using various marker projection schemes. RMSE, Root-mean-square-error;R^2, Correlation index

For internal and external hip rotation motions, hip rotation joint angle errors computed using offset-projected markers significantly ($p < 0.05$) reduced by 63.5% and by 79.6% respectively for the Ball model (Figures 4.4 a, 4.5 a, $p < 0.05$) and by 33.5% and 85.2% respectively for the 6DoF model (Figures 4.4 a, 4.5 a, $p < 0.05$). Non-significant reductions in hip rotation joint angle errors were computed using closestPoint-projected markers for internal hip rotation (Ball model: reductions of 59.4%; 6DoF model: reductions by 82.8%, Figure 4.4 a), with significant reductions obtained for external hip rotation ($p < 0.05$, Figure 4.5 a). Significant reductions ($p < 0.05$) in hip rotation angle errors during external hip rotation were obtained using Begon-projected markers with reductions of 78.6% obtained for the Ball model and reductions of 73.0% for the 6DoF model (Figure 4.5 a). Non-significant reductions of 34.7% (Ball model) and 18.7% (6DoF model) were obtained using Begon-projected markers during internal hip rotation (Figure 4.4). Additionally, correlation with artefact-free bone movement increased for hip rotations computed using offset-projected markers for both the Ball model (0.80->0.89) and the 6DoF model (0.78->0.88) during external hip rotation (Table 4.4). For internal hip rotation, correlation of hip rotation angles computed using offset-

projected markers increased for the 6DoF model (0.80->0.81) but decreased for the Ball model (0.90->0.87, Table 4.3); no improvements were observed when using closestPoint-projected markers or Begon-projected markers (Table 4.3 - 4.4).

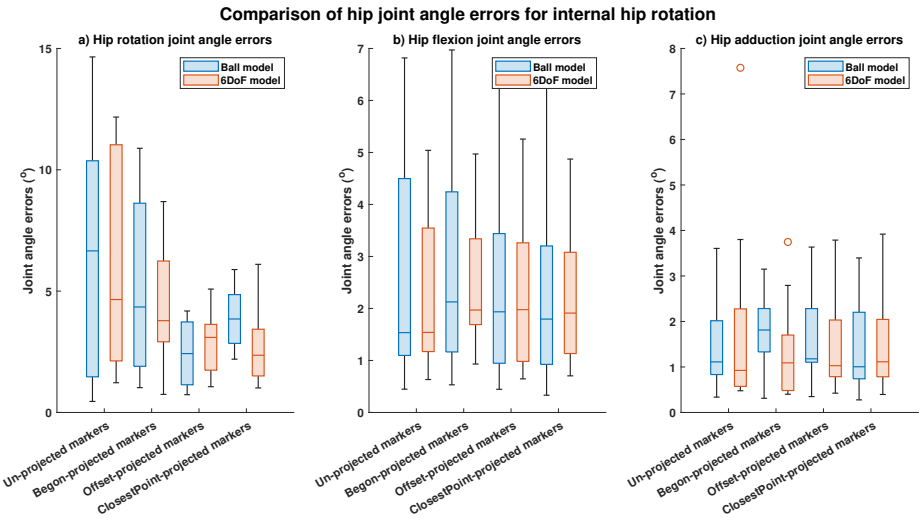

Figure 4.4: Comparison of median and spread of joint angle errors computed using four different projection methods (conventional (un-projected) skin-mounted marker, Begon-projection, offset-projection and closestPoint-projection) during internal hip rotation: a) Hip rotation joint angle errors. b) Hip flexion joint angle errors. c) Hip adduction joint angle errors.

Model	Joint Angles	Hip Flexion		Hip Rotation		Hip Adduction	
	Projections	RMSE (°)	R^2	RMSE (°)	R^2	RMSE (°)	R^2
Ball joint	Skin-mounted markers (No projections)	2.7	0.971	6.2	0.902	1.4	0.964
	Begon Projection	2.7	0.954	**5.2**	0.666	**1.8**	0.965
	Offset Projection	2.4	0.969	**2.4 (p=0.03)***	0.87	1.6	0.968
	Closest Point Projection	2.3	0.971	**3.9**	0.605	1.5	0.967
6 degree of freedom joint	Skin-mounted markers (No projections)	2.3	0.967	6.5	0.809	1.8	0.937
	Begon Projection	2.5	0.905	**4.3**	0.657	1.4	0.946
	Offset Projection	**2.3**	0.967	**2.9 (p=4.5e-7)***	0.818	1.5	0.947
	Closest Point Projection	**2.2**	0.964	**2.8 (p=0.022)***	0.422	1.6	0.945
bold and * : p <0.05							

Table 4.3: Joint angle root mean square errors (RMSE) and correlation coefficients (R^2) for hip flexion, rotation and adduction angles computed using the different projection methods for internal hip rotation. Significance was computed as a comparison between joint angle errors obtained conventional (un-projected) markers and joint angle errors obtained using various marker projection schemes. RMSE, Root-mean-square-error;R^2, Correlation index

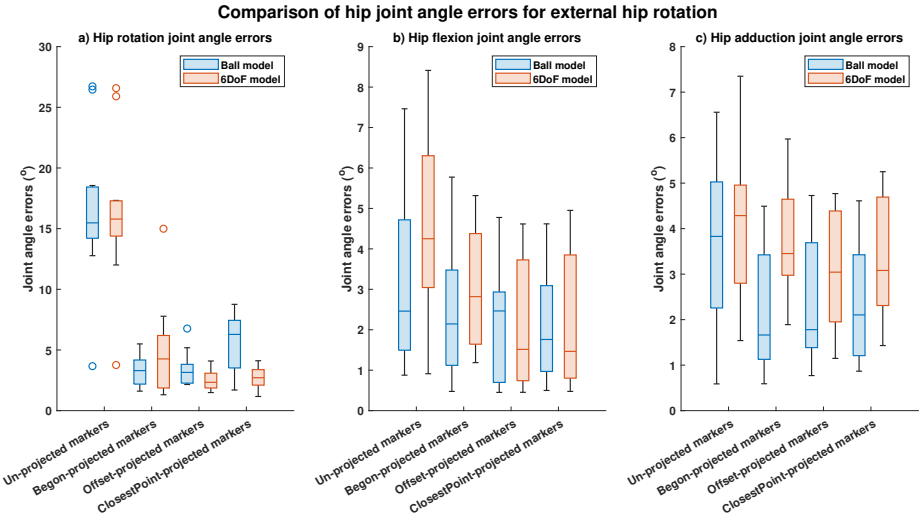

Figure 4.5: Comparison of median and spread of joint angle errors computed using four different projection methods (conventional (un-projected) skin-mounted marker, Begon-projection, offset-projection and closestPoint-projection) during external hip rotation: a) Hip rotation joint angle errors. b) Hip flexion joint angle errors. c) Hip adduction joint angle errors.

Model	Joint Angles	Hip Flexion		Hip Rotation		Hip Adduction	
	Projections	RMSE (°)	R^2	RMSE (°)	R^2	RMSE (°)	R^2
Ball joint	Skin-mounted markers (No projections)	3.3	0.709	16.6	0.809	3.7	0.706
	Begon Projection	2.5	0.693	**3.3 (p=1.32e-6)***	0.663	**2.2 (p=0.04)***	0.772
	Offset Projection	2.1	0.767	**3.4 (p=1.48e-6)***	0.893	2.3	0.779
	Closest Point Projection	2.1	0.629	**5.6 (p=2.58e-5)***	0.649	2.3	0.757
6 degree of freedom joint	Skin-mounted markers (No projections)	4.4	0.46	16.3	0.782	4.1	0.682
	Begon Projection	2.9	0.117	**4.9 (p=5.2e-5)***	0.649	3.7	0.614
	Offset Projection	**2.1 (p=0.01)***	0.591	**2.5 (p=4.54e-7)***	0.887	3.1	0.731
	Closest Point Projection	**2.2 (p=0.01)***	0.477	**2.7 (p=5.56e-7)***	0.542	3.4	0.64
bold and * : p <0.05							

Table 4.4: Joint angle root mean square errors (RMSE) and correlation coefficients (R^2) for hip flexion, rotation and adduction angles computed using the different projection methods for external hip rotation. Significance was computed as a comparison between joint angle errors obtained conventional (un-projected) markers and joint angle errors obtained using various marker projection schemes. RMSE, Root-mean-square-error;R^2, Correlation index

Reductions in hip flexion angle errors and hip adduction angle errors were not significant for internal and external hip rotations using any marker projection schemes. Of note, hip flexion joint angle errors computed using conventional (un-projected) skin-mounted markers and 6DoF model was lower for the internal hip rotation motion when compared with offset-projected markers and Begon-projected markers(Figure 4.4 b). Hip adduction joint angle errors computed using conventional (un-projected) skin-mounted markers and the Ball model was lower when compared with offset-projected markers and Begon-projected markers for both internal and external rotation (Figure 4.4 - 4.5 c). The RMS joint angle errors and correlation (R^2) values for internal and external hip rotations are given in Tables 4.3 - 4.4.

Residual errors computed using projected markers were lesser than those computed using conventional (un-projected) skin-mounted markers for all investigated motions and for both the Ball and 6DoF model (Figure 4.6).

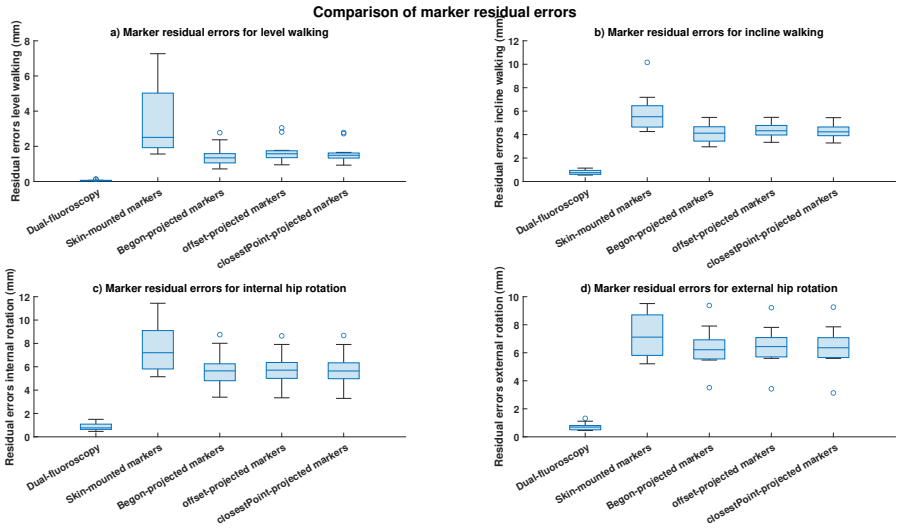

Figure 4.6: Comparison of residual errors between five markersets obtained for all investigated motions. Top left are the residual errors during level walking, top right the residual errors for incline walking, bottom left the residual errors for internal rotation and bottom right the residual errors for external rotation.

4.5 Discussion

The results of our study indicate that the projection of skin-mounted markers onto the bone surface reduces joint angle errors when compared with conventional methods of movement analysis (un-projected skin-mounted markers), thereby improving kinematic accuracy. In addition, we also observed an increase in correlation between kinematics computed using artefact-free bone movement and projected markers when compared with the correlation obtained using conventional (un-projected) skin-mounted markers, indicating an increase in the quality of the computed kinematics. Both joint angle errors and correlation were computed by leveraging kinematics obtained from artefact-free bone movement acquired using dual-fluoroscopy which do not suffer from STA and thereby indicate the efficacy of our method in reducing the influence of STA on computed kinematics. Furthermore, the data used in this study incorporated skin-mounted marker data obtained from participants of varying BMI scores, with our proposed marker-projection schemes reducing joint angle errors for all participants, underscoring its applicability and generalisability.

Previous studies quantifying STA and its impact on kinematics have indicated that internal/external rotation and abduction/adduction are significantly affected by STA, with the magnitude of joint angle errors comparable to that of actual

bone movement [39, 45, 46]. In their study using the same dataset as the one used in this study [94, 95, 96], the authors reported that hip joint angles computed using conventional (un-projected) skin-mounted markers were underestimated when compared with kinematics computed using DF-markers, and that neither the DoF of the model (joint model) nor the marker configuration reduced joint angle errors during walking or hip rotation activities [96]. Additionally, they reported hip rotation joint angle errors of 8° , 9° , 12° and 8° using conventional (un-projected) skin-mounted markers during level walking, incline walking, internal abduction and external abduction respectively [94, 96]. Their findings, one of the first to report the effect of STA on hip kinematics, underscored the need for a solution to ameliorate the effects of STA.

Whilst we obtained similar hip rotation errors using conventional (un-projected) markers, we noted a significant ($p < 0.05$) decrease in internal/external rotation errors during level walking, incline walking and internal and external hip rotations using markers projected on to the bone surface. Additionally, we observed lower hip flexion and adduction errors during most activities using projected markers compared with conventional (un-projected) markers; however, these differences were not significant. These results underscore the efficacy of our proposed methods to reduce the effects of STA on computed kinematics, specifically in rotations most affected by STA.

We also obtained lower kinematic errors, through projection of markers, for models incorporating different joint models. The efficacy of various methods proposed to reduce the effects of STA have been reported to vary based on the joint model incorporated [43], with the 6DoF and ball joints reported to produce kinematics and kinetics with higher accuracy than anatomically realistic joint models [29, 195, 211, 211]. We tested our projection schemes on models incorporating both, 6DoF and ball joints, with our results indicating improvements in computed hip rotation, flexion and adduction angles for both the models, underscoring the generalisability and applicability of our proposed method.

Our results also indicate that improved joint angle estimation is obtained when markers are projected onto the bone surface, compared with markers projected onto the longitudinal axis of the segment [43]. Whilst the projection of a subset of markers (or markers on the cuff) was reported to reduce joint angle errors in the upper extremity body during activities of daily living [43], the projection of all markers onto the longitudinal axis increased joint angle error. The cause of this increase in joint angle error was attributed to a loss of 3d information, which occurs when the coordinates of two axes were set to 0 [43].

In our study, we observed that, whilst the projection of markers onto the longitudinal axis does improve kinematic accuracy, it is also associated with a reduction in correlation with the actual bone movement when compared with conventional

(un-projected) skin-mounted markers. These issues were ameliorated by projecting markers onto the bone surface, with offset-projected markers improving the quality of joint angle estimation (as indicated by improved correlation compared with skin-mounted markers) and closestPoint-projected markers indicating a similar correlation to those obtained using markers projected onto the longitudinal axis.

Linking this study to the findings of the previous chapter (Chapter 3), our results additionally indicate that projecting skin-mounted markers onto the bone surface produces lesser residual errors. Residual errors are used as a goodness-of-fit metric between the underlying model and the experimental data [42, 178, 235], with lower residual errors reported to be an indication of : superior pose reconstruction capability of the proposed model [137] and improved STA compensation [30]. Therefore, our results indicate that projecting the markers onto the bone surface improves kinematic accuracy as indicated by lower joint angle errors and lower residual errors.

Whilst there are currently no methods to reduce STA which are incorporated in clinical practice, the reductions in joint angle errors computed using our proposed marker projection schemes were observed to be greater than those obtained using various non-marker projection STA compensation methods reported in literature such as novel pose estimators [80], novel joint constraints [211, 236] or STA models [49, 54]. The comparison between our marker projection schemes and some key examples are provided in Table 4.5.

height**Paper**	**Root mean square error (°)/ Marker residual error (mm)**	**Remarks**
Begon [43]	4.4° - 5.3°	Evaluated humerus rotational kinematics
Bonnet [52]	Using MKO: 2.1° Using EKF: 1.7°	Error reduction was obtained when an STA model was incorporated
Clement [73]	2.2±1.2° - 6.0±3.9°	Analysed the effect of subject specific knee models. The errors was for knee rotations
Richard [211]	Knee kinematics errors varied between 10.2° and 13.2°	Had a wide discrepancy in knee kinematics results across degrees of freedom (DoFs), models and motor tasks
Smale [236]	Significant differences in computed kinematics with and without adaptive knee joint boundaries	No ground truth knee kinematics so no RMSE was computed
De Groote [80]	Marker residual errors of 0.03 mm compared to 10.27 mm for global optimisation and 10.27 mm for local marker estimation	No ground truth knee kinematics so no RMSE was computed

Table 4.5: Comparison of joint angle errors/marker residual errors as reported by other studies proposing soft tissue reduction solutions.

The reason why our marker-projection schemes outperform other marker-projection schemes and other STA reduction strategies, could be attributed to the fact that our marker projection schemes ensure that the true motion of the bones, which are reflected in the movement of markers, are conserved or retained, with the projection removing the excessive movement obtained due to soft tissues. For example, in Begon-projection, by setting the markers coordinates to 0 except on the longitudinal axis, we lose information relating to the movement of bones. This has been alleviated in our marker projection schemes.

An application which would benefit from our proposed marker projection schemes is the pre-operative planning and criterion determination for performing femoral derotation osteotomies in children with CP as highlighted in the introduction.

Joint angles computed using our marker-projection schemes show a significant reduction in joint angle errors, and improved quality of computed kinematics in hip rotations – specifically internal/external hip rotation. These angles are leveraged in pre-operative planning and criterion determination for femoral osteotomies, and are the angles which are generally most affected by STA. Furthermore, the reduction in joint angle errors and increase in correlation with ground-truth kinematics were obtained for a wide variety of participants performing various tasks, thereby underscoring the potential generalisability clinical usability of both our proposed marker projection schemes.

Our proposed projection schemes may also be used to expand and validate the idea that projection of markers on to the bone surface may ameliorate the effects of STA on kinematics [129, 160, 161]. As discussed in the introduction, two notable methods leveraging ultrasound imaging were proposed to reduce the effects of STA on kinematics [129, 160, 161]. Although the proposed ultrasound methods were validated on either phantoms or through in-vitro experiments [161], no improvement in kinematic accuracy during movement analysis has been reported.

In Chapter 3 we highlighted how the most widely used method to reduce STA, MKO methods, reduces in efficacy when applied to data with high magnitudes of STA or to data obtained from subjects with high BMI scores. The reduction in efficacy was found to increase joint angle errors, reducing the usability of clinical gait analysis. In this chapter, we have proposed two marker projection schemes, which reduces joint angle errors for various motions and for subjects with varying BMI scores. Additionally, the a significant reduction in error was obtained for joint angles most affected by STA and which is leveraged in pre-operative planning. Our results highlight the generalisability and efficacy of our proposed solutions. In the subsequent chapters, we shall investigate methods to enable projection of markers.

4.6 Conclusion, technical novelty and take-away messages

We investigated the efficacy of our proposed projection of markers schemes in reducing kinematic errors and improving kinematic fidelity. Our results indicate that projection of markers onto the bone surface reduces kinematic errors when compared with conventional (un-projected) skin-mounted markers, and when compared with other marker projection schemes proposed in literature. In summary, we have shown that:

1. Offset-projected markers reduces kinematic errors and also improves correlation with artefact-free bone movement

2. closestPoint-projected markers reduces kinematic errors. However, correlation is in line with un-projected skin-mounted markers

3. Our proposed projection of markers methods outperforms conventional (un-projected) skin-mounted markers and other projection schemes proposed in literature, specifically, in joint angles significantly affected by STA

The novelty of our results are:

1. The marker projection schemes proposed in this chapter not only significantly reduce errors compared with conventional (un-projected) markers and other marker projection schemes, but also improve the quality of computed kinematics

2. The reductions in joint angle errors and increase in quality of computed kinematics were most observable in internal/external joint rotations — the joint rotations most affected by STA — which are clinically important, especially in pre-operative planning for a variety of surgical interventions. The results of this study have been published in Scientific Reports [203].

Our study has a few limitations. The challenges faced in marker projection were in the method used to determine the actual bone location and in the method employed to calculate the trajectories of projected markers. Whilst we endeavoured to determine the actual bone location using informed approximations based on dual-fluoroscopy markers in the LCS, the location may not reflect real-world locations during motion. Secondly, the determination of the trajectories of projected markers was based on kinematics computed using inverse kinematic pipelines applied to dual-fluoroscopy data, and may therefore be affected by model constraints and the MKO method. Thus, in future investigations, we will aim to compare our results with actual artefact-free bone movement.

In conclusion, we have proposed and validated a novel method to reduce the deleterious impact of STA on computed kinematics, which can be applied for a range of motions and participants. Our proposed marker projection schemes reduce kinematic errors significantly when compared to conventional (un-projected) markers and outperform other marker projection schemes. Additionally, they improve the quality of computed kinematics as evidenced by higher correlation values.

Chapter 5

Investigating the feasibility of applying microwave imaging in biomechanical applications: Simulation

5.1 Introduction

In this chapter we investigate the feasibility of applying microwave imaging to detect the location of the bone from the skin surface using wearable antennas; with the location of the bone used to facilitate projection of markers onto the bone surface, which we have shown reduces joint angle errors in the previous chapter (Chapter 4). Section 5.2 introduces the background for this chapter with Section 5.3 describing the methods used in this study. Section 5.4 presents the results of the study with discussions of the results provided in Section 5.5. Section 5.6 concludes this study with our key-takeaways from this study.

5.2 Background

In the previous chapter (Chapter 4) we proposed two novel marker projection techniques to reduce the effects of soft tissue artefacts (STA) on computed kinematics, specifically internal/external hip rotations. Our results indicated that projecting skin-mounted markers onto the bone surface reduces joint angle errors significantly when compared with conventional (un-projected) skin-mounted markers. Furthermore, our results indicated that projection of markers onto the bone surface improves the quality of computed kinematics when compared to kinematics computed

using conventional (un-projected) skin-mounted markers (indicated by increased correlation with artefact-free bone movement). The reduction in kinematic errors, and the increase in correlation with actual bone movement (artefact-free bone movement) for joint angles used for surgical planning for children with CP indicates the potential clinical usability of our proposed marker projection schemes. Specifically, our results indicated a significant reduction in errors for internal/external hip rotations, which are used for planning of femoral derotation osteotomies [186, 260], with internal/external hip rotations greatly affected by STA as indicated in Chapter 2. Furthermore, the reduction in kinematic errors and the increase in correlation with artefact-free bone movement, was obtained for participants with varying body mass, which is currently not achieved by clinically applied methods for clinical gait analysis (Refer to Chapter 2 and Chapter 3).

In order to project the markers onto the bone surface, determining the location of the bone in the global coordinate system (lab coordinate system) during static and motion, is critical. The location of the bone in the global coordinate system can be calculated from two vectors: the location of skin-mounted marker in the global coordinate system (as acquired from optoelectronic systems) and the distance of the bone from the skin surface [159]. This chapter and the next investigate a method to compute the second vector: the distance of the bone from the skin surface.

Whilst imaging modalities such as fluoroscopy, computed-tomography and MRI [128, 173, 177] (which have previously been applied to determine artefact-free bone movement as discussed in Chapter 2) can be leveraged to determine the distance of the bone from the skin surface during motion, they are expensive, offer limited field-of-view, and in the case of fluoroscopy and computed-tomography, expose the subject to harmful (ionising) radiation.

Alternatively, two studies have proposed using ultrasound imaging [129, 130, 160, 161], which is a safe, real-time imaging modality, to determine the location of the bone from the skin surface. Jia [129, 130] proposed a system combining ultrasound imaging with an optoelectronic system (CAT & MAUS), to determine the location of the greater trochanter in the global coordinate system, by placing an ultrasound probe above the greater trochanter during motion and imaging the actual location of the greater trochanter during motion. Similarly, Masum [159, 160] proposed an intelligent ultrasound sensor which would be capable of determining the distance between bone and skin during motion and thereby reduce the effects of STA on computed kinematics. However, the intelligent sensor proposed by Masum [159] has not been validated either on tissue-mimicking phantoms or on humans, with the system proposed by Jia [130] currently tailored for only detecting the greater trochanter. Additionally, the system requires coupling liquid to improve image resolution and radiologist input to ensure that images can

clearly discriminate between bones and soft tissues.

As indicated in Chapter 2 ultrasound imaging has also been applied in clinical gait analysis for applications other than imaging the underlying bone. Mainly, ultrasound imaging has been leveraged to assess muscle and tendon lengths, and muscle-tendon function during walking and other activities [77] in both typically developing children/adults and in children with CP [37, 132]. Therefore, it can be assumed that ultrasound imaging is a mature imaging modality in gait analysis.

However, whilst ultrasound imaging is a safe and cost-effective imaging modality when compared with MRI, fluoroscopy or CT, and has been integrated in gait analysis for both typically developing children and children with CP, it has the following limitations: the need for a probe to be held at the location to be imaged, the need for coupling liquid to improve resolution and the need for a radiologist's input when images are unclear. Specifically, pertinent to our goal of improving the quality of kinematics computed during clinical gait analysis, several practical limitations have been associated with applying ultrasound imaging during gait analysis: the tilt angle of the probe, the probe weight, and the associated muscle compression.

Whilst the study which complemented optoelectronic systems with ultrasound (CAT & MAUS, [129, 130]), as described above, did not explicitly detail the difficulties in attaching an ultrasound probe to the body during motion, a study analysing the effect of probe weight on children with CP and typically developing children, found significant differences in sagittal plane kinematics obtained with and without the probe [171]. Specifically they reported that attaching a probe (with holder) with an overall weight of 300g to the thigh, resulted in increased step length, reduced hip extension, reduced knee flexion and reduced ankle plantarflexion, when the probe was attached [171]. Similarly, a paper reported non-significant differences in sagittal plane kinematics with and without a probe when tested on adolescents and young adults [62].

Pertinent to our potential application of surgical planning for CP, the above papers only reported results on sagittal plane kinematics: which are least effected from any source of error (STA, marker placement etc). Therefore, we hypothesise that the addition of an ultrasound probe on children would produce even greater differences in coronal and transverse plane kinematics, which may negatively impact surgical planning.

To overcome the limitations of ultrasound imaging as described above, in this thesis we instead analyse the feasibility of leveraging microwave imaging to image the bone. Microwave imaging, also a safe (non-ionising), low power (negligible heating effects) and cost-effective imaging modality, is operator-independent with the potential to be applied for imaging any part of the human body [232].Microwave imaging leverages the difference in electrical properties (permittivity and conduc-

tivity) between various tissues and between healthy and diseased tissues to detect and image the object of interest, and has been extensively applied in breast and brain tumour imaging [207, 219, 233] (a substantial review of different microwave imaging algorithms and applications can be found in Chapter 2).

A typical microwave imaging system incorporates an imaging domain, a radio-frequency switch, a vector network analyser and antennas. Antennas are placed rigidly around the imaging domain, with both the antennas and imaging domain immersed in a coupling liquid [170] (Figure 5.1). A large number of antennas (minimum of 32) or scanning positions (when antennas are rotated around the imaging domain) are generally used, in order to acquire sufficiently large amounts of data to reconstruct the object of interest. The systems are generally static and are of considerable size: an enclosure of radius 22.4 cm and height 44.4 cm was used to image human forearms [105]; a tank of height 8.2 cm and radius 2.7 cm was used to validate a bone phantom [24].

Therefore, a typical microwave imaging system cannot be easily integrated into biomechanical applications which ideally require a system which is portable, wearable and has a small form-factor. Despite, guidelines being proposed for a wearable microwave imaging system [21], the study focused on potential improvements which could be achieved in the reconstructed images, and did not elucidate how such a system may be applied in a portable fashion or be applied during motion [21]. Hence, whilst microwave imaging has been applied to determine the electrical properties of the bone in the human forearm [105], leg [22] and in the heel [165], key developments in typical microwave imaging systems and their mode of application need to be investigated prior to their incorporation in biomechanical applications.

Our preliminary investigation using wearable antennas placed on the skin surface of a thigh of a virtual population (ViP) model available in Sim4Life [70, 106], without the use of coupling liquid, indicated that there were variations in scattering parameters obtained when the electrical properties of femur bone were varied [204]. This indicated that scattering parameters were sensitive to the electrical properties of the femur and that wearable antennas, in the absence of coupling liquid, could be applied to image the underlying bone. As discussed in Chapter 2, differences in scattering parameters, or S-parameters, are used to develop an image of the object of interest. Therefore, in this chapter we aim to expand on our initial investigation and assess the feasibility of applying microwave imaging in clinical gait analysis, specifically to determine the distance of the bone from the skin surface in order to enable projection of skin-mounted markers. We validate the feasibility of applying microwave imaging by applying the following conditions during data collection: no-coupling liquid (direct contact of the antenna with the skin), reduced number of antennas and the need for the system to detect the loca-

tion of the bone in both a static pose and in a gait mimicking pose. Through the above analysis we aim to determine the potential of microwave imaging to be used as an alternative imaging modality to ultrasound imaging, specifically in clinical gait analysis.

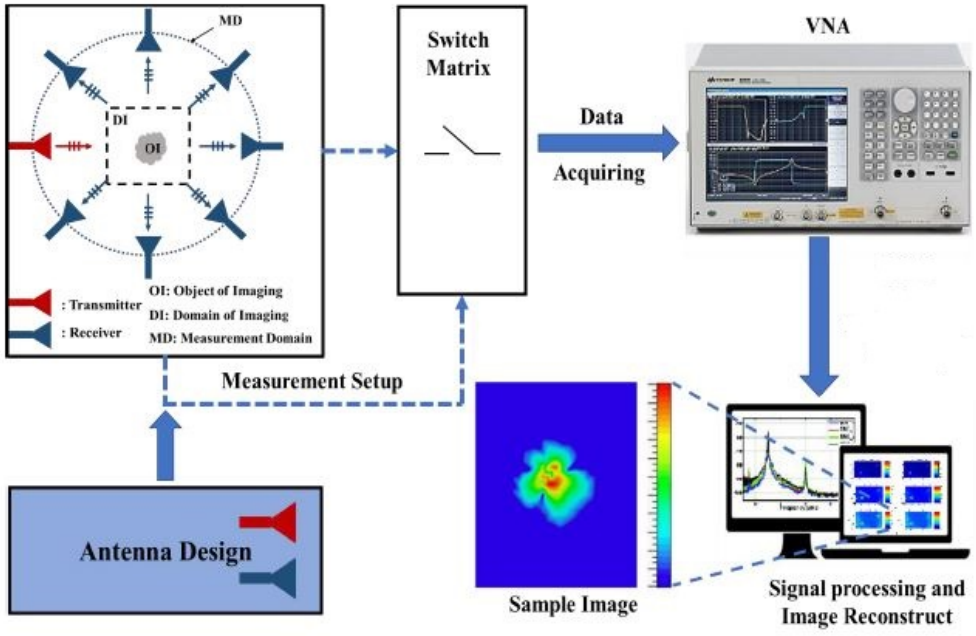

Figure 5.1: General setup of microwave imaging systems which consist of an imaging domain, an array of antennas, vector network analyser and a radio-frequency switch [126].

5.3 Methods

In order to investigate the feasibility of applying microwave imaging in biomechanical applications, data was collected under specific conditions leveraging models of antennas and models of humans of different BMI scores:

- No coupling liquid was to be used in the system with the antennas making direct contact with the skin. This was to ensure that the system developed could translate to a wearable and portable system, whilst also ensuring there was sufficient coupling between the antennas and the human body (thereby reducing the reflection of electrical field at the air-skin interface)

- The number of antennas was restricted to 8. This was to ensure that the time for data collection is minimal and can record data during different phases of a gait/motion cycle i.e at each data collection instance the tissues encompassed by the antennas can be considered to be static
- The location of the bone from the skin surface should be detected both in static pose and in poses mimicking gait

The antennas and human models used for the investigation are described in the following subsections.

5.3.1 Antennas investigated

As reviewed in Chapter 2, various antennas operating at different frequencies have been proposed for microwave imaging. Even amongst microwave imaging studies analysing the dielectric properties of the bone, different antennas have been leveraged: microstrip antennas operating in the frequency range of 1.5–4.5 GHz were used to monitor bone health [24], monopole antennas operating in the frequency range of 0.5-3 GHz were leveraged to detect variations in bone density due to injuries [165], and dipole antennas operating in the frequency range of 0.8–1.2 GHz were used to study human forearms [105]. The frequency ranges were chosen to optimise image resolution and penetration into the human body. Based on the reviewed studies, we have determined the optimal frequency range — for both image resolution and sufficient penetration into the human body — to be between 0.5–3 GHz.
Three antennas, tuned for different frequencies, were investigated in this study (Figure 5.2 a): a dipole antenna tuned to resonate at 900MHz (in air) [12], a triangular patch monopole antenna which was proposed for brain tumour detection and was tuned to operate between 1–3GHz when immersed in a coupling liquid [110], and a wideband monopole patch antenna proposed for brain stroke monitoring and tuned to operate in a frequency range of 1-1.75GHz when immersed in a coupling liquid with dielectric permittivity of 20 [251].
The two patch antennas were further tuned for maximum coupling into the human body (Figure 5.2 b) by parametrically altering the dimensions of the patch and antenna size to determine the optimal shape for maximal coupling into a slab of muscle in Sim4Life [11]. The dipole antenna was judged to have good coupling with the human body based on its S11 (reflection) parameters.

The three different antennas are henceforth referred to as *antennas types* with the dipole antenna referred to as Antenna A, the modified wideband monopole antenna as Antenna B and the modified triangular monopole patch antenna as Antenna C.

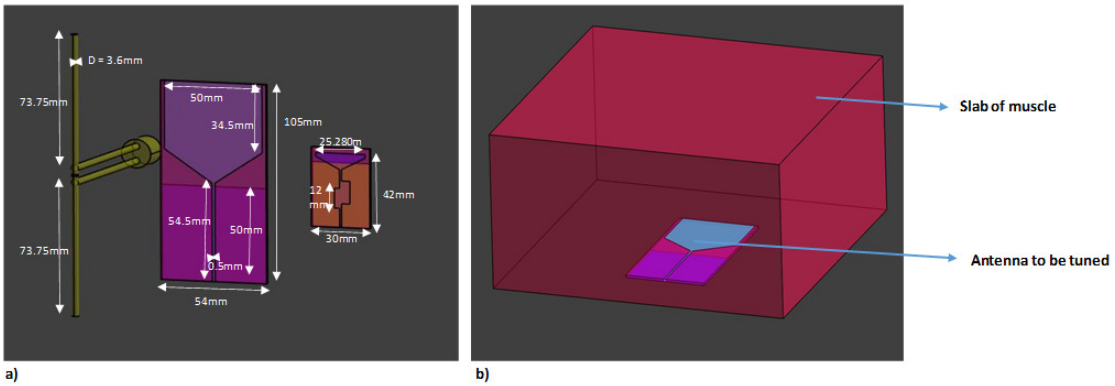

Figure 5.2: a) The three antennas investigated in this study. The leftmost antenna is the dipole antenna (antenna 1), the centre antenna is the modified triangular monopole patch antenna (antenna 3) and the rightmost antenna is the modified wideband monopole antenna (antenna 2). b) Method to tune the patch antennas by maximiming coupling into a slab of muscle.

As indicated in the background section and in Chapter 2, most studies have leveraged a large number of antennas or a large number of scanning positions to image the object of interest. However, this would increase the time needed to capture data and would increase the weight of the potential wearable system, restricting its applicability in clinical gait analysis, which is the main goal of this study. Theoretical studies have proposed that the number of antennas required to successfully reconstruct an image and to avoid aliasing effects that can lead to spurious artefacts is governed by Equation 5.1:

$$M = 2kR \tag{5.1}$$

- M: Minimum number of antennas required for sufficient spatial sampling.
- k: Wavenumber in the imaging medium, defined as $k = \frac{2\pi}{\lambda}$.
- λ: Wavelength of the electromagnetic wave in the medium.
- R: Radius of the reconstruction (or imaging) domain.

Using a frequency of 0.75 GHz, the minimum number of antennas required to image the bone would be 15 antennas. However, in our study we decided to use 8 antennas of each *antenna type*. This was informed by two factors:

- Other studies operating at a similar frequency to our proposed antennas [18, 134] have reported that using 8 antennas has provided images with sufficient clarity

- Findings from our initial investigation into the feasibility of microwave imaging, wherein we aimed to image the femur, fibula and tibia using 5 antennas placed around the thigh and shank respectively [200]. Specifically, whilst the images produced using 5 antennas indicated the presence of all three bones (Figure 5.3, the results for the femur were not repeatable for different antennas or for different human models. No images were produced when the number of antennas were reduced below 5.

Based on the above two factors, we determined that 8 antennas would provide a balance between accuracy and time taken for capturing data (if potentially made into a wearable device).

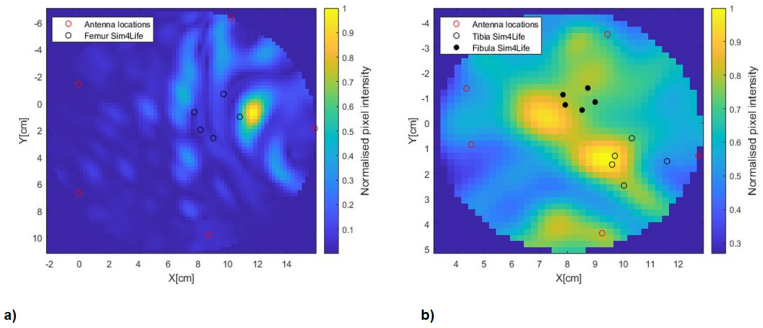

Figure 5.3: a) Reconstructed image showing the femur located at (11.62 cm, 0.82 cm). Imaged femur is identified as pixels with high intensity values. The black circles indicate the surface of the femur as calculated in Sim4Life. Red circles show the centres of the dipole antennas. b) Reconstructed image of the tibia and fibula located at (9.29 cm, 1.57 cm) and (7.29 cm, -0.17 cm) respectively. The imaged tibia and fibula are identified as pixels with high intensity values. The black and white circles indicate the surface of the tibia and fibula respectively, as calculated by Sim4Life. The red circles show the centres of the dipole antennas.

5.3.2 Virtual population models investigated

Four virtual population (ViP) models available in Sim4Life [70, 106] were leveraged in this study. Duke, a male anatomical model, and Ella, a female anatomical model, were the baseline models used in the study. Additionally, two morphed models of Ella — where the fat and muscle content were increased to mimic humans with different BMI scores, whilst preserving the internal organ placement and tissue distribution [106] — were also leveraged. The characteristics of the four anatomical models used in this study are given in Table 5.1.

The following investigations were carried out using the four models:

- The antennas were placed around the thigh of the Duke model to image the femur. The model was in a static (standing) pose
- The antennas were placed around the thigh for each of the Ella models — Ella-22 (Ella with a BMI of 22), Ella-26 (Ella with a BMI of 26) and Ella-30 (Ella with a BMI of 30) — to image the femur. The models were in a static pose (Figure 5.4 a)
- The antennas placed around the thigh for the Ella-22 and Ella-30 models were rotated and translated with the thigh to image the femur in a pose mimicking a phase of the gait cycle (the hip flexed by 40° followed by hip internally rotated by 5° and with the knee flexed by 30° , Figure 5.4 b). The two models (Ella-22 and Ella-30) were chosen since they represent humans with a healthy and obese BMI score.

Anatomical model name	**Age (years)**	**Sex**	**Height (m)**	**Mass (kg)**	**BMI (kg/m^2)**
Duke	34	Male	1.74	70	23.1
Ella - 22	26	Female	1.63	57.3	22
Ella - 26	26	Female	1.63	69.4	26
Ella - 30	26	Female	1.63	79.7	30

Table 5.1: Characteristics of the four anatomical models used in this study. Duke is a male anatomical model with Ella-22 a female anatomical model of body mass index (BMI) score of 22. Ella-26 and Ella-30 are morphed models of Ella-22 with BMI scores of 26 and 30 respectively.

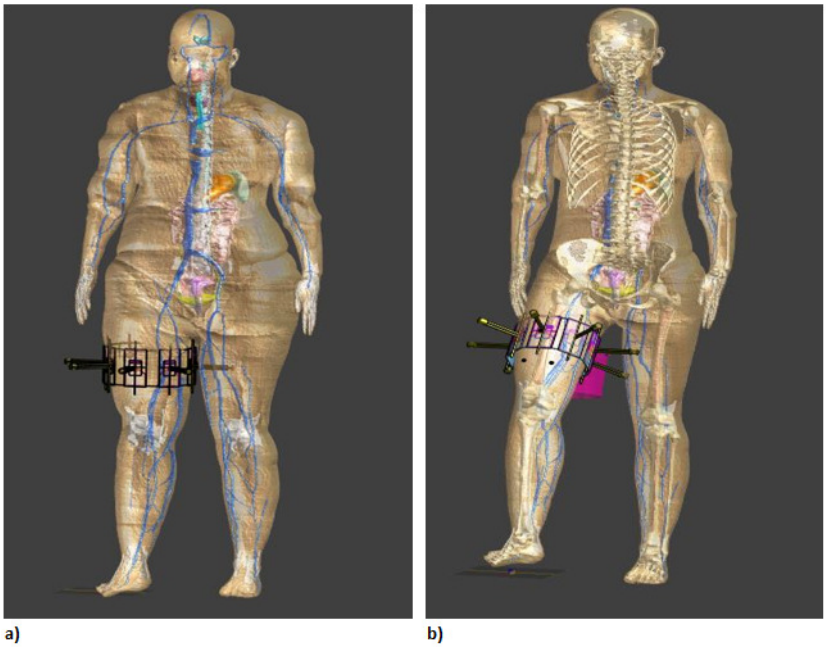

Figure 5.4: a) Exemplar depiction of 8 antennas placed around Ella-30 model in static (standing pose). b)Exemplar depiction of 8 antennas placed around Ella-22 model in a pose mimicking a phase of the gait cycle. ViP: Virtual population models

In all the above cases, eight antennas of each *antenna type* (dipole, triangular patch monopole and patch monopole) were placed at equidistant points around the thigh. In order to ensure proper placement, a cylinder — whose circumference matched that of the thigh to be imaged — was used to calculate the antenna locations. The cylinder was attributed with electrical properties of the skin, thereby increasing the skin thickness in locations where the circumference of the cylinder was larger than that of the thigh. This ensured that the antennas were making direct contact with the skin.

Antenna locations for the posed model were determined based on a transformation matrix calculated using three points on the skin (the location of three points during the standing pose and the location of the three points during the posed state) rather than the rotation and translation of the underlying bone (femur). This was to ensure that the deformations of the soft tissues and skin were accounted for when the model is posed, as the deformations are different for Ella-22 and Ella-30 models (due to varying volumes of soft tissues).

The deformations of the soft tissues and skin — due to the model transitioning from the standing pose to a pose mimicking a phase of the gait cycle (hip flexion of 40° , hip rotation of 5° and knee flexion of 30°) — were calculated based

on a physics-simulation-based approach, wherein the user-prescribed motions of the bone are used to perform a tissue mechanical simulation of the deformations. These deformations also depend on the volume of soft tissues [106]. The above steps were undertaken to ensure that the movement of antennas was similar to the movement wearable antennas would undergo in similar situations i.e the antennas would move based on soft tissue movement and not just the movement of bones.

5.3.3 Simulations

In total eighteen investigations were carried out, one investigation per antenna type for each of the models: Duke-Femur, Ella-22-Femur, Ella-26-Femur, Ella-30-Femur, Ella-22-Femur-Posed and Ella-30-Femur-Posed. For the first four investigations (performed on Duke-Femur, Ella-22-Femur, Ella-26-Femur and Ella-30-Femur), the following two simulations were performed:

- Simulation 1: where the bone (cortical and cancellous femur) was attributed with electrical properties of the muscle
- Simulation 2: where the bone (cortical and cancellous femur) was attributed with electrical properties of the bone

The results of Simulation 1 were used as the reference scan or empty scan data, which was then subtracted from the data of the second simulation prior to being used as input into the imaging algorithms. In addition, electric field values calculated using the first simulation were recorded at every pixel location inside the thigh to be used in-lieu of the Green's function for the MUSIC and Kirchhoff migration algorithms. Empty scan data of Ella-22-Femur and Ella-30-Femur were used for the the posed model investigations.

For all simulations, a Gaussian pulse centred at the resonant frequency for each antenna and with a bandwidth of 3 GHz was used as the input waveform. The models were voxeled using the automatic voxelling tool in Sim4Life [11].

5.3.4 Qualitative algorithms investigated

Four qualitative imaging algorithms were investigated: the confocal imaging algorithm, Delay and sum (DAS)[233] and its variant delay multiply and sum (DMAS) [149]; the multiple signal classification algorithm (MUSIC) [82, 220]; and the Kirchhoff migration algorithm [17, 238]. Implementations of DAS and DMAS found in the Microwave Radar-based Imaging Toolbox (MERIT) [182] were leveraged. Modifications were made to the functions used to determine the imaging domain and the antenna delays, to tailor them for our purposes. Additionally, an offset — determined using the breast tumour datasets provided in the toolbox — was

subtracted from the true bone locations obtained from Sim4Life [11] whilst investigating the validity of the reconstructed images obtained using DAS and DMAS.

MUSIC is based on the principle of time-reversal imaging and has been extensively applied in microwave imaging applications. In our study, the multi-frequency variant of MUSIC was leveraged, where images reconstructed at each frequency were non-coherently summed to produce the final image. This was done to reduce artefacts in the reconstructed image and build on additional information obtained at multiple frequencies [220]. In addition, electric field values inside the thigh (computed in the simulations) were used in-lieu of the Green's function as computation of Green's functions for an inhomogenous background (the thigh) would be computationally expensive and inaccurate. Similarly, we have investigated a multi-frequency variant of Kirchhoff migration in this study. Kirchhoff migration has also been widely applied in microwave imaging applications [17, 238] and has been reported to be a fast, stable and effective imaging technique for detecting small scatterers [144]. The multi-frequency variation of Kirchhoff migration was reported to produce better results than its single-frequency variations [188].

The above four qualitative algorithms were investigated due to their widespread adoption in microwave imaging, their ability to generate images in real-time, and as collected scattering parameters (S-parameters) can be directly applied to the imaging algorithms without any need for conversion to electric-field values. Additionally, only transmission parameters (S21 parameters) were provided to the imaging algorithms. This was informed based on previous studies leveraging transmission parameters collected from diametrically opposite antennas to the transmitting antenna to generate images [102, 103], and from our initial investigation into microwave imaging [200, 204].

Whilst the four qualitative algorithms have been previously applied in microwave imaging, none of the algorithms have previously been applied to image a large scatterer, such as the bone. Additionally, for MUSIC and Kirchhoff migration, we substitute the Green's function with electric field values computed from Simulation 1. This is to overcome the limitations of inhomogenous Green function computation and to increase the accuracy of the imaging algorithms [114, 115].

5.3.5 Metrics

Visual verification of the reconstructed images was initially done to determine if a hotspot (indication of a scatterer) was present close to the true bone locations determined using Sim4Life [11]. In addition, metrics commonly applied in breast tumour detection were used to evaluate the accuracy of the reconstructed image [208, 219]: Signal-to-cluster ratio (SCR), signal-to-mean ratio (SMR) and localisation error. SCR compares the maximum response inside the object of interest to the maximum response in the region outside the object of interest, and SMR

compares the maximum response in the object of interest to the average response outside the object of interest. Localisation error is the difference between the expected centre of the object of interest to that of the maximum response in the image. A higher SCR and SMR indicates a high-contrast localised region within the image. For example SCR and SMR values greater than 0 dB were obtained for breast tumour studies [208], however negative SCR values were obtained for breast tumour detection in heterogeneous breasts. For all our investigations the object of interest was the bone (specifically, the femur).

5.4 Results

5.4.1 Antennas

The tuned antennas were observed to have good coupling with a slab of muscle based on their reflection parameters (S11) parameters (Figure 5.5), with the resonant frequencies for Antenna A at 0.6 GHz (black curve), Antenna B at 1.6 GHZ (red curve) and Antenna C at 0.8 GHz (blue curve) when propagating into muscle. Good coupling was indicated by S11 parameters being less than -10dB at the resonant frequencies. The overall dimensions of the tuned antennas are given in Table 5.2.

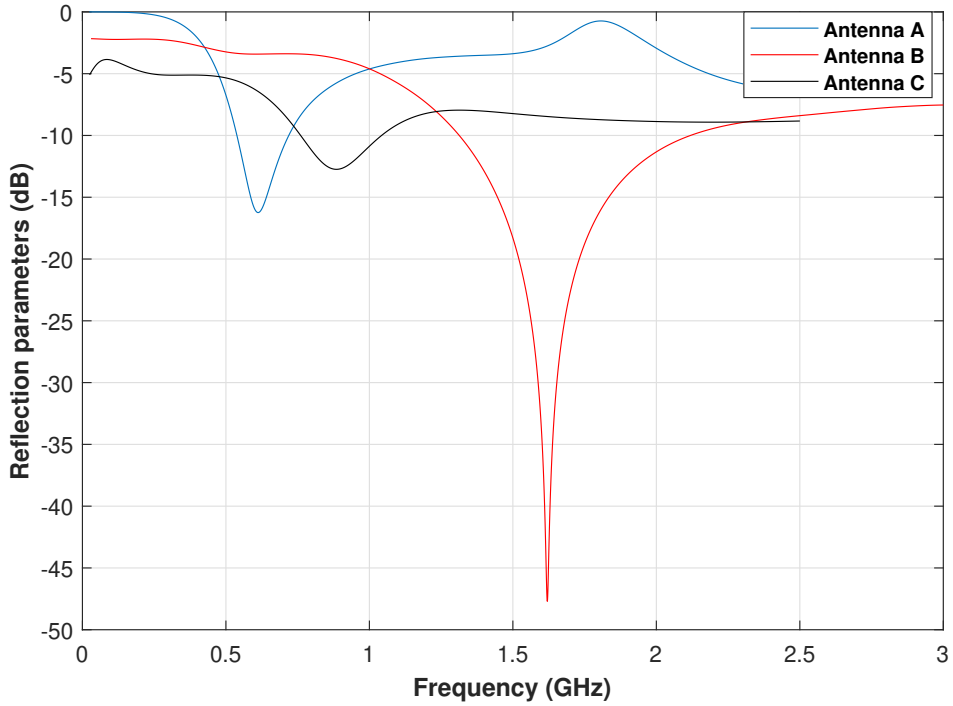

Figure 5.5: Reflection parameters (S11) for the three antennas when placed against a slab of muscle

Antenna type	Length (mm)	Breadth (mm)	Width (mm)
Antenna A (dipole antenna)	73.75 (half dipole)		1.8 (radius)
Antenna B (wideband monopole antenna)	105	54	1.6
Antenna C (microstrip triangular monopole patch antenna)	42	30	1.6

Table 5.2: Dimensions of the three antennas investigated in the study

5.4.2 Image reconstruction

Our results indicate that the location of the bone from the skin surface was determined for every anatomical model using each of the three antenna types through microwave imaging. Additionally, the location of the bone was determined both, in the static pose and a pose mimicking a phase of the gait cycle, using atleast one antenna type.

For the sake of brevity, only reconstructed images obtained using Antenna C are shown with the remaining reconstructed images found in Appendix B. Reconstructed images of Antenna C were chosen due to two primary reasons: the resonant frequency of Antenna C lies between Antenna A and Antenna B and

therefore results obtained using Antenna C can be viewed as in-between those obtained using Antenna A and Antenna B; reconstructed images using Antenna C were able to detect the bone in both a static pose and a pose mimicking a phase of the gait cycle. Simulations in the posed state were not possible using Antenna A due to high computational demands on Sim4Life [11], and the reconstructed images of the posed model and using Antenna B did not indicate the location of the bone.

The images were reconstructed using four qualitative imaging algorithms: DAS, DMAS, MUSIC and Kirchhoff migration. As detailed in the methods section, the MERIT toolbox was leveraged to reconstruct images using DAS and DMAS with an offset correction — calculated using the breast tumour dataset available in the MERIT toolbox (Figure B.1) — applied to the true bone locations calculated in Sim4Life [11].

The location of the femur in the Duke anatomical model was visually detected using each of the four imaging algorithms (Figure 5.6). SMR was highest for the image reconstructed using DMAS (SMR: 26.8214dB) and lowest for the image reconstructed using MUSIC (SMR: 5.11dB). Images reconstructed using DAS had the highest SCR (SCR: -0.3083dB) with images reconstructed using Kirchhoff migration having the lowest (SCR: -3.3dB). Localisation error was the lowest for images reconstructed using Kirchhoff migration (Localisation error: 0.69 cm), with maximum error obtained using the DAS algorithm (Localisation error: 1.90cm, Table 5.3).

Whilst reconstructed images using the other antennas successfully indicated the location of the bone (Appendix B) — through visual verification — SMR, SCR and localisation errors varied between the three antennas (Appendix B). Antenna A had higher SMR for images reconstructed using all imaging algorithms with Antenna B having the least SCR for images reconstructed using all imaging algorithms. Localisation errors were smaller for Antenna C and Antenna A compared to Antenna B when using MUSIC and Kirchhoff migration while Antenna B had the least localisation error when computed using confocal imaging algorithms (DAS and DMAS). Localisation errors for all antennas and calculated using all imaging algorithms were less than 2cm.

Anatomical model	Algorithm	SMR (dB)	SCR (dB)	Localisation error (cm)
Duke	DAS	18.8088	-0.3083	1.9008
	DMAS	26.8214	-0.6868	1.7946
	MUSIC	5.114	-2.557	1.4052
	Kirchhoff	6.0287	-3.3893	0.6969
Ella - 22	DAS	13.98	-2.7514	1.1133
	DMAS	14.57	-7.5473	1.1752
	MUSIC	5.3665	-2.7663	1.48
	Kirchhoff	2.0461	-3.241	0.9815
Ella - 26	DAS	18.8732	-3.0647	1.0533
	DMAS	23.3552	-6.8105	1.0533
	MUSIC	8.245	-1.9048	1.75
	Kirchhoff	6.7864	-1.3686	1.9332
Ella - 30	DAS	19.4456	-3.7721	0.7647
	DMAS	24.641	-6.179	0.7647
	MUSIC	7.1731	-1.3928	2.85
	Kirchhoff	5.145	-1.2754	2.488
Ella - 22 Posed	DAS	-	-	-
	DMAS	-	-	-
	MUSIC	2.8905	-4.913	2.6766
	Kirchhoff	-0.1612	-4.7139	2.0088
Ella - 30 Posed	DAS	-	-	-
	DMAS	-	-	-
	MUSIC	7.8944	-3.3131	1.6901
	Kirchhoff	-1.2796	-3.67141	1.202

Table 5.3: Metrics of reconstructed images computed using data collected from Antenna C. Values with '-' indicate the bone could not be determined in the reconstructed image. SCR, signal-to-cluster ratio; SMR, signal-to-mean ratio; DAS, delay-and-sum confocal imaging; DMAS, delay-multiply-and-sum confocal imaging; MUSIC, multiple signal classification;

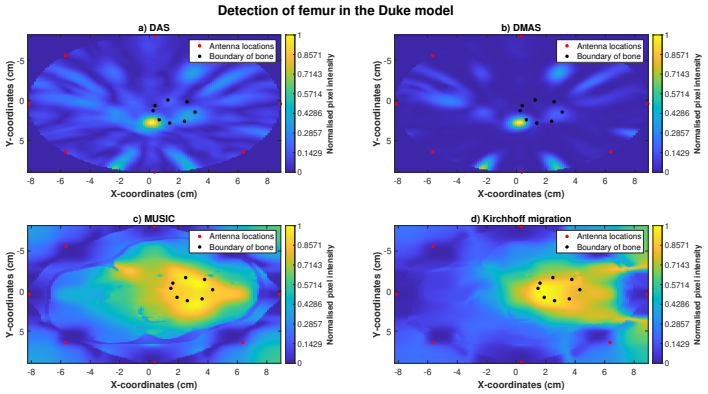

Figure 5.6: Reconstructed images of the thigh and femur using Antenna C and the Duke anatomical model. The hotspot indicates the location of the bone. The black dots indicate the true circumference of the bone as obtained from Sim4Life and the red dots indicate the location of the antennas. a) Reconstructed image obtained using delay-and-sum (DAS). b) Reconstructed image obtained using delay-multiply-and-sum (DMAS). c) Reconstructed image obtained using multiple signal classification (MUSIC). d) Reconstructed image obtained using Kirchhoff migration. The colour scale represents the normalised magnitude of scattering calculated using the imaging algorithms.

Reconstructed images of Ella-22 (Figure 5.7), Ella-26 (Figure 5.8) and Ella-30 (Figure 5.9) visually indicated the location of the bone when imaged using all four imaging algorithms. SMR and SCR values generally increased with BMI scores for each imaging algorithm with maximum SMR (DAS: 19.4456dB, DMAS: 24.6410dB, MUSIC: 7.1731dB, Kirchhoff: 5.14dB) and SCR (DAS: -3.7721dB, DMAS: -6.1790dB, MUSIC: -1.3928dB, Kirchhoff: -1.27dB) obtained for the Ella-30 model. Localisation errors for images reconstructed using confocal imaging (DAS and DMAS) reduced with higher BMI scores, with the smallest error obtained for the Ella-30 model (DMAS: 0.7647mm). However, localisation errors obtained using MUSIC and Kirchhoff migration increased with BMI scores (Table 5.3). Within each model, SMR was highest for images reconstructed using DMAS with highest SCR obtained using Kirchhoff migration for Ella-26 and Ella-30 models. While comparable localisation errors were obtained between the four algorithms for Ella-22, localisation errors obtained using the confocal imaging algorithms were lesser than those obtained using MUSIC or Kirchhoff migration for Ella-26 and Ella-30 models. Similarly, whilst images obtained using Antenna B and Antenna A visually indicated the location of the bone (Appendix B), SMR were highest for Antenna A when calculated using confocal imaging algorithms and highest for Antenna B when calculated using MUSIC and Kirchhoff migra-

tion (Appendix B). Localisation errors for Antenna B were generally higher than Antenna A and Antenna C. Analogous to Antenna C, localisation errors reduced for Antenna A and B with increased BMI scores when calculated using confocal imaging algorithms and increased with BMI scores when calculated using MUSIC and Kirchhoff migration (Appendix B).

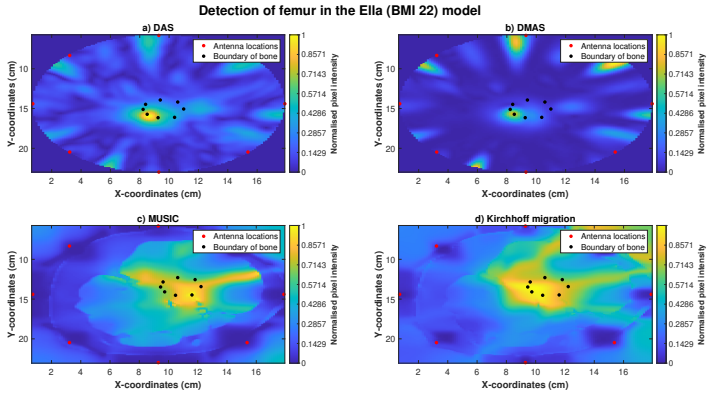

Figure 5.7: Reconstructed images of the thigh and femur using Antenna C and the Ella-22 anatomical model. The hotspot indicates the location of the bone. The black dots indicate the true circumference of the bone as obtained from Sim4Life and the red dots indicate the location of the antennas. a) Reconstructed image obtained using delay-and-sum (DAS). b) Reconstructed image obtained using delay-multiply-and-sum (DMAS). c) Reconstructed image obtained using multiple signal classification (MUSIC). d) Reconstructed image obtained using Kirchhoff migration. The colour scale represents the normalised magnitude of scattering calculated using the imaging algorithms.

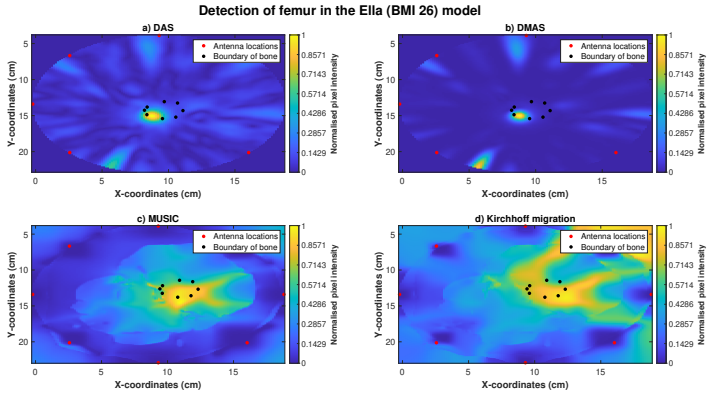

Figure 5.8: Reconstructed images of the thigh and femur using Antenna C and the Ella-26 anatomical model. The hotspot indicates the location of the bone. The black dots indicate the true circumference of the bone as obtained from Sim4Life and the red dots indicate the location of the antennas. a) Reconstructed image obtained using delay-and-sum (DAS). b) Reconstructed image obtained using delay-multiply-and-sum (DMAS). c) Reconstructed image obtained using multiple signal classification (MUSIC). d) Reconstructed image obtained using Kirchhoff migration. The colour scale represents the normalised magnitude of scattering calculated using the imaging algorithms.

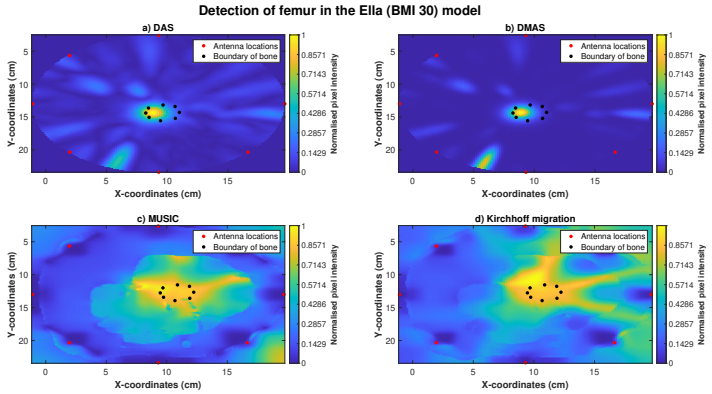

Figure 5.9: Reconstructed images of the thigh and femur using Antenna C and the Ella-30 anatomical model. The hotspot indicates the location of the bone. The black dots indicate the true circumference of the bone as obtained from Sim4Life and the red dots indicate the location of the antennas. a) Reconstructed image obtained using delay-and-sum (DAS). b) Reconstructed image obtained using delay-multiply-and-sum (DMAS). c) Reconstructed image obtained using multiple signal classification (MUSIC). d) Reconstructed image obtained using Kirchhoff migration. The colour scale represents the normalised magnitude of scattering calculated using the imaging algorithms.

Reconstructed images obtained using MUSIC and Kirchhoff migration methods for the Ella-22-posed (Figure 5.10) and the Ella-30-posed (Figure 5.11) models visually indicated the location of the bone. Localisation errors were within 2.5cm for both models using both the imaging algorithms, with SMR calculated using MUSIC greater than that calculated using Kirchhoff migration. Reconstructed images obtained using confocal imaging algorithms (DAS and DMAS) and Antenna C failed to identify the bone with images produced using Antenna B and any algorithm failing to to produce images of the bone.

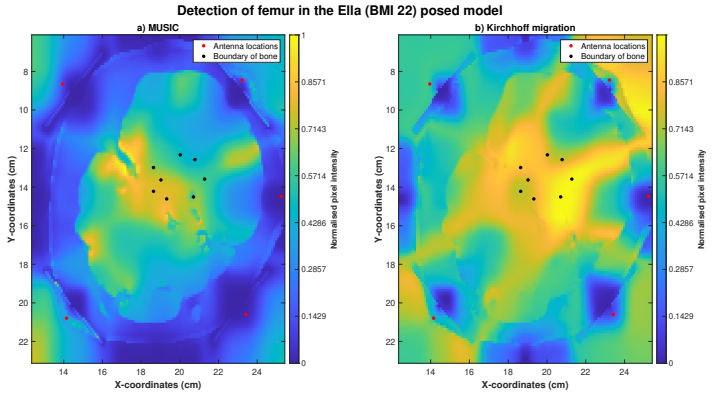

Figure 5.10: Reconstructed images of the thigh and femur using Antenna C and the Ella-22 anatomical model in a pose mimicking a phase of the gait cycle. The hotspot indicates the location of the bone. The black dots indicate the true circumference of the bone as obtained from Sim4Life and the red dots indicate the location of the antennas. a) Reconstructed image obtained using multiple signal classification (MUSIC). b) Reconstructed image obtained using Kirchhoff migration. The colour scale represents the normalised magnitude of scattering calculated using the imaging algorithms.

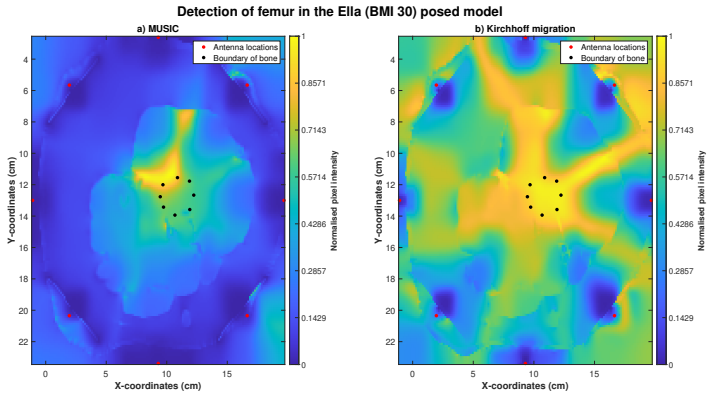

Figure 5.11: Reconstructed images of the thigh and femur using Antenna C and the Ella-30 anatomical model in a pose mimicking a phase of the gait cycle. The hotspot indicates the location of the bone. The black dots indicate the true circumference of the bone as obtained from Sim4Life and the red dots indicate the location of the antennas. a) Reconstructed image obtained using multiple signal classification (MUSIC). b) Reconstructed image obtained using Kirchhoff migration. The colour scale represents the normalised magnitude of scattering calculated using the imaging algorithms.

5.5 Discussion

The results of our study indicate the femur can be successfully detected from the skin surface — in both static and posed configurations— using microwave imaging, with data collected from a limited number of wearable antennas in the absence of coupling liquid. In addition to the above, the applicability and generalisability of our results are underscored by our detection of the femur in anatomical models of varying BMI scores and genders.

Various antennas have been proposed for microwave biomedical imaging applications, with a frequency range between 0.5-3GHz proposed for optimal penetration into the human body and for optimal image resolution. We investigated three *antenna types* operating in the above frequency range — a dipole antenna [12], a triangular patch antenna [110] and a wideband patch antenna [251] — in this study. The two patch antennas were originally designed to work when immersed in a coupling liquid and proposed for brain tumour detection. The dipole antenna was selected due to its availability with the software, Sim4Life, and due to its resonant frequency being within the optimised range. We parametrically altered the shapes of the two patch antennas — in order to apply them in the absence of coupling liquid and whilst making direct contact with the human body — to optimise coupling with the human body. Our results indicate that the three antennas resonated at different frequencies, with all frequencies being within the optimal range. Additionally, the three antennas had sufficient coupling with the slab of muscle as indicated by S11 $<$ -10dB. The three antennas were tested on four anatomical models, representing different sexes and people of different BMI scores.

Images were reconstructed using confocal imaging, DAS and DMAS, the MUSIC algorithm and the Kirchhoff migration algorithm. These imaging algorithms have predominantly been applied to detect the location of small scatterers such as tumours in the breast and brain [149, 206, 233] with very few studies investigating the application of these algorithms to detect extended scatterers like the bone (embedded in muscle) [187, 217]. Therefore, our successful application of the above algorithms to detect the bone, with data collected under specific conditions, underscore the novelty of our investigation and results.

For all images reconstructed using confocal imaging algorithms, we observed maximum localisation errors of less than 2cm, with both SMR and SCR showing the presence of a scatterer (femur is considered a scatterer in muscle due to the difference in electric properties between muscle and bone). The localisation error was in a similar range to those obtained for tumour detection [206, 234], and bone imaging studies applying different imaging algorithms [217]. Additionally, similar to other studies comparing DAS and DMAS confocal imaging algorithms,

we obtained less artefacts and smaller localisation errors with DMAS compared with DAS. Contrary to our initial assumption, localisation errors reduced with BMI scores, with the smallest localisation obtained for the Ella-30 model. We hypothesise that this may be attributed to a closer match between the calculated velocity (to time-shift the signal) to that of the actual velocity, as the permittivity of muscle is used to determine the velocity and the Ella-30 model has a higher proportion of muscle (by volume) compared with other models.

We also observed that the reconstructed images, obtained using confocal imaging algorithms, are not able to accurately represent the shape and size of the underlying bone, with the reconstructed bone shown at the muscle-bone interface. We hypothesise that this is a limitation of confocal imaging, which uses a simplified calculation of speed to time-shift the signal, thereby it only focuses on the location of maximum scattering, which is ideal for small scatterers (such as tumours) but not for extended scatterers (such as bones). Despite this, the location of the scatterer is within 2cm of the actual bone centre, which is sufficient for the projection of markers.

Results obtained from MUSIC were not only able to successfully determine the location of the femur from the skin surface in all anatomical models, but were also able to obtain the general shape and size of the bone. Similar to confocal imaging algorithms, MUSIC has predominantly been applied for imaging small scatterers [218, 219]. However, Ruvio [217] leveraged a variation of MUSIC (interferometeric MUSIC) to qualitatively image the bone. Specifically, they immersed a pig shank (with muscle, fat and bone layers) in a coupling liquid alongside the antennas, and reconstructed images at each frequency were multiplied with each other to reduce image artefacts. The authors reported reconstruction errors (localisation errors) of 2.78cm and 4.23cm, with no SMR or SCR values reported.

In our investigation, we leveraged a variation of MUSIC (wideband MUSIC) wherein images reconstructed at each frequency were summed together to reduce image artefacts. We obtained a maximum localisation error of 2.85cm across the four anatomical models, with both SMR and SCR values indicating the presence of a scatterer. We observed increases in SMR values with BMI scores, similar to the trend observed in confocal imaging algorithms. However, localisation errors also increased with BMI scores, in contrary to confocal imaging algorithms. Higher SMR values with higher BMI scores may be attributed to a lower mean scattering value in regions outside the object of interest (the bone) due to an increase in volume of the region outside the bone. However, the increase in localisation error with BMI scores when using MUSIC may be due to the decrease in the magnitude of electric field values — a key component of the MUSIC algorithm — inside the body with higher BMI scores, as there would be greater losses with higher volumes of soft tissues.

Similar results were obtained using Kirchhoff migration, with both the location and the shape and size of the bone successfully reconstructed in all anatomical models. Kirchhoff migration has been applied as an alternative imaging algorithm to MUSIC, with results indicating that Kirchhoff migration is a fast, stable and effective imaging technique for detecting both large and small scatterers [144], although its efficacy does reduce for large scatterers. As applied above, Kirchhoff migration, has not previously been investigated for bone imaging.

Our results indicate that Kirchhoff migration produces images with smaller reconstruction errors than MUSIC and comparable reconstruction errors to confocal imaging, whilst also reconstructing the shape and size of the bone. Similar to MUSIC, localisation errors increased with BMI scores. However, SMR values were comparable across BMI scores. This difference could be attributed to the difference in algorithms between MUSIC and Kirchhoff migration, wherein MUSIC detects a scatterer based on projection of the scattering matrix onto the noise subspace, whilst Kirchhoff migration utilises the entire scattering matrix to determine the location of the scatterer.

Our results indicate that microwave imaging was able to detect the location of the bone from the skin surface in models mimicking a phase of the gait cycle. Validating the efficacy of microwave imaging in posed models was critical to evaluate the feasibility of microwave imaging for biomechanical applications. This is because, as soft tissue deforms during motion, the distance of the bone from the skin surface in a posed state would be different to that obtained at static poses. Therefore, we also tested microwave imaging on the posed Ella-22 and Ella-30 models, as different magnitudes of soft tissue deformations were obtained from the two models for the same pose, due to their differences in soft tissue volume. The reconstructed images obtained using both MUSIC and Kirchhoff migration clearly indicate the location of the bone, with localisation errors obtained using MUSIC and Kirchhoff migration less than 2.8cm. Neither of the confocal imaging algorithms, DAS or DMAS, were able to successfully reconstruct the bone, with their reconstructed images showing a number of artefacts. Whilst we cannot say for sure, we hypothesise that the efficacy of confocal imaging algorithms may be affected by the computed imaging domain, with the angled imaging domain obtained in posed models potentially affecting the back-scattering ability of confocal imaging algorithms.

Whilst the results discussed above were primarily of those obtained using Antenna C, reconstructed images obtained using Antenna A and Antenna B also visually indicated the location of the femur within the thigh (Appendix B). In general SMR values for Antenna A were higher than Antenna B and Antenna C for all anatomical models and for all imaging algorithms; notable exceptions were for images reconstructed using MUSIC and Kirchhoff migration for Ella-26 and

Ella-30 models wherein Antenna B had the highest SMR value. For images reconstructed using confocal imaging algorithms, Antenna B had the smallest SCR values, with no specific trend observed for images reconstructed using MUSIC and Kirchhoff migration. Similar to Antenna C, localisation errors for Antenna A and Antenna B reduced with increasing BMI scores when computed using confocal imaging algorithms and increased with BMI scores when computed using MUSIC and Kirchhoff migration, with localisation errors obtained using Antenna B generally higher than Antenna A and Antenna C. This may be attributed to the decrease in electric field penetration obtained from Antenna B due to its higher frequency of operation, resulting in greater scattering at the boundary of muscle and fat rather than muscle and bone. Lesser penetration of electric field may also attribute to increased power losses thereby reducing the magnitude of scattered signals picked up at diametrically opposite antennas. With images reconstructed using transmission parameters (S21 parameters), factors affecting S21 parameters would affect the reconstructed image. The reduction in electric field penetration could also be the reason why reconstructed images obtained using Antenna B failed to successfully indicate the location of the bone for the posed models using any of the imaging algorithms. Simulations using Antenna A and the posed models could not be performed due to high computational demands.

In Chapter 3 we highlighted the reduction in efficacy of the most widely used method to reduce STA, MKO methods, when applied to data with high magnitudes of STA or to data obtained from subjects with high BMI scores. In Chapter 4, we proposed a generalisable solution wherein markers were projected onto the bone surface. Our results highlighted the potential clinical suitability and generalisability of our proposed solution. Combining the results from the previous chapter and this chapter, we have proposed a safe and cost-effective method to reduce joint angle errors — specifically on hip joint angles most affected by STA — which may have clinical applications. A potential prototype of our system would incorporate a circular ring of wearable antennas[139] placed around the thigh with reflective markers (or cluster of markers) attached on the ring. The absolute position of the ring would be provided by the optoelectronic system, with the distance of the bone from the ring computed using microwave imaging. This would enable the projection of the cluster of markers onto the bone surface to reduce the effects of STA. In the next chapter, we will expand our investigation of microwave imaging to experimental validation.

5.6 Conclusion, technical novelty and take-away messages

In conclusion, our results have indicated that microwave imaging can be successfully applied in biomechanical applications, specifically to determine the location of the bone from the skin surface. Our results were obtained under specific conditions to evaluate the feasibility of microwave imaging: lesser number of antennas and no coupling liquid. The conditions are pertinent for the development of a wearable system, which is crucial for both the reduction of STA. In summary we have shown that:

- Microwave imaging can be leveraged to locate the bone from skin surface using wearable antennas. This is crucial for projecting skin-mounted markers onto the bone surface to reduce the effects of STA
- Images were reconstructed under very stringent conditions underscoring the viability of microwave imaging. The conditions were: lesser number of antennas and no coupling liquid
- The femur was successfully located in anatomical models emulating different BMI scores and in poses mimicking standing and a phase of the gait cycle

The novelty of our results are:

1. We were able to detect the femur for different ViP models mimicking various BMI scores in both a standing pose and a pose mimicking a phase of the gait cycle
2. The scattering data were collected under stringent conditions: No coupling liquid and 8 antennas
3. The localisation error was less than 2cm in all locations
4. We believe this was the first study which applied the four investigated qualitative imaging algorithms (DAS, DMAS, MUSIC and Kirchhoff Migration) to detect the location of the bone (a large scatterer)

The results of this chapter have been published in Scientific Reports [203], with the two initial studies published in international conferences [200, 204].

The limitations of our study were primarily in the metrics utilised: SMR, SCR and localisation error. These metrics were predominantly created for small scatterers, such as breast tumours, which have a higher permittivity than the surrounding medium. Whereas, in our investigation, the object of interest (the

bone) is an extended target and is of a lower permittivity to that of the background medium. Additionally, the imaging domain is made of heterogeneous layers — skin, fat,muscle and bone — resulting in scattering at various boundaries. The above reasons may have contributed to the negative SCR values and varying SMR values. Whilst positive SCR scores have been used as an indicator of tumours in breast imaging studies, Reimer [208] reported negative SCR values for heterogeneous and denser breasts. Similarly, localisation error has predominantly been applied for small scatterers. Localisation error is calculated as the distance between the location of the maximum intensity in the image to that of the expected location of the scatterer. Therefore, localisation errors can be affected by: large hotspots, wherein the maximum intensity may not be at the centre of the hotspot or the maximum intensity may be obtained at a different hotspot than that of the object of interest.

Another limitation in our microwave imaging investigation is the spread of the high-intensity region in the reconstructed images. The spread of hotspots in the reconstructed images obtained using MUSIC and Kirchhoff migration may also be attributed to scattering obtained at multiple interfaces. Additionally, hotspots at locations different to that of the bone may be caused by scattering at fat/muscle interfaces, or by scattering from muscle/blood vessel interfaces. These interfaces are more pronounced in images reconstructed using MUSIC and Kirchhoff migration than images obtained using confocal imaging algorithms, as confocal imaging algorithms do not leverage electric field values to generate images. To visually verify if the reconstructed hotspots represented the bone, images were reconstructed for simulations where the bone was attributed with electric properties of the muscle, thereby removing the presence of the bone. This was also recommended by Reimer [209] to determine locations of hotspot-artefacts, which are high-intensity regions created at areas where there are no scatterers. Images in the supplementary data (Appendix B) indicate reconstructions of both healthy scan data and data with the bone present. Whilst healthy scan reconstructions using Kirchhoff migration and confocal imaging algorithms are empty due to the nature of the algorithms, healthy scan images reconstructed using MUSIC indicate scattering by fat/muscle interfaces and muscle/blood vessel interfaces.

Therefore, despite the above limitations of applying metrics designed for detecting small scatterers to applications with extended scatterers, we have shown that microwave imaging can be applied in biomechanical applications, specifically to locate the location of the bone from the skin surface.

Chapter 6

Investigating the feasibility of applying microwave imaging in biomechanical applications: Experimental

6.1 Introduction

In the previous chapter (Chapter 5) we determined the feasibility of applying microwave imaging in clinical gait analysis; in this chapter we expand our investigation to experimental verification. The study carried out in this chapter aims to expand and complement the simulation results obtained in the previous chapter (Chapter 5). Section 6.2 provides the background for this chapter with the methodology for the development of on-body antennas and tissue-mimicking phantom detailed in Section 6.3. Results of the study are presented in Section 6.4 with the results discussed in Section 6.5. Section 6.6 concludes this chapter with the key-takeaways from this study.

6.2 Background

Results from the previous chapter (Chapter 5) indicated that microwave imaging can be applied to determine the location of the bone from the skin surface using wearable antennas, to enable the projection of skin-mounted markers onto the bone surface, which we have shown aids in reducing joint angle errors (Refer to Chapter 4). The scattering data for generating the images were obtained without the use of coupling liquid and through the use of a limited number of antennas (8

antennas). In addition, the bone was successfully located in the reconstructed images of anatomical models mimicking humans of varying body mass index (BMI) scores and was also detected in models emulating a static pose and a pose mimicking a phase of the gait cycle. The results underscored the viability of leveraging microwave imaging in gait analysis, specifically to determine the position of the bone from the skin surface.

The primary aim of detecting the location of the bone from the skin surface is to project markers onto the bone surface, to reduce the deleterious effect of soft tissue artefacts (STA, refer to Chapter 4) on computed kinematics. Our investigation described in Chapter 4 indicated that our proposed marker projection schemes — wherein a cluster of markers is projected onto the bone surface — reduces joint angle errors significantly, specifically in joint angles (internal/external hip rotation) which are leveraged in surgical planning for children with CP [186, 260] and which are most affected by STA (Refer to Chapter 2).

As previously reviewed, various imaging modalities can be applied to determine the distance of the bone from the skin-surface. Amongst the imaging modalities, two notable studies have proposed incorporating ultrasound imaging — a non-ionising and cost-effective imaging modality compared to MRI, CT and fluoroscopy — to determine the location of the bone and hence compensate for STA [129, 130, 160, 161].

However, in order to overcome the drawbacks of ultrasound imaging, specifically in gait analysis — the need for a probe to be held at the location to be imaged, the need for coupling liquid to improve resolution and the differences in gait caused by the weight of the probe and associated cables [77, 171] — we proposed leveraging microwave imaging, also a safe (non-ionising), low power (negligible heating effects) and cost-effective imaging modality [67].

Our results from the previous chapter (Chapter 5) indicated the viability of applying microwave imaging in clinical gait analysis, wherein the femur was detected on simulated, dielectrically accurate human models of varying body mass index (BMI) scores. The data was collected under conditions aimed to emulate a wearable system: limited number of antennas and antennas making direct contact with the skin (no coupling liquid).

In this chapter we aim to expand our investigation to experimental phantoms, wherein the goal is to detect a bone mimicking phantom by applying microwave imaging to data collected without coupling liquid and through the use of a limited number of antenna/scanning positions.

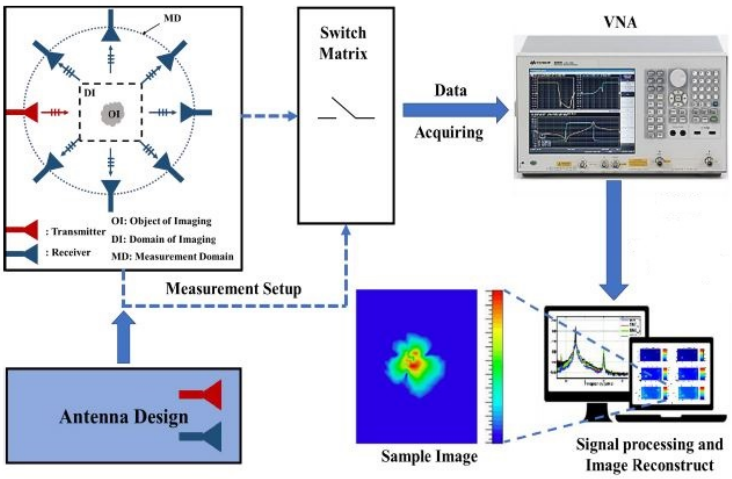

Figure 6.1: The general setup of microwave imaging systems, which consist of an imaging domain, an array of antennas, a vector network analyser and a radio-frequency switch [126].

6.3 Methods

6.3.1 Antenna development

The antennas developed for this study were based on the dual-patch antiphase antennas, proposed to work in the absence of any coupling medium whilst making direct contact with the skin [156]. The original design of the antennas incorporated a balun (180° phase and power splitter) with probe feeds placed on the opposite and far-side of the patches, to increase the penetration of the electric field into the human body. However, the balun leveraged in the initial [156] study (ZFSCJ-2-232-S+, Mini-circuits [4]) did not allow for the development of a wearable device, with the baluns and matching circuit connected via cables (Figure 6.2 a). Therefore, the following changes were made to the antenna proposed in the initial study [156] to tailor it for our investigation:

- The incorporation of a surface mount (SMT) balun (SYPJ-2-222+, Mini-circuits [5]) to allow for the development of a wearable antenna
- The use of varying patch and substrate sizes to develop three antennas operating at different frequency ranges

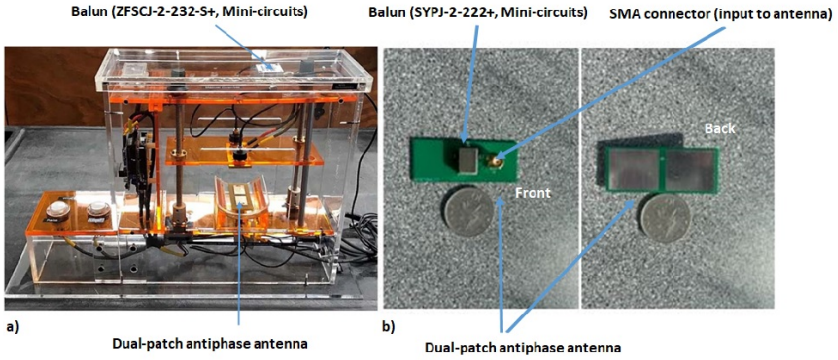

Figure 6.2: Comparison of antenna proposed by Makarov [156] and our antenna. a) The dual patch antiphase antenna proposed by Makarov [156] where the balun is connected by cables. b) Front and back sides of our modified dual patch antiphase antenna with a surface mount balun and SMA connector. SMA: SubMiniature Version A

The antenna structure (printed circuit board [PCB], land design and traces on the antenna) were re-developed to incorporate an SMT balun. Probe fields were placed on the near-side (and opposite) of the patches to reduce power losses (Figure 6.2 b).

To investigate the effect of varying frequency ranges on reconstructed images, three dual-patch antiphase antennas operating at differing frequency ranges were developed. Three different resonant frequency ranges were chosen: < 0.750 GHz, 0.750 GHz – 1.2 GHz and > 1.5 GHz. These frequency ranges were chosen to optimise both, penetration into the human body and resolution of the reconstructed image [24, 105, 165]. Using our SMT antenna as the base, a parametric study was performed in Ansys High Frequency Simulation Software (HFSS) Electronics Desktop 2023R2 [15], where the substrate height and patch sizes were altered to maximise antenna efficiency (S11 and S21 parameters) at the requested centre frequency. A high fidelity model of the antennas (including the traces, matching circuits, SMA connector and balun) were developed in Ansys HFSS [15], with two antennas placed on either side of a cuboid (block) attributed with the dielectric properties of muscle (Figure 6.3). The conditions for determining the most efficient antenna design were:

- Increased coupling with the muscle block, identified through lower S11 (reflection) levels. The condition was set as 'S11 (in dB) $<$ -10dB'.
- Increased coupling with the antenna on the other side of the muscle block, therefore increasing penetration into the human body. This was identified through higher S21 (transmission) levels. The condition was set as 'S21 (in

dB) >= -30dB'. The second condition had a greater weight than the first condition.

The electrical properties of muscle were chosen for the cuboid as they are the largest tissue by volume at the thigh, and muscle has an absorbing and highly resistive nature to the flow of electrical field. The block was of a sufficiently large size to prevent S21 parameters from being affected by surface currents (length: 18 cm, breadth: 18 cm, height: 6 cm). The three developed antennas are henceforth referred to as the three antenna types.

Additionally, two antennas from each of the three developed antenna types were fabricated using commercially available materials for experimental validation.

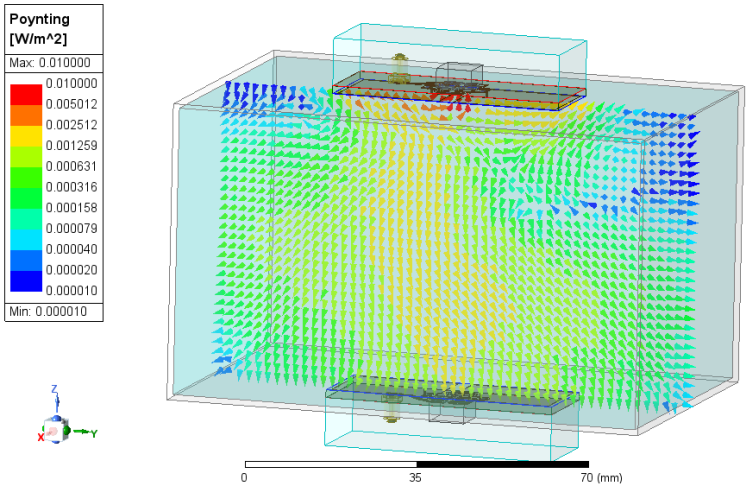

Figure 6.3: Setup for the parametric study to optimise antennas. The block is attributed with properties of muscle with the conditions of the study to determine the best parameters which optimise coupling and transmission through the block.

6.3.2 Experimental phantom development

A two layer phantom of muscle and bone was developed to experimentally validate the feasibility of applying microwave imaging to detect the location of the bone from the muscle surface. The two layer phantom was designed to represent the thigh of a human with an average BMI score where muscle makes up the largest proportion of tissue.

Cylindrical moulds were 3d printed in acrylonitrile butadiene styrene (ABS), to cast both the muscle and bone portions of the phantom. The bone and muscle were designed to have a radius of 2.25 cm and 6.25 cm respectively, with both having a height of 20 cm. The bone was fabricated using polyurethane impregnated with carbon black powder to provide the requisite permittivity and conductivity [23].

Isopropanol was added to the mixture to reduce the viscosity during the casting stage, aiding in the removal of large voids. The ratios are provided in Table 6.1.

Once the mixture had settled, the bone phantoms were removed from the ABS moulds and positioned in the moulds for the muscle. The muscle mixture was made from a mixture of ethanediol, deionised water, and salt held together with gelatine [214]. The mixture required heating to 60°C to ensure complete incorporation of the gelatine. The ratios of the materials used for the muscle layer are provided in Table 6.1. The muscle mixture was subsequently poured into the muscle mold (with the bone phantom placed in it) when the gelatine had been completely absorbed.

Tissue mimicking material	**Dimensions**		**Composition**
	Height (cm)	**Radius (cm)**	
Bone	20	2.25	Carbon black: 4% (specific volume) Polyurethane: 96% (specific volume) Isopropanol: 3mL/100g
Muscle	20	Inner radius = 2.25 Outer radius = 6.25	Ethanediol: 48% Water: 40% Salt: 2% Gelatine: 10%

Table 6.1: Dimensions and composition of leg phantom created to validate microwave imaging algorithms and the antennas

Three phantoms were created using the above steps with two phantoms containing a bone layer and one phantom containing just the muscle-mimicking layer.

A layer of skin-mimicking material was not added to the phantom due to the following reasons:

- Whilst the gelatinous nature of the muscle provided sufficient support for the placement of antennas, it did not provide support for a solid layer of skin to be added, as the weight of a skin layer is substantially higher than that of the antennas.
- Alternative recipes for skin-mimicking phantoms required a higher temperature, which would have resulted in the melting of the gelatinous layer.

The dielectric properties of the phantom materials were validated using the principle of resonant cavity perturbation (RCP) [213]. Specifically, the system contains a hollow metal cylinder, with holes in the top and bottom plates, which resonates at approximately 1 GHz, with a Q-factor of 3000, when empty. When a sample of dielectric material is inserted into the sensor (Figure 6.4), the resonant frequency and Q-factor reduce. This variation in resonant frequency and Q-factor is measured by a network analyser connected to the cavity, which determines the

complex permittivity of the sample. Detailed descriptions of the setup is provided in Appendix C.

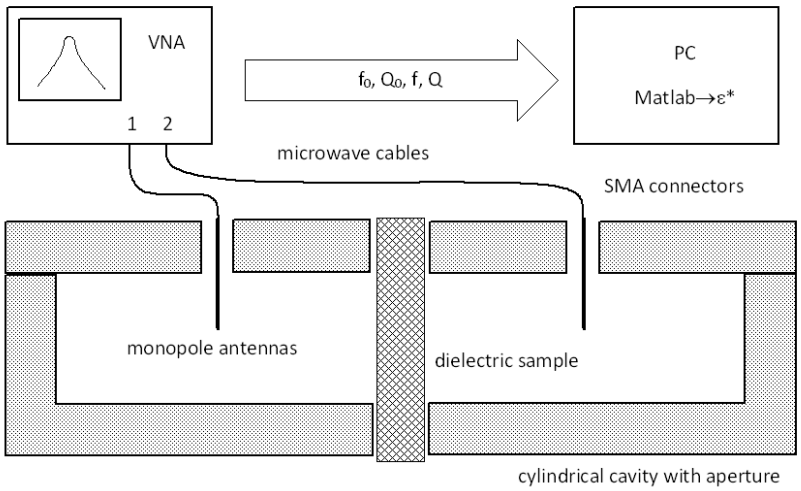

Figure 6.4: Schematic of the setup for the resonant cavity perturbation method for determining dielectric properties of tissue-mimicking materials [213].

6.3.3 Data collection: Simulation

Three simulated phantoms — of the same dimensions and materials as the experimental phantoms — were modelled in Ansys HFSS Electronics Desktop 2023R2 [15]. Two of the phantoms were modelled with bones, with the bone in one phantom (simulation phantom 1) placed almost at a diametrically opposite location to the bone in the other phantom (simulation phantom 2). The bones were modelled as cuboids — to differentiate from experimental phantoms — with a width of 2.5 cm and height of 20 cm. The third phantom (simulation phantom 3) only consisted of the muscle layer and was used to obtain the reference or empty scan data.

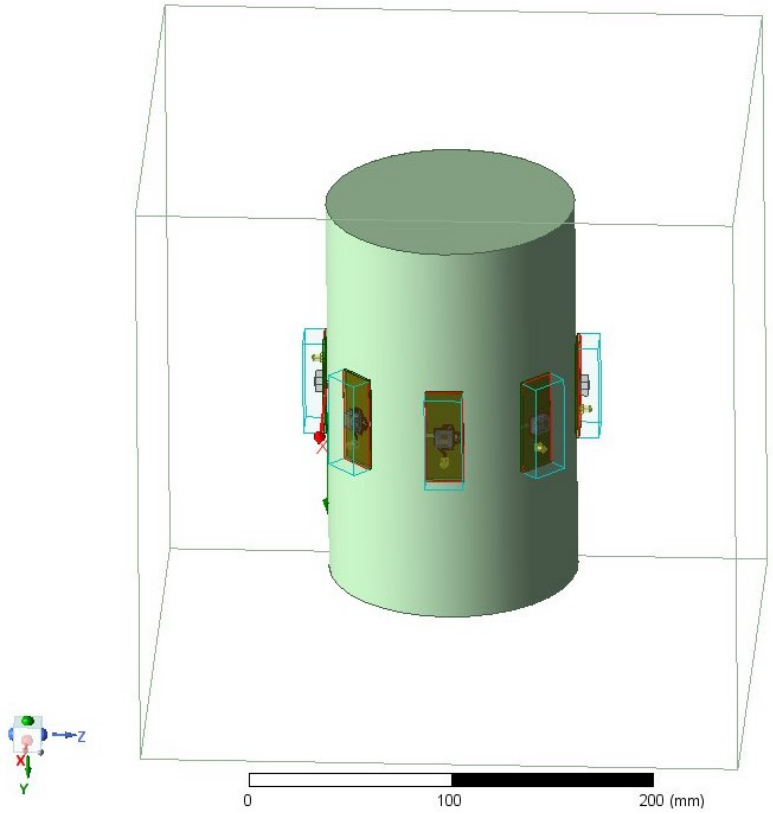

Figure 6.5: Simulation environment of simulated phantom 1, where the square bone is embedded in a cylindrical muscle and 8 antennas are placed around and in contact with the cylinder. Cylinder is of height 20 cm and radius 6.25 cm.

During simulation, 8 antennas (of a single antenna type) were placed equidistant on a circle around the phantom, with the dual-patches of the antennas in direct contact with the muscle layer (Figure 6.5). Three simulations were performed for each of the three antenna types using: simulation phantom 1, simulation phantom 2 and simulation phantom 3 (empty phantom).

For all simulations, the model (a phantom and eight antennas) was surrounded by a radiation boundary of appropriate size, to absorb the inward radiation incident on it. Additionally, all simulations were performed at the resonant frequency of the antenna with a maximum delta S value of 0.005, to ensure that both S21 and S11 parameters were accurate up to -60dB, with an additional interpolating sweep in the frequency range of $0.5 - 2.3$ GHz at steps of 0.01 GHz. The automatic adaptive mesh setting with lambda refinement was chosen for all simulations.

S-parameters (both reflection and transmission) were recorded in each simulation. Additionally, electric field values inside simulation phantom 3 were recorded for each antenna type. A grid of 5 mm spacing was used to record the electric field

values. The electric field was used in-lieu of the Green's functions for the imaging algorithms discussed below. Computation of Green's functions for inhomogenous background medium are computationally expensive, and whilst the phantom used in this study has only muscle-mimicking material, the phantom is supposed to represent the human thigh, which is inhomogenous.

To compare experimental and simulated models of the antennas, one antenna from each of the three antenna types was also simulated radiating into air and into muscle.

6.3.4 Data collection: Experimental

An antenna holder with eight slots was 3D printed to be placed around the experimental phantom to collect data. Two antennas of each type were fabricated. The data from the antennas were collected using a vector network analyser (VNA, 8714ES Hewlett Packard) with the VNA calibrated prior to data collection. S-parameters (S11 and S21) were collected in the frequency range of 0.5–2.3 GHz.

For each antenna type, the two fabricated antennas were slotted into the antenna holder placed around the phantom, and reflection (S11) and transmission (S21) parameters were recorded (Figure 6.6). One of the antennas was moved around the phantom (using the remaining slots) and 35 measurements were recorded for each type of antenna and for each phantom. At each instant only two slots had antennas in them with the other slots left unused. We assumed that the effect of the unused slots on the overall transmission parameters were minimal. Additionally, care was taken to not flex (bend) the coaxial cables during data collection, thereby reducing the effect of flexed cables on S21 parameters.

Overall, each type of antenna had three sets of data (experimental phantom 1, experimental phantom 2 and experimental phantom 3) with 35 measurements per set of data.

In addition, reflection parameters (S11) were recorded for each antenna type with the antenna radiating into air and when placed against the skin (radiating into the human body). This was done to compare simulated and fabricated models of the antenna.

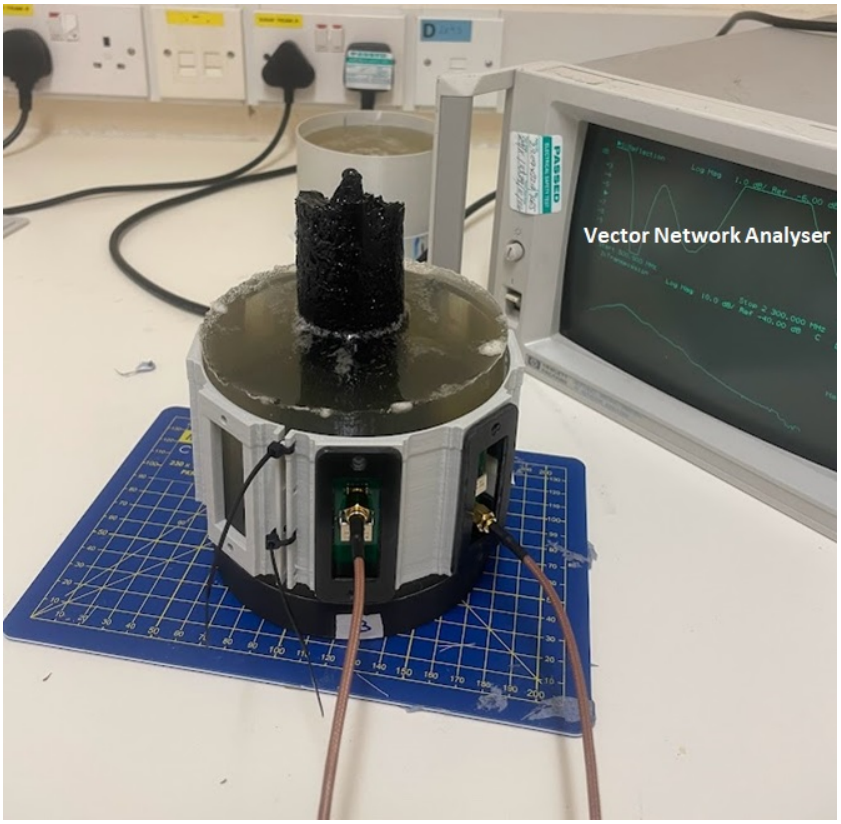

Figure 6.6: Data collection from the experimental phantom using the antenna holder. The antenna slot closest to the camera is the location for antenna 1 and the second antenna is rotated around the phantom

6.3.5 Imaging algorithms and metrics

Two qualitative imaging algorithms, the multiple signal classification algorithm (MUSIC) [82, 218] and the Kirchhoff migration algorithm [17, 238] were investigated. MUSIC is built on the principle of time-reversal and has been extensively applied in microwave imaging [190, 219]. In this study, the multi-frequency variant of MUSIC was leveraged to reconstruct images at each frequency and non-coherently sum them to produce the final image. This was done to reduce artefacts in the reconstructed image and build on additional information obtained at multiple frequencies [220]. In addition, electric field values inside the phantom — computed in the empty phantom simulations (simulation phantom 3) — were used in-lieu of the Green's function. Similarly, a multi-frequency variant of Kirchhoff migration was investigated in this study. Kirchhoff migration has also been widely applied in microwave imaging [17, 238] and has been reported to be a fast, stable and effective imaging technique for detecting small scatterers [144].

The multi-frequency variation of Kirchhoff migration reportedly produces better results than its single-frequency variations [188].

For both experimental and simulated S-parameters, data from a phantom containing a bone were subtracted from data recorded using the empty phantom, which were then fed to the imaging algorithm to reconstruct images and determine the location of the bone from the muscle surface. For all phantoms (both simulated and experimental), the electric fields recorded using the empty simulated phantom (simulation phantom 3) for each antenna type were used in lieu of the Green's function. For image reconstruction based on experimental data, two analyses were pursued: for experimental phantom 1 reconstruction, the difference in data collected from experimental phantom 1 and the simulation phantom 3 is leveraged; for experimental phantom 2 reconstruction, the difference in data collected from the experimental phantom 2 and experimental phantom 3 is used. This was to validate whether simulated empty scans can be used in-lieu of experimental empty scans. For both simulated and experimental phantom image reconstructions, only transmission data (S21) were leveraged. This was informed by both, studies leveraging transmission parameters collected from antennas diametrically opposite to the transmitting antenna [102, 103] to detect the object of interest, and from our initial investigation into microwave imaging [200].

Visual verification of the reconstructed images was initially done to determine if a hotspot (an indication of a scatterer) was present close to the true bone locations. In addition to visual verification, three metrics were used to evaluate the accuracy of the reconstructed image [208, 219]: Signal-to-cluster ratio (SCR), signal-to-mean ratio (SMR) and localisation error. SCR compares the maximum response within the object of interest to the maximum response in the region outside the object of interest, and SMR compares the maximum response within the object of interest to the average response outside the object of interest. Localisation error is the difference between the expected centre of the object of interest to that of the maximum response in the image. A higher SCR and SMR, typically > 0, indicates a high-contrast localised region within the image. However, negative SCR values have been reported for tumour imaging studies leveraging dense breasts [206]. For all the metrics, the object of interest was the bone (specifically, the femur).

6.4 Results

6.4.1 Antennas

Three antennas incorporating an SMT balun and operating at different frequencies were developed through the parametric study (Figure 6.7). Antenna 1 had the same overall size as the antenna model proposed in the original study [156], but

with a centre frequency at 0.653 GHz (whereas the antenna model proposed in the original study resonated at 0.9 GHz). Antenna 2 resonated at 0.85 GHz and had a smaller substrate thickness and smaller patch sizes compared with antenna 1. Antenna 3 resonated at 1.75 GHz and had the same substrate thickness as antenna 1 but with smaller patch sizes. The dimensions of the three antennas are provided in Table 6.2.

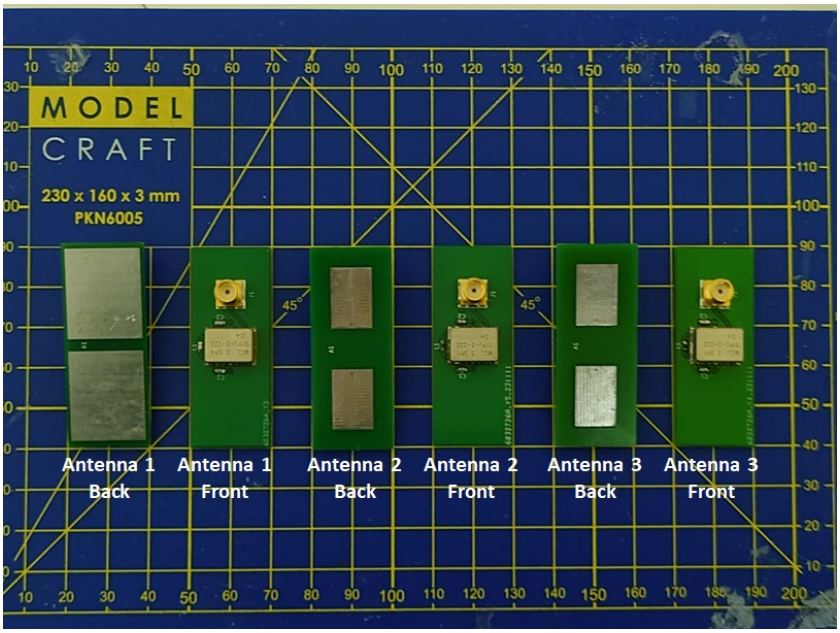

Figure 6.7: Three variations of antennas developed based on the dual-patch antiphase antenna proposed by [156]

Antenna	Length (mm)	Breadth (mm)	Height (mm)
Antenna 1	Board: 50 Patch: 22	Board: 20 Patch: 18	Board: 1.6
Antenna 2	Board: 50 Patch: 14	Board: 20 Patch: 10	Board: 1.2
Antenna 3	Board: 50 Patch: 14	Board: 20 Patch: 10	Board: 1.6

Table 6.2: Dimensions of the three variations of dual-patch antiphase antennas developed for this study

The three antennas were fabricated on commercially available FR-4 substrates

of varying thickness (Table 6.2). All antennas were fabricated with outer copper weight of 1oz. S11-parameters of the fabricated antennas closely matched the S11-parameters of the simulated antennas when radiating into air (Figure 6.8 a-c) and muscle (Figure 6.8 d-f).

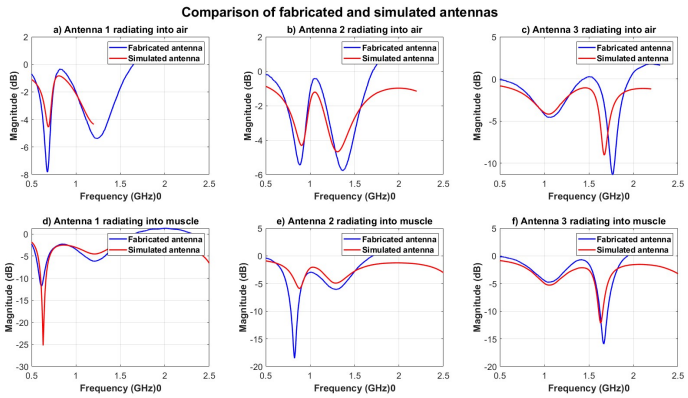

Figure 6.8: Comparisons of reflected parameters (S11) between simulated and fabricated antennas when antennas are radiating into air (a-c) and muscle (d-f)

6.4.2 Phantom properties

Three tissue-mimicking multi-layered bone phantoms were created (Figure 6.9), with two phantoms, experimental phantom 1 and experimental phantom 2, having the bone located at two different locations; the third phantom (experimental phantom 3) was made of just muscle-mimicking material, which was then used to obtain the reference or empty scan data. Phantom 1 had the bone located on the line connecting diametrically opposite antennas, antenna position 1 and antenna position 5, with the position slightly closer to antenna position 5 (Figure 6.9 a). Therefore, the bone was placed away from the centre position when viewed from antenna position 1. Phantom 2 had the bone located in the region spanned by antenna position 5 and antenna position 7. Therefore, the bone was located towards the left and away from the centre when viewed from antenna position 1 (Figure 6.9 b). Experimental data were collected using the antenna holder and two antennas of each antenna type (Figure 6.6).

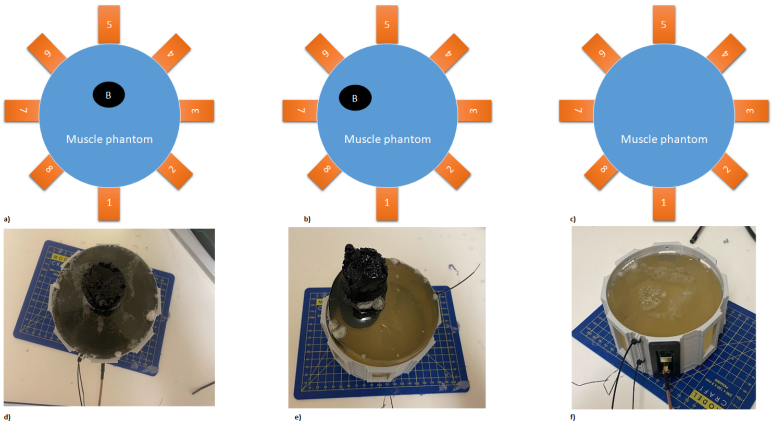

Figure 6.9: Schematic vs manufactured phantoms. a) Schematic of phantom 1. b) Schematic of phantom 2. c) Schematic of phantom 3. d) Manufactured phantom 1. e) Manufactured phantom 2. f) Manufactured phantom 3. The black circle in the schematic represents the location of the bone, the blue circle that of muscle and the orange rectangles the location of the antennas.

Cylindrical samples of length 40 mm and diameter 12 mm were created from the bone and muscle phantoms. These samples were used to determine the dielectric properties of each tissue-mimicking layer through the principle of RCP. The permittivity of the bone and muscle samples, in addition to theoretical values obtained from the IT'IS database [111] are provided in Table 6.3.

Tissue name	**Theoretical value at 1GHz**		**Experimental value at 1GHz**	
	Permittivity (F/m)	**Conductivity (S/m)**	**Permittivity (F/m)**	**Conductivity (S/m)**
Bone	12.4	0.2	12.5215	0.3414
Muscle	54	0.9	35	0.4

Table 6.3: Comparison of permittivity values between manufactured muscle and bone mimicking tissues and theoretical values at 1 GHz

6.4.3 Image reconstruction

Our results indicate that the bone was detected — in both simulated and experimental phantoms — for the three antenna types (antennas resonating at different frequencies) and for all investigated imaging algorithms. The presence of the bone (scatterer) was indicated by visual verification and through the three metrics: SMR, SCR and localisation error. Images could not be reconstructed for experimental phantom 2 using data collected from antenna 3, due to corruption of a subset of data. Subsequent data collection for experimental phantom 2 was impeded by shrinking of the phantom due to evaporation of water from mus-

cle tissue-mimicking layer. Additionally, the outcome of experimental phantoms could only be verified visually; metrics could not be computed as the true location of the bone in the phantom could not be computed.

6.4.3.1 Image reconstruction: simulated phantoms

Bones were visually detected in both of the simulated phantoms (simulation phantom 1 and simulation phantom 2) using all three antenna types and both the imaging algorithms (Figures 6.10-6.12 a-d). Metrics indicated that images reconstructed using antenna 3 detected the presence of the bone with higher fidelity and accuracy than antennas 1 and 2. SMR values were maximum for images reconstructed using antenna 3 for both the simulated phantoms and using both the algorithms (MUSIC: 13.3 dB, 11.92 dB; Kirchhoff migration: 16.35 dB, 14.62 dB) (Table 6.4) with images reconstructed using antenna 1 having the smallest SMR values (MUSIC: 7.27 dB, 7.04 dB; Kirchhoff migration: 8.86 dB, 8.57 dB). Within antenna SMR values for simulated phantom 1 were greater than for simulated phantom 2, for both the imaging algorithms and all the antenna types (Table 6.4). For images computed using MUSIC, localisation errors reduced from antenna 1 to antenna 3, with maximum localisation errors less than 2.4 cm. For images computed using Kirchhoff migration, comparable localisation errors were obtained for all antennas, with maximum localisation error less than 2.4 cm (Table 6.4). SCR values were between -1 and 1 dB for all reconstructed images.

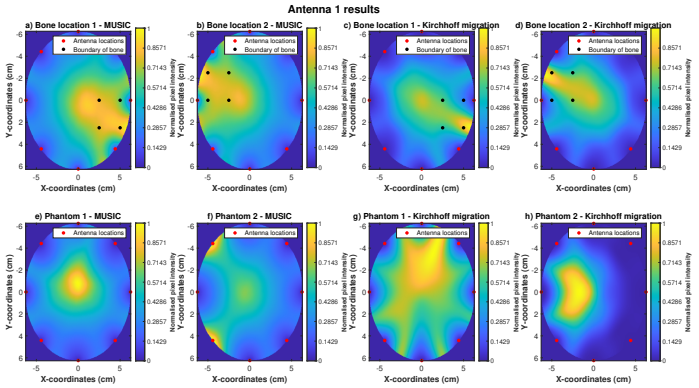

Figure 6.10: Reconstructed images of simulated and experimental phantoms using antenna 1. a) Reconstructed image of simulation phantom 1 computed using MUSIC. b) Reconstructed image of simulation phantom 2 computed using MUSIC. c) Reconstructed image of simulation phantom 1 computed using Kirchhoff migration. d) Reconstructed image of simulation phantom 2 computed using Kirchhoff migration. e) Reconstructed image of experimental phantom 1 computed using MUSIC. f) Reconstructed image of experimental phantom 2 computed using MUSIC. g) Reconstructed image of experimental phantom 1 computed using Kirchhoff migration. h) Reconstructed image of experimental phantom 2 computed using Kirchhoff migration. In all reconstructed images the red dots indicate antenna locations and the black dots indicate the location of the bone.

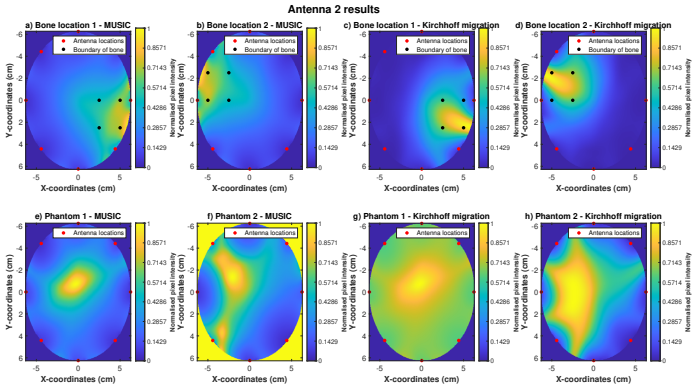

Figure 6.11: Reconstructed images of simulated and experimental phantoms using antenna 2. a) Reconstructed image of simulation phantom 1 computed using MUSIC. b) Reconstructed image of simulation phantom 2 computed using MUSIC. c) Reconstructed image of simulation phantom 1 computed using Kirchhoff migration. d) Reconstructed image of simulation phantom 2 computed using Kirchhoff migration. e) Reconstructed image of experimental phantom 1 computed using MUSIC. f) Reconstructed image of experimental phantom 2 computed using MUSIC. g) Reconstructed image of experimental phantom 1 computed using Kirchhoff migration. h) Reconstructed image of experimental phantom 2 computed using Kirchhoff migration. In all reconstructed images the red dots indicate antenna locations and the black dots indicate the location of the bone.

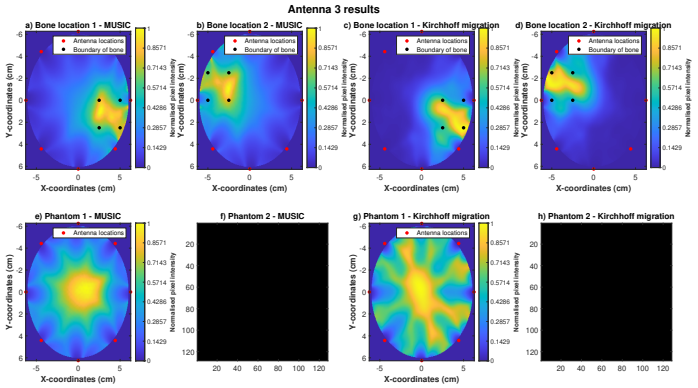

Figure 6.12: Reconstructed images of simulated and experimental phantoms using antenna 3. a) Reconstructed image of simulation phantom 1 computed using MUSIC. b) Reconstructed image of simulation phantom 2 computed using MUSIC. c) Reconstructed image of simulation phantom 1 computed using Kirchhoff migration. d) Reconstructed image of simulation phantom 2 computed using Kirchhoff migration. e) Reconstructed image of experimental phantom 1 computed using MUSIC. f) Reconstructed image of experimental phantom 2 computed using MUSIC. g) Reconstructed image of experimental phantom 1 computed using Kirchhoff migration. h) Reconstructed image of experimental phantom 2 computed using Kirchhoff migration. In all reconstructed images the red dots indicate antenna locations and the black dots indicate the location of the bone.

Phantom	**Algorithm**	**SMR (dB)**	**SCR (dB)**	**Localisation error (cm)**
Simulated phantom 1	MUSIC	7.27	-0.69	2.11
		11.12	0.14	1.45
		13.30	0.39	0.39
	Kirchoff	8.86	-0.89	2.30
		14.48	-0.2072	2.30
		16.35	-0.08	2.27
Simulated phantom 2	MUSIC	7.04	-0.31	2.11
		10.57	0.62	1.35
		11.92	0.27	0.53
	Kirchoff	8.57	-0.78	2.31
		13.0	0.01	2.28
		14.62	0.26	2.23

Table 6.4: Comparison of SMR, SCR and localisation errors between the three antenna types, using the two imaging algorithms for the two simulated phantoms. SCR, signal-to-cluster ratio; SMR, signal-to-mean ratio; MUSIC, multiple signal classification;

6.4.3.2 Image reconstruction: experimental phantoms

Bones were also visually located in reconstructed images of experimental phantoms. Through visual verification, our results indicated that reconstructed images using antenna 2 showed the location of the bone with higher accuracy than antenna 1 and 3. For antenna 1, images reconstructed using MUSIC indicated the location of the bone with greater clarity than images reconstructed using Kirchhoff migration (Figure 6.10 e-h). Specifically, reconstructed images of experimental phantom 1 using MUSIC accurately represented the location of the bone with images reconstructed using Kirchhoff migration indicated a spread and an offset. Reconstructed images of experimental phantom 2 using MUSIC and Kirchhoff migration represented the location to a high accuracy, with images reconstructed using MUSIC affected by scattering at the edge of the domain and images reconstructed using Kirchhoff migration again indicating spread and an offset (Figure 6.10 e-h).

Reconstructed images using data collected from antenna 2 (Figure 6.11 e-h) indicated that the bone could be successfully located in both experimental phantom 1 and experimental phantom 2 when MUSIC was leveraged with Kirchhoff migration representing the location of the bone to high accuracy for experimental phantom 1, and with lesser accuracy in experimental phantom 2.

Bones were again visually located in experimental phantom 1 (Figure 6.12 e-h) using data collected from antenna 3 and leveraging both MUSIC and Kirchhoff migration, with reconstructed images indicating that MUSIC produced lesser artefacts and spread compared to Kirchhoff migration.

6.5 Discussion

The primary aim of this investigation was to validate — experimentally and in simulation — the efficacy of applying microwave imaging in biomechanics, specifically to determine the location of the bone from the skin surface. The data were collected under specific conditions, with a limited number of antenna positions and no coupling liquid, to mimic a wearable system. Our results indicate that microwave imaging can be applied to determine the location of the bone from the muscle surface, with the bone located successfully in reconstructed images of both simulated and experimental phantoms.

Various antenna models have been proposed for microwave imaging applications, with the majority of the designs optimised to work when immersed in a coupling liquid [210, 217, 219]. However, the need to incorporate coupling liquid makes the development of a wearable system infeasible or not cost-effective and cumbersome. Novel antennas — incorporating metamaterials [121, 125, 127], custom-made materials [25] or unique designs [92, 156] — have been proposed to

alleviate the need for coupling liquid. For example, one suggestion which removed the need for a coupling liquid and provided direct contact with the imaged body was an ultra-wide band horn antenna incorporating a substrate of dielectric value equal to that of the average permittivity of the breast tissue [26]. However, the antenna was fabricated using expensive materials, thereby increasing the cost and reducing the cost-effectiveness of microwave imaging applications.

The novel on-body antenna design that was chosen as the baseline model in this study, was designed to work in the absence of any coupling liquid and maintain direct contact with the skin [156]. The proposed antenna model incorporated two patches, fed in antiphase through a balun, with the antennas fabricated using commercially available materials (FR-4) and established fabrication techniques, thereby making them a more cost-effective option. The antenna model was reported to radiate lesser power into the body than a typical cellphone (radiating 0.1 W into the wrist [156]) and had been applied to distinguish transmission (S21) parameters acquired from healthy and osteopenic bones. However, the components used in the antenna were not conducive with a wearable device.

In our study, we built on this baseline antenna model [156] to develop wearable antennas which have the same form factor as the initial design, but with all the components mounted on the antenna. This was accomplished by modifying the existing design to incorporate an SMT balun, thereby requiring a change in the overall design to reduce power loss. Additionally, we also developed three antennas operating at different frequencies to evaluate the effect of frequency on microwave imaging results. The development was done using a parametric study to optimise both coupling into a slab of muscle and penetration into the muscle. The developed antennas exhibited reasonable coupling and penetration, with the three antennas resonating at three different centre frequencies. The three antenna types were furthermore fabricated using commercially available materials, with all antennas being lightweight allowing for the development of a wearable device using 8 antennas. The experimental reflection (S11) parameters of the fabricated antennas showed a good match to the simulated S11 parameters when the antennas radiated in air and when the antennas were placed against a human body. Furthermore, the S11 parameters also indicated that the antennas were optimised to work when in direct contact with the human body.

The phantom developed in our study was a multi-layered solid bone phantom comprising of muscle and bone layers. The bone phantom was made of carbon black, graphite, urethane and isopropanol[23] with the muscle phantom made using mixtures of ethanediol, deionised water and gelatine[214]. The developed tissue-mimicking materials showed both a good match to theoretical values (specifically the bone), but more pertinently indicated a large enough contrast between bone and muscle layers, which is crucial for microwave imaging. The phantom also

indicated good mechanical stability during data collection, as it was able to support 2 antennas and the antenna holder.

Reconstructed images of both the simulated phantoms and the experimental phantoms indicated that the location of the bone could be identified. In simulated phantoms, antenna 3 was able to visually detect the location of the bone with higher accuracy than antennas 1 and 2. Notably, the images reconstructed using antenna 1 had a significant spread and the images reconstructed using antenna 2 only detected the edges of the bone closest to the muscle surface. This was also reflected in the SMR and localisation metrics, as the reconstructed images produced using antenna 3 had the highest SMR values and smallest localisation errors. The smallest SMR and SCR values were obtained for images reconstructed using antenna 1, which can be attributed to the hotspot artefact (a high-intensity region that does not correspond to any known locations of scatterers [209]) observed close to the center.

The poorer performance of antenna 1 can likely be attributed to the relationship between lower frequencies and loss in image resolution. Antenna 1 resonates at a frequency considerably lower than that of antenna 3 (0.63 GHz versus 1.65 GHz respectively) and hence would have proportionally poorer image resolution. The reason antenna 2 was only able to detect edges closest to the muscle surface, can likely be attributed to the antenna model. Despite the antenna resonating at a center frequency (0.8 GHz) which allows for both considerable improvements in resolution and penetration, the S11 parameters of simulated antenna 2 indicated that only 40% of the signal was being transmitted into the phantom. The improved performance of Antenna 3 can be attributed to a high image resolution obtained by its high resonant frequency and the considerable coupling achieved with the phantom: as indicated by its S11 and S12 parameters (Figure 6.8).

The variation in the results between simulation phantom 1 and simulation phantom 2 for each antenna type can be attributed to the difference in the location of the bone in the muscle phantom. The bone phantom was located closer to the surface in simulation phantom 1 compared to simulation phantom 2.

Our experimental results indicate that microwave imaging can be applied to locate the bone from the surface of the phantom. Visual verification — which is widely applied in microwave imaging applications [219, 253, 254] — indicates that the bone was successfully located in both the phantoms. In contrast to the simulation results, reconstructed images of experimental phantom 1 using antenna 3 indicated an offset with considerable spread of the high-intensity region (when reconstructed using both MUSIC and Kirchhoff migration). Whereas reconstructed images using both antennas 1 (leveraging MUSIC) and 2 indicated a very high accuracy in determining the location of the underlying bone in both the experimental phantoms.

Images of experimental phantom 1 were reconstructed using the difference between data collected using experimental phantom 1 and simulation phantom 3, whilst images of experimental phantom 2 were reconstructed using the difference between data collected using experimental phantom 1 and experimental phantom 3. Electric field values recorded inside simulation phantom 3 were used in-lieu of Green's function for reconstructed images of both experimental phantom. This may account for the differences in reconstructed images of the two experimental phantoms when using data collected from the same antenna. As our results indicate, the permittivity values of both experimental tissue-mimicking layers varies from their respective theoretical (simulated) counterparts. Therefore, Green's function computed using simulated phantoms may not match the Green's function of the experimental phantom. As reconstructed images are sensitive to the accuracy of the Green's function[16, 123, 124], this discrepancy may affect the reconstructed images of experimental phantoms.

The variation in antenna performance in reconstructed images of simulated and experimental phantoms can, in part, be attributed to the differences between fabricated and simulated antennas, coupled with the differences between simulated and experimental phantoms as discussed above. Our results show that fabricated antenna 2 had better coupling with human-tissue equivalent materials compared to simulated antenna 2. This could have affected the performance of simulated antenna 2. Antenna 3's poorer performance on experimental phantoms could be attributed to the differences in permittivity between simulated and experimental phantoms, thereby affecting its performance.

Notably, our results indicate that images can be successfully reconstructed using experimentally collected data with reference (empty scan) data obtained from simulations. Therefore, empty experimental phantoms do not need to be manufactured for most applications, thereby underscoring the applicability of microwave imaging in biomechanical applications.

Additionally, qualitative microwave imaging algorithms — MUSIC and Kirchhoff migration — were applied, to reduce computational demand and enable real-time processing. These two algorithms have primarily been applied to detect small scatterers[190, 219, 220]. Studies investigating the application of these algorithms (and similar variations like direct sampling method[124], orthogonality sampling method[133]) to extended scatterers (scatterers whose size is comparable to the wavelength of the wave in the surrounding medium) have reported varying efficacies[151, 190], with results indicating that the full shape of an extended scatterer may not be reconstructed[190] and that redesigning the imaging function may improve the reconstructed images[123]. In addition, whilst microwave imaging is primarily applied to detect scatterers with higher permittivity compared to their background medium, the bone has a lower permittivity compared to its

background medium (muscle) which has also been reported to affect the quality of reconstructed images[189]. Compounding these challenges, the data was obtained using a limited number of antennas which has been reported to reduce the sensitivity and accuracy of the reconstructed image[133].

The above factors may have had an effect on our reconstructed images. Our results obtained using MUSIC, particularly those from the experimental phantoms using antenna 3, indicated a spread of high-intensity area which represents multiple scattering inside the phantom instead of localising scattering at the boundary of bone and muscle. Similar results were obtained in studies investigating extended scatterers[190], who reported that whilst MUSIC can be successfully be applied to determine the location of the scatterer, its ability to determine shape is less effective for extended scatterers.

Our results obtained using Kirchhoff migration indicated that the quality of reconstructed images — assessed visually in terms of detecting the location of the bone — improved with higher frequencies, in both simulated and experimental phantoms. Whilst Kirchhoff migration has been noted as a fast, stable and effective imaging technique [144], it is more sensitive to model assumptions and noise compared with MUSIC. We hypothesise that this may explain our results obtained using Kirchhoff migration, as they exhibit a greater spread and offset when compared with images reconstructed using MUSIC. Despite the spread, the location of the bone was successfully determined from images reconstructed using Kirchhoff migration for all experimental phantoms.

This study has addressed the challenges posed by STA in gait analysis, as outlined in Chapter 2, through the development and validation of novel solutions detailed in Chapters 3 and 4. The implications of these findings for clinical practice are discussed in Chapter 5, highlighting the potential for improved diagnosis and treatment of gait disorders.In summary, Chapter 2 outlined the challenged posed by STA with Chapter 3 highlighting the reduction in efficacy of the most widely used method to reduce STA, MKO methods, when applied to data with high magnitudes of STA or to data obtained from subjects with high BMI scores. In Chapter 4, we proposed a generalisable solution wherein markers were projected onto the bone surface. Our results highlighted the potential clinical suitability and generalisability of our proposed solution. In Chapter 5 we investigated the suitability of leveraging microwave imaging to detect the location of the bone from the skin surface: to enable projection of markers (our solution in Chapter 4). Our results from simulated models indicated that microwave imaging can be applied in clinical gait analysis, with the femur detected in simulated models of varying BMI scores and in different poses. Combining the results from Chapter 4 and Chapter 5, a potential prototype of our system would incorporate a circular ring of wearable antennas[139] placed around the thigh with reflective markers (or

cluster of markers) attached on the ring. The absolute position of the ring would be provided by the optoelectronic system, with the distance of the bone from the ring computed using microwave imaging. In this Chapter, we expanded our investigation from simulation to experimental validation. Our results indicate that the bone was detected in tissue-mimicking phantoms using wearable antennas. The results from this study underscore the potential applicability of our proposed solution.

6.6 Conclusion, technical novelty and take-away messages

In conclusion, this study has validated — both experimentally and in simulation — the effectiveness of applying microwave imaging in gait analysis, specifically to determine the location of the bone from the skin (muscle) surface. The proposed solutions significantly enhance gait analysis accuracy, with promising implications for clinical applications.

The data collected in this study were taken under specific conditions — fewer number of antenna positions and no coupling liquid — to facilitate the development of a wearable system. In summary we have shown that:

- Microwave imaging can be leveraged to locate the bone from skin surface using wearable antennas in experimental phantoms. This is crucial for projecting skin-mounted markers onto the bone surface to reduce the effects of STA
- Development of antennas — optimised to be used in the absence of coupling liquid — is a crucial element for the successful implementation of microwave imaging
- Our novel multi-layered bone phantom represents the dielectric contrast found in an average human thigh - with large percentage of the thigh being muscle tissue
- Both, MUSIC and Kirchhoff migration, can be leveraged to detect the location of the bone. But images reconstructed using Kirchhoff migration may contain additional artefacts and an offset
- Reference scan data obtained from simulations may be used in-lieu of reference scan data obtained from phantoms not incorporating the object of interest. However, the simulations should incorporate high fidelity models of the experimental setup

The novelty of our results are:

1. We were able to detect the femur in experimental tissue-mimicking phantoms
2. The scattering data were collected under stringent conditions: no coupling liquid and lesser number of antennas
3. The bone was also detected in analysis using data collected from simulated empty phantom in-lieu of experimental empty phantom data. This highlights the generalisability of the approach.

The two key limitations of this investigation were the mismatch between theoretical[7] and experimental permittivity values of the muscle-mimicking layer, and the lack of true bone position in experimental phantoms which rendered the computation of imaging metrics for experimental phantoms infeasible. Two distinct recipes for tissue-mimicking phantoms were leveraged to develop the multi-layered phantom, with the muscle-mimicking layer having a large discrepancy in dielectric values compared to theoretical values[7]. Whilst the difference in dielectric values between bone and muscle were sufficient to image the bone, the above discrepancy could affect the reliability of the results. This may be alleviated in future investigations by leveraging multi-layered recipes proposed for the knee[245].

The second limitation, of not determining the exact location of the bone phantom in the muscle phantom, was an operational mistake which resulted in calculation of imaging metrics unfeasible. Whilst visual verification can be applied to detect the accuracy of reconstructed images, future work would ensure that the position is calculated to enable calculation of metrics.

An additional limitation of this study is that the metrics used for the detection of point-like scatterers were applied to extended scatters. The metrics leveraged were predominantly created for small scatterers, such as breast tumours, which have a higher permittivity than the surrounding medium. Whereas, in our investigation, the object of interest (the bone) is an extended target and is of a lower permittivity to that of the background medium. This may have attributed to the negative SCR and varying SMR values, with negative SCR values been reported for heterogeneous and denser breasts[208]. Additionally, localisation error which is calculated as the distance between the location of the maximum intensity in the image to that of the expected location of the scatterer, can be affected by large hotspots or hotspots not centered at the location of the bone thereby producing a large value.

We believe our results may be used to further research into the biomechanical application of microwave imaging; in particular, as an alternative to currently used imaging modalities such as ultrasound imaging.

Chapter 7

Conclusions and future work

7.1 Introduction

In this chapter we discuss the results and findings of all the investigations carried out in this thesis with the aim to provide a cohesive summary of the novelty and breadth of work carried out in this thesis. We also highlight key areas for future work which would enable further development of the key ideas proposed in this thesis for clinical application.

7.2 Discussion and conclusion

The worldwide incidence of cerebral palsy (CP) is 2-3 per 1000 livebirths [246], with intoeing gait one of the most common gait abnormalities in children with CP. The surgical treatment for intoeing gait is femoral derotation osteotomy.

Femoral derotation osteotomy can be carried out proximally, diaphyseally or distally [176], with success of the surgical intervention depending on pre-operative, intra-operative and post-operative factors. Criteria for performing the surgery varies [83, 186], with one proposed criteria suggesting passive internal rotation greater than 50° , external hip rotation less than 30° and at least 15° of internal hip rotation during the stance phase of gait.

The above joint angles are generally computed through clinical gait analysis, wherein markers mounted on the patient's skin are used to compute joint angles during walking. Whilst the marker-based optoelectronic systems can provide sub-millimeter accuracies in tracking of the markers, the clinical usability of the computed joint angles are affected by soft tissue artefacts (STA).

STA are discrepancies in bone movement computed using skin-mounted markers when compared with actual bone movement, and are primarily caused by the sliding, stretching and movement of active and passive soft tissues between the

skin-mounted markers and the underlying bone. STA are subject- and task-specific with a frequency similar to that of actual bone movement, rendering traditional filtering methods ineffective [58]. Kinematic errors due to STA can be in magnitude of 20° invalidating the clinical usability of skin-mounted marker based data [194]. For example, the recommendation of 15° was to account for inaccuracies in clinical gait analysis due to STA [228], with McGinley [163] reporting that the hip internal/external rotation angle had the most error in 3-D gait analysis, undermining pre-operative planning for femoral derotation osteotomies.

Various solutions have been proposed to reduce the impact of STA on computed kinematics: STA models, novel segment optimisation methods, novel pose estimators and novel multibody kinematic optimisation (MKO) methods. Amongst the numerous solutions proposed, MKO methods are the most widely applied solution to ameliorate the impact of STA and have been integrated in commercially available musculoskeletal modelling software [78, 81]. Despite their widespread adoption, MKO methods (and most proposed solutions) have two main limitations: no single solution has been found to be effective in reducing the impact of STA for all studied motions and participants; most of the proposed methods have been validated on participants with healthy body mass index (BMI) scores, despite evidence indicating a positive correlation between STA magnitude and BMI scores [54].

In this thesis we have proposed and investigated methods to reduce the impact of STA on computed kinematics during clinical gait analysis, with a focus on joint angles most affected by STA and which are leveraged in surgical planning for children with CP.

Firstly in Chapter 3, our initial study, we evaluated the efficacy of MKO methods when applied to data obtained from participants of varying BMI scores. This was to highlight the challenges posed by STA in gait analysis and the ineffectiveness of current methods applied in clinical gait analysis. Both of these challenges were highlighted through our literature review in Chapter 2.

Additionally, we also investigated the usability of residual error as a goodness of fit metric. Residual errors, or marker residual errors, have been widely used as a measure of kinematic accuracy with lower residual errors indicative of higher kinematic accuracy [137, 195]. However, studies have questioned the validity of residual errors as a goodness of fit metric.

We therefore investigated the impact of the MKO pipeline on residual errors and determined if there was a causal relationship between residual errors and joint angle errors. Through our study we aimed to: underscore the importance of testing proposed MKO methods on subjects of varying BMI scores; and determine whether residual errors can be used as a metric in the absence of artefact-free bone movement. Our results indicated that residual errors are significantly affected by

each step of the MKO pipeline, and an increase in residual errors is correlated with increases in joint angle errors when employing the same MKO pipeline. Additionally, we also reported that residual errors increase with BMI scores when MKO methods are applied to data with varying magnitudes of STA or data obtained from subjects of varying BMI scores, indicating that the efficacy of MKO methods reduces when applied to data obtained from participants with higher BMI scores. Through this study we underscored the importance of the investigations carried out in the thesis and the necessity of an STA solution which can be applied to a wide variety of participants.

With the results of our initial study (Chapter 3) underscoring the current lack of a generalisable solution to reduce STA in gait analysis, we proposed and evaluated two novel marker projection schemes to reduce the impact of STA in Chapter 4. Our proposed marker projection schemes were built on the projection scheme proposed by Begon [43], wherein we proposed projecting markers onto the bone surface rather than on a requested axis as proposed by Begon [43]. We hypothesised that our projection schemes would be able to overcome the limitations of the projection scheme proposed by Begon [43] and additionally leverage artefact-free bone movement to improve accuracy of computed kinematics. We leveraged a dataset — containing both skin-mounted markers and artefact-free bone movement acquired using fluoroscopy (which was used as reference) — to evaluate our marker projection schemes. Our results indicated that our proposed projection schemes not only significantly reduced kinematic errors in joint rotations most affected by STA, but also improved the quality of computed kinematics, as evidenced by a higher correlation with artefact-free bone movement when compared with kinematics computed using un-projected markers. Additionally, our results indicated that our proposed projection schemes performed better than the one proposed by Begon [43]. With the dataset covering a wide variety of subjects and motions, our findings also indicate that our proposed solution may be generalisable. The results of this chapter — wherein errors in joint angles used in surgical planning were reduced — highlighted the potential clinical usability of our proposed solutions.

With our proposed, novel projection of markers schemes indicating its capability to reduce errors due to STA, we further investigated a novel method to determine the location of the bone from the skin surface, to enable projecting the markers onto the bone surface. As the soft tissues deform during motion, the location of the bone from the skin surface would vary, thereby necessitating a wearable system. Whilst MRI, fluoroscopy and CT have been previously applied in biomechanics to visualise the movement of bones, they are not cost-effective nor do they offer a wide field of view, with fluoroscopy and CT exposing the subject to potentially harmful (ionising) radiation. Two studies have proposed ultrasound

imaging as an alternative imaging modality [129, 159] to reduce the effects of STA. However, incorporating ultrasound imaging in biomechanical applications have the following drawbacks: the need for a probe to be held at the location to be imaged, a radiologist's input when images are unclear, and the need for a coupling liquid. In addition, attaching an ultrasound probe to the body has found to alter the gait of children with CP due to the weight of the probe and holder [171]. To overcome these limitations we investigated another safe, cost-effective imaging modality: microwave imaging.

Microwave imaging has been widely applied in breast and brain tumour detection. Microwave imaging leverages the differences in electrical parameters (permittivity and conductivity) between various tissues and between healthy and pathological tissue to reconstruct images of the object of interest. Some applications of microwave imaging determine both the location and electric properties of the object of interest, with algorithms for such applications solving a nonlinear and ill-posed problem. These algorithms, quantitative or tomographic imaging algorithms, are computationally demanding and require significant *a priori* knowledge [16, 165, 167] of the object to be imaged, the background permittivity and conductivity and the value of the electric field at each point in the imaging domain at every iteration. Another class of algorithms, qualitative imaging algorithms, which work in real-time and are computationally less demanding, only locate the object of interest and do not determine the electrical properties of the object of interest. We investigated these algorithms as they are more suitable for biomechanical applications. However, these algorithms have only been applied to detect small scatterers and have not been applied to detect extended scatterers, like the bone embedded in muscle. Additionally, generic microwave imaging setups — for both classes of algorithms — are static and require both the antennas and the object to be imaged to be immersed in a coupling liquid. With these requirements, microwave imaging has not been applied in biomechanical applications to the best of our knowledge.

We investigated the suitability of applying microwave imaging in gait analysis in Chapter 5. The suitability was verified by collecting data under specific conditions, which we hypothesised would facilitate the development of a wearable system. The conditions were: limited number of antenna (antenna positions) and no coupling liquid. We performed two feasibility studies: a simulation study using dielectrically accurate anatomical models of varying BMI scores in both a standing pose and a pose mimicking a phase of the gait cycle; an experimental validation where we developed a novel multi-layered bone phantom containing muscle and bone layers to determine the location of the bone from the muscle surface. For both the studies we proposed novel antennas which were based on pre-existing designs but modified to work in the absence of coupling liquid and to optimise

propagation into the human body.

Results from our simulation study (Chapter 5) indicated that microwave imaging can be applied in gait analysis, with the reconstructed images visually indicating the location of the femur for all anatomical models, both in the standing pose and in a pose mimicking a phase of the gait cycle. The errors between the reconstructed bone and actual bone location were less than 3cm.

Based on the promising results of Chapter 5, in Chapter 6 we expanded our investigation of applying microwave imaging in gait analysis to experimental validation. We fabricated antennas and tissue-mimicking phantoms, with the phantoms consisting of a muscle-mimicking outer layer and a bone-mimicking inner cylinder. Through data collected using the same conditions as the previous chapter — limited number of antenna (antenna positions) and no coupling liquid — our results indicated that the bone phantom was detected in all tissue-mimicking phantoms. Additionally, the antennas had a small form-factor with all the required components mounted on the surface of the antenna, allowing for a wearable device, with the weight of the overall system similar to EMG sensors commonly applied in clinical gait analysis.

In conclusion, we proposed and investigated a method to reduce STA, which not only reduced kinematic errors in joint rotations most affected by STA, but also improved correlation with true bone movement. Our results, specifically the marker projection schemes, significantly reduce errors in computed internal/external hip rotation, with non-significant reductions in hip flexion/extension and hip adduction/abduction. In addition, the results were obtained for a wide variety of participants performing various tasks. The reduction in errors are in joint rotations used for pre-operative planning for femoral osteotomies, thereby potentially improving the clinical accuracy of optoelectronic data and improving the outcome of femoral osteotomies. This underscores the clinical usability of both our proposed marker projection schemes and the overall project.

We further complemented these findings by investigating an imaging modality, not previously applied in biomechanics, which would allow for determination of the bone location during motion. The imaging modality, microwave imaging, is cost-effective and safe, with our results from both simulation and experimental studies indicating that microwave imaging can be applied to detect the location of the bone from the skin surface for subjects of varying BMI scores and that it can be applied in a wearable fashion.

Combining the results from the thesis, we have proposed a safe and cost-effective method to reduce joint angle errors — specifically on hip joint angles most affected by STA — which may have the capacity to be applied clinically. A potential prototype of our system would incorporate a circular ring of wearable antennas[139] placed around the thigh with reflective markers (or cluster of mark-

ers) attached on the ring. The absolute position of the ring would be provided by the optoelectronic system, with the distance of the bone from the ring computed using microwave imaging. This would enable projection of the cluster of markers onto the bone surface to reduce the effects of STA.

7.3 Limitations and future directions

Whilst to the best of our knowledge, the investigations in this thesis are the first to combine biomechanics and microwave imaging, we have identified areas wherein future work would enable development and subsequent clinical implementation of the ideas proposed in this thesis.

In each chapter, we have provided limitations of the methodology we adopted and the assumptions we made. In this section, we shall expand on those limitations with a focus on how future work could complement our findings and further validate the effectiveness of our findings in solving issues in clinical gait analysis for a diverse population.

In Chapter 3 where we investigated the efficacy of MKO methods and suitability of residual marker errors as a metric, we leveraged a dataset containing experimental data collected from healthy participants of varying BMI scores in the lab, and a dataset containing simulated data wherein STA — modelled based on published STA models — were added to the skin-mounted markers. We believe that this investigation and our findings could be further enhanced by leveraging a dataset containing both skin-mounted marker data and artefact-free bone movement data from participants with a wide range of BMI scores. We believe findings from such a study would not only underscore our results but also highlight the deleterious effect of STA on clinical gait analysis and the effect higher BMI scores could have on solutions currently implemented in clinical gait analysis to reduce the effect of STA, specifically multibody kinematic optimisation methods.

Such a dataset would also aid the further validation of our marker projection schemes proposed in Chapter 4. Our current results highlight the benefit our marker projection schemes may have on clinical applications such as surgical planning for intoeing gait in children with CP. Validation of the proposed marker projection schemes in locations other than the femur, and for a greater range of motions and participant characteristics, may highlight other clinical benefits. We therefore believe the development of such a database would benefit the field of biomechanics, specifically clinical gait analysis.

In chapters 5 and 6, we investigated microwave imaging as a potential alternative to ultrasound imaging. This was primarily to overcome the limitations of attaching ultrasound probes to the subject, and to investigate a new imaging modality with prior applications in breast and brain tumour imaging.

Our investigation into the feasibly of applying microwave imaging in clinical gait analysis was limited by several factors, not excluding time-constraints on software and availability of ViP models, financial constraints limiting phantom development, and equipment constraints limiting what investigations could be carried out. Therefore, we believe the future work listed below could help take the research forward and validate the effectiveness of applying microwave imaging in clinical gait analysis.

In Chapter 5:

1. Investigating the feasibility of detecting the bone on different ViP models and in poses mimicking the entire gait cycle

2. Analysing different antenna models such as antennas with coupling liquid integrated into the design [109, 215]. Further investigation using antennas developed for wearable applications such as those proposed for breast monitoring [196], may further aid the research

3. In our study, qualitative microwave imaging algorithms were investigated as they were deemed the most suitable due to their applicability in real-time, no need for *a priori* information and their less computationally demanding nature. However, investigating different qualitative algorithms, time-domain algorithms [197], quantitative algorithms and machine learning may complement our findings

In chapter 6:

1. Investigating the feasibility of imaging the bone using advanced phantoms [245] would aid the research

2. Similarly to chapter 5, a comprehensive study using alternative antenna designs may help identify ones which are optimal for application in clinical gait analysis

3. Whilst the antenna developed in this thesis allowed for the development of a wearable system, data were collected from a table-based vector network analyser (VNA). We believe incorporation of portable VNAS and antennas would allow for the further development and evaluation of a wearable device

Lastly, whilst we investigated microwave imaging as an alternative imaging modality to ultrasound imaging, studies incorporating both ultrasound imaging and microwave imaging have reported results with greater accuracy and with the potential to image deep tissues [165, 168]. For example, a study has highlighted the benefits of leveraging structural information acquired from ultrasound imaging

with electromagnetic information acquired from microwave imaging to image fine structural details[183]. This hybrid imaging modality may also be further explored to aid subject-specific modelling for clinical gait analysis and provide not only the location of the bone during motion but also the electrical properties of the bones which maybe used for osteoporosis detection.

In conclusion, we believe our investigations have laid the foundations of a solution which may be applied clinically to reduce the effect of STA and improve the accuracy of clinical gait analysis. Specifically, our solution improves the quality and reduces errors of joint angles which are used for pre-operative planning of intoeing gait but which are also most affected by STA. Therefore, our solution could potentially improve the clinical usability of the joint angles computed from clinical gait analysis. However, further work based on the key areas listed above would allow for further validation of the effectiveness of our proposed solution in diverse populations and in real-world settings.

Appendices

Appendix A

Supplementary figures from chapter 3

A.1 Impact of MKO pipeline on residual errors

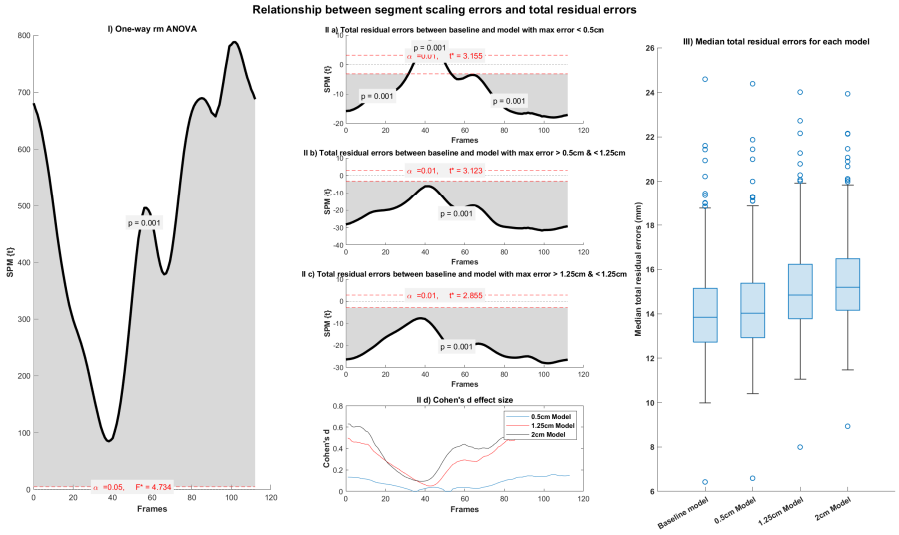

Appendix Figure A.1: How to read SPM figures: The red lines (upper and lower for t-tests) indicate the critical threshold set at the respective alpha values (0.05 for ANOVA and 0.01 for post-hoc analyses). For ANOVA tests, if the critical f-statistic field vector (the thick black line) is above the critical threshold, the independent variables have a significant effect on the dependent variables. For paired t-tests if the t-statistic field vector (the thick black line) is either below or above the critical thresholds , the null hypothesis of equal means is rejected for those frames. The t-values are differences between the mean of the two sample sets and the variation that exists within the sample sets. For post-hoc analyses, if the t-statistic field vector is above the upper critical threshold, then (meanA>meanB) and vice versa if it is below the lower critical threshold. For all the post-hoc analyses, meanA was the mean of the baseline model and meanB the mean of the error incorporated model.
I) Results of a nonparametric one-way ANOVA analysis between total residual errors acquired using the baseline model and three models with segment scaling errors. The shaded area indicates scaling errors have a significant effect on total residual errors (p=0.001). II) (a–c) Results of the post-hoc analyses using paired t-tests in SPM between total residual errors acquired using the baseline model and each of the models with segment scaling errors. The shaded area shows a significant difference (p=0.001) in total residual errors with models with segment scaling errors having statistically greater total residual errors. d) Cohen's d effect sizes between baseline model and three models with segment scaling errors. III) The box plot shows the median total residual error between the four models.

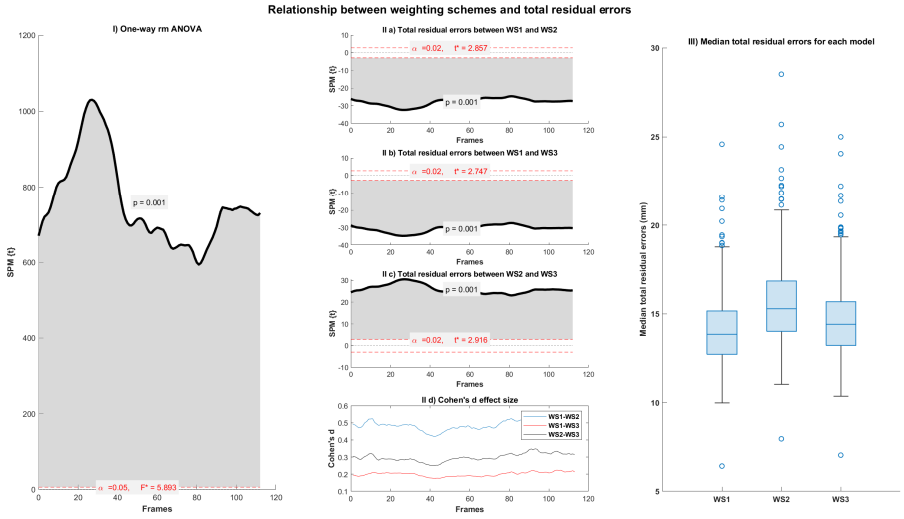

Appendix Figure A.2: How to read SPM figures: The red lines (upper and lower for t-tests) indicate the critical threshold set at the respective alpha values (0.05 for ANOVA and 0.02 for post-hoc analyses). For ANOVA tests, if the critical f-statistic field vector (the thick black line) is above the critical threshold, the independent variables have a significant effect on the dependent variables. For paired t-tests if the t-statistic field vector (the thick black line) is either below or above the critical thresholds , the null hypothesis of equal means is rejected for those frames. The t-values are differences between the mean of the two sample sets and the variation that exists within the sample sets. For post-hoc analyses, if the t-statistic field vector is above the upper critical threshold, then (meanA>meanB) and vice versa if it is below the lower critical threshold.
I) Results of a nonparametric one-way ANOVA analysis between total residual errors acquired using the three markersets. The shaded area indicates marker weights have a significant effect on total residual errors (p=0.001). II) Post-hoc analysis using paired t-tests in SPM between total residual errors acquired using each of the markersets. a) The shaded area indicates markerset with unequal marker weights had a statistically higher total residual errors (p=0.001) compared to the markerset with equal weights. MeanA is the WS1 and meanB is WS2. b) Results indicate that total residual errors for the markerset with no thigh markers is significantly higher (p=0.001) than the markerset with equal weights. MeanA is the WS1 and meanB is WS3. c) Unequal marker weights resulted in statistically higher (p=0.001) total residual errors compared to markerset with no thigh markers as indicated by the shaded region. MeanA is the WS2 and meanB is WS3. d) Cohen's d effect sizes between the three different weighting strategies. III) The box plot shows the median total residual errors acquired using the three markersets.

A.2 Relationship between residual errors and joint angles

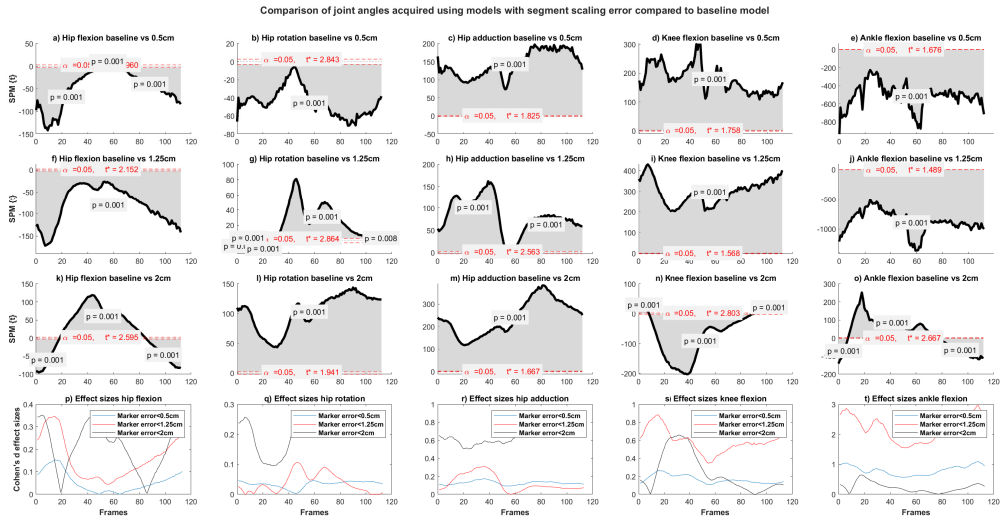

Appendix Figure A.3: How to read SPM figures: The red lines (upper and lower) indicate the critical threshold set at the alpha values of 0.05. For paired *t*-tests if the t-statistic field vector (the thick black line) is either below or above the critical thresholds , the null hypothesis of equal means is rejected for those frames. The t-values are differences between the mean of the two sample sets and the variation that exists within the sample sets. For paired *t*-tests, if the t-statistic field vector is above the upper critical threshold, then (meanA>meanB) and vice versa if it is below the lower critical threshold. For all the paired *t*-tests, meanA was the mean of the baseline model and meanB the mean of the error incorporated model.
a–e) Paired *t*-tests between joint angles acquired using baseline model and model with maximum marker error of <0.5cm. Shaded region indicates significant variation in joint angles (p=0.001). f–j) Paired *t*-tests between joint angles acquired using baseline model and model with maximum marker error of <1.25cm with shaded region indicating significant variation between joint angles (p=0.001). k–o) Paired *t*-tests between joint angles acquired using baseline model and model with maximum marker error of <2cm. Shaded region indicates significant variation in joint angles (p=0.001). p–t) Cohen's d effect sizes between the three models for hip flexion, hip rotation, hip adduction, knee flexion and ankle flexion. The columns are for hip flexion, hip rotation, hip adduction, knee flexion and ankle flexion joint angles respectively.

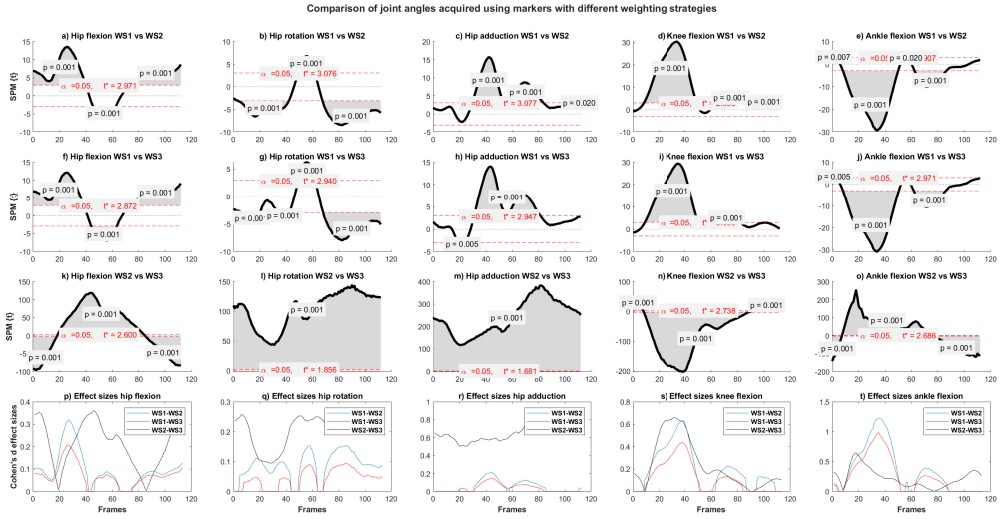

Appendix Figure A.4: How to read SPM figures: The red lines (upper and lower) indicate the critical threshold set at the alpha values of 0.05. For paired t-tests if the t-statistic field vector (the thick black line) is either below or above the critical thresholds , the null hypothesis of equal means is rejected for those frames. The t-values are differences between the mean of the two sample sets and the variation that exists within the sample sets. For paired t-tests, if the t-statistic field vector is above the upper critical threshold, then (meanA>meanB) and vice versa if it is below the lower critical threshold.
a–e) Paired t-tests between joint angles acquired using weighting strategy 1 and 2. Shaded region indicates significant variation in joint angles (p=0.001). MeanA was WS1 and meanB WS2. f–j) Paired t-tests between joint angles acquired using weighting strategy 1 and 3 with shaded region indicating significant variation between joint angles (p=0.001). MeanA was WS1 and meanB WS3. k–o) Paired t-tests between joint angles acquired using weighting strategy 2 and 3. Shaded region indicates significant variation in joint angles (p=0.001). MeanA was WS2 and meanB WS3. p–t) Cohen's d effect sizes between the three weighting strategies for hip flexion, hip rotation, hip adduction, knee flexion and ankle flexion. The columns are for hip flexion, hip rotation, hip adduction, knee flexion and ankle flexion joint angles respectively.

A.3 Joint angles computed from each model

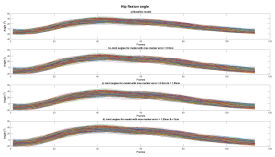

(a) Hip Flexion Angle

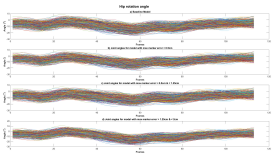

(b) Hip Rotation Angle

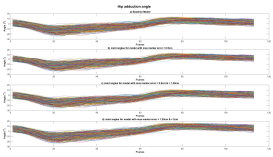

(c) Hip Adduction Angle

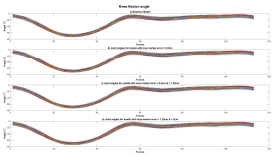

(d) Knee Flexion Angle

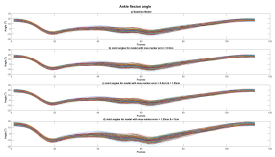

(e) Ankle Flexion Angle

Appendix Figure A.5: Kinematic angles computed for 501 trials using the baseline model and models emulating marker registration errors

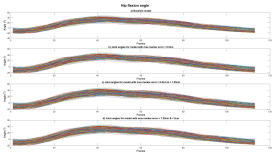

(a) Hip Flexion Angle

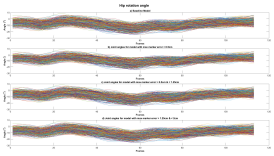

(b) Hip Rotation Angle

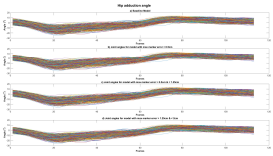

(c) Hip Adduction Angle

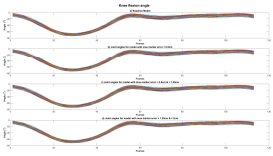

(d) Knee Flexion Angle

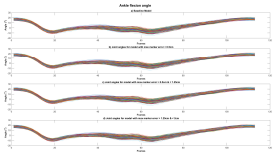

(e) Ankle Flexion Angle

Appendix Figure A.6: Kinematic angles computed for 501 trials using the baseline model and models emulating segment scaling errors

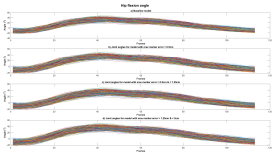

(a) Hip Flexion Angle

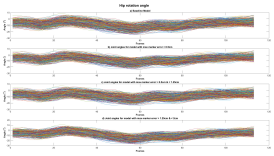

(b) Hip Rotation Angle

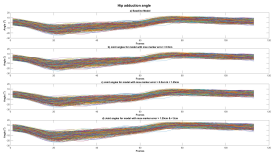

(c) Hip Adduction Angle

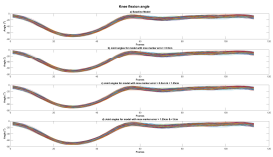

(d) Knee Flexion Angle

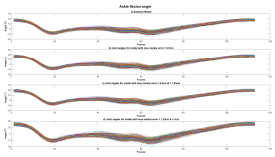

(e) Ankle Flexion Angle

Appendix Figure A.7: Kinematic angles computed for 501 trials using the baseline model and models with different marker weights

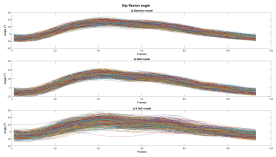

(a) Hip Flexion Angle

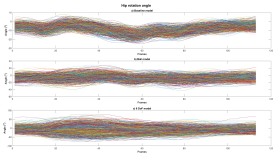

(b) Hip Rotation Angle

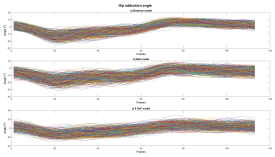

(c) Hip Adduction Angle

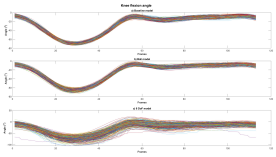

(d) Knee Flexion Angle

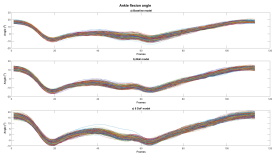

(e) Ankle Flexion Angle

Appendix Figure A.8: Kinematic angles computed for 501 trials using the baseline model and models with different joint constraints

Appendix B

Supplementary data from Chapter 5

B.1 Offset calculation for confocal imaging algorithms

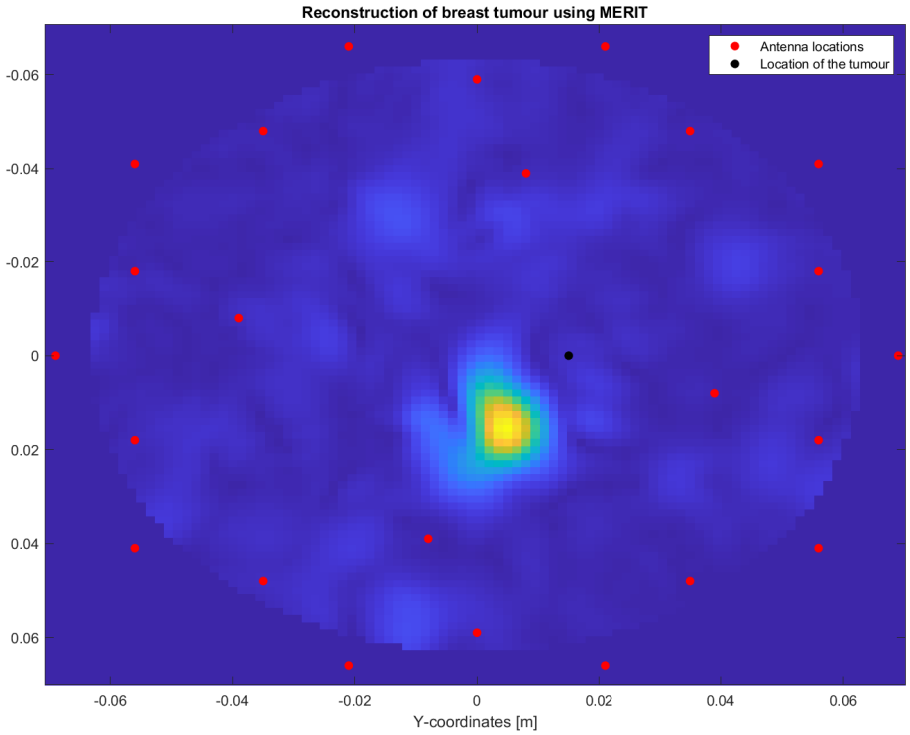

Appendix Figure B.1: Reconstructed image of a breast tumour obtained using delay-multiply-and-sum (DMAS) confocal imaging algorithm. The breast tumour datasets available in the MERIT toolbox [182] were leveraged to calculate the offset. The black dot represents the expected location of the tumour and the red dots indicate the location of the antennas.

B.2 Antenna A results

Anatomical model	Algorithm	SMR (dB)	SCR (dB)	Localisation error (cm)
Duke	DAS	22.3	-0.7811	1.2644
	DMAS	33.66	-1.8504	1.2636
	MUSIC	8.45	-1.3063	1.2251
	Kirchoff	9.8599	-1.54	0.4567
Ella - 22	DAS	25.8654	-1.2039	1.1259
	DMAS	34.4102	-2.7342	1.2423
	MUSIC	5.5651	-2.2525	1.1798
	Kirchoff	3.3058	-0.0879	2.822
Ella - 26	DAS	23.349	-2.6896	1.1418
	DMAS	34.4086	-1.2473	0.9838
	MUSIC	10.9836	-1.0424	0.6225
	Kirchoff	8.9	-0.3356	3.6982
Ella - 30	DAS	24.1648	-1.2733	0.6279
	DMAS	34.7851	-2.3189	-0.6279
	MUSIC	11.8334	-0.6269	0.4949
	Kirchoff	7.77551	-0.0206	3.1134
Ella - 22 Posed	DAS	NA	NA	NA
	DMAS	NA	NA	NA
	MUSIC	NA	NA	NA
	Kirchoff	NA	NA	NA
Ella - 30 Posed	DAS	NA	NA	NA
	DMAS	NA	NA	NA
	MUSIC	NA	NA	NA
	Kirchoff	NA	NA	NA

Table B.1: Metrics of reconstructed images computed using data collected from Antenna A

B.2.1 Duke

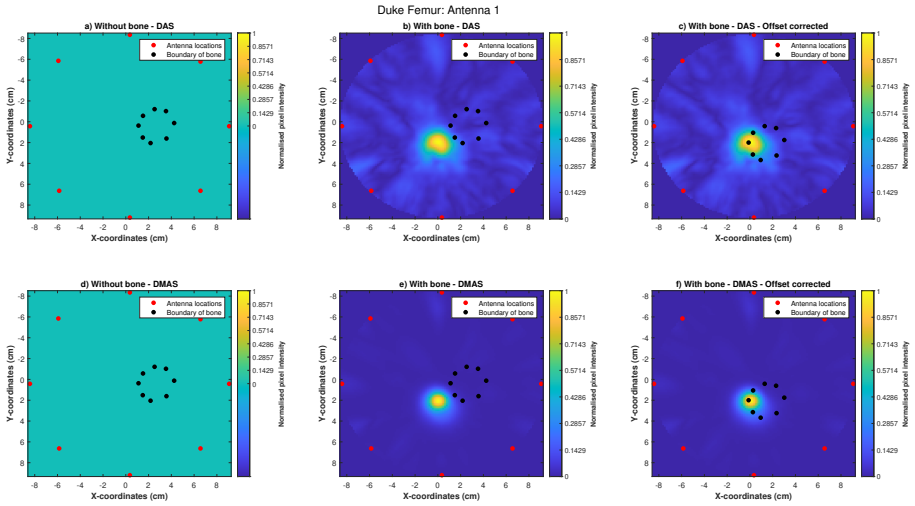

Appendix Figure B.2: Reconstructed image of the duke femur using confocal imaging algorithms. a) Reconstructed image when no data is provided using DAS (healthy scan - healthy scan). b) Reconstructed image of the femur using DAS. No offset-correction has been applied to the true bone locations (black dots). c) Reconstructed image of the femur using DAS. Offset-correction has been applied to the true bone locations (black dots). d) Reconstructed image when no data is provided using DMAS (healthy scan - healthy scan). e) Reconstructed image of the femur using DMAS. No offset-correction has been applied to the true bone locations (black dots). f) Reconstructed image of the femur using DMAS. Offset-correction has been applied to the true bone locations (black dots). Red dots in all images indicate the location of the antennas and black dots indicate the true location of the bones as determined from Sim4Life.

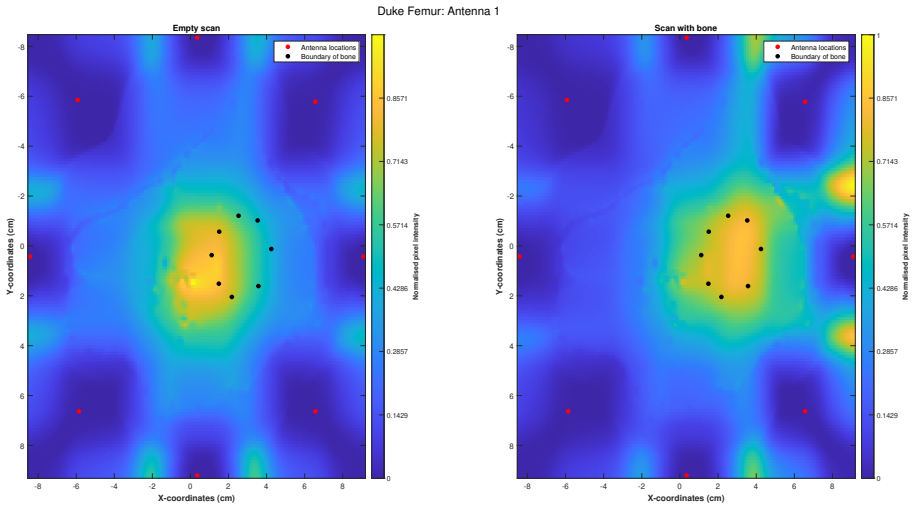

Appendix Figure B.3: Reconstructed image of the duke femur using the MUSIC algorithm. a) Reconstructed image when no data is provided using MUSIC (healthy scan - healthy scan). b) Reconstructed image of the femur using MUSIC. Red dots in all images indicate the location of the antennas and black dots indicate the true location of the bones as determined from Sim4Life.

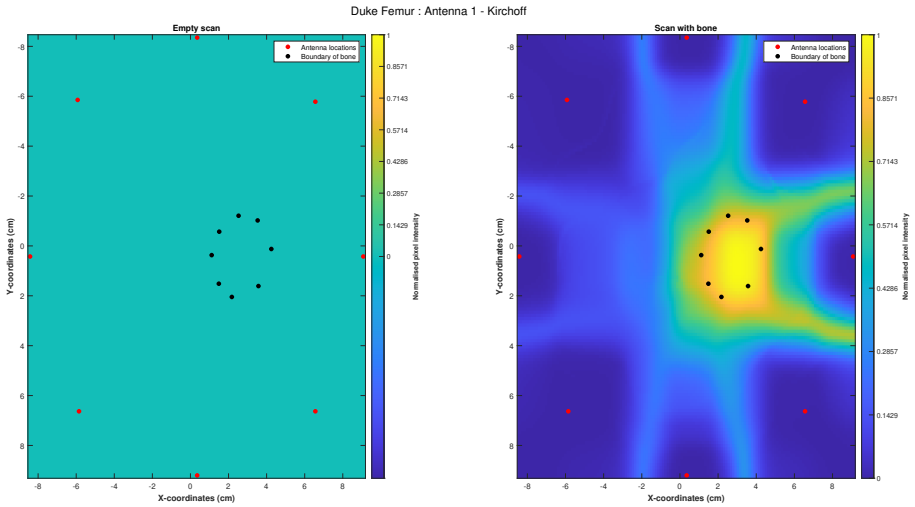

Appendix Figure B.4: Reconstructed image of the duke femur using the Kirchhoff migration algorithm. a) Reconstructed image when no data is provided using Kirchhoff migration (healthy scan - healthy scan). b) Reconstructed image of the femur using Kirchhoff migration. Red dots in all images indicate the location of the antennas and black dots indicate the true location of the bones as determined from Sim4Life.

B.2.2 Ella-22

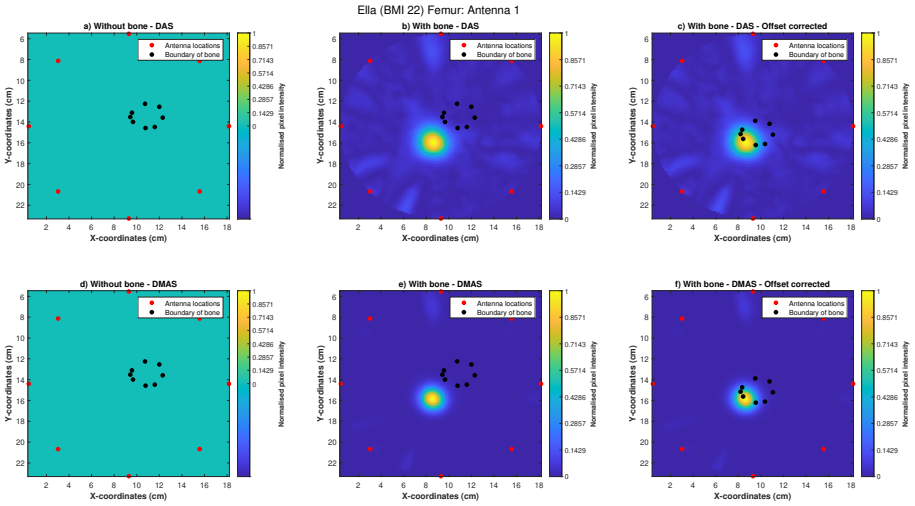

Appendix Figure B.5: Reconstructed image of the Ella-22 femur using confocal imaging algorithms. a) Reconstructed image when no data is provided using DAS (healthy scan - healthy scan). b) Reconstructed image of the femur using DAS. No offset-correction has been applied to the true bone locations (black dots). c) Reconstructed image of the femur using DAS. Offset-correction has been applied to the true bone locations (black dots). d) Reconstructed image when no data is provided using DMAS (healthy scan - healthy scan). e) Reconstructed image of the femur using DMAS. No offset-correction has been applied to the true bone locations (black dots). f) Reconstructed image of the femur using DMAS. Offset-correction has been applied to the true bone locations (black dots). Red dots in all images indicate the location of the antennas and black dots indicate the true location of the bones as determined from Sim4Life.

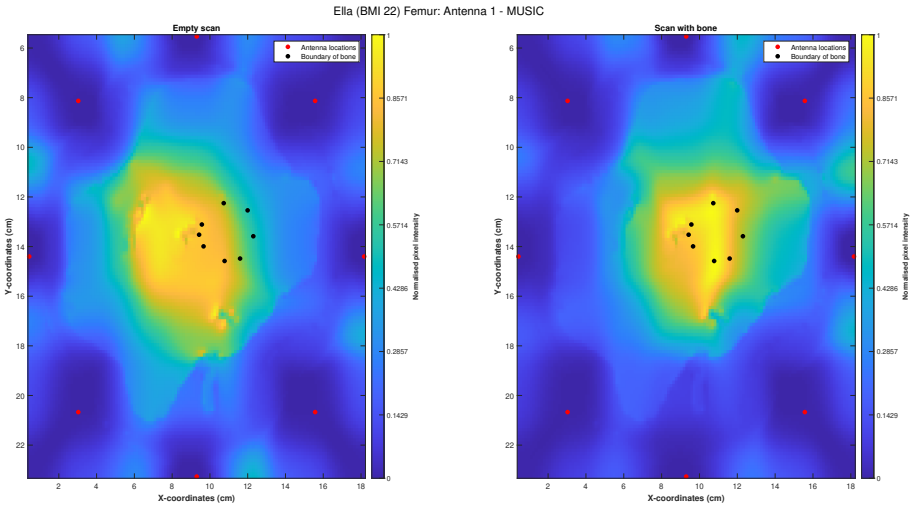

Appendix Figure B.6: Reconstructed image of the Ella-22 femur using the MUSIC algorithm. a) Reconstructed image when no data is provided using MUSIC (healthy scan - healthy scan). b) Reconstructed image of the femur using MUSIC. Red dots in all images indicate the location of the antennas and black dots indicate the true location of the bones as determined from Sim4Life.

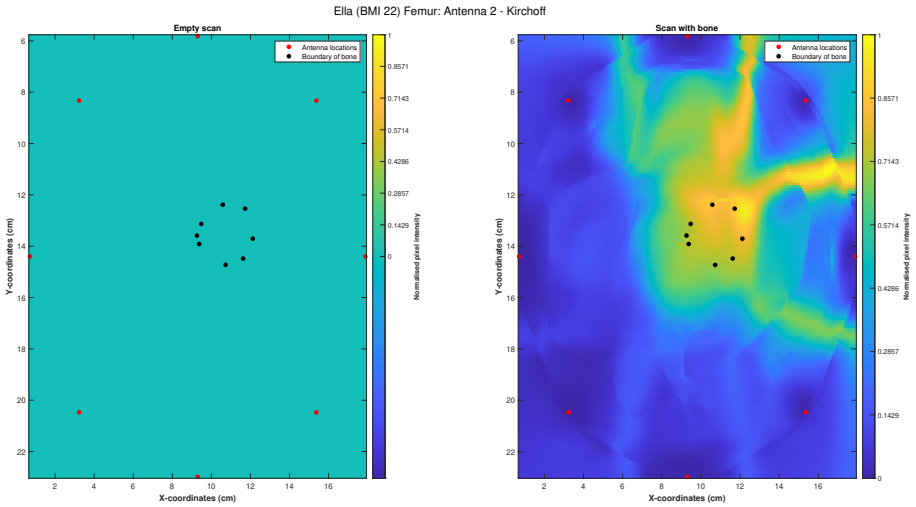

Appendix Figure B.7: Reconstructed image of the Ella-22 femur using the Kirchhoff migration algorithm. a) Reconstructed image when no data is provided using Kirchhoff migration (healthy scan - healthy scan). b) Reconstructed image of the femur using Kirchhoff migration. Red dots in all images indicate the location of the antennas and black dots indicate the true location of the bones as determined from Sim4Life.

B.2.3 Ella-26

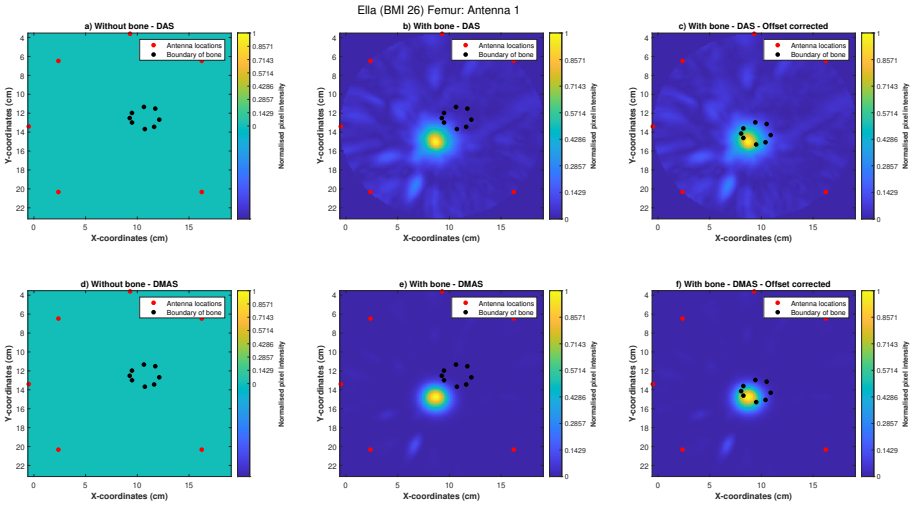

Appendix Figure B.8: Reconstructed image of the Ella-26 femur using confocal imaging algorithms. a) Reconstructed image when no data is provided using DAS (healthy scan - healthy scan). b) Reconstructed image of the femur using DAS. No offset-correction has been applied to the true bone locations (black dots). c) Reconstructed image of the femur using DAS. Offset-correction has been applied to the true bone locations (black dots). d) Reconstructed image when no data is provided using DMAS (healthy scan - healthy scan). e) Reconstructed image of the femur using DMAS. No offset-correction has been applied to the true bone locations (black dots). f) Reconstructed image of the femur using DMAS. Offset-correction has been applied to the true bone locations (black dots). Red dots in all images indicate the location of the antennas and black dots indicate the true location of the bones as determined from Sim4Life.

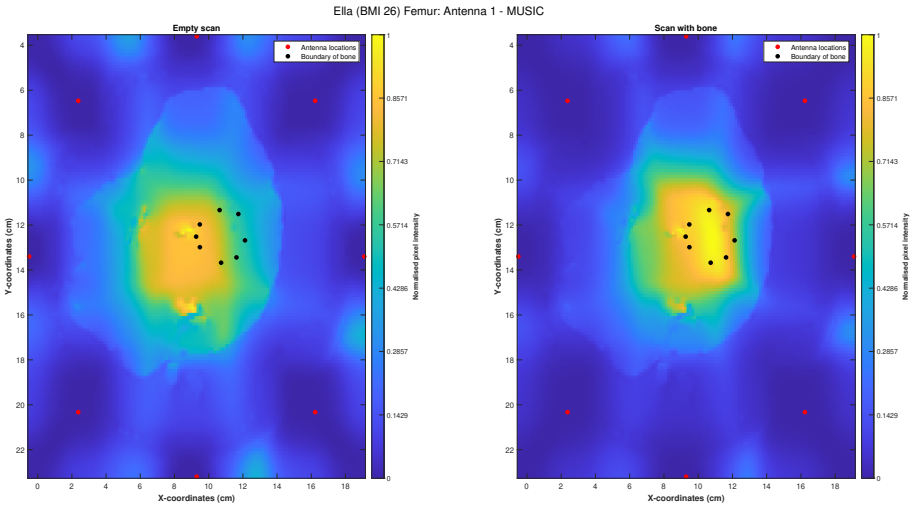

Appendix Figure B.9: Reconstructed image of the Ella-26 femur using the MUSIC algorithm. a) Reconstructed image when no data is provided using MUSIC (healthy scan - healthy scan). b) Reconstructed image of the femur using MUSIC. Red dots in all images indicate the location of the antennas and black dots indicate the true location of the bones as determined from Sim4Life.

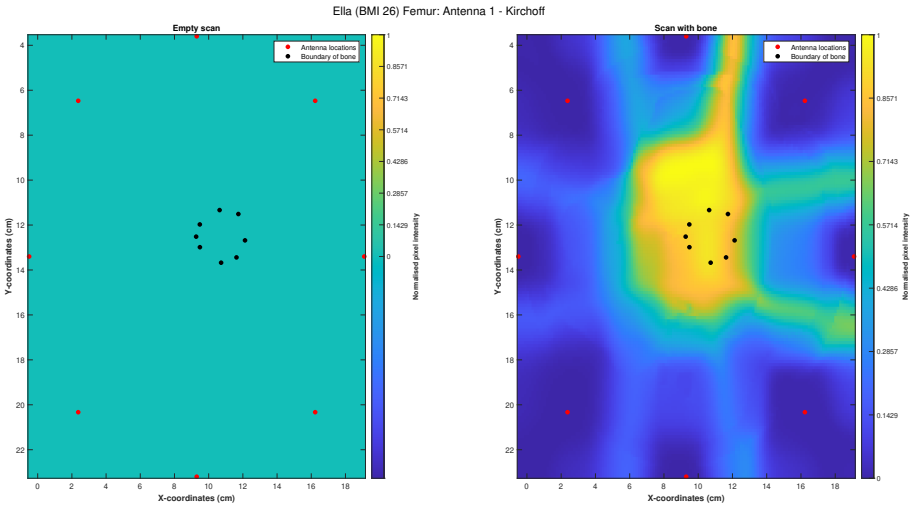

Appendix Figure B.10: Reconstructed image of the Ella-26 femur using the Kirchhoff migration algorithm. a) Reconstructed image when no data is provided using Kirchhoff migration (healthy scan - healthy scan). b) Reconstructed image of the femur using Kirchhoff migration. Red dots in all images indicate the location of the antennas and black dots indicate the true location of the bones as determined from Sim4Life.

B.2.4 Ella-30

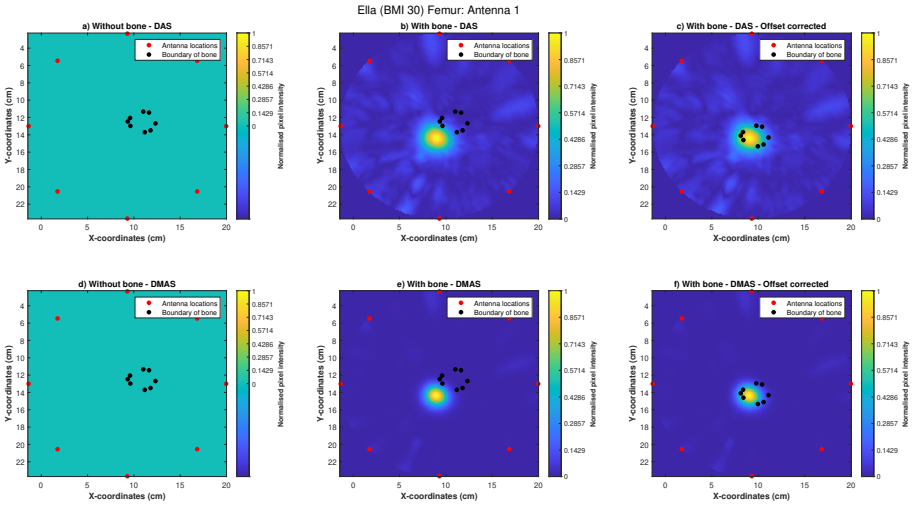

Appendix Figure B.11: Reconstructed image of the Ella-30 femur using confocal imaging algorithms. a) Reconstructed image when no data is provided using DAS (healthy scan - healthy scan). b) Reconstructed image of the femur using DAS. No offset-correction has been applied to the true bone locations (black dots). c) Reconstructed image of the femur using DAS. Offset-correction has been applied to the true bone locations (black dots). d) Reconstructed image when no data is provided using DMAS (healthy scan - healthy scan). e) Reconstructed image of the femur using DMAS. No offset-correction has been applied to the true bone locations (black dots). f) Reconstructed image of the femur using DMAS. Offset-correction has been applied to the true bone locations (black dots). Red dots in all images indicate the location of the antennas and black dots indicate the true location of the bones as determined from Sim4Life.

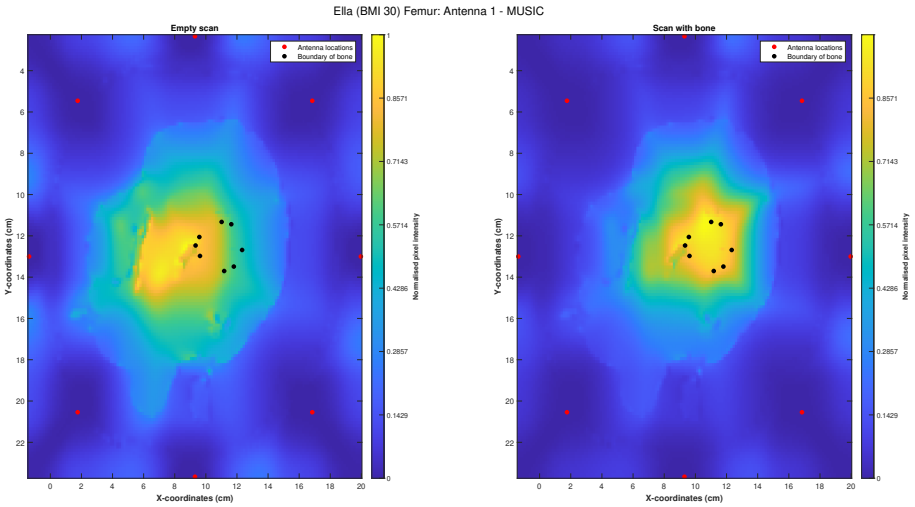

Appendix Figure B.12: Reconstructed image of the Ella-30 femur using the MUSIC algorithm. a) Reconstructed image when no data is provided using MUSIC (healthy scan - healthy scan). b) Reconstructed image of the femur using MUSIC. Red dots in all images indicate the location of the antennas and black dots indicate the true location of the bones as determined from Sim4Life.

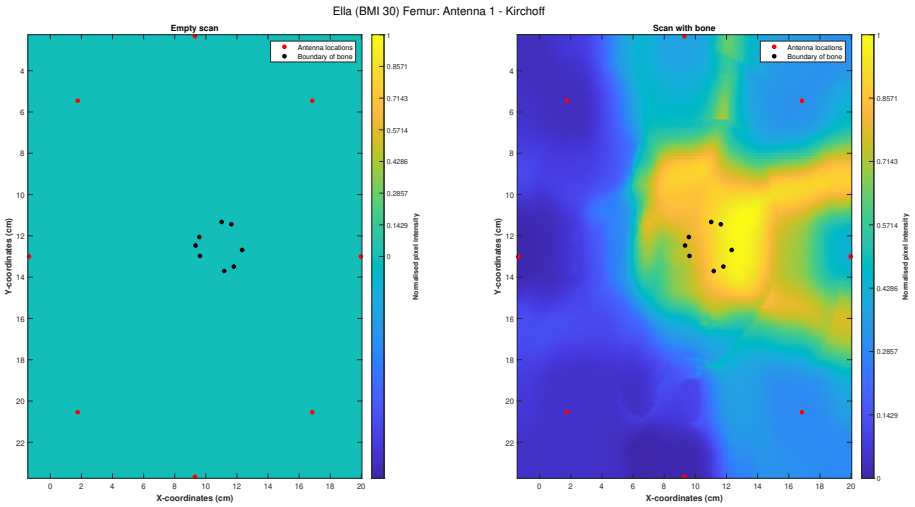

Appendix Figure B.13: Reconstructed image of the Ella-30 femur using the Kirchhoff migration algorithm. a) Reconstructed image when no data is provided using Kirchhoff migration (healthy scan - healthy scan). b) Reconstructed image of the femur using Kirchhoff migration. Red dots in all images indicate the location of the antennas and black dots indicate the true location of the bones as determined from Sim4Life.

B.3 Antenna B results

Anatomical model	Algorithm	SMR (dB)	SCR (dB)	Localisation error (cm)
Duke	DAS	13.3602	-14.6164	1.101
	DMAS	15.45	-25.4	1.1
	MUSIC	8.0271	-4.2086	2.0798
	Kirchoff	6.0287	-3.3893	2.7305
Ella - 22	DAS	12.1513	-9.49	1.3062
	DMAS	17.8581	-14.14	1.0945
	MUSIC	4.44	-2.6587	1.4424
	Kirchoff	4.8225	-1.1626	1.9915
Ella - 26	DAS	12.8605	-9.5323	1.2936
	DMAS	16.2551	-17.45	1.1665
	MUSIC	11.0217	0.9914	2.7
	Kirchoff	10.77	-0.151	3.84
Ella - 30	DAS	14.11	-4.7	0.5764
	DMAS	20.4013	-9.8519	0.5764
	MUSIC	9.9998	-1.2784	4.0728
	Kirchoff	5.145	-1.2754	2.5728
Ella - 22 Posed	DAS	-	-	-
	DMAS	-	-	-
	MUSIC	-	-	-
	Kirchoff	-	-	-
Ella - 30 Posed	DAS	-	-	-
	DMAS	-	-	-
	MUSIC	-	-	-
	Kirchoff	-	-	-

Table B.2: Metrics of reconstructed images computed using data collected from Antenna B

B.3.1 Duke

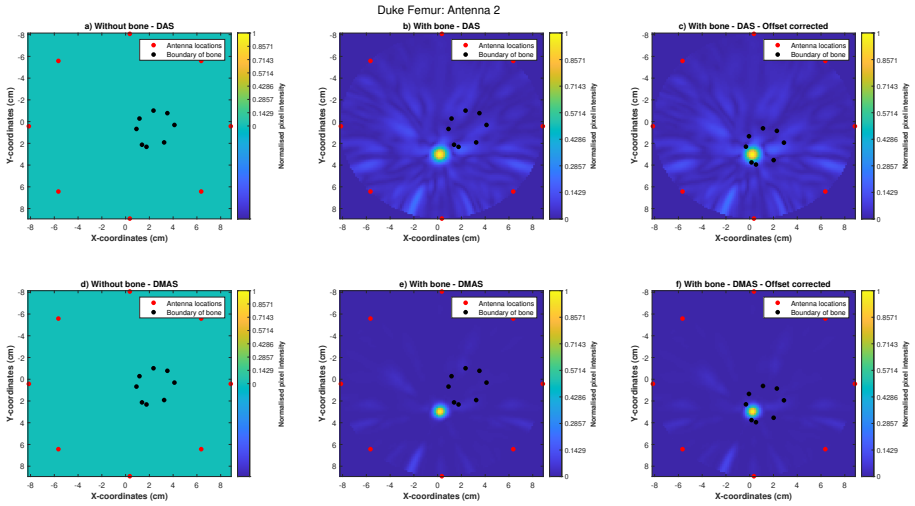

Appendix Figure B.14: Reconstructed image of the duke femur using confocal imaging algorithms. a) Reconstructed image when no data is provided using DAS (healthy scan - healthy scan). b) Reconstructed image of the femur using DAS. No offset-correction has been applied to the true bone locations (black dots). c) Reconstructed image of the femur using DAS. Offset-correction has been applied to the true bone locations (black dots). d) Reconstructed image when no data is provided using DMAS (healthy scan - healthy scan). e) Reconstructed image of the femur using DMAS. No offset-correction has been applied to the true bone locations (black dots). f) Reconstructed image of the femur using DMAS. Offset-correction has been applied to the true bone locations (black dots). Red dots in all images indicate the location of the antennas and black dots indicate the true location of the bones as determined from Sim4Life.

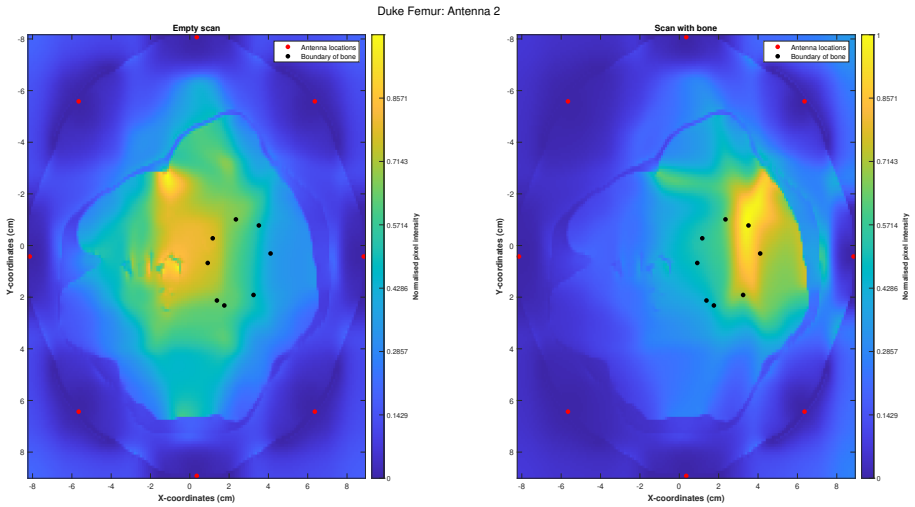

Appendix Figure B.15: Reconstructed image of the duke femur using the MUSIC algorithm. a) Reconstructed image when no data is provided using MUSIC (healthy scan - healthy scan). b) Reconstructed image of the femur using MUSIC. Red dots in all images indicate the location of the antennas and black dots indicate the true location of the bones as determined from Sim4Life.

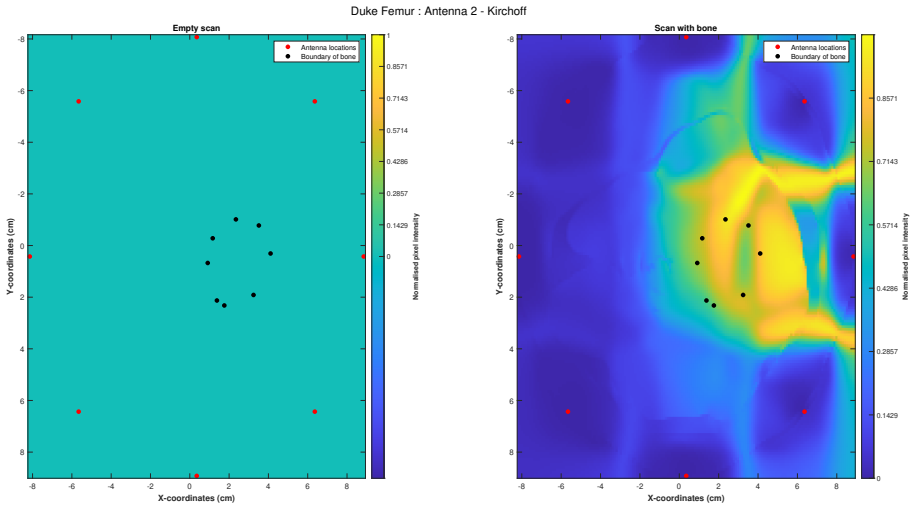

Appendix Figure B.16: Reconstructed image of the duke femur using the Kirchhoff migration algorithm. a) Reconstructed image when no data is provided using Kirchhoff migration (healthy scan - healthy scan). b) Reconstructed image of the femur using Kirchhoff migration. Red dots in all images indicate the location of the antennas and black dots indicate the true location of the bones as determined from Sim4Life.

B.3.2 Ella-22

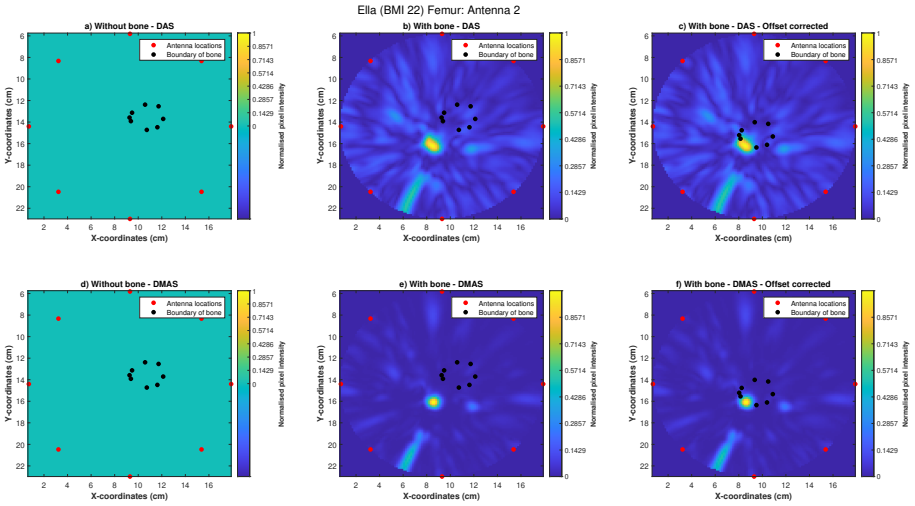

Appendix Figure B.17: Reconstructed image of the Ella-22 femur using confocal imaging algorithms. a) Reconstructed image when no data is provided using DAS (healthy scan - healthy scan). b) Reconstructed image of the femur using DAS. No offset-correction has been applied to the true bone locations (black dots). c) Reconstructed image of the femur using DAS. Offset-correction has been applied to the true bone locations (black dots). d) Reconstructed image when no data is provided using DMAS (healthy scan - healthy scan). e) Reconstructed image of the femur using DMAS. No offset-correction has been applied to the true bone locations (black dots). f) Reconstructed image of the femur using DMAS. Offset-correction has been applied to the true bone locations (black dots). Red dots in all images indicate the location of the antennas and black dots indicate the true location of the bones as determined from Sim4Life.

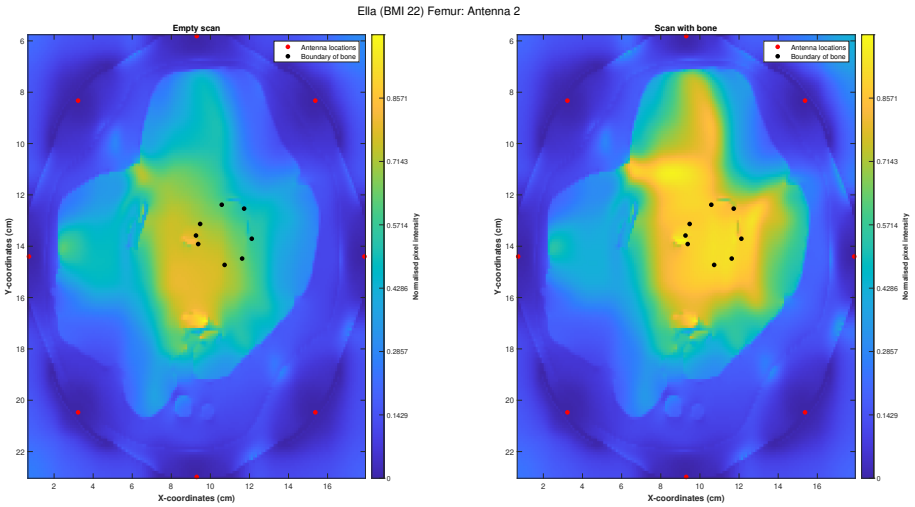

Appendix Figure B.18: Reconstructed image of the Ella-22 femur using the MUSIC algorithm. a) Reconstructed image when no data is provided using MUSIC (healthy scan - healthy scan). b) Reconstructed image of the femur using MUSIC. Red dots in all images indicate the location of the antennas and black dots indicate the true location of the bones as determined from Sim4Life.

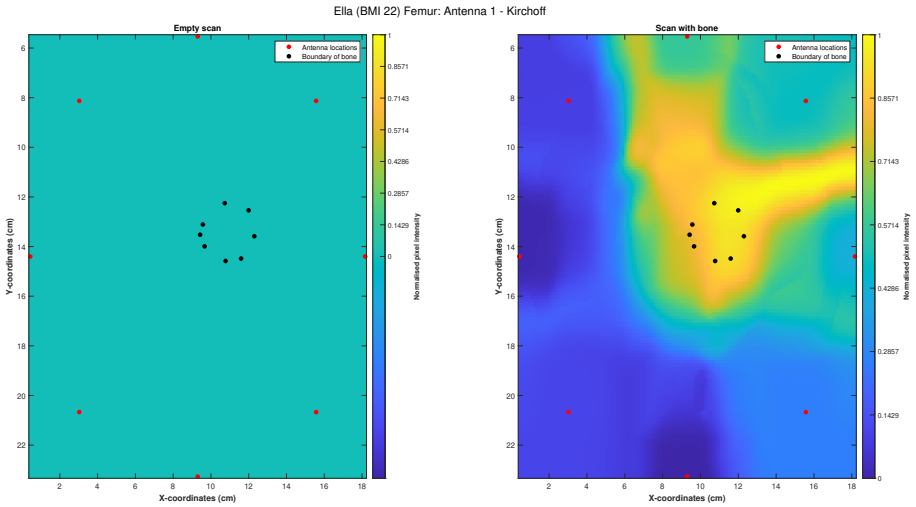

Appendix Figure B.19: Reconstructed image of the Ella-22 femur using the Kirchhoff migration algorithm. a) Reconstructed image when no data is provided using Kirchhoff migration (healthy scan - healthy scan). b) Reconstructed image of the femur using Kirchhoff migration. Red dots in all images indicate the location of the antennas and black dots indicate the true location of the bones as determined from Sim4Life.

B.3.3 Ella-26

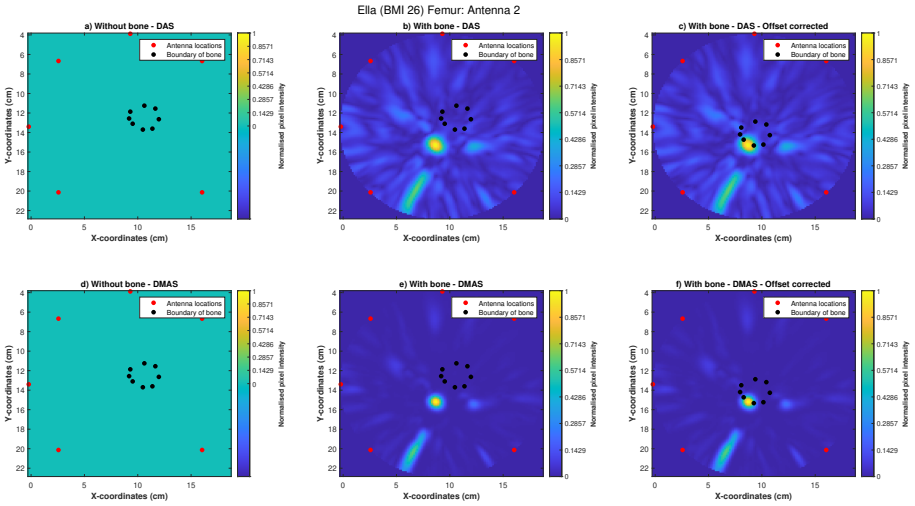

Appendix Figure B.20: Reconstructed image of the Ella-26 femur using confocal imaging algorithms. a) Reconstructed image when no data is provided using DAS (healthy scan - healthy scan). b) Reconstructed image of the femur using DAS. No offset-correction has been applied to the true bone locations (black dots). c) Reconstructed image of the femur using DAS. Offset-correction has been applied to the true bone locations (black dots). d) Reconstructed image when no data is provided using DMAS (healthy scan - healthy scan). e) Reconstructed image of the femur using DMAS. No offset-correction has been applied to the true bone locations (black dots). f) Reconstructed image of the femur using DMAS. Offset-correction has been applied to the true bone locations (black dots). Red dots in all images indicate the location of the antennas and black dots indicate the true location of the bones as determined from Sim4Life.

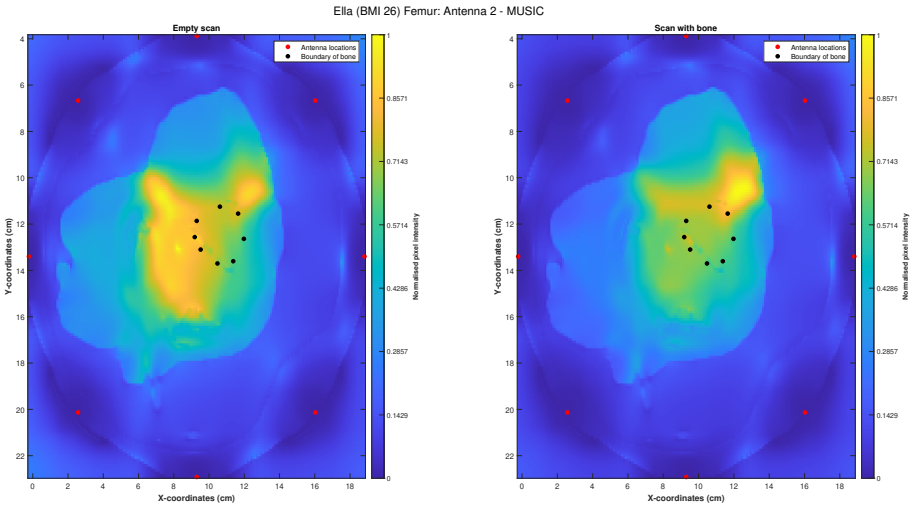

Appendix Figure B.21: Reconstructed image of the Ella-26 femur using the MUSIC algorithm. a) Reconstructed image when no data is provided using MUSIC (healthy scan - healthy scan). b) Reconstructed image of the femur using MUSIC. Red dots in all images indicate the location of the antennas and black dots indicate the true location of the bones as determined from Sim4Life.

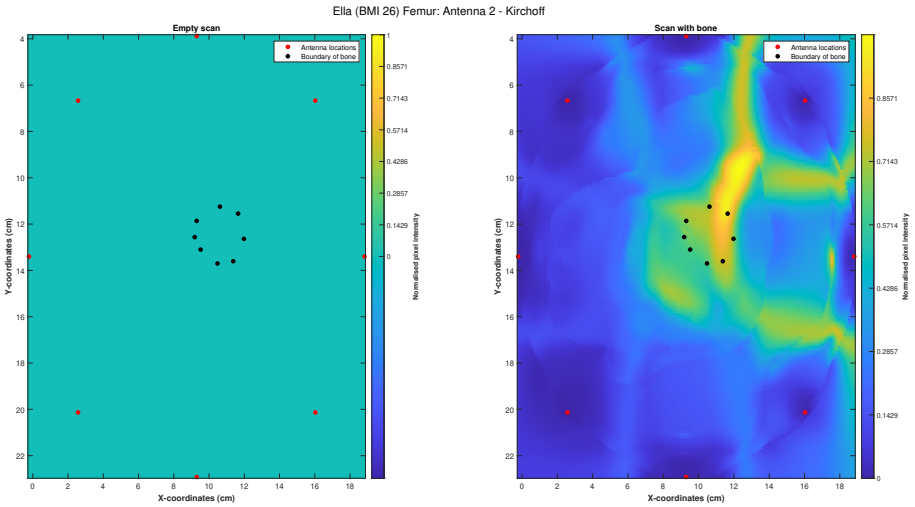

Appendix Figure B.22: Reconstructed image of the Ella-26 femur using the Kirchhoff migration algorithm. a) Reconstructed image when no data is provided using Kirchhoff migration (healthy scan - healthy scan). b) Reconstructed image of the femur using Kirchhoff migration. Red dots in all images indicate the location of the antennas and black dots indicate the true location of the bones as determined from Sim4Life.

B.3.4 Ella-30

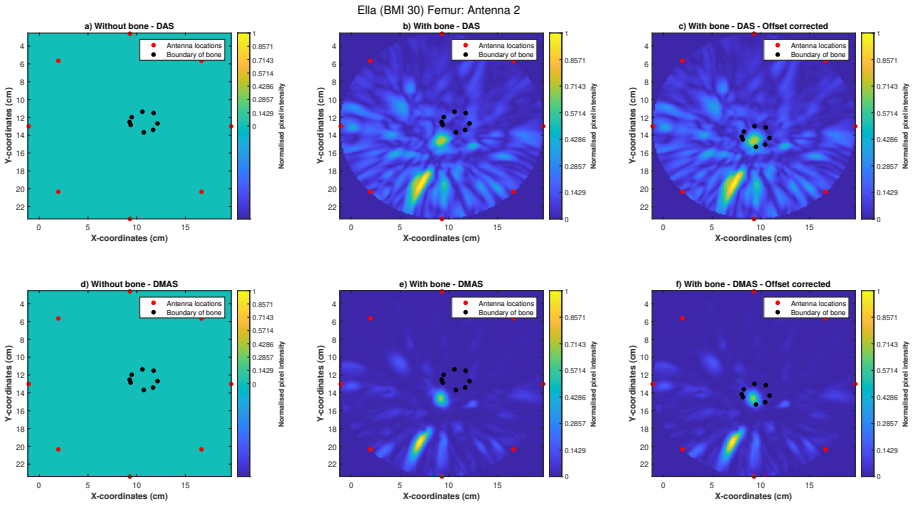

Appendix Figure B.23: Reconstructed image of the Ella-30 femur using confocal imaging algorithms. a) Reconstructed image when no data is provided using DAS (healthy scan - healthy scan). b) Reconstructed image of the femur using DAS. No offset-correction has been applied to the true bone locations (black dots). c) Reconstructed image of the femur using DAS. Offset-correction has been applied to the true bone locations (black dots). d) Reconstructed image when no data is provided using DMAS (healthy scan - healthy scan). e) Reconstructed image of the femur using DMAS. No offset-correction has been applied to the true bone locations (black dots). f) Reconstructed image of the femur using DMAS. Offset-correction has been applied to the true bone locations (black dots). Red dots in all images indicate the location of the antennas and black dots indicate the true location of the bones as determined from Sim4Life.

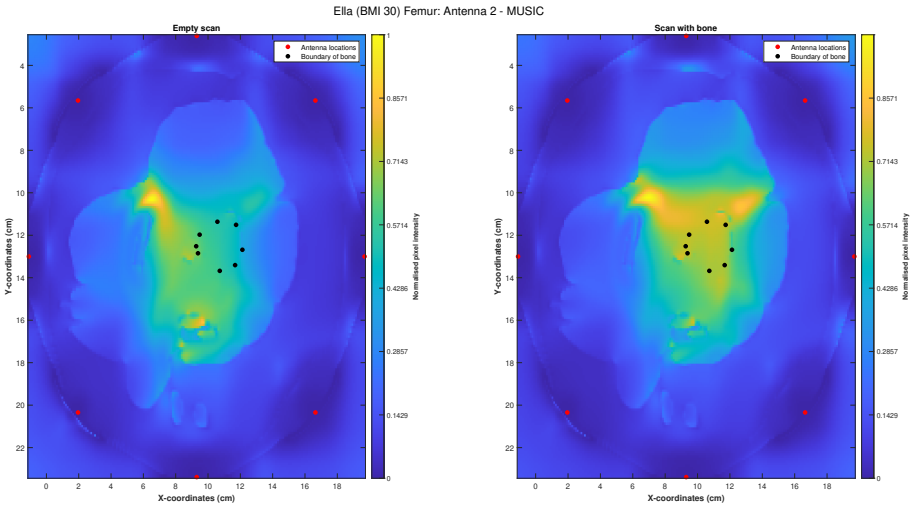

Appendix Figure B.24: Reconstructed image of the Ella-30 femur using the MUSIC algorithm. a) Reconstructed image when no data is provided using MUSIC (healthy scan - healthy scan). b) Reconstructed image of the femur using MUSIC. Red dots in all images indicate the location of the antennas and black dots indicate the true location of the bones as determined from Sim4Life.

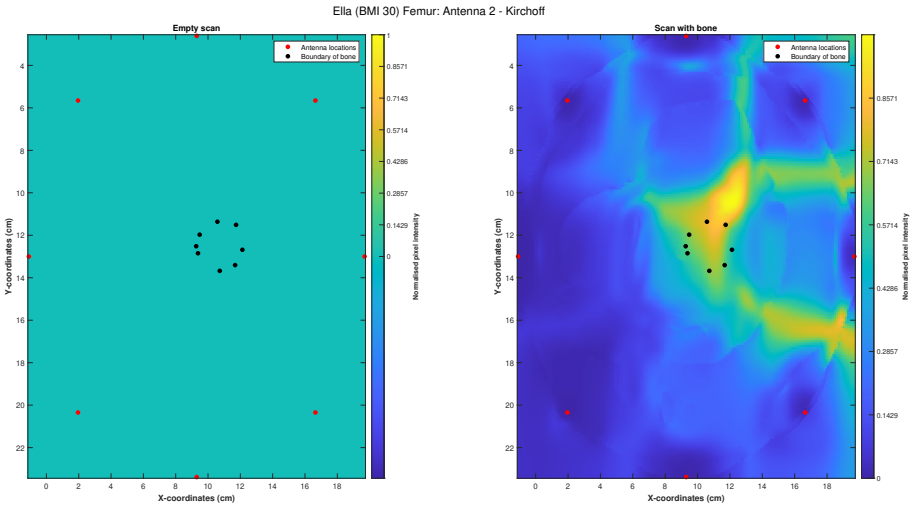

Appendix Figure B.25: Reconstructed image of the Ella-30 femur using the Kirchhoff migration algorithm. a) Reconstructed image when no data is provided using Kirchhoff migration (healthy scan - healthy scan). b) Reconstructed image of the femur using Kirchhoff migration. Red dots in all images indicate the location of the antennas and black dots indicate the true location of the bones as determined from Sim4Life.

B.4 Antenna C results

Anatomical model	Algorithm	SMR (dB)	SCR (dB)	Localisation error (cm)
Duke	DAS	18.8088	-0.3083	1.9008
	DMAS	26.8214	-0.6868	1.7946
	MUSIC	5.114	-2.557	1.4052
	Kirchoff	6.0287	-3.3893	0.6969
Ella - 22	DAS	13.98	-2.7514	1.1133
	DMAS	14.57	-7.5473	1.1752
	MUSIC	5.3665	-2.7663	1.48
	Kirchoff	2.0461	-3.241	0.9815
Ella - 26	DAS	18.8732	-3.0647	1.0533
	DMAS	23.3552	-6.8105	1.0533
	MUSIC	8.245	-1.9048	1.75
	Kirchoff	6.7864	-1.3686	1.9332
Ella - 30	DAS	19.4456	-3.7721	0.7647
	DMAS	24.641	-6.179	0.7647
	MUSIC	7.1731	-1.3928	2.85
	Kirchoff	5.145	-1.2754	2.488
Ella - 22 Posed	DAS	-	-	-
	DMAS	-	-	-
	MUSIC	2.8905	-4.913	2.6766
	Kirchoff	-0.1612	-4.7139	2.0088
Ella - 30 Posed	DAS	-	-	-
	DMAS	-	-	-
	MUSIC	7.8944	-3.3131	1.6901
	Kirchoff	-1.2796	-3.67141	1.202

Table B.3: Metrics of reconstructed images computed using data collected from Antenna C

B.4.1 Duke

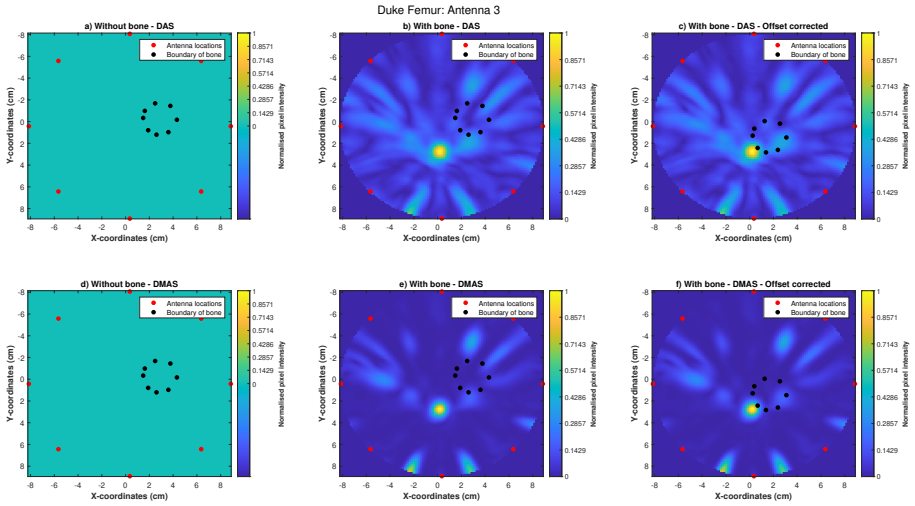

Appendix Figure B.26: Reconstructed image of the duke femur using confocal imaging algorithms. a) Reconstructed image when no data is provided using DAS (healthy scan - healthy scan). b) Reconstructed image of the femur using DAS. No offset-correction has been applied to the true bone locations (black dots). c) Reconstructed image of the femur using DAS. Offset-correction has been applied to the true bone locations (black dots). d) Reconstructed image when no data is provided using DMAS (healthy scan - healthy scan). e) Reconstructed image of the femur using DMAS. No offset-correction has been applied to the true bone locations (black dots). f) Reconstructed image of the femur using DMAS. Offset-correction has been applied to the true bone locations (black dots). Red dots in all images indicate the location of the antennas and black dots indicate the true location of the bones as determined from Sim4Life.

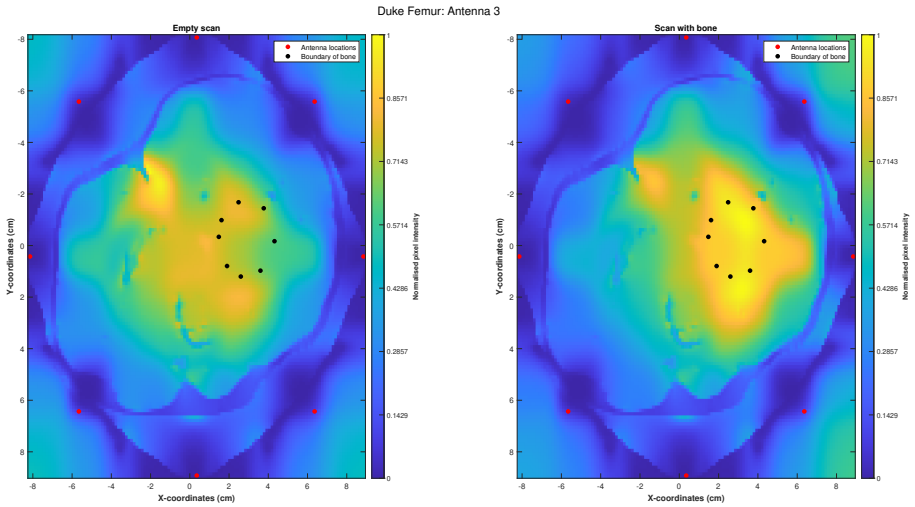

Appendix Figure B.27: Reconstructed image of the duke femur using the MUSIC algorithm. a) Reconstructed image when no data is provided using MUSIC (healthy scan - healthy scan). b) Reconstructed image of the femur using MUSIC. Red dots in all images indicate the location of the antennas and black dots indicate the true location of the bones as determined from Sim4Life.

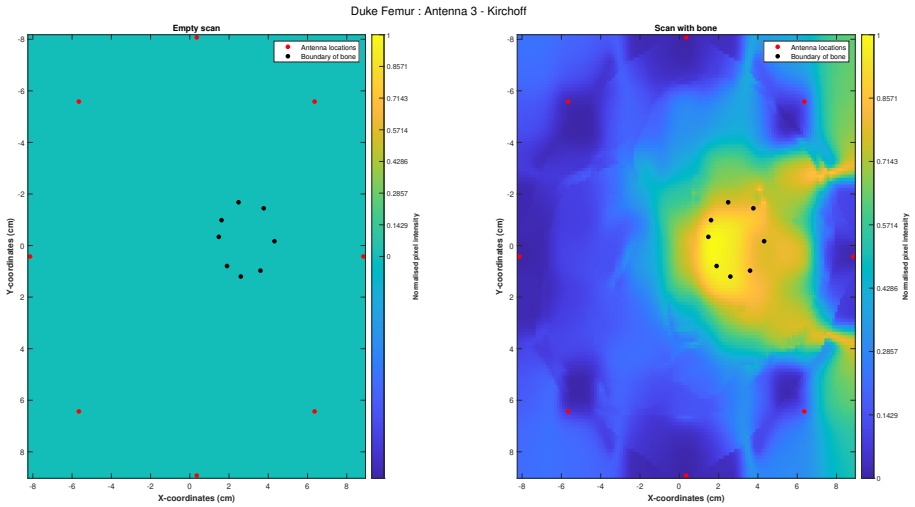

Appendix Figure B.28: Reconstructed image of the duke femur using the Kirchhoff migration algorithm. a) Reconstructed image when no data is provided using Kirchhoff migration (healthy scan - healthy scan). b) Reconstructed image of the femur using Kirchhoff migration. Red dots in all images indicate the location of the antennas and black dots indicate the true location of the bones as determined from Sim4Life.

B.4.2 Ella-22

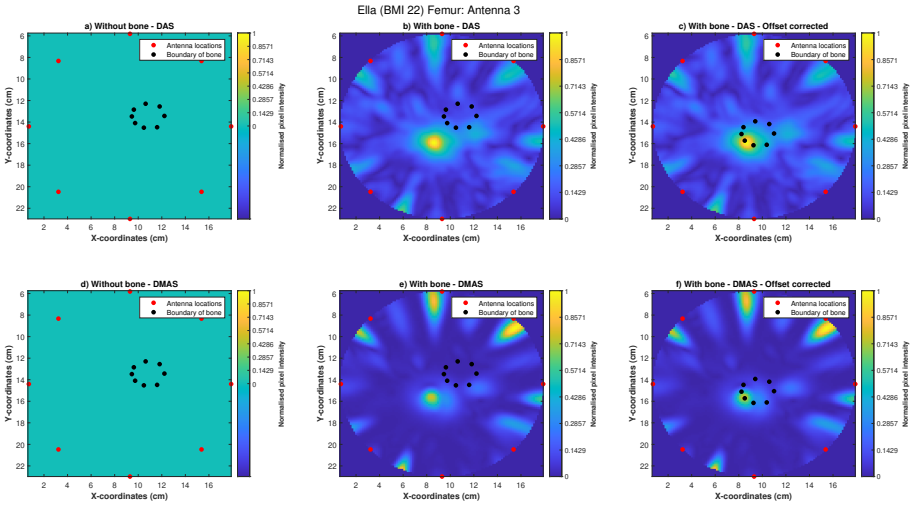

Appendix Figure B.29: Reconstructed image of the Ella-22 femur using confocal imaging algorithms. a) Reconstructed image when no data is provided using DAS (healthy scan - healthy scan). b) Reconstructed image of the femur using DAS. No offset-correction has been applied to the true bone locations (black dots). c) Reconstructed image of the femur using DAS. Offset-correction has been applied to the true bone locations (black dots). d) Reconstructed image when no data is provided using DMAS (healthy scan - healthy scan). e) Reconstructed image of the femur using DMAS. No offset-correction has been applied to the true bone locations (black dots). f) Reconstructed image of the femur using DMAS. Offset-correction has been applied to the true bone locations (black dots). Red dots in all images indicate the location of the antennas and black dots indicate the true location of the bones as determined from Sim4Life.

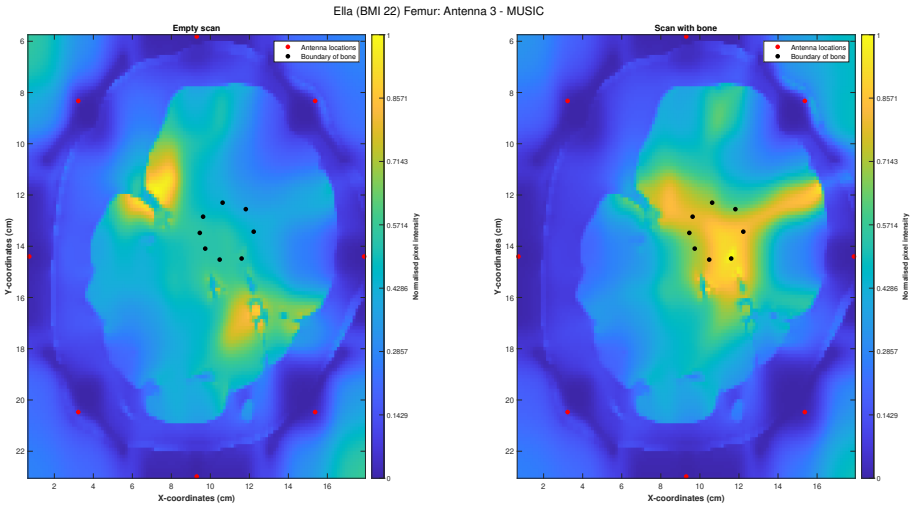

Appendix Figure B.30: Reconstructed image of the Ella-22 femur using the MUSIC algorithm. a) Reconstructed image when no data is provided using MUSIC (healthy scan - healthy scan). b) Reconstructed image of the femur using MUSIC. Red dots in all images indicate the location of the antennas and black dots indicate the true location of the bones as determined from Sim4Life.

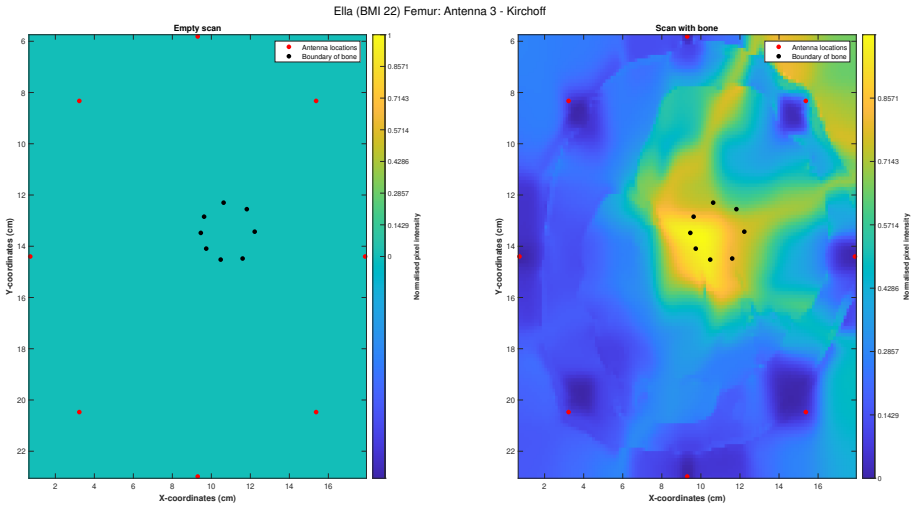

Appendix Figure B.31: Reconstructed image of the Ella-22 femur using the Kirchhoff migration algorithm. a) Reconstructed image when no data is provided using Kirchhoff migration (healthy scan - healthy scan). b) Reconstructed image of the femur using Kirchhoff migration. Red dots in all images indicate the location of the antennas and black dots indicate the true location of the bones as determined from Sim4Life.

B.4.3 Ella-26

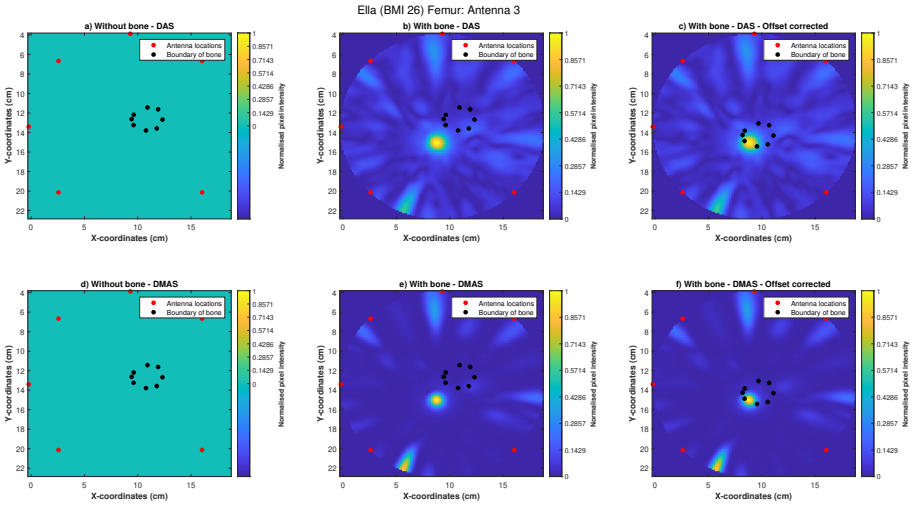

Appendix Figure B.32: Reconstructed image of the Ella-26 femur using confocal imaging algorithms. a) Reconstructed image when no data is provided using DAS (healthy scan - healthy scan). b) Reconstructed image of the femur using DAS. No offset-correction has been applied to the true bone locations (black dots). c) Reconstructed image of the femur using DAS. Offset-correction has been applied to the true bone locations (black dots). d) Reconstructed image when no data is provided using DMAS (healthy scan - healthy scan). e) Reconstructed image of the femur using DMAS. No offset-correction has been applied to the true bone locations (black dots). f) Reconstructed image of the femur using DMAS. Offset-correction has been applied to the true bone locations (black dots). Red dots in all images indicate the location of the antennas and black dots indicate the true location of the bones as determined from Sim4Life.

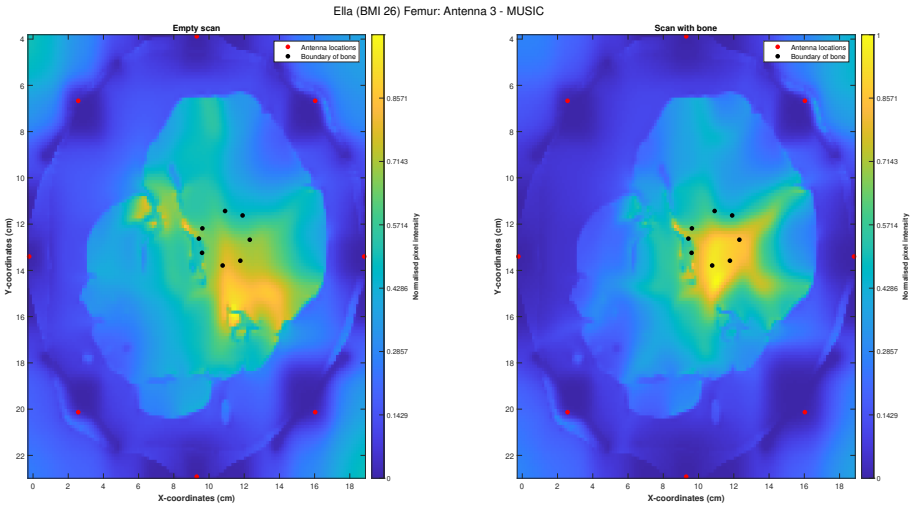

Appendix Figure B.33: Reconstructed image of the Ella-26 femur using the MUSIC algorithm. a) Reconstructed image when no data is provided using MUSIC (healthy scan - healthy scan). b) Reconstructed image of the femur using MUSIC. Red dots in all images indicate the location of the antennas and black dots indicate the true location of the bones as determined from Sim4Life.

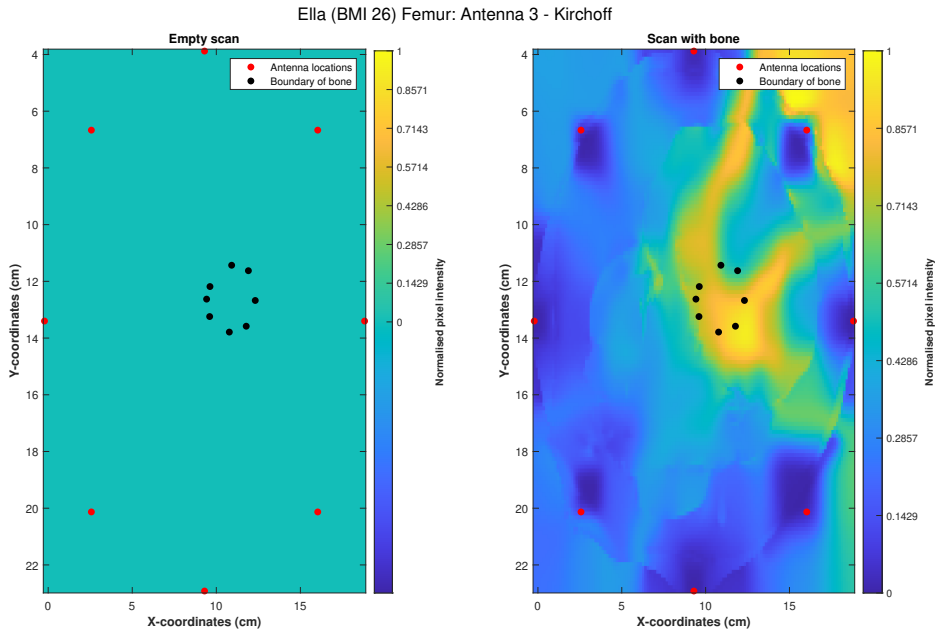

Appendix Figure B.34: Reconstructed image of the Ella-26 femur using the Kirchhoff migration algorithm. a) Reconstructed image when no data is provided using Kirchhoff migration (healthy scan - healthy scan). b) Reconstructed image of the femur using Kirchhoff migration. Red dots in all images indicate the location of the antennas and black dots indicate the true location of the bones as determined from Sim4Life.

B.4.4 Ella-30

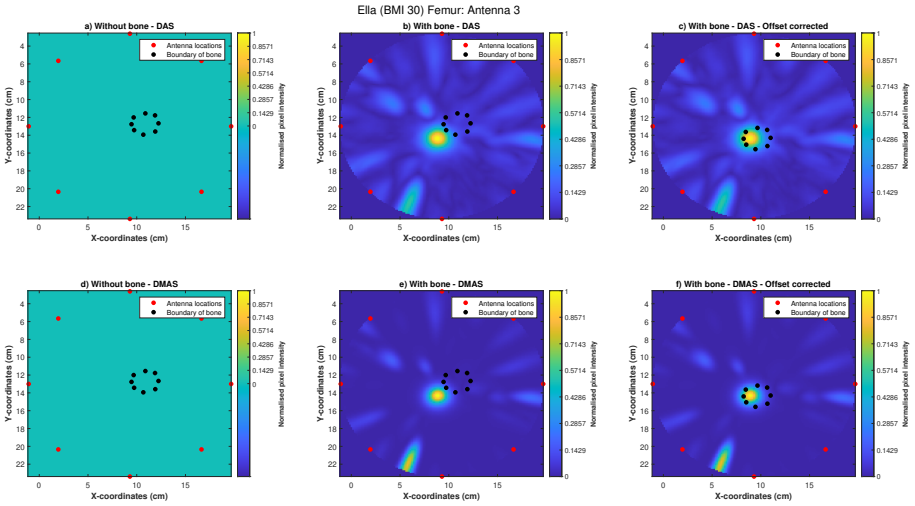

Appendix Figure B.35: Reconstructed image of the Ella-30 femur using confocal imaging algorithms. a) Reconstructed image when no data is provided using DAS (healthy scan - healthy scan). b) Reconstructed image of the femur using DAS. No offset-correction has been applied to the true bone locations (black dots). c) Reconstructed image of the femur using DAS. Offset-correction has been applied to the true bone locations (black dots). d) Reconstructed image when no data is provided using DMAS (healthy scan - healthy scan). e) Reconstructed image of the femur using DMAS. No offset-correction has been applied to the true bone locations (black dots). f) Reconstructed image of the femur using DMAS. Offset-correction has been applied to the true bone locations (black dots). Red dots in all images indicate the location of the antennas and black dots indicate the true location of the bones as determined from Sim4Life.

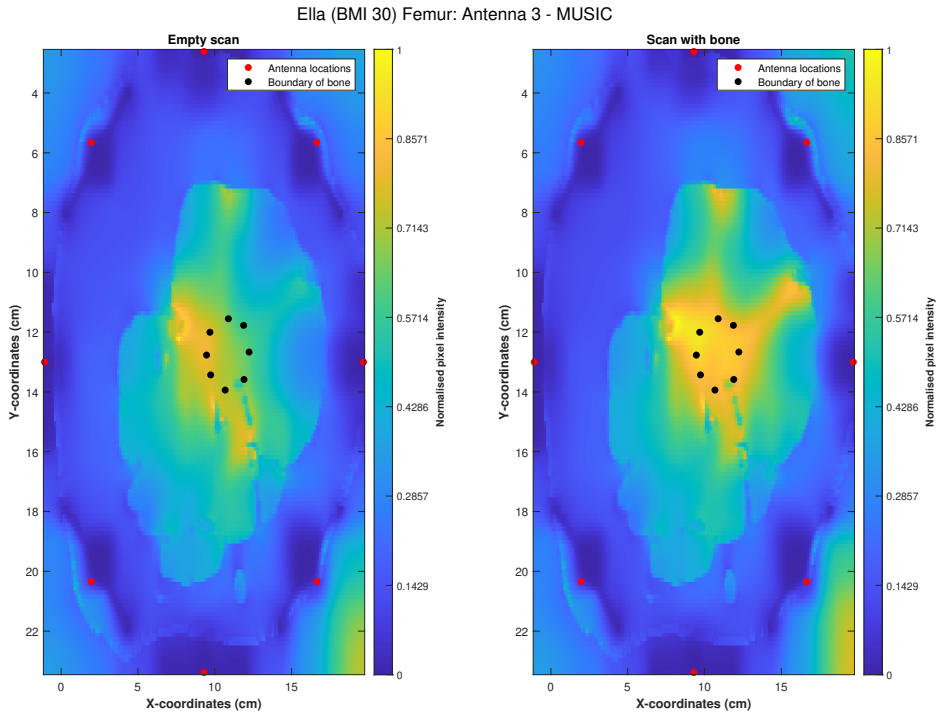

Appendix Figure B.36: Reconstructed image of the Ella-30 femur using the MUSIC algorithm. a) Reconstructed image when no data is provided using MUSIC (healthy scan - healthy scan). b) Reconstructed image of the femur using MUSIC. Red dots in all images indicate the location of the antennas and black dots indicate the true location of the bones as determined from Sim4Life.

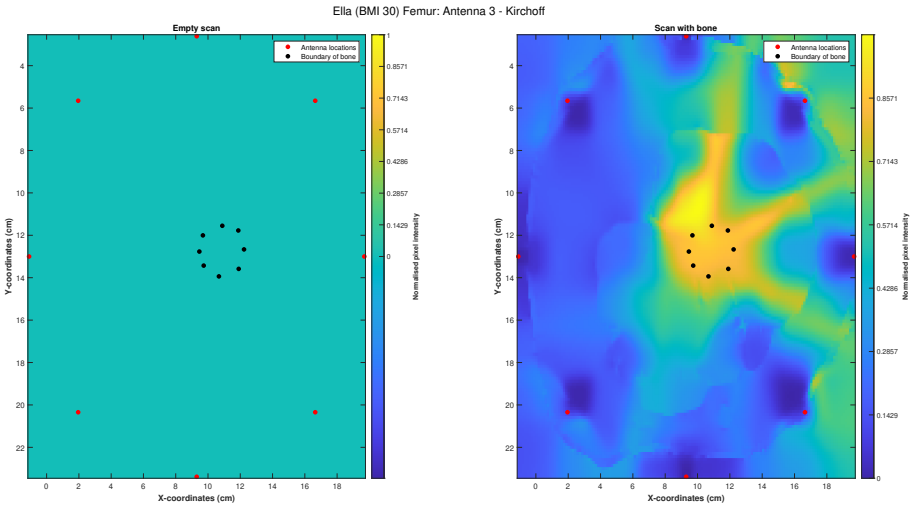

Appendix Figure B.37: Reconstructed image of the Ella-30 femur using the Kirchhoff migration algorithm. a) Reconstructed image when no data is provided using Kirchhoff migration (healthy scan - healthy scan). b) Reconstructed image of the femur using Kirchhoff migration. Red dots in all images indicate the location of the antennas and black dots indicate the true location of the bones as determined from Sim4Life.

Appendix C

Supplementary data for chapter 6

C.1 Dielectric Measurements on Phantom Materials (Unpublished work by Martin Robinson)

C.1.1 Introduction

This document details the methods used to measure the dielectric properties of phantom materials, as part of Vignesh Radhakrishnan's research into bone detection by microwaves. The methods for this particular application have not yet been published. I hope that this information will be useful for future papers and thesis chapters.

C.1.2 Method

The principle of the method is resonant cavity perturbation (RCP)[213], as shown in Figure C.1. A hollow metal cylinder with holes in top and bottom plates resonates, when empty, at approximately 1GHz, with a Q of about 3000. When a sample of dielectric material is inserted into the sensor, this generally reduces both the resonant frequency and the Q-factor. These changes are measured by a network analyser connected to the cavity. A Matlab program calculates the complex permittivity ε^* of the sample from the perturbation. The sensor must be calibrated beforehand with materials of known permittivity. Both solid and liquid samples can be measured.

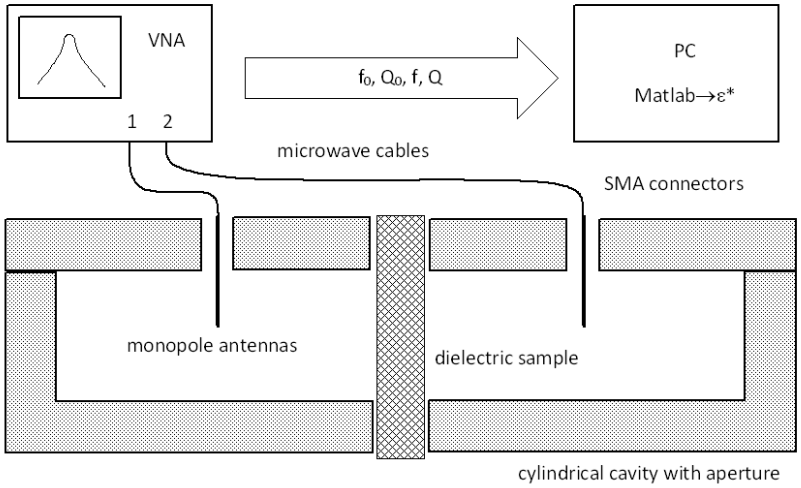

Appendix Figure C.1: Schematic of the setup for the resonant cavity perturbation method for determining dielectric properties of tissue-mimicking materials [213].

C.1.3 Cavity

The sensor is a disc-shaped cavity formed in two parts from 10mm thick aluminium. The outer diameter is 240mm and the height 47mm. The parts are tightly fixed by 24 screws, at distance 5mm from the rim and equally spaced around it. Holes of diameter 12.5mm in the centre of the two parts are aligned with the axis, to allow the sample to be easily inserted. On the top plate are two SMA connectors on opposite sides of the sample hole, at 55mm from the axis. The centre conductor of each is attached to a 8mm vertical monopole antenna inside the cavity, i.e. a short wire. By measuring the transmission coefficient S21 between the antennas over an appropriate frequency range, the resonant peak in the frequency response can be detected. A small depression in the cavity lid (not shown in figure) allows a thermocouple to be inserted so that temperature can be read with a digital thermometer (RS 52).

C.1.4 Network Analyser

Two SMA cables connect the cavity antennas to Ports 1 and 2 of a vector network analyser (VNA, also called automated network analyser, ANA). The VNA sweeps through a sequence of frequencies, at each one sending a signal out from Port 1, and measuring what is received at Port 2 (reflection measurements are also possible). The display is configured to show S21 in decibels against frequency (linear). A cavity resonance shows, on the display, as a peak in the trace. The analyser is set

up to find the resonant frequency f by continuously searching for the maximum S21. The Q of the resonance can also be displayed by setting markers at the half-power (-3dB) level; the VNA calculates Q from the ratio of f to bandwidth. The value of f typically shifts negatively by 5 to 100MHz depending on the material. The Q can be almost unchanged for a low-loss material, or fall to as low as 16. To perform a measurement, the parameters for the empty cavity f0 and Q0 are first recorded. The sample is then inserted through the holes, and the VNA display read again for the 'loaded' f and Q. Temperature is also recorded. For the measurements on phantom materials, the VNA was Hewlett Packard HP8753D, with initial settings: frequency range 1020-1060MHz, 1601 points, intermediate frequency bandwidth (IFBW) 300Hz, tracking on, search 'max', widths on, Δ-mode 'Δref=1'. If the frequency shift ever became so large that the peak went out of range, the VNA frequency span was temporarily increased.

C.1.5 Program

Data transfer is not yet automated, although this might be implemented in future. The f and Q values from the VNA are copied into a Matlab m-file, which is then run to output the required ε^*.

New m-files are created by copying an existing one and editing the parameters therein. It is possible to have several measurements in one file, providing the calibration constants are the same, or to split them over separate files.

The program first combines the changes in f and Q into a single quantity, the complex frequency shift:

$$\Delta\Omega = \frac{\Delta f}{f_0} + \frac{1}{2} j \Delta \left(\frac{1}{Q} \right) \tag{C.1}$$

The complex permittivity is then obtained from the complex frequency shift and two calibration parameters: A is 'shape', k is 'sensitivity':

$$\varepsilon^* = 1 - \frac{\Delta\Omega}{A\Delta\Omega + k} \tag{C.2}$$

The real part of ε^* is the (relative) real permittivity or dielectric constant. The imaginary part (without the minus sign) is the loss factor. The ratio of these two is the loss tangent. The conductivity (including dielectric losses) is given by:

$$\sigma = -2\pi f \,\mathrm{Im}\left(\varepsilon^*\right) \tag{C.3}$$

C.1.6 Solid and Liquid Samples

Solid samples should be machined or moulded into a cylindrical rod, length 40mm, diameter 12mm. For such samples the calibration parameters are A=0.0038324, k=0.0046842. Three plastic samples are available to perform a quality check. These should yield permittivity measurements close to the following values: PTFE 2.0901 - 0.0004i, Perspex (acrylic) 2.7516 - 0.0206i, Nylon 3.1650 - 0.0460i. Liquid samples need to be contained in a cylindrical vessel which has the same outer diameter as the solid samples. Low-loss plastics are ideal for this purpose. The 'empty' measurement is made with the vessel in place but not yet filled. For the measurements on phantom materials, the container was a hollow vial made from ABS. The calibration parameters in this case are A= 0.017561, k=0.0028196. Measurements on liquids can be checked by testing a material of known dielectric properties. Water and saline (NaCl) solutions have been well characterised and a parametric model has been published by Stogryn [244] that gives ε^* at the required concentration and temperature. A Matlab function, stog3.m, has been written to implement the Stogryn model. For example, distilled water at 20.8°C has a concentration of zero, which gives an estimated permittivity of 79.56 - 4.41i. Alternatively, data has been published by NPL [107] on the permittivity of several liquids often found in laboratories, including methanol, ethanol and ethylene glycol (ethanediol). It may be necessary to interpolate ε^* between the frequencies and temperatures of the data tables in that report.

C.1.7 Calibration

The sensor has been calibrated by observing its output for several materials of known ε^*, in order to optimise the values of A and k. A cost function is defined as the rms absolute difference between 'measured' and 'literature' values.

$$\mathrm{f_{cost}} = \sqrt{\left\langle |\varepsilon^*{}_{\mathrm{meas}} - \varepsilon^*{}_{\mathrm{lit}}|^2 \right\rangle} \tag{C.4}$$

A simple parameter sweep of A and k is performed several times, with the range being narrowed on each run until no further reduction in the cost function is seen. It is not necessary to perform a full calibration, unless the size and shape of the sample changes. Otherwise, it is sufficient to do a quality check with a test sample as detailed above.

Bibliography

[1] C-motion inc. https://c-motion.com/. Accessed: 2024-7-21.

[2] Carnegie mellon university - CMU graphics lab - motion capture library. http://mocap.cs.cmu.edu/. Accessed: 2024-7-21.

[3] Carnegie mellon university - CMU graphics lab - motion capture library. https://mocap.cs.cmu.edu/. Accessed: 2025-5-31.

[4] Connector 180° hybrid, 5 - 2300 MHz. https://www.minicircuits.com/WebStore/dashboard.html?model=ZFSCJ-2-232-S%2B. Accessed: 2024-7-21.

[5] Core & wire 180° hybrid, 500 - 2250 MHz, 50Ω. https://www.minicircuits.com/WebStore/dashboard.html?model=SYPJ-2-222%2B. Accessed: 2024-7-21.

[6] Helen hayes lower (19). https://docs.optitrack.com/markersets/lower/helen-hayes-lower-19. Accessed: 2024-7-21.

[7] ITIS database for thermal and electromagnetic parameters of biological tissues, version 2.2. https://www.researchgate.net/publication/258219467_ITIS_Database_for_thermal_and_electromagnetic_parameters_of_biological_tissues_Version_22. Accessed: 2024-7-21.

[8] Micrima. https://www.micrima.com/. Accessed: 2024-7-21.

[9] OpenSim documentation. https://simtk-confluence.stanford.edu:8443/display/OpenSim/Overview+of+OpenSim+Workflows. Accessed: 2024-7-21.

[10] OptiTrack documentation. https://docs.optitrack.com/. Accessed: 2024-9-22.

[11] Sim4Life. https://zmt.swiss/sim4life/. Accessed: 2024-7-21.

[12] V&V dipoles (¿300 MHz) SPEAG, schmid & partner engineering AG. https://speag.swiss/components/emv-and-v-sources/sar/v-and-v-dipoles-300-mhz/. Accessed: 2024-7-21.

[13] Anatomical planes. https://teachmeanatomy.info/the-basics/anatomical-terminology/planes/, March 2012. Accessed: 2024-9-20.

[14] Homepage. https://www.emtensor.com/, October 2018. Accessed: 2024-7-21.

[15] Ansys 2023 R2: Ansys HFSS, SIwave, and Q3D what's new. https://www.ansys.com/en-gb/webinars/ansys-2023-r2-ansys-hfss-siwave-and-q3d-whats-new, May 2023. Accessed: 2024-7-21.

[16] A Abubakar, W Hu, P M van den Berg, and T M Habashy. A finite-difference contrast source inversion method. *Inverse Probl.*, 24(6):065004, December 2008.

[17] Chi Young Ahn, Taeyoung Ha, and Won-Kwang Park. Kirchhoff migration for identifying unknown targets surrounded by random scatterers. *Appl. Sci. (Basel)*, 9(20):4446, October 2019.

[18] Syed Ahsan, Ziwen Guo, Zhenzhuang Miao, Ioannis Sotiriou, Maria Koutsoupidou, Efthymios Kallos, George Palikaras, and Panagiotis Kosmas. Design and experimental validation of a multiple-frequency microwave tomography system employing the DBIM-TwIST algorithm. *Sensors (Basel)*, 18(10):3491, October 2018.

[19] Massoud Akbarshahi, Anthony G Schache, Justin W Fernandez, Richard Baker, Scott Banks, and Marcus G Pandy. Non-invasive assessment of soft-tissue artifact and its effect on knee joint kinematics during functional activity. *J. Biomech.*, 43(7):1292–1301, May 2010.

[20] E J Alexander and T P Andriacchi. Correcting for deformation in skin-based marker systems. *J. Biomech.*, 34(3):355–361, March 2001.

[21] Mohanad Alkhodari, Amer Zakaria, and Nasser Qaddoumi. Guidelines towards a wearable microwave tomography system. In *2019 IEEE Asia-Pacific Microwave Conference (APMC)*, pages 1423–1425. IEEE, December 2019.

[22] Mohanad Alkhodari, Amer Zakaria, and Nasser Qaddoumi. Monitoring bone density using microwave tomography of human legs: A numerical feasibility study. *Sensors (Basel)*, 21(21):7078, October 2021.

[23] Bilal Amin, Atif Shahzad, Martin O'Halloran, and Muhammad Adnan Elahi. Microwave bone imaging: A preliminary investigation on numerical bone phantoms for bone health monitoring. *Sensors (Basel)*, 20(21):6320, November 2020.

[24] Bilal Amin, Atif Shahzad, Martin O'halloran, Barry Mcdermott, and Adnan Elahi. Experimental validation of microwave imaging prototype and DBIM-IMATCS algorithm for bone health monitoring. *IEEE Access*, 10:42589–42600, 2022.

[25] Reza K Amineh, Maryam Ravan, Ali Khalatpour, and Natalia K Nikolova. Three-dimensional near-field microwave holography using reflected and transmitted signals. *IEEE Trans. Antennas Propag.*, 59(12):4777–4789, December 2011.

[26] Reza K Amineh, Maryam Ravan, Aastha Trehan, and Natalia K Nikolova. Near-field microwave imaging based on aperture raster scanning with TEM horn antennas. *IEEE Trans. Antennas Propag.*, 59(3):928–940, March 2011.

[27] Andrea Ancillao, Erwin Aertbeliën, and Joris De Schutter. Effect of the soft tissue artifact on marker measurements and on the calculation of the helical axis of the knee during a gait cycle: A study on the CAMS-knee data set. *Hum. Mov. Sci.*, 80(102866):102866, December 2021.

[28] M S Andersen, M Damsgaard, and J Rasmussen. Kinematic analysis of over-determinate biomechanical systems. *Comput. Methods Biomech. Biomed. Engin.*, 12(4):371–384, August 2009.

[29] Michael S Andersen, Daniel L Benoit, Michael Damsgaard, Dan K Ramsey, and John Rasmussen. Do kinematic models reduce the effects of soft tissue artefacts in skin marker-based motion analysis? an in vivo study of knee kinematics. *J. Biomech.*, 43(2):268–273, January 2010.

[30] Michael S Andersen, Michael Damsgaard, John Rasmussen, Dan K Ramsey, and Daniel L Benoit. A linear soft tissue artefact model for human movement analysis: proof of concept using in vivo data. *Gait Posture*, 35(4):606–611, April 2012.

[31] T P Andriacchi, E J Alexander, M K Toney, C Dyrby, and J Sum. A point cluster method for in vivo motion analysis: applied to a study of knee kinematics. *J. Biomech. Eng.*, 120(6):743–749, December 1998.

[32] S Ausejo, Ángel Suescun, J Celigueta, and Xuguang Wang. Robust human motion reconstruction in the presence of missing markers and the absence of markers for some body segments. July 2006.

[33] Ko Ayusawa, Yosuke Ikegami, and Yoshihiko Nakamura. Simultaneous global inverse kinematics and geometric parameter identification of human skeletal model from motion capture data. *Mech. Mach. Theory*, 74:274–284, April 2014.

[34] Carl Baker. Obesity statistics. Technical Report 03336, House of Commons, March 2022.

[35] Duncan Bakke and Thor Besier. Shape model constrained scaling improves repeatability of gait data. *J. Biomech.*, 107(109838):109838, June 2020.

[36] Duncan Bakke and Thor Besier. Shape-model scaled gait models can neglect segment markers without consequential change to inverse kinematics results. *J. Biomech.*, 137(111086):111086, May 2022.

[37] Lee Barber, Chris Carty, Luca Modenese, John Walsh, Roslyn Boyd, and Glen Lichtwark. Medial gastrocnemius and soleus muscle-tendon unit, fascicle, and tendon interaction during walking in children with cerebral palsy. *Dev. Med. Child Neurol.*, 59(8):843–851, August 2017.

[38] Arnaud Barre and Stéphane Armand. Biomechanical ToolKit: Open-source framework to visualize and process biomechanical data. *Comput. Methods Programs Biomed.*, 114(1):80–87, April 2014.

[39] Arnaud Barre, Jean-Philippe Thiran, Brigitte M Jolles, Nicolas Theumann, and Kamiar Aminian. Soft tissue artifact assessment during treadmill walking in subjects with total knee arthroplasty. *IEEE Trans. Biomed. Eng.*, 60(11):3131–3140, November 2013.

[40] Arnaud Barré, Brigitte M Jolles, Nicolas Theumann, and Kamiar Aminian. Soft tissue artifact distribution on lower limbs during treadmill gait: Influence of skin markers' location on cluster design. *J. Biomech.*, 48(10):1965–1971, July 2015.

[41] Alexander S Beaverstone, Denys S Shumakov, and Natalia K Nikolova. Frequency-domain integral equations of scattering for complex scalar responses. *IEEE Trans. Microw. Theory Tech.*, 65(4):1120–1132, April 2017.

[42] Mickaël Begon, Michael Skipper Andersen, and Raphaël Dumas. Multibody kinematics optimization for the estimation of upper and lower limb human

joint kinematics: A systematized methodological review. *J. Biomech. Eng.*, 140(3), March 2018.

[43] Mickaël Begon, Colombe Bélaise, Alexandre Naaim, Arne Lundberg, and Laurence Chèze. Multibody kinematics optimization with marker projection improves the accuracy of the humerus rotational kinematics. *J. Biomech.*, 62:117–123, September 2017.

[44] Mickaël Begon, Fabien Dal Maso, Anton Arndt, and Tony Monnet. Can optimal marker weightings improve thoracohumeral kinematics accuracy? *J. Biomech.*, 48(10):2019–2025, July 2015.

[45] D L Benoit, M Damsgaard, and M S Andersen. Surface marker cluster translation, rotation, scaling and deformation: Their contribution to soft tissue artefact and impact on knee joint kinematics. *J. Biomech.*, 48(10):2124–2129, July 2015.

[46] Daniel L Benoit, Dan K Ramsey, Mario Lamontagne, Lanyi Xu, Per Wretenberg, and Per Renström. Effect of skin movement artifact on knee kinematics during gait and cutting motions measured in vivo. *Gait Posture*, 24(2):152–164, October 2006.

[47] Sina Beyraghi, Fardin Ghorbani, Javad Shabanpour, Mir Emad Lajevardi, Vahid Nayyeri, Pai-Yen Chen, and Omar M Ramahi. Microwave bone fracture diagnosis using deep neural network. *Sci. Rep.*, 13(1):16957, October 2023.

[48] Y Blache, R Dumas, A Lundberg, and M Begon. Main component of soft tissue artifact of the upper-limbs with respect to different functional, daily life and sports movements. *J. Biomech.*, 62:39–46, September 2017.

[49] Tecla Bonci, Valentina Camomilla, Raphael Dumas, Laurence Chèze, and Aurelio Cappozzo. A soft tissue artefact model driven by proximal and distal joint kinematics. *J. Biomech.*, 47(10):2354–2361, July 2014.

[50] E J Bond, Xu Li, S C Hagness, and B D Van Veen. Microwave imaging via space-time beamforming for early detection of breast cancer. *IEEE Trans. Antennas Propag.*, 51(8):1690–1705, August 2003.

[51] V Bonnet, R Dumas, A Cappozzo, V Joukov, G Daune, D Kulić, P Fraisse, S Andary, and G Venture. A constrained extended kalman filter for the optimal estimate of kinematics and kinetics of a sagittal symmetric exercise. *J. Biomech.*, 62:140–147, September 2017.

[52] Vincent Bonnet, Vincent Richard, Valentina Camomilla, Gentiane Venture, Aurelio Cappozzo, and Raphaël Dumas. Joint kinematics estimation using a multi-body kinematics optimisation and an extended kalman filter, and embedding a soft tissue artefact model. *J. Biomech.*, 62:148–155, September 2017.

[53] Christopher Buckley, Lisa Alcock, Ríona McArdle, Rana Zia Ur Rehman, Silvia Del Din, Claudia Mazzà, Alison J Yarnall, and Lynn Rochester. The role of movement analysis in diagnosing and monitoring neurodegenerative conditions: Insights from gait and postural control. *Brain Sci.*, 9(2):34, February 2019.

[54] V Camomilla, T Bonci, and A Cappozzo. Soft tissue displacement over pelvic anatomical landmarks during 3-D hip movements. *J. Biomech.*, 62:14–20, September 2017.

[55] V Camomilla, T Bonci, R Dumas, L Chèze, and A Cappozzo. A model of the soft tissue artefact rigid component. *J. Biomech.*, 48(10):1752–1759, July 2015.

[56] Valentina Camomilla, Andrea Cereatti, Laurence Chèze, and Aurelio Cappozzo. A hip joint kinematics driven model for the generation of realistic thigh soft tissue artefacts. *J. Biomech.*, 46(3):625–630, February 2013.

[57] Valentina Camomilla, Marco Donati, Rita Stagni, and Aurelio Cappozzo. Non-invasive assessment of superficial soft tissue local displacements during movement: a feasibility study. *J. Biomech.*, 42(7):931–937, May 2009.

[58] Angelo Cappello, Rita Stagni, Silvia Fantozzi, and Alberto Leardini. Soft tissue artifact compensation in knee kinematics by double anatomical landmark calibration: performance of a novel method during selected motor tasks. *IEEE Trans. Biomed. Eng.*, 52(6):992–998, June 2005.

[59] A Cappozzo, F Catani, U Della Croce, and A Leardini. Position and orientation in space of bones during movement: anatomical frame definition and determination. *Clin. Biomech. (Bristol, Avon)*, 10(4):171–178, June 1995.

[60] P Carberry, A Nazarian, and S Makarov. Cavity-backed slotted patch antennas radiating into a lossy human body. In *2016 10th European Conference on Antennas and Propagation (EuCAP)*, pages 1–5. IEEE, April 2016.

[61] CDC. Causes of obesity. `https://www.cdc.gov/obesity/basics/causes.html`, April 2022. Accessed: 2022-10-14.

[62] Francesco Cenni, Nathalie Alexander, Iida Laatikainen-Raussi, Maria Sukanen, and Taija Finni. Wearing an ultrasound probe during walking does not influence lower limb joint kinematics in adolescents with cerebral palsy and typically developing peers. *Gait Posture*, 112:134–139, July 2024.

[63] P Cerveri, A Pedotti, and G Ferrigno. Robust recovery of human motion from video using kalman filters and virtual humans. *Hum. Mov. Sci.*, 22(3):377–404, August 2003.

[64] P Cerveri, A Pedotti, and G Ferrigno. Kinematical models to reduce the effect of skin artifacts on marker-based human motion estimation. *J. Biomech.*, 38(11):2228–2236, November 2005.

[65] P Cerveri, M Rabuffetti, A Pedotti, and G Ferrigno. Real-time human motion estimation using biomechanical models and non-linear state-space filters. *Med. Biol. Eng. Comput.*, 41(2):109–123, March 2003.

[66] N Chahat, M Zhadobov, R Sauleau, and K Mahdjoubi. Parametric analysis of on-body dual-band antenna performance: Dependence on the human body morphology. In *Proceedings of the 5th European Conference on Antennas and Propagation (EUCAP)*, pages 437–440. IEEE, April 2011.

[67] Rohit Chandra, Anders J Johansson, Mats Gustafsson, and Fredrik Tufvesson. A microwave imaging-based technique to localize an in-body RF source for biomedical applications. *IEEE Trans. Biomed. Eng.*, 62(5):1231–1241, May 2015.

[68] Rohit Chandra, Huiyuan Zhou, Ilangko Balasingham, and Ram M Narayanan. On the opportunities and challenges in microwave medical sensing and imaging. *IEEE Trans. Biomed. Eng.*, 62(7):1667–1682, July 2015.

[69] W C Chew and Y M Wang. Reconstruction of two-dimensional permittivity distribution using the distorted born iterative method. *IEEE Trans. Med. Imaging*, 9(2):218–225, 1990.

[70] Andreas Christ, Wolfgang Kainz, Eckhart G Hahn, Katharina Honegger, Marcel Zefferer, Esra Neufeld, Wolfgang Rascher, Rolf Janka, Werner Bautz, Ji Chen, Berthold Kiefer, Peter Schmitt, Hans-Peter Hollenbach, Jianxiang Shen, Michael Oberle, Dominik Szczerba, Anthony Kam, Joshua W Guag, and Niels Kuster. The virtual family–development of surface-based anatomical models of two adults and two children for dosimetric simulations. *Phys. Med. Biol.*, 55(2):N23–38, January 2010.

[71] L Chèze, B J Fregly, and J Dimnet. A solidification procedure to facilitate kinematic analyses based on video system data. *J. Biomech.*, 28(7):879–884, July 1995.

[72] J Clément, N Hagemeister, R Dumas, M Kanhonou, and J A de Guise. Influence of biomechanical multi-joint models used in global optimisation to estimate healthy and osteoarthritis knee kinematics. *Comput. Methods Biomech. Biomed. Engin.*, 17 Suppl 1(sup1):76–77, 2014.

[73] Julien Clément, Raphaël Dumas, Nicola Hagemeister, and Jaques A de Guise. Soft tissue artifact compensation in knee kinematics by multi-body optimization: Performance of subject-specific knee joint models. *J. Biomech.*, 48(14):3796–3802, November 2015.

[74] John Cockcroft, Quinette Louw, and Richard Baker. Proximal placement of lateral thigh skin markers reduces soft tissue artefact during normal gait using the conventional gait model. *Comput. Methods Biomech. Biomed. Engin.*, 19(14):1497–1504, November 2016.

[75] Thomas D Collins, Salim N Ghoussayni, David J Ewins, and Jenny A Kent. A six degrees-of-freedom marker set for gait analysis: repeatability and comparison with a modified helen hayes set. *Gait Posture*, 30(2):173–180, August 2009.

[76] Andre Costa Batista, Lucas S Batista, and Ricardo Adriano. A quadratic programming approach for microwave imaging. *IEEE Trans. Antennas Propag.*, 69(8):4923–4934, August 2021.

[77] Neil J Cronin and Glen Lichtwark. The use of ultrasound to study muscle-tendon function in human posture and locomotion. *Gait Posture*, 37(3):305–312, March 2013.

[78] Michael Damsgaard, John Rasmussen, Søren Tørholm Christensen, Egidijus Surma, and Mark de Zee. Analysis of musculoskeletal systems in the AnyBody modeling system. *Simul. Model. Pract. Theory*, 14(8):1100–1111, November 2006.

[79] Roy B Davis, III, Sylvia Õunpuu, Dennis Tyburski, and James R Gage. A gait analysis data collection and reduction technique. *Hum. Mov. Sci.*, 10(5):575–587, October 1991.

[80] F De Groote, T De Laet, I Jonkers, and J De Schutter. Kalman smoothing improves the estimation of joint kinematics and kinetics in marker-based human gait analysis. *J. Biomech.*, 41(16):3390–3398, December 2008.

[81] Scott L Delp, Frank C Anderson, Allison S Arnold, Peter Loan, Ayman Habib, Chand T John, Eran Guendelman, and Darryl G Thelen. OpenSim: open-source software to create and analyze dynamic simulations of movement. *IEEE Trans. Biomed. Eng.*, 54(11):1940–1950, November 2007.

[82] A J Devaney. Time reversal imaging of obscured targets from multistatic data. *IEEE Trans. Antennas Propag.*, 53(5):1600–1610, May 2005.

[83] T Dreher, S Wolf, F Braatz, D Patikas, and L Döderlein. Internal rotation gait in spastic diplegia–critical considerations for the femoral derotation osteotomy. *Gait Posture*, 26(1):25–31, June 2007.

[84] R Dumas, V Camomilla, T Bonci, L Cheze, and A Cappozzo. Generalized mathematical representation of the soft tissue artefact. *J. Biomech.*, 47(2):476–481, January 2014.

[85] R Dumas and L Chèze. 3D inverse dynamics in non-orthonormal segment coordinate system. *Med. Biol. Eng. Comput.*, 45(3):315–322, March 2007.

[86] James J Dunne, Thomas K Uchida, Thor F Besier, Scott L Delp, and Ajay Seth. A marker registration method to improve joint angles computed by constrained inverse kinematics. *PLoS One*, 16(5):e0252425, May 2021.

[87] Sonia Duprey, Laurence Cheze, and Raphaël Dumas. Influence of joint constraints on lower limb kinematics estimation from skin markers using global optimization. *J. Biomech.*, 43(14):2858–2862, October 2010.

[88] Muhammad Adnan Elahi, Declan O'Loughlin, Benjamin R Lavoie, Martin Glavin, Edward Jones, Elise C Fear, and Martin O'Halloran. Evaluation of image reconstruction algorithms for confocal microwave imaging: Application to patient data. *Sensors (Basel)*, 18(6), May 2018.

[89] Ahmed A Elsheikh, George W V Cross, Jonathan Wright, William David Goodier, and Peter Calder. Miserable malalignment syndrome associated knee pain: a case for infra-tubercle tibial de-rotation osteotomy using an external fixator. *J. Orthop. Surg. Res.*, 18(1):768, October 2023.

[90] Elise C Fear, Xu Li, Susan C Hagness, and Maria A Stuchly. Confocal microwave imaging for breast cancer detection: localization of tumors in three dimensions. *IEEE Trans. Biomed. Eng.*, 49(8):812–822, August 2002.

[91] Alessandro Fedeli, Valentina Schenone, Andrea Randazzo, Matteo Pastorino, Tommy Henriksson, and Serguei Semenov. Nonlinear S-parameters inversion for stroke imaging. *IEEE Trans. Microw. Theory Tech.*, 69(3):1760–1771, March 2021.

[92] Joao M Felicio, Jose M Bioucas-Dias, Jorge R Costa, and Carlos A Fernandes. Microwave breast imaging using a dry setup. *IEEE Trans. Comput. Imaging*, 6:167–180, 2020.

[93] Alberto Ferrari, Maria Grazia Benedetti, Esteban Pavan, Carlo Frigo, Dario Bettinelli, Marco Rabuffetti, Paolo Crenna, and Alberto Leardini. Quantitative comparison of five current protocols in gait analysis. *Gait Posture*, 28(2):207–216, August 2008.

[94] Niccolo M Fiorentino, Penny R Atkins, Michael J Kutschke, K Bo Foreman, and Andrew E Anderson. Soft tissue artifact causes underestimation of hip joint kinematics and kinetics in a rigid-body musculoskeletal model. *J. Biomech.*, 108(109890):109890, July 2020.

[95] Niccolo M Fiorentino, Penny R Atkins, Michael J Kutschke, K Bo Foreman, and Andrew E Anderson. In-vivo quantification of dynamic hip joint center errors and soft tissue artifact. *Gait Posture*, 50:246–251, October 2016.

[96] Niccolo M Fiorentino, Penny R Atkins, Michael J Kutschke, Justine M Goebel, K Bo Foreman, and Andrew E Anderson. Soft tissue artifact causes significant errors in the calculation of joint angles and range of motion at the hip. *Gait Posture*, 55:184–190, June 2017.

[97] Vincent Fohanno, Mickaël Begon, Patrick Lacouture, and Floren Colloud. Estimating joint kinematics of a whole body chain model with closed-loop constraints. *Multibody Syst. Dyn.*, 31(4):433–449, April 2014.

[98] Vincent Fohanno, Patrick Lacouture, and Floren Colloud. Improvement of upper extremity kinematics estimation using a subject-specific forearm model implemented in a kinematic chain. *J. Biomech.*, 46(6):1053–1059, April 2013.

[99] Vincent Fohanno, Patrick Lacouture, and Floren Colloud. Influence of the marker set on the reconstruction of the whole-body kinematics. *Mov. Sport Sci.*, 90(90):29–36, 2015.

[100] S Gabriel, R W Lau, and C Gabriel. The dielectric properties of biological tissues: III. parametric models for the dielectric spectrum of tissues. *Phys. Med. Biol.*, 41(11):2271–2293, November 1996.

[101] Xavier Gasparutto, Nicola Sancisi, Eric Jacquelin, Vincenzo Parenti-Castelli, and Raphaël Dumas. Validation of a multi-body optimization with knee kinematic models including ligament constraints. *J. Biomech.*, 48(6):1141–1146, April 2015.

[102] J M Geffrin and P Sabouroux. Continuing with the fresnel database: experimental setup and improvements in 3D scattering measurements. *Inverse Probl.*, 25(2):024001, February 2009.

[103] Jean-Michel Geffrin, Pierre Sabouroux, and Christelle Eyraud. Free space experimental scattering database continuation: experimental set-up and measurement precision. *Inverse Problems*, 21(6):S117, November 2005.

[104] Colin Gilmore, Puyan Mojabi, Amer Zakaria, Majid Ostadrahimi, Cameron Kaye, Sima Noghanian, Lotfollah Shafai, Stephen Pistorius, and Joe LoVetri. A wideband microwave tomography system with a novel frequency selection procedure. *IEEE Trans. Biomed. Eng.*, 57(4):894–904, April 2010.

[105] Colin Gilmore, Amer Zakaria, Stephen Pistorius, and Joe Lovetri. Microwave imaging of human forearms: pilot study and image enhancement. *Int. J. Biomed. Imaging*, 2013:673027, August 2013.

[106] Marie-Christine Gosselin, Esra Neufeld, Heidi Moser, Eveline Huber, Silvia Farcito, Livia Gerber, Maria Jedensjö, Isabel Hilber, Fabienne Di Gennaro, Bryn Lloyd, Emilio Cherubini, Dominik Szczerba, Wolfgang Kainz, and Niels Kuster. Development of a new generation of high-resolution anatomical models for medical device evaluation: the virtual population 3.0. *Phys. Med. Biol.*, 59(18):5287–5303, September 2014.

[107] A P Gregory and R N Clarke. Tables of the complex permittivity of dielectric reference liquids at frequencies up to 5 GHz. September 2001.

[108] E Grimpampi, V Camomilla, A Cereatti, P de Leva, and A Cappozzo. Metrics for describing soft-tissue artefact and its effect on pose, size, and shape of marker clusters. *IEEE Trans. Biomed. Eng.*, 61(2):362–367, February 2014.

[109] Laura Guerrero Orozco, Lars Peterson, and Andreas Fhager. Microwave antenna system for muscle rupture imaging with a lossy gel to reduce multipath interference. *Sensors (Basel)*, 22(11):4121, May 2022.

[110] W Guo, S Ahsan, M He, M Koutsoupidou, and P Kosmas. Printed monopole antenna designs for a microwave head scanner. In *2018 18th Mediterranean Microwave Symposium (MMS)*, pages 384–386. IEEE, October 2018.

[111] P Hasgall, E Neufeld, E Neufeld, Marie-Christine Gosselin, A Klingenbock, N Kuster, P Hasgall, and Marie-Christine Gosselin. IT'IS database for thermal and electromagnetic parameters of biological tissues. 2012.

[112] Mark Haynes, Steven Clarkson, and Mahta Moghaddam. Electromagnetic inverse scattering algorithm and experiment using absolute source characterization. *IEEE Trans. Antennas Propag.*, 60(4):1854–1867, April 2012.

[113] Mark Haynes and Mahta Moghaddam. Multipole and S-parameter antenna and propagation model. *IEEE Trans. Antennas Propag.*, 59(1):225–235, January 2011.

[114] Mark Haynes and Mahta Moghaddam. Vector green'S function for S-parameter measurements of the electromagnetic volume integral equation. In *2011 IEEE International Symposium on Antennas and Propagation (APSURSI)*, pages 1100–1103. IEEE, July 2011.

[115] Mark Haynes, John Stang, and Mahta Moghaddam. Real-time microwave imaging of differential temperature for thermal therapy monitoring. *IEEE Trans. Biomed. Eng.*, 61(6):1787–1797, June 2014.

[116] Lee Herrington, Islay McEwan, and Jeanette Thom. Quantification of patella position by ultrasound scanning and its criterion validity. *Ultrasound Med. Biol.*, 32(12):1833–1836, December 2006.

[117] Tetsuo Higuchi, Yuji Arai, Hisatake Takamiya, Tatsuya Miyamoto, Daisaku Tokunaga, and Toshikazu Kubo. An analysis of the medial patellofemoral ligament length change pattern using open-MRI. *Knee Surg. Sports Traumatol. Arthrosc.*, 18(11):1470–1475, November 2010.

[118] John P Holden, John A Orsini, Karen Lohmann Siegel, Thomas M Kepple, Lynn H Gerber, and Steven J Stanhope. Surface movement errors in shank kinematics and knee kinetics during gait. *Gait Posture*, 5(3):217–227, June 1997.

[119] B Horsak, B Pobatschnig, C Schwab, A Baca, A Kranzl, and H Kainz. Reliability of joint kinematic calculations based on direct kinematic and inverse kinematic models in obese children. *Gait Posture*, 66:201–207, October 2018.

[120] Brian Horsak, Caterine Schwab, Fabien Leboeuf, and Andreas Kranzl. Reliability of walking and stair climbing kinematics in a young obese population using a standard kinematic and the CGM2 model. *Gait Posture*, 83:96–99, January 2021.

[121] Amran Hossain, Mohammad Tariqul Islam, Gan Kok Beng, Saad Bin Abul Kashem, Mohamed S Soliman, Norbahiah Misran, and Muhammad E H Chowdhury. Microwave brain imaging system to detect brain tumor using

metamaterial loaded stacked antenna array. *Sci. Rep.*, 12(1):16478, October 2022.

[122] Md Delwar Hossain, Ananda Sanagavarapu Mohan, and Mohammed Jainul Abedin. Beamspace time-reversal microwave imaging for breast cancer detection. *IEEE Antennas Wirel. Propag. Lett.*, 12:241–244, 2013.

[123] Songming Hou, Knut Solna, and Hongkai Zhao. Imaging of location and geometry for extended targets using the response matrix. *J. Comput. Phys.*, 199(1):317–338, September 2004.

[124] Songming Hou, Knut Solna, and Hongkai Zhao. A direct imaging algorithm for extended targets. *Inverse Probl.*, 22(4):1151–1178, August 2006.

[125] M T Islam, M Z Mahmud, M Tarikul Islam, S Kibria, and M Samsuzzaman. A low cost and portable microwave imaging system for breast tumor detection using UWB directional antenna array. *Sci. Rep.*, 9(1):15491, October 2019.

[126] Md Shazzdatul Islam. *Development of flexible antenna for breast cancer application*. PhD thesis, 2020.

[127] Mohammad Shahidul Islam, Mohammad Tariqul Islam, and Ali F Almutairi. A portable non-invasive microwave based head imaging system using compact metamaterial loaded 3D unidirectional antenna for stroke detection. *Sci. Rep.*, 12(1):8895, May 2022.

[128] Kohta Ito, Koh Hosoda, Masahiro Shimizu, Shuhei Ikemoto, Shinnosuke Kume, Takeo Nagura, Nobuaki Imanishi, Sadakazu Aiso, Masahiro Jinzaki, and Naomichi Ogihara. Direct assessment of 3D foot bone kinematics using biplanar X-ray fluoroscopy and an automatic model registration method. *J. Foot Ankle Res.*, 8(1):21, June 2015.

[129] Rui Jia, Stephen Mellon, Paul Monk, David Murray, and J Alison Noble. A computer-aided tracking and motion analysis with ultrasound (CAT & MAUS) system for the description of hip joint kinematics. *Int. J. Comput. Assist. Radiol. Surg.*, 11(11):1965–1977, November 2016.

[130] Rui Jia, Paul Monk, David Murray, J Alison Noble, and Stephen Mellon. CAT & MAUS: A novel system for true dynamic motion measurement of underlying bony structures with compensation for soft tissue movement. *J. Biomech.*, 62:156–164, September 2017.

[131] H Kainz, L Modenese, D G Lloyd, S Maine, H P J Walsh, and C P Carty. Joint kinematic calculation based on clinical direct kinematic versus inverse kinematic gait models. *J. Biomech.*, 49(9):1658–1669, June 2016.

[132] Gursharan Kalsi, Nicola R Fry, and Adam P Shortland. Gastrocnemius muscle-tendon interaction during walking in typically-developing adults and children, and in children with spastic cerebral palsy. *J. Biomech.*, 49(14):3194–3199, October 2016.

[133] Sangwoo Kang, Seongje Chae, and Won-Kwang Park. A study on the orthogonality sampling method corresponding to the observation directions configuration. *Results Phys.*, 33(105108):105108, February 2022.

[134] Olympia Karadima, Mohammed Rahman, Ioannis Sotiriou, Navid Ghavami, Pan Lu, Syed Ahsan, and Panos Kosmas. Experimental validation of microwave tomographywith the DBIM-TwIST algorithm for brain StrokeDetection and classification. *Sensors (Basel)*, 20(3):840, February 2020.

[135] Banafsheh Khalesi, Gianluigi Tiberi, Navid Ghavami, Mohammad Ghavami, and Sandra Dudley. Skin cancer detection through microwaves: Validation on phantom measurements. In *2018 IEEE International Conference on Imaging Systems and Techniques (IST)*, pages 1–6. IEEE, October 2018.

[136] Mei-Ying Kuo, Tsung-Yuan Tsai, Cheng-Chung Lin, Tung-Wu Lu, Horng-Chaung Hsu, and Wu-Chung Shen. Influence of soft tissue artifacts on the calculated kinematics and kinetics of total knee replacements during sit-to-stand. *Gait Posture*, 33(3):379–384, March 2011.

[137] Maria Laitenberger, Maxime Raison, Delphine Périé, and Mickael Begon. Refinement of the upper limb joint kinematics and dynamics using a subject-specific closed-loop forearm model. *Multibody Syst. Dyn.*, 33(4):413–438, April 2015.

[138] Giuliano Lamberto, Saulo Martelli, Aurelio Cappozzo, and Claudia Mazzà. To what extent is joint and muscle mechanics predicted by musculoskeletal models sensitive to soft tissue artefacts? *J. Biomech.*, 62:68–76, September 2017.

[139] Timo Lauteslager, Mathias Tommer, Tor S Lande, and Timothy G Constandinou. Dynamic microwave imaging of the cardiovascular system using ultra-wideband radar-on-chip devices. *IEEE Trans. Biomed. Eng.*, 69(9):2935–2946, September 2022.

[140] Alberto Leardini, Claudio Belvedere, Fabrizio Nardini, Nicola Sancisi, Michele Conconi, and Vincenzo Parenti-Castelli. Kinematic models of lower limb joints for musculo-skeletal modelling and optimization in gait analysis. *J. Biomech.*, 62:77–86, September 2017.

[141] Alberto Leardini, Lorenzo Chiari, Ugo Della Croce, and Aurelio Cappozzo. Human movement analysis using stereophotogrammetry. part 3. soft tissue artifact assessment and compensation. *Gait Posture*, 21(2):212–225, February 2005.

[142] F Leboeuf, R Baker, A Barré, J Reay, R Jones, and M Sangeux. The conventional gait model, an open-source implementation that reproduces the past but prepares for the future. *Gait Posture*, 69:235–241, March 2019.

[143] F Leboeuf, A Barre, K Aminian, and M Sangeux. On the accuracy of the conventional gait model: Distinction between marker misplacement and soft tissue artefact errors. *J. Biomech.*, 159(111774):111774, October 2023.

[144] Kwang-Jae Lee, Seong-Ho Son, and Won-Kwang Park. A real-time microwave imaging of unknown anomaly with and without diagonal elements of scattering matrix. *Results Phys.*, 17(103104):103104, June 2020.

[145] F Lefebvre, I Rogowski, N Long, and Y Blache. Influence of marker weights optimization on scapular kinematics estimated with a multibody kinematic optimization. *J. Biomech.*, 159(111795):111795, October 2023.

[146] Zachary F Lerner, Wayne J Board, and Raymond C Browning. Effects of an obesity-specific marker set on estimated muscle and joint forces in walking. *Med. Sci. Sports Exerc.*, 46(6):1261–1267, June 2014.

[147] Zachary F Lerner, Wayne J Board, and Raymond C Browning. Effects of obesity on lower extremity muscle function during walking at two speeds. *Gait Posture*, 39(3):978–984, March 2014.

[148] X Li, S K Davis, S C Hagness, D W vanderWeide, and B D VanVeen. Microwave imaging via space–time beamforming: Experimental investigation of tumor detection in multilayer breast phantoms. *IEEE Trans. Microw. Theory Tech.*, 52(8):1856–1865, August 2004.

[149] Hooi Been Lim, Nguyen Thi Tuyet Nhung, Er-Ping Li, and Nguyen Duc Thang. Confocal microwave imaging for breast cancer detection: delay-multiply-and-sum image reconstruction algorithm. *IEEE Trans. Biomed. Eng.*, 55(6):1697–1704, June 2008.

[150] Yeong-Fwu Lin, Mei-Hwa Jan, Da-Hon Lin, and Cheng-Kung Cheng. Different effects of femoral and tibial rotation on the different measurements of patella tilting: An axial computed tomography study. *J. Orthop. Surg. Res.*, 3(1):5, February 2008.

[151] Xiao-Fei Liu, Bing-Zhong Wang, and Le-Wei Li. Time reversal DORT and MUSIC methods for extended targets detection and imaging. In *2013 IEEE INTERNATIONAL CONFERENCE ON MICROWAVE TECHNOLOGY & COMPUTATIONAL ELECTROMAGNETICS*, pages 304–307. IEEE, August 2013.

[152] Claire Livet, Théo Rouvier, Christophe Sauret, Hélène Pillet, Georges Dumont, and Charles Pontonnier. A penalty method for constrained multibody kinematics optimisation using a levenberg-marquardt algorithm. *Comput. Methods Biomech. Biomed. Engin.*, 26(7):864–875, May 2023.

[153] T W Lu and J J O'Connor. Bone position estimation from skin marker co-ordinates using global optimisation with joint constraints. *J. Biomech.*, 32(2):129–134, February 1999.

[154] Tung-Wu Lu and Chu-Fen Chang. Biomechanics of human movement and its clinical applications. *Kaohsiung J. Med. Sci.*, 28(2 Suppl):S13–25, February 2012.

[155] Morten Enemark Lund, Michael Skipper Andersen, Mark de Zee, and John Rasmussen. Scaling of musculoskeletal models from static and dynamic trials. *Int. Biomech.*, 2(1):1–11, January 2015.

[156] Sergey N Makarov, Gregory M Noetscher, Seth Arum, Robert Rabiner, and Ara Nazarian. Concept of a radiofrequency device for osteopenia/osteoporosis screening. *Sci. Rep.*, 10(1):3540, February 2020.

[157] Giulia Mantovani and Mario Lamontagne. How different marker sets affect joint angles in inverse kinematics framework. *J. Biomech. Eng.*, 139(4), April 2017.

[158] Samuel E Masters and John H Challis. The effects of wobbling mass components on joint dynamics during running. *J. Appl. Biomech.*, 38(2):69–75, April 2022.

[159] M A Masum, M R Pickering, A J Lambert, J M Scarvell, and P N Smith. Multi-slice ultrasound image calibration of an intelligent skin-marker for soft tissue artefact compensation. *J. Biomech.*, 62:165–171, September 2017.

[160] Md Abdullah Masum, Andrew J Lambert, Mark R Pickering, J M Scarvell, and P N Smith. Precision analysis of an intelligent skin marker for non-invasive kinematic analysis of knee joints. In *2012 9th IEEE International Symposium on Biomedical Imaging (ISBI)*, pages 1495–1498. IEEE, May 2012.

[161] Md Abdullah Masum, Mark Pickering, Andrew Lambert, Jennie Scarvell, and Paul Smith. Accuracy assessment of tri-plane B-mode ultrasound for non-invasive 3D kinematic analysis of knee joints. *Biomed. Eng. Online*, 13(1):122, August 2014.

[162] Viktor Mattsson, Leanne L G C Ackermans, Bappaditya Mandal, Mauricio D Perez, Maud A M Vesseur, Paul Meaney, Jan A Ten Bosch, Taco J Blokhuis, and Robin Augustine. MAS: Standalone microwave resonator to assess muscle quality. *Sensors (Basel)*, 21(16):5485, August 2021.

[163] Jennifer L McGinley, Richard Baker, Rory Wolfe, and Meg E Morris. The reliability of three-dimensional kinematic gait measurements: a systematic review. *Gait Posture*, 29(3):360–369, April 2009.

[164] P M Meaney, K D Paulsen, B W Pogue, and M I Miga. Microwave image reconstruction utilizing log-magnitude and unwrapped phase to improve high-contrast object recovery. *IEEE Trans. Med. Imaging*, 20(2):104–116, February 2001.

[165] Paul M Meaney, Douglas Goodwin, Amir H Golnabi, Tian Zhou, Matthew Pallone, Shireen D Geimer, Gregory Burke, and Keith D Paulsen. Clinical microwave tomographic imaging of the calcaneus: a first-in-human case study of two subjects. *IEEE Trans. Biomed. Eng.*, 59(12):3304–3313, December 2012.

[166] Maryam Mohtajeb, Jolanda Cibere, Angelo Graffos, Michelle Mony, Honglin Zhang, Michael A Hunt, and David R Wilson. Open MRI validation of a hip model driven with subject-specific motion capture data in predicting anterior femoroacetabular clearance. *BMC Musculoskelet. Disord.*, 22(1):972, November 2021.

[167] P Mojabi and J LoVetri. Microwave biomedical imaging using the multiplicative regularized gauss–newton inversion. *IEEE Antennas Wirel. Propag. Lett.*, 8:645–648, 2009.

[168] Pedram Mojabi and Joe LoVetri. Experimental evaluation of composite tissue-type ultrasound and microwave imaging. *IEEE J. Multiscale Multiphys. Comput. Tech.*, 4:119–132, 2019.

[169] Puyan Mojabi. Investigation and development of algorithms and techniques for microwave tomography. April 2010.

[170] Puyan Mojabi, Majid Ostadrahimi, Lotfollah Shafai, and Joe LoVetri. Microwave tomography techniques and algorithms: A review. In *2012 15 International Symposium on Antenna Technology and Applied Electromagnetics*, pages 1–4. IEEE, June 2012.

[171] Babette Mooijekind, Eline Flux, Annemieke I Buizer, Marjolein M van der Krogt, and Lynn Bar-On. The influence of wearing an ultrasound device on gait in children with cerebral palsy and typically developing children. *Gait Posture*, 101:138–144, March 2023.

[172] Antoine Muller, Charles Pontonnier, and Georges Dumont. Uncertainty propagation in multibody human model dynamics. *Multibody Syst. Dyn.*, 40(2):177–192, June 2017.

[173] Koji Murakami, Satoshi Hamai, Ken Okazaki, Yifeng Wang, Satoru Ikebe, Hidehiko Higaki, Takeshi Shimoto, Hideki Mizu-Uchi, Yukio Akasaki, and Yasuharu Nakashima. In vivo kinematics of gait in posterior-stabilized and bicruciate-stabilized total knee arthroplasties using image-matching techniques. *Int. Orthop.*, 42(11):2573–2581, November 2018.

[174] Casey A Myers, Peter J Laz, Kevin B Shelburne, and Bradley S Davidson. A probabilistic approach to quantify the impact of uncertainty propagation in musculoskeletal simulations. *Ann. Biomed. Eng.*, 43(5):1098–1111, May 2015.

[175] Levon N Nazarian. The top 10 reasons musculoskeletal sonography is an important complementary or alternative technique to MRI. *AJR Am. J. Roentgenol.*, 190(6):1621–1626, June 2008.

[176] Manfred Nelitz. Femoral derotational osteotomies. *Curr. Rev. Musculoskelet. Med.*, 11(2):272–279, June 2018.

[177] E Nomura, Y Horiuchi, and M Inoue. Correlation of MR imaging findings and open exploration of medial patellofemoral ligament injuries in acute patellar dislocations. *Knee*, 9(2):139–143, May 2002.

[178] J Ojeda, J Martínez-Reina, and J Mayo. A method to evaluate human skeletal models using marker residuals and global optimization. *Mech. Mach. Theory*, 73:259–272, March 2014.

[179] J Ojeda, J Martínez-Reina, and J Mayo. The effect of kinematic constraints in the inverse dynamics problem in biomechanics. *Multibody Syst. Dyn.*, 37(3):291–309, July 2016.

[180] Bárbara L Oliveira, Declan O'Loughlin, Martin O'Halloran, Emily Porter, Martin Glavin, and Edward Jones. Microwave breast imaging: experimental tumour phantoms for the evaluation of new breast cancer diagnosis systems. *Biomed. Phys. Eng. Express*, 4(2):025036, February 2018.

[181] Declan O'Loughlin, Barbara L Oliveira, Adam Santorelli, Emily Porter, Martin Glavin, Edward Jones, Milica Popovic, and Martin O'Halloran. Sensitivity and specificity estimation using patient-specific microwave imaging in diverse experimental breast phantoms. *IEEE Trans. Med. Imaging*, 38(1):303–311, January 2019.

[182] Declan O'Loughlin, Bárbara L Oliveira, Muhammad Adnan Elahi, Martin Glavin, Edward Jones, Milica Popović, and Martin O'Halloran. Parameter search algorithms for microwave radar-based breast imaging: Focal quality metrics as fitness functions. *Sensors (Basel)*, 17(12), December 2017.

[183] Muhammad Omer, Pedram Mojabi, Douglas Kurrant, Joe LoVetri, and Elise Fear. Proof-of-concept of the incorporation of ultrasound-derived structural information into microwave radar imaging. *IEEE J. Multiscale Multiphys. Comput. Tech.*, 3:129–139, 2018.

[184] M Ostadrahimi, P Mojabi, C Gilmore, A Zakaria, S Noghanian, S Pistorius, and J LoVetri. Analysis of incident field modeling and incident/scattered field calibration techniques in microwave tomography. *IEEE Antennas Wirel. Propag. Lett.*, 10:900–903, 2011.

[185] Majid Ostadrahimi, Puyan Mojabi, Amer Zakaria, Joe LoVetri, and Lotfollah Shafai. Enhancement of gauss–newton inversion method for biological tissue imaging. *IEEE Trans. Microw. Theory Tech.*, 61(9):3424–3434, September 2013.

[186] Sylvia Ounpuu, Peter DeLuca, Roy Davis, and Mark Romness. Long-term effects of femoral derotation osteotomies: an evaluation using three-dimensional gait analysis. *J. Pediatr. Orthop.*, 22(2):139–145, March 2002.

[187] Jihong Park, Matthew K Seeley, Devin Francom, C Shane Reese, and J Ty Hopkins. Functional vs. traditional analysis in biomechanical gait data: An alternative statistical approach. *J. Hum. Kinet.*, 60:39–49, December 2017.

[188] Won-Kwang Park. Multi-frequency subspace migration for imaging of perfectly conducting, arc-like cracks. *arXiv [math-ph]*, pages 52–80, June 2013.

[189] Won-Kwang Park. Real-time microwave imaging of unknown anomalies via scattering matrix. *Mech. Syst. Signal Process.*, 118:658–674, March 2019.

[190] Won-Kwang Park, Hwa Pyung Kim, Kwang-Jae Lee, and Seong-Ho Son. MUSIC algorithm for location searching of dielectric anomalies from S-parameters using microwave imaging. *J. Comput. Phys.*, 348:259–270, November 2017.

[191] Todd C Pataky, Mark A Robinson, and Jos Vanrenterghem. Vector field statistical analysis of kinematic and force trajectories. *J. Biomech.*, 46(14):2394–2401, September 2013.

[192] Todd C Pataky, Jos Vanrenterghem, and Mark A Robinson. Zero- vs. one-dimensional, parametric vs. non-parametric, and confidence interval vs. hypothesis testing procedures in one-dimensional biomechanical trajectory analysis. *J. Biomech.*, 48(7):1277–1285, May 2015.

[193] Alana Peters, Brook Galna, Morgan Sangeux, Meg Morris, and Richard Baker. Quantification of soft tissue artifact in lower limb human motion analysis: a systematic review. *Gait Posture*, 31(1):1–8, January 2010.

[194] Alana Peters, Morgan Sangeux, Meg E Morris, and Richard Baker. Determination of the optimal locations of surface-mounted markers on the tibial segment. *Gait Posture*, 29(1):42–48, January 2009.

[195] Zoé Pomarat, Sacha Guitteny, Raphaël Dumas, and Antoine Muller. Kinetics influence of multibody kinematics optimisation for soft tissue artefact compensation. *J. Biomech.*, 150(111514):111514, March 2023.

[196] Emily Porter, Hadi Bahrami, Adam Santorelli, Benoit Gosselin, Leslie A Rusch, and Milica Popovic. A wearable microwave antenna array for time-domain breast tumor screening. *IEEE Trans. Med. Imaging*, 35(6):1501–1509, June 2016.

[197] Emily Porter, Adam Santorelli, Mark Coates, and Milica Popovic. Time-domain microwave breast cancer detection: extensive system testing with phantoms. *Technol. Cancer Res. Treat.*, 12(2):131–143, April 2013.

[198] Brigitte M Potvin, Mohammad S Shourijeh, Kenneth B Smale, and Daniel L Benoit. A practical solution to reduce soft tissue artifact error at the knee using adaptive kinematic constraints. *J. Biomech.*, 62:124–131, September 2017.

[199] P Puchaud, C Sauret, A Muller, N Bideau, G Dumont, H Pillet, and C Pontonnier. Accuracy and kinematics consistency of marker-based scaling approaches on a lower limb model: a comparative study with imagery data. *Comput. Methods Biomech. Biomed. Engin.*, 23(3):114–125, February 2020.

[200] Vignesh Radhakrishnan, Peter Ellison, Samadhan Patil, Adar Pelah, and Martin Robinson. Determining bone position from wearable antennas using microwave imaging: A feasibility study. In *2023 XXXVth General Assembly and Scientific Symposium of the International Union of Radio Science (URSI GASS)*, pages 1–4. IEEE, August 2023.

[201] Vignesh Radhakrishnan, Samadhan Patil, Adar Pelah, and Peter Ellison. Influence of multibody kinematic optimisation pipeline on marker residual errors. *J. Biomech.*, 177(112395):112395, November 2024.

[202] Vignesh Radhakrishnan, Samadhan Bhaulal Patil, Adar Pelah, and Peter John Ellison. Analysing the effect of body fat on musculoskeletal modelling systems:a pilot study. In *Annual Meeting of the Clinical Movement Analysis Society 2023*, GBR, April 2023.

[203] Vignesh Radhakrishnan, Martin Robinson, Niccolo M Fiorentino, Samadhan Patil, and Adar Pelah. Reducing soft tissue artefacts through projection of markers and microwave imaging: An exploratory study. *Research Square*, September 2024.

[204] Vignesh Radhakrishnan, Martin Paul Robinson, Peter John Ellison, Samadhan Bhaulal Patil, and Adar Pelah. Determining bone position using microwave imaging: A feasibility study. In *IPEM Science, Technology and Engineering Forum 2023*, February 2023.

[205] Apoorva Rajagopal, Christopher L Dembia, Matthew S DeMers, Denny D Delp, Jennifer L Hicks, and Scott L Delp. Full-body musculoskeletal model for muscle-driven simulation of human gait. *IEEE Trans. Biomed. Eng.*, 63(10):2068–2079, October 2016.

[206] T Reimer, D Rodriguez Herrera, M S Nepote, and S Pistorius. The use of a novel microwave radar reconstruction algorithm to image lesions in realistic 3D breast phantoms. In *12th European Conference on Antennas and Propagation (EuCAP 2018)*, pages 1–5. Institution of Engineering and Technology, April 2018.

[207] Tyson Reimer, Jordan Krenkevich, and Stephen Pistorius. An open-access experimental dataset for breast microwave imaging. In *2020 14th European*

Conference on Antennas and Propagation (EuCAP), pages 1–5. IEEE, March 2020.

[208] Tyson Reimer and Stephen Pistorius. An optimization-based approach to radar image reconstruction in breast microwave sensing. *Sensors (Basel)*, 21(24):8172, December 2021.

[209] Tyson Reimer and Stephen Pistorius. Review and analysis of tumour detection and image quality analysis in experimental breast microwave sensing. *Sensors (Basel)*, 23(11), May 2023.

[210] Tyson Reimer, Mario Solis-Nepote, and Stephen Pistorius. The application of an iterative structure to the delay-and-sum and the delay-multiply-and-sum beamformers in breast microwave imaging. *Diagnostics (Basel)*, 10(6):411, June 2020.

[211] Vincent Richard, Aurelio Cappozzo, and Raphaël Dumas. Comparative assessment of knee joint models used in multi-body kinematics optimisation for soft tissue artefact compensation. *J. Biomech.*, 62:95–101, September 2017.

[212] D Gordon E Robertson, Graham E Caldwell, Joseph Hamill, Gary Kamen, and Saunders N Whittlesey. *Research Methods in Biomechanics*. Human Kinetics, Champaign, IL, 2 edition, November 2013.

[213] M P Robinson, I D Flintoft, L Dawson, J Clegg, J G Truscott, and X Zhu. Application of resonant cavity perturbation toin vivosegmental hydration measurement. *Meas. Sci. Technol.*, 21(1):015804, January 2010.

[214] M P Robinson, M J Richardson, J L Green, and A W Preece. New materials for dielectric simulation of tissues. *Phys. Med. Biol.*, 36(12):1565–1571, December 1991.

[215] David O Rodriguez-Duarte, Jorge A Tobon Vasquez, Rosa Scapaticci, Lorenzo Crocco, and Francesca Vipiana. Brick-shaped antenna module for microwave brain imaging systems. *IEEE Antennas Wirel. Propag. Lett.*, 19(12):2057–2061, December 2020.

[216] Nicholas Rowe, Cassandra E Robertson, Stuti Singh, John T Campbell, and Clifford L Jeng. Weightbearing CT analysis of the transverse tarsal joint during eversion and inversion. *Foot Ankle Int.*, 43(1):123–130, January 2022.

[217] Giuseppe Ruvio, Antonio Cuccaro, Raffaele Solimene, Adriana Brancaccio, Bruno Basile, and Max J Ammann. Microwave bone imaging: a preliminary

scanning system for proof-of-concept. *Healthc. Technol. Lett.*, 3(3):218–221, September 2016.

[218] Giuseppe Ruvio, Raffaele Solimene, Antonio Cuccaro, and Max J Ammann. Comparison of noncoherent linear breast cancer detection algorithms applied to a 2-D numerical model. *IEEE Antennas Wirel. Propag. Lett.*, 12:853–856, 2013.

[219] Giuseppe Ruvio, Raffaele Solimene, Antonio Cuccaro, Domenico Gaetano, Jacinta E Browne, and Max J Ammann. Breast cancer detection using interferometric MUSIC: experimental and numerical assessment: Breast cancer detection using interferometric MUSIC. *Med. Phys.*, 41(10):103101, October 2014.

[220] Giuseppe Ruvio, Raffaele Solimene, Antonietta D'Alterio, Max J Ammann, and Rocco Pierri. RF breast cancer detection employing a noncharacterized vivaldi antenna and a MUSIC-inspired algorithm. *Int. J. RF Microw. Comput-Aid. Eng.*, 23(5):598–609, September 2013.

[221] Imran Saied and Tughrul Arslan. Microwave imaging algorithm for detecting brain disorders. In *2019 29th International Conference Radioelektronika (RADIOELEKTRONIKA)*, pages 1–5. IEEE, April 2019.

[222] Sara M Salvador, Elise C Fear, Michal Okoniewski, and John R Matyas. Exploring joint tissues with microwave imaging. *IEEE Trans. Microw. Theory Tech.*, 58(8):2307–2313, August 2010.

[223] Kesia C Santos, Carlos A Fernandes, and Jorge R Costa. Validation of a compact microwave imaging system for bone fracture detection. *IEEE Access*, 11:63690–63700, 2023.

[224] M Sati, J A de Guise, S Larouche, and G Drouin. Quantitative assessment of skin-bone movement at the knee. *Knee*, 3(3):121–138, August 1996.

[225] Amir Hossein Saveh, Hamid Reza Katouzian, and Mahmoud Chizari. Measurement of an intact knee kinematics using gait and fluoroscopic analysis. *Knee Surg. Sports Traumatol. Arthrosc.*, 19(2):267–272, February 2011.

[226] Nicola Scafetta, Damiano Marchi, and Bruce J West. Understanding the complexity of human gait dynamics. *Chaos*, 19(2):026108, June 2009.

[227] R Schmidt. Multiple emitter location and signal parameter estimation. *IEEE Trans. Antennas Propag.*, 34(3):276–280, March 1986.

[228] Michael H Schwartz, Joyce P Trost, and Roy A Wervey. Measurement and management of errors in quantitative gait data. *Gait Posture*, 20(2):196–203, October 2004.

[229] Serguei Semenov, James Kellam, Peter Althausen, Thomas Williams, Aria Abubakar, Alexander Bulyshev, and Yuri Sizov. Microwave tomography for functional imaging of extremity soft tissues: feasibility assessment. *Phys. Med. Biol.*, 52(18):5705–5719, September 2007.

[230] Serguei Semenov, James Kellam, Bindu Nair, Thomas Williams, Michael Quinn, Yuri Sizov, Alexei Nazarov, and Andrey Pavlovsky. Microwave tomography of extremities: 2. functional fused imaging of flow reduction and simulated compartment syndrome. *Phys. Med. Biol.*, 56(7):2019–2030, April 2011.

[231] Ajay Seth, Michael Sherman, Peter Eastman, and Scott Delp. Minimal formulation of joint motion for biomechanisms. *Nonlinear Dyn.*, 62(1):291–303, October 2010.

[232] Seyed Abbas Shah Karam, Declan O'Loughlin, Barbara Luz Oliveira, Martin O'Halloran, and Babak Mohammadzadeh Asl. Weighted delay-and-sum beamformer for breast cancer detection using microwave imaging. *Measurement (Lond.)*, 177(109283):109283, June 2021.

[233] J M Sill and E C Fear. Tissue sensing adaptive radar for breast cancer detection: preliminary experimental results. In *IEEE MTT-S International Microwave Symposium Digest, 2005*, pages 1789–1792. IEEE, 2005.

[234] J M Sill and E C Fear. Tissue sensing adaptive radar for breast cancer detection—experimental investigation of simple tumor models. *IEEE Trans. Microw. Theory Tech.*, 53(11):3312–3319, November 2005.

[235] Annelise A Slater, Todd J Hullfish, and Josh R Baxter. The impact of thigh and shank marker quantity on lower extremity kinematics using a constrained model. *BMC Musculoskelet. Disord.*, 19(1):399, November 2018.

[236] Kenneth B Smale, Brigitte M Potvin, Mohammad S Shourijeh, and Daniel L Benoit. Knee joint kinematics and kinetics during the hop and cut after soft tissue artifact suppression: Time to reconsider ACL injury mechanisms? *J. Biomech.*, 62:132–139, September 2017.

[237] Behnaz Sohani, Banafsheh Khalesi, Navid Ghavami, Mohammad Ghavami, Sandra Dudley, Amir Rahmani, and Gianluigi Tiberi. Detection of haemorrhagic stroke in simulation and realistic 3-D human head phantom using

microwave imaging. *Biomed. Signal Process. Control*, 61(102001):102001, August 2020.

[238] Seong-Ho Son, Kwang-Jae Lee, and Won-Kwang Park. Real-time tracking of moving objects from scattering matrix in real-world microwave imaging. *AIMS Math.*, 9(6):13570–13588, 2024.

[239] C W Spoor and F E Veldpaus. Rigid body motion calculated from spatial co-ordinates of markers. *J. Biomech.*, 13(4):391–393, 1980.

[240] R Stagni, A Leardini, A Cappozzo, M Grazia Benedetti, and A Cappello. Effects of hip joint centre mislocation on gait analysis results. *J. Biomech.*, 33(11):1479–1487, November 2000.

[241] Rita Stagni, Silvia Fantozzi, and Angelo Cappello. Double calibration vs. global optimisation: performance and effectiveness for clinical application. *Gait Posture*, 29(1):119–122, January 2009.

[242] Rita Stagni, Silvia Fantozzi, Angelo Cappello, and Alberto Leardini. Quantification of soft tissue artefact in motion analysis by combining 3D fluoroscopy and stereophotogrammetry: a study on two subjects. *Clin. Biomech. (Bristol, Avon)*, 20(3):320–329, March 2005.

[243] Katherine M Steele, Ajay Seth, Jennifer L Hicks, Michael H Schwartz, and Scott L Delp. Muscle contributions to vertical and fore-aft accelerations are altered in subjects with crouch gait. *Gait Posture*, 38(1):86–91, May 2013.

[244] A Stogryn. Equations for calculating the dielectric constant of saline water (correspondence). *IEEE Trans. Microw. Theory Tech.*, 19(8):733–736, August 1971.

[245] Kamel S Sultan, Beadaa Mohammed, Mohamed Manoufali, and Amin M Abbosh. Portable electromagnetic knee imaging system. *IEEE Trans. Antennas Propag.*, 69(10):6824–6837, October 2021.

[246] Jennifer Summers, Bola Coker, Saskia Eddy, Maria Elstad, Catey Bunce, Elli Bourmpaki, Mark Pennington, Kristian Aquilina, Stephanie Cawker, Richard Edwards, John Goodden, Sally Hawes, Kate McCune, Benedetta Pettorini, Jennifer Smith, Christine Sneade, Michael Vloeberghs, Hannah Patrick, Helen Powell, Christopher Verity, Janet L Peacock, and Selective Dorsal Rhizotomy Steering Committee. Selective dorsal rhizotomy in ambulant children with cerebral palsy: an observational cohort study. *Lancet Child Adolesc. Health*, 3(7):455–462, July 2019.

[247] Inge Söderkvist and Per-Åke Wedin. Determining the movements of the skeleton using well-configured markers. *J. Biomech.*, 26(12):1473–1477, December 1993.

[248] William R Taylor, Rainald M Ehrig, Georg N Duda, Hanna Schell, Petra Seebeck, and Markus O Heller. On the influence of soft tissue coverage in the determination of bone kinematics using skin markers. *J. Orthop. Res.*, 23(4):726–734, July 2005.

[249] William R Taylor, Pascal Schütz, Georg Bergmann, Renate List, Barbara Postolka, Marco Hitz, Jörn Dymke, Philipp Damm, Georg Duda, Hans Gerber, Verena Schwachmeyer, Seyyed Hamed Hosseini Nasab, Adam Trepczynski, and Ines Kutzner. A comprehensive assessment of the musculoskeletal system: The CAMS-knee data set. *J. Biomech.*, 65:32–39, December 2017.

[250] A Thouzé, T Monnet, C Bélaise, P Lacouture, and M Begon. A chain kinematic model to assess the movement of lower-limb including wobbling masses. *Comput. Methods Biomech. Biomed. Engin.*, 19(7):707–716, 2016.

[251] Jorge A Tobon Vasquez, Rosa Scapaticci, Giovanna Turvani, Gennaro Bellizzi, Nadine Joachimowicz, Bernard Duchêne, Enrico Tedeschi, Mario R Casu, Lorenzo Crocco, and Francesca Vipiana. Design and experimental assessment of a 2D microwave imaging system for brain stroke monitoring. *Int. J. Antennas Propag.*, 2019(1):1–12, May 2019.

[252] Thomas K Uchida and Ajay Seth. Conclusion or illusion: Quantifying uncertainty in inverse analyses from marker-based motion capture due to errors in marker registration and model scaling. *Front. Bioeng. Biotechnol.*, 10:874725, May 2022.

[253] Rahmat Ullah, Imran Saied, and Tughrul Arslan. Multistatic radar-based imaging in layered and dispersive media for biomedical applications. *Biomed. Signal Process. Control*, 82(104568):104568, April 2023.

[254] Shahid Ullah and Caroline F Finch. Applications of functional data analysis: A systematic review. *BMC Med. Res. Methodol.*, 13(1):43, March 2013.

[255] Peter M van den Berg and Ralph E Kleinman. A contrast source inversion method. *Inverse Probl.*, 13(6):1607–1620, December 1997.

[256] Antonie J van den Bogert and Anne Su. XXXIII congress of the société de biomécanique: 1-3 september 2008 université de technologie de compiègne centre pierre guillaumat compiègne, france. *Comput. Methods Biomech. Biomed. Engin.*, 11(1):3–9, February 2008.

[257] F E Veldpaus, H J Woltring, and L J Dortmans. A least-squares algorithm for the equiform transformation from spatial marker co-ordinates. *J. Biomech.*, 21(1):45–54, 1988.

[258] Y M Wang and W C Chew. An iterative solution of the two-dimensional electromagnetic inverse scattering problem. *Int. J. Imaging Syst. Technol.*, 1(1):100–108, June 1989.

[259] David E Westberry, Linda I Wack, Roy B Davis, and James W Hardin. Femoral anteversion assessment: Comparison of physical examination, gait analysis, and EOS biplanar radiography. *Gait Posture*, 62:285–290, May 2018.

[260] Tishya A L Wren, Christopher Lening, Susan A Rethlefsen, and Robert M Kay. Impact of gait analysis on correction of excessive hip internal rotation in ambulatory children with cerebral palsy: a randomized controlled trial. *Dev. Med. Child Neurol.*, 55(10):919–925, October 2013.

[261] Tishya A L Wren, Susan Rethlefsen, and Robert M Kay. Prevalence of specific gait abnormalities in children with cerebral palsy: influence of cerebral palsy subtype, age, and previous surgery. *J. Pediatr. Orthop.*, 25(1):79–83, January 2005.

[262] G Wu and P R Cavanagh. ISB recommendations for standardization in the reporting of kinematic data. *J. Biomech.*, 28(10):1257–1261, October 1995.

[263] Ge Wu, Sorin Siegler, Paul Allard, Chris Kirtley, Alberto Leardini, Dieter Rosenbaum, Mike Whittle, Darryl D D'Lima, Luca Cristofolini, Hartmut Witte, Oskar Schmid, and Ian Stokes. ISB recommendation on definitions of joint coordinate system of various joints for the reporting of human joint motion—part I: ankle, hip, and spine. *J. Biomech.*, 35(4):543–548, April 2002.

[264] G T Yamaguchi and F E Zajac. A planar model of the knee joint to characterize the knee extensor mechanism. *J. Biomech.*, 22(1):1–10, 1989.

[265] Mehmet E Yavuz and Fernando L Teixeira. On the sensitivity of time-reversal imaging techniques to model perturbations. *IEEE Trans. Antennas Propag.*, 56(3):834–843, March 2008.

[266] Amer Zakaria, Colin Gilmore, and Joe LoVetri. Finite-element contrast source inversion method for microwave imaging. *Inverse Probl.*, 26(11):115010, November 2010.

[267] Fatima-Ezzahra Zerrad, Mohamed Taouzari, El Mostafa Makroum, Jamal El Aoufi, Mohammad Tarikul Islam, Vedat Özkaner, Yadgar I Abdulkarim, and Muharrem Karaaslan. Multilayered metamaterials array antenna based on artificial magnetic conductor's structure for the application diagnostic breast cancer detection with microwave imaging. *Med. Eng. Phys.*, 99(103737):103737, January 2022.